UNIVERSITAT POLITÈCNICA DE CATALUNYA

Minimisation of the wire position uncertainties of the new CERN vacuum wire scanner

Juan F. Herranz Álvarez

Barcelona, January 2016

UNIVERSITAT POLITÈCNICA DE CATALUNYA

Departament d'Enginyeria Mecànica

Escola Tècnica Superior d'Enginyeria Industrial de Barcelona

Minimisation of the wire position uncertainties of the new CERN vacuum wire scanner

Tesi presentada per obtenir el títol de
Doctor per la Universitat Politècnica de Catalunya
en el programa d'Enginyeria Mecànica, Fuids i Aeronàutica

per

Juan F. Herranz Álvarez

Directors:

Dr. Ana Barjau Condomines
Dr. Bernd Dehning

Barcelona, Gener 2016

Abstract

In the next years the luminosity of the LHC will be significantly increased. This will require a much higher accuracy of beam profile measurement than actually achievable by the current wire scanner. The new fast wire scanner is foreseen to measure small emittance beams throughout the LHC injector chain, which demands a wire travelling speed up to 20 ms^{-1} and position measurement accuracy of the order of a few microns. The vibrations of the mechanical parts of the system, and particularly the vibrations of the thin carbon wire, were identified as the major error sources of wire position uncertainty. Therefore the understanding of the wire vibrations is a high priority for the design and operation of the new device. This document presents the work performed to understand the main causes of the wire vibrations observed in one of the existing wire scanner and the new proposed design.

Key words: wire-scanner, wire vibration measurements, piezoresistive effect, strain gauges, wire dynamic models, motion pattern.

Preface

The particle production of an accelerator is characterised by the accelerated species of particles, by their number and energy. The particle rate is determined by the production cross section, a natural constant and the accelerator dependent parameter luminosity. The luminosity is proportional to the number of particles in each beam and inversely proportional to the particle beam transverse dimensions. The luminosity increases with the particle beam density and therefore the probability of interactions too. To optimize the transverse beam sizes, profile monitors are used to measure parameter depending changes.

Different monitors can provide beam transversal profile measurements (Wire Scanners, Synchrotron Light Monitors, Rest Gas Profile Monitors), however the wire scanner monitor is considered to be the most accurate of all monitors. Wire scanner instruments measure the transverse beam density profile in a particle accelerator by means of moving a thin wire in an intermittent manner.

In the next years the luminosity of the Large Hadron Collider (LHC) will be significantly increased and more accurate beam profile measurement will be necessary. The new performance demands a wire travelling speed up to 20 m/s and a position measurement accuracy of the order of few microns. The existing wire scanners do not reach the new requirements as their accuracy achieved is limited by the motorization, the angular position measurement system located outside of the vacuum vessels and the vibration of the thin carbon wire which has been identified as one of the major error sources reducing the knowledge of the wire position. Therefore the development of a new device whose accuracy meets the new requirements was mandatory.

This thesis work aims to provide suitable inputs for the design and operation of this new fast wire scanner in order to minimize the uncertainties in the wire position. To accomplish the aims the understanding of the wire vibrations in such a system is one of the main goals of this work. More specifically, the development of a suitable vibration measurement system and the construction of dynamic models of the system are the two goals aimed. For the new scanner design this work intend to propose the conceptual design, the optimization of the most critical parts and the operation procedure that will allow the new device to reach the required performances imposed by the forthcoming LHC conditions.

Acknowledgments

In the following lines I would like to use my mother tongue, I consider it more appropriate to express my feelings in a precise manner.

En primer lugar quiero agradecer a mis supervisores Dra. Ana Barjau y Dr. Bernd Dehning el haberme dado la oportunidad de realizar este trabajo bajo su supervisión y especialmente su constante disponibilidad a la hora de resolver tantas y tantas cuestiones. Sobre todo les quiero dejar constar mi más sincero agradecimiento por haberme transmitido su entusiasmo y constancia por la investigación, esto es sin duda la mejor lección que he recibido de ellos.

Mi gratitud también a todo el grupo de Beam Instrumentation y de manera particular a los equipos de las secciones BL y ML, por su ayuda, apoyo y amistad. De manera especial me gustaría agradecer a Jonathan Emery todo el tiempo que me ha dedicado, sobre todo porque a pesar de sus muchas e importantes obligaciones, siempre ha encontrado un momento para responder a mis preguntas y ayudarme a realizar todas esas medidas.

A Ewald Effiger y a Eduardo Nebot Del Busto les quiero dar las gracias de todo corazón, no sólo por su ayuda en innumerables cuestiones relacionadas con este trabajo, sino también y de manera muy especial, por haberme alentado en esta "carrera" de una manera tan sincera y desinteresada.

De manera muy especial quiero agradecer el apoyo de la persona que más me ha ayudado a seguir adelante cada día y a la que sin duda más tiempo de convivencia y momentos de felicidad le he robado con esta aventura. A ella, y a mi familia les quiero dedicar este trabajo por su incondicional ayuda en los momentos difíciles.

Contents

List of Figures

List of Tables

1. Introduction

The subject of the thesis is embedded in the luminosity optimization program for the Large Hadron Collider (LHC) at CERN.

CERN, the European Organization for Nuclear Research, is an intergovernmental organization with 21 Member States. Its seat is in Geneva but its premises are located on both sides of the French-Swiss border. CERN's mission is to enable international collaboration in the field of high-energy particle physics research and to this end it designs, builds and operates particle accelerators and the associated experimental areas. At present more than 10 000 scientific users from research institutes all over the world are using CERN's installations for their experiments.

The accelerator complex at CERN is a succession of machines with increasingly higher energies. Each machine injects the beam into the next one, which takes over to bring the beam to an even higher energy. The flagship of this complex is the LHC as presented in Figure 1.1, which is an illustration of the CERN accelerator infrastructure.

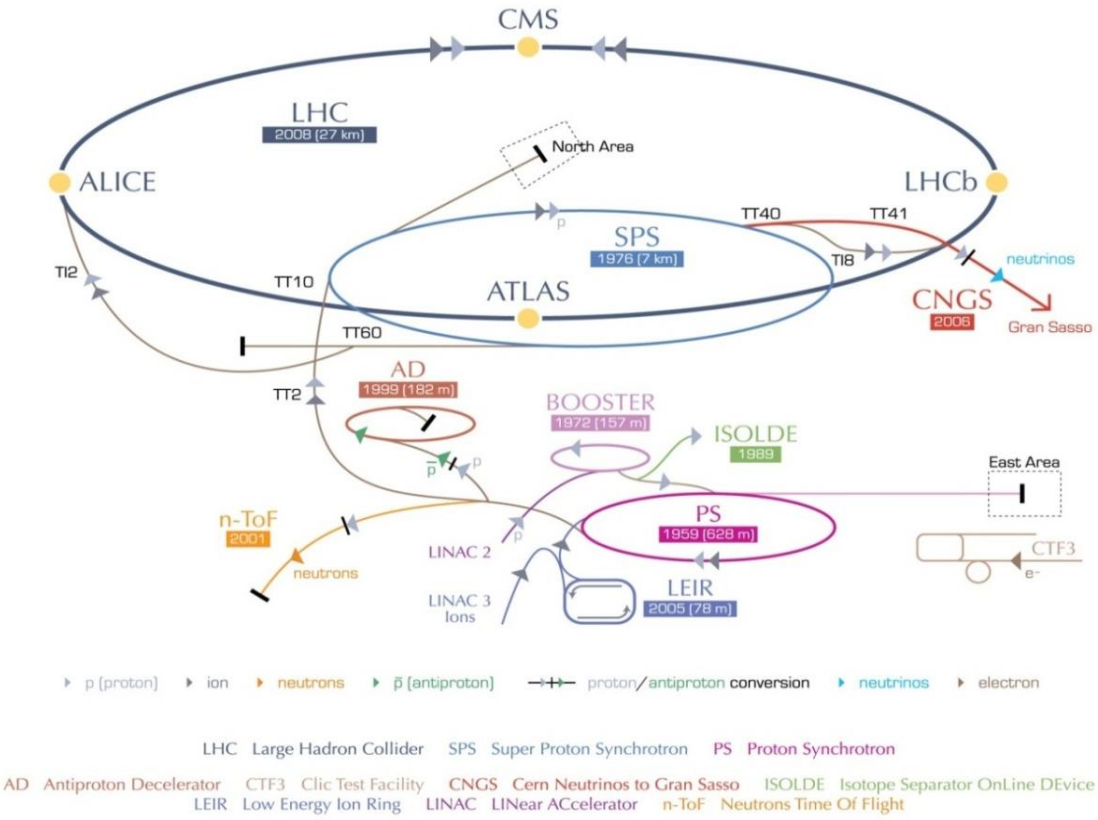

Figure 1.1: Schematic of the CERN accelerators complex with the proton source at LINAC 2 providing the particles for collision at the LHC ring detectors CMS, LHCb, ATLAS and ALICE.

1.1. Introduction to LHC

The LHC is the world's largest and most powerful particle accelerator. It first started up on 10 September 2008, and remains the latest addition to CERN's accelerator complex. The LHC machine accelerates and collides proton beams and also heavier ions up to lead. It is installed in a 27 km circumference tunnel, about 100 m underground. The LHC consists of a 27-kilometre ring, which includes superconducting twin-aperture cryo-magnets operating in a superfluid helium bath at 1.9 K, and accelerating structures needed to boost the energy of the particles.

Just prior to the collision points, magnets are also used to "squeeze" the particles closer together to increase the chances of collisions. The beams collide at four locations around the accelerator ring, corresponding to the positions of four particle detectors CMS, LHCb, ATLAS and ALICE (see Figure 1.1).

1.1.1. Particle production considerations

The particle production requirements of an accelerator are determined by the desired particle type, quantity, energy, emittance and energy spread. The particle rate ($\dot{n}$) is determined by the production cross section (σ), a natural constant and the accelerator dependent parameter luminosity (L).

$$\dot{n} = L\sigma \tag{1.1}$$

Considering two beams colliding at zero crossing angle with the same transverse particles distribution, luminosity can be calculated as follow:

$$L = f\frac{n_1 n_2}{4\pi\sigma_x\sigma_y} \tag{1.2}$$

n_1 and n_2 are the number of particles per bunch in the two colliding beams, f is the collision repetition frequency and σ_x and σ_y are the parameters describing the beam sizes.

Therefore L is proportional to the number of particles in each beam and inversely proportional to the particle beam transverse dimensions. Although the beam transversal dimension $\sigma_{x,y}$ varies at different location *s* of the accelerator and cannot be measured at the colliding points (where beam sizes are needed to predict the luminosity), it can be associated with the beam transverse emittance (ε) which is invariant:

$$\sigma_{x,y}(s) = \sqrt{\beta_{x,y}(s)\ \ \varepsilon_{x,y}} \tag{1.3}$$

Hence measuring the transverse beam intensity distribution $\sigma_{x,y}$, at a location in the ring and knowing the beam optical function $\beta_{x,y}(s)$ allows to determine the beam emittance and consequently the beam sizes at the interaction points. Therefore the luminosity can be derived and the collider performance predicted.

1.1.2. Beam profile measurement

In a very simplified way one could say that beam profile measurements would provide the beam particle density distribution at a cross-section perpendicular to the beam travel direction. Typically beam profile measurements provide the beam particle distribution along two transverse orthogonal axes, vertical and horizontal of the beam cross-section.

In the LHC three different types of profile monitors are installed:

- Wire Scanners.
- Synchrotron Light Monitors.
- Rest Gas Profile Monitors.

The wire scanner monitor is considered to be the most accurate of the three and serves as a calibration device for the others. So far the wire scanner is the only instrument capable of making high-accuracy absolute beam size measurements. However its application for the circulating beams is limited to lower beam intensities due to the heat deposition of the particle beams in the wire and the secondary particles created in the wire impacting in the superconducting magnets. The synchrotron light monitors and the rest gas profile monitors allow a continuous beam observation, but with a limited accuracy in terms of beam position resolution.

1.2. Wire scanner description

A wire scanner (Figure 1.2) is an electro-mechanical device which measures the transverse beam density profile of a particle beam by means of moving a thin wire across the beam in an intermittent manner. As the wire passes through the beam the interaction generates a cascade of secondary particles. These are intercepted by a scintillator, which couples the photons generated by the incident particle to a photomultiplier (PMT), which provides an electrical signal proportional to the incident photon flux.

Typically for CERN rotating wire scanners, such as those used at the Proton Synchrotron (PS) and Super Proton Synchrotron (SPS), the wire position is measured with a precision rotary potentiometer. The potentiometer signal and the scintillator photomultiplier signal are digitized with synchronized ADCs to reconstruct the beam profile. Wire scanners are installed and operated on a daily basis at all CERN circular accelerators. However they present several drawbacks:

- For high intensity beams the energy deposited by the incident particles on the wire may be sufficient to melt or sublimate the wire.

- The wire can melt or sublimate also due to the energy transferred by the beam to the wire through its accompanying electromagnetic field.

- Inaccuracy of position measurements primarily due to vibrations and deflections of the wire and its supporting fork.

This work is mainly related to the latter of the drawbacks, the inaccuracy of position measurements. In the following lines this topic is briefly developed.

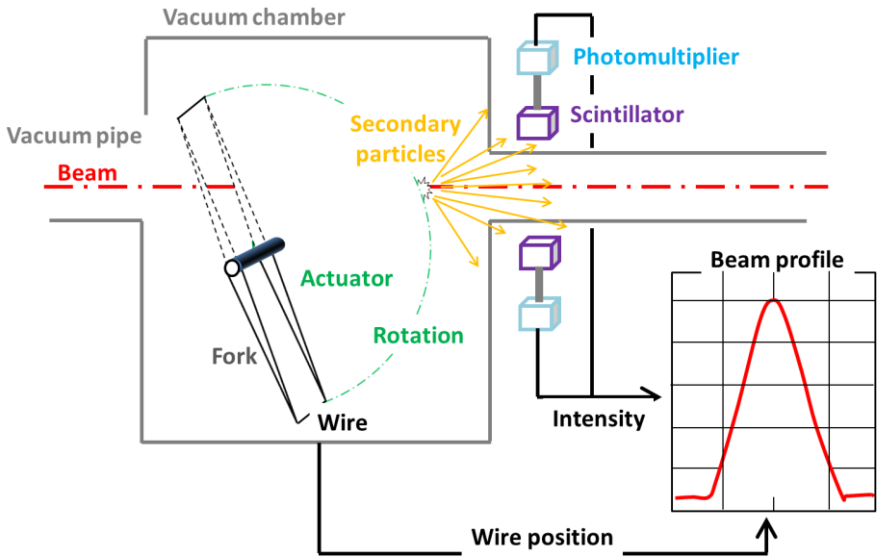

Figure 1.2: Illustration of the rotating wire scanner instrument.

The wire is stretched by a fork directly mounted on a shaft. The wire, fork and shaft are located in a vacuum chamber while the actuator is outside that chamber. The actuator provides a motion pattern consisting of three distinct phases (acceleration, constant speed and deceleration, Figure 1.3) fulfilling a set of requirements in order to achieve a suitable wire speed and position at beam crossing. Therefore the wire is crossing the beam in motion and consequently subjected to dynamic effects.

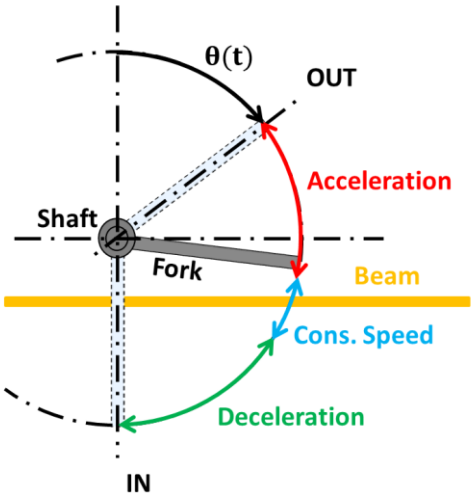

Figure 1.3: Illustration of a scan cycle.

As is explained in more detail in Chapter 3, the strong peak acceleration in the motion pattern induces deflections and vibrations on the measurement chain (shaft, fork and wire), which result in discrepancies between the true position of the wire and the position measured by the position sensor.

Errors on the wire position when intersecting the beam have a direct consequence on the profile and position measurement accuracy. Thus, identifying and minimizing the uncertainties and error sources is a priority.

1.3. System requirements

The most demanding requirements of the wire scanner system are.

- Measurement accuracy
- Wire speed

Before discussing and justifying these requirements some considerations regarding beam profile measurement and related parameters are necessary.

1.3.1. Accuracy requirements

The requirement of beam size measurement accuracy is related to the accuracy needed for the luminosity determination.

The relative beam width measurement error (δ^{rel}) is defind as follows:

$$\delta^{\mathrm{rel}} = \mu_{\sigma}^{\mathrm{rel}} \pm \delta_{\sigma}^{\mathrm{rel}} \tag{1.4}$$

$\mu_{\sigma}^{\mathrm{rel}}$ and $\delta_{\sigma}^{\mathrm{rel}}$ are the systematic and statistical relative errors respectively.

Under the assumption that systematic error contribution can be neglected by a proper calibration, $\mu_{\sigma}^{\mathrm{rel}} = 0$ and $\delta^{\mathrm{rel}} = \delta_{\sigma}^{\mathrm{rel}}$.

1.3.2. Wire Speed requirements

The wire speed requirement stems from the wire damage threshold. The wire is considered to be damaged when it is partially sublimated. Therefore the wire temperature needs to be kept significantly below the sublimation temperature. The temperature increase is mainly given by the heat capacity of the wire and by the particle beam energy deposition in the wire. Cooling mechanisms are insignificant, because of the short duration of energy deposition. Therefore higher wire traveling speed will reduce the energy deposition in the wire and in the downstream magnets.

Two effects lead to energy deposition in the wire:

- Charged particles interact with the wire lattice electrons (described by Bethe Bloch formula)
- Resistive heating by induced currents due to the electromagnetic fields of charged particle beams

In addition to the energy deposition in the wire by the beam the secondary particles can cause a quench of the downstream magnets. A part of the superconducting coil could undergo a transition from the superconducting state to the normal conducting state due to the deposited energy. Although the probability that a quench occurs is very low, because the magnet coils are protected by a measurement system, which dumps the beam if safety levels limits of particle impacts are exceeded. Frequent beam abort events reduce the operational efficiency of the LHC.

1.3.3. Final considerations

The measurement requirement of the transverse beam distribution in the LHC rings [1] established the maximum uncertainty for the beam size determination for the LHC beam to be 1.8%. Considering that the minimum LHC beam size is in the range of 160 μm, the uncertainty in the beam size determination by the wire scanner (δ_s) therefore has to be lower than 2.8 μm.

Experimental studies consisting of scanning a LHC beam at different speeds have been performed in order to determine wire damage limits. These studies also established wire damage levels as result of the beam-wire energy deposition as function of the wire speed [2]. The conclusions of these studies advocate a wire traveling speed on the range of 20m/s.

Therefore in order to improve the optimization of the luminosity in the LHC, the new performance demands a wire travelling speed of up to 20 m/s and position measurement accuracy of the order of 2.8 μm.

The achieved accuracy of existing 20 m/s scan speed devices is limited by the angular position measurement system located outside of the vacuum vessel and the bellows used to feed the movement into the vacuum tank. The lever arm based mechanisms (see Chapter 3) that increase the speed of the wire introduce further uncertainties. Moreover the residual vibrations produced in the mechanical parts of the system and in the wire by its motion represent an important source of a statistical error in the measurements.

Because of the limitations of the current wire scanner design in terms of its accuracy a new design of the wire scanner instrument was mandatory.

The minimization of vibrations can be achieved through the redesign of the main components of the system (optimize geometries, materials and configuration) and the optimization of the wire motion pattern. Both aspects call for the understanding of the dynamics of the system in order to predict its behaviour under such modifications. The development of a suitable dynamic model is thus necessary.

The wire position measurement errors are generated by different elements of the system; therefore it is required to have a good knowledge of the different error sources and their contribution to the total measured error. The analysis of accuracy limitations implies:

- Development of suitable experimental techniques to quantify the vibrations amplitude.
- Define calibration test bench designs to be used for the determination of the systematic measurement error.
- Propose suitable correction factor to the beam profile measurements.

1.4. Work description

The general objective of this thesis subject is to determine the sources of error yielding wire position measurement uncertainties of rotating wire scanners devices in order to provide suitable inputs for the optimal design and operation of the new fast wire scanner. The central subject of this work is the development of vibration measurement systems and the construction of dynamic models. The structure of this thesis subject and their interrelation are graphically shown in Figure 1.4.

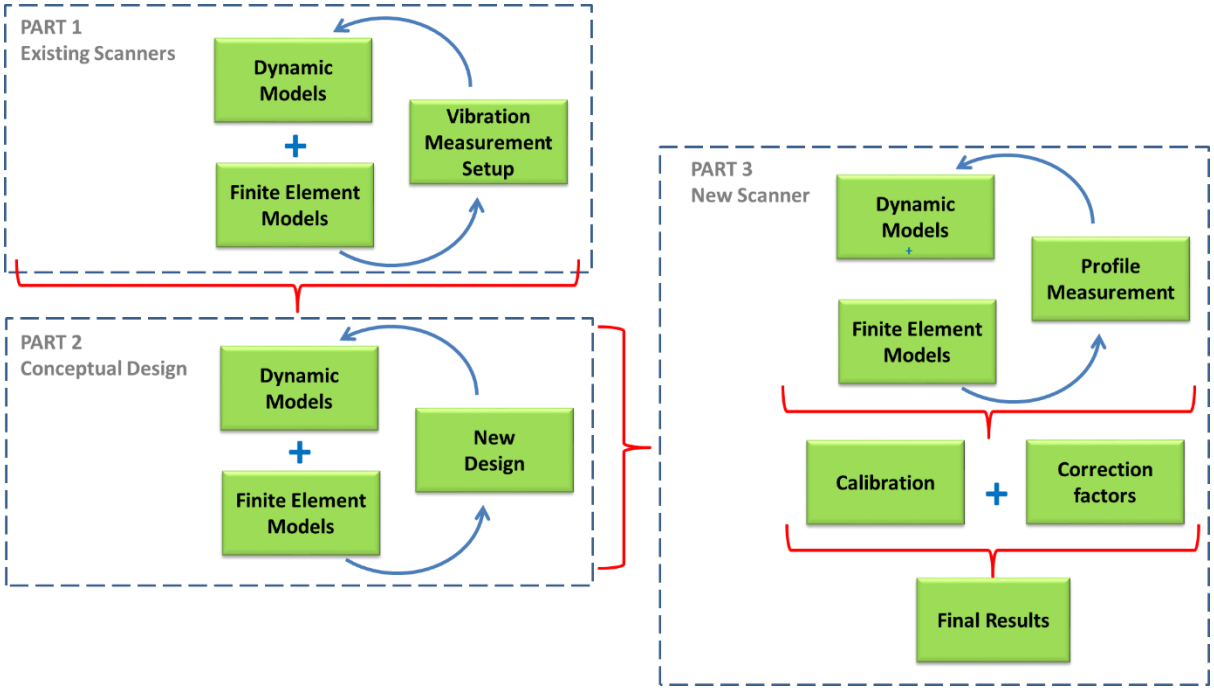

Figure 1.4: Interrelation between the different parts of this thesis work.

In part one of the work, several dynamic models and Finite Element Analyses (FEA) were developed to determine the expected vibrational behaviour of the system. The work also included the development of a vibration measurement system and its application on the existing PS scanner. This system has been used to measure the dynamic behaviour of the PS wire scanner and provide experimental data to tune and validate the dynamic and Finite Element Models (FEM).

The second part of the work involved a new conceptual design for a device to minimize or eliminate the different sources of error, based on the findings and conclusions from the first part of the work. This second part concludes with a final design for this new device, where the main parts of the system have been optimized with the help of the previous dynamic models and FEM.

Finally, the last part of the work, involves the optimisation of the device in operation, where the systematic measurement errors were corrected using specifically developed calibration test benches. Less predictable errors such as vibrations were corrected applying different correction strategies based on the experience gained with the vibration measurement setup and the dynamic models of the system.

The presentation of this work is organized in 7 Chapters. After this introduction, Chapter 2 provides an overview of the state of the art for the wire scanner instrument as well as for other technics used in this work (such as the measurement of vibrations). Chapter 3 presents the work performed on the existing wire scanners in order to analyse and determine the accuracy limitations in the current rotating wire scanners. The development and optimization of the experimental systems to measure the vibrations of different scanner elements is presented in Chapter 4. The access to existing rotating wire scanners currently in operation at CERN, PS and SPS has been a source of valuable information for the completion of these two previous chapters. Chapter 5 is devoted to the dynamic model developments and its tuning of the parameters based on the vibration measurement setups. Chapter 6 presents the new wire scanner design based on the findings and conclusions of Chapter 4 and 5. For each single source of error, an improvement is proposed to eliminate or minimize its contribution to the total error. In particular, the main parts of the system are optimized to minimize the residual vibration in the wire. Chapter 6 treats the new design for the wire scanner instrument, and also includes experimental measurements performed in a first prototype of wire scanner. A comparison of these measurements and those performed in the current design is also described. Finally, Chapter 7 presents the conclusions of this work.

2. State of the art

The present chapter summarizes the literature review performed for this thesis work. Although this work is mainly related to the wire scanner devices, other topics also relevant to the development of the work are included in the literature review. The performed literature review is focused on the following topics:

- Wire scanners instrument
- Wire vibration measurement
- Wire dynamic models

2.1. Wire scanners

As described in the introduction, wire scanner instruments are used on a regular basis in particle accelerators in order to provide valuable information for their operation.

For the purpose of this work the following criteria have been considered as most relevant for the classification of wire scanners:

Travel speed

According to the wire travel speed, scanners can be classified into *slow scanners* and *fast scanners* [3]. The speed of the scan is determined by the melting temperature of the wire [4] and the amount of secondary particles produced in the interaction between the wire and the beam of particles. Slow scanners are commonly used in linacs (linear accelerators) and transfer lines. Fast scanners are typically used in circular machines.

Type of displacement

In regards to the type of movement used to displace the wire, scanners can be *linear,* when the wire follows a linear trajectory, and *rotatory* when the trajectory followed by the wire is circular. Linear scanners cannot reach as high a wire speed as a rotatory one.

Bosser [3] classifies the wire scanner for circular machines as *linear* and *pendulum*, the latter could be classified also as rotatory as the wire trajectory is circular. Figure 2.1 shows some examples of linear and rotatory wire scanner.

Although in general the wire is stretched between the tips of a fork which performs a linear or rotatory motions, Wilke [4] describes another type of rotatory wire scanner instrument where the wire is not fixed at the tips of a fork. In this concept the wire is fixed between two points of a partially open disk which rotates around an axis parallel to the beam of particles (Figure 2.2).

Blokland [5] describes the wire scanner used in Tevatron (Fermi National Laboratory – US). This wire scanner belongs to the family of rotatory instruments, and has a travel angle of 540 degrees. This angle, greater than a complete tour (360 degrees), enables the wire to cross the beam of particles twice, see Figure 2.3.

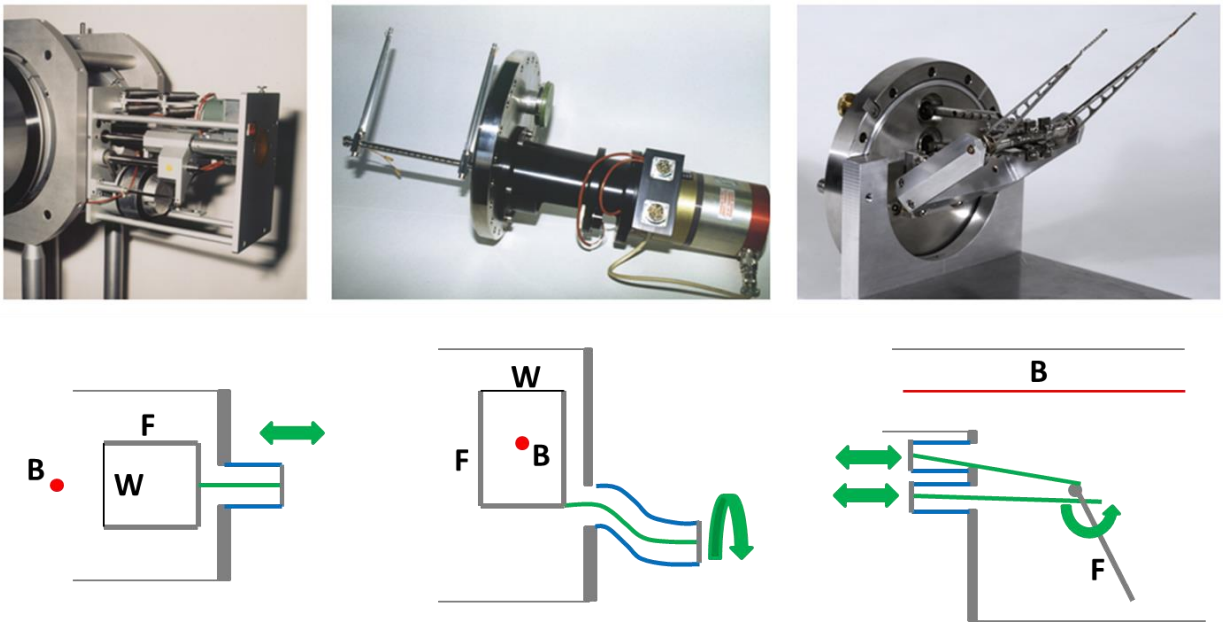

Figure 2.1: Three types of wire scanner today in operation at CERN.

Figure 2.1 shows from left to the right: linear, rotatory, rotatory (pendulum). The last two perform an oscillating movement where the travel angle is less than 180 degrees. The lower part of the figure shows a simplified description of the movement for each type of scanner. The red colour indicates the beam of particles (also indicated with the letter "B"); in blue, the vacuum bellows; in green, the transmission elements and the direction of the movement. The fork is indicated with "F" and the wire with "W". The wire and the vacuum tank are represented in grey

2.1.1. Currently operating wire scanner

Gilpatrick [6] discusses a variety of beam profile monitoring device choices for two high-average-current accelerators. In this study a good overview of the state of the art for the fast wire scanner instruments at that time is presented. Gilpatrick, describes the following devices:

In the Tevatron accelerator at Fermi National Laboratory a rotational scanner is used that could reach up to 5 m/s, using a mono filament of carbon 33 µm in diameter, with a repetitivity of 1%. Blokland [5] explains that this device, used in Tevatron, performs a rotation of 540 degrees. In this way, at each scan cycle the wire crosses the beam twice.

According to Gilpatrick [6] CERN had linear wire scanners operating in the Large Electron Positron Collider (LEP), with speed between 0.1 to 2 m/s, using different materials for the wire, 36 µm C, 10 µm SiC, and 7 µm SiO_2.

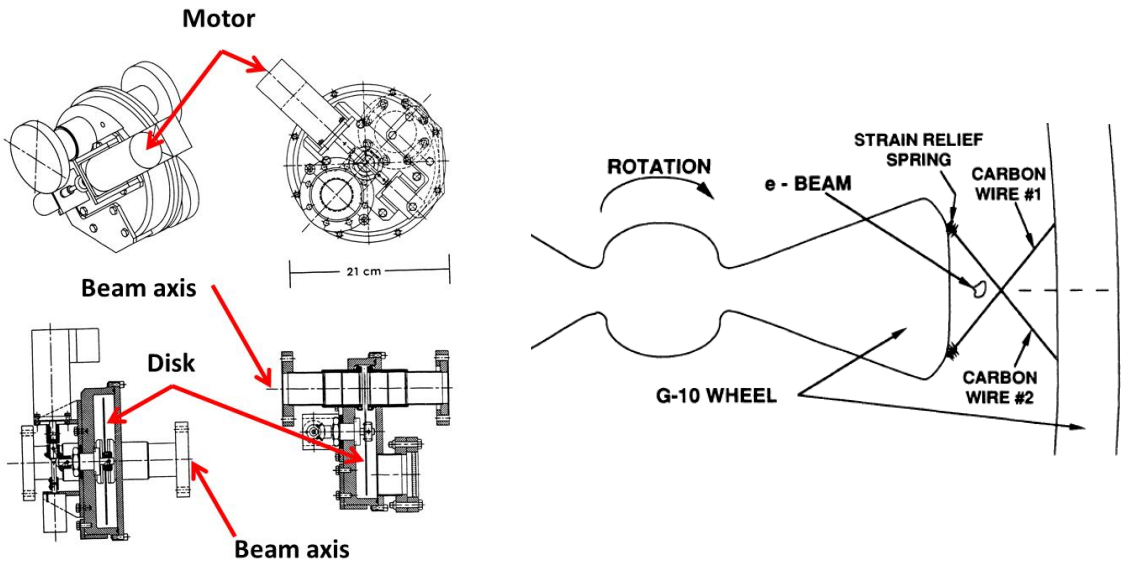

Figure 2.2: Engineering drawings of the APLE/HPO flying wire (left), illustration of the wheel used to rotate the wire in APLE/HPO flying wire [4].

Also Gilpatrick explains that CERN at that time operated rotatory wire scanners using 30 µm carbon fiber and wire translation velocities of 10 to 20 meters per second. Gilpatrick also refers to the fact that Los Alamos National Laboratory had developed a rotationally wire scanner using carbon fibers of 35 µm and a peak speed of 5m/s [6].

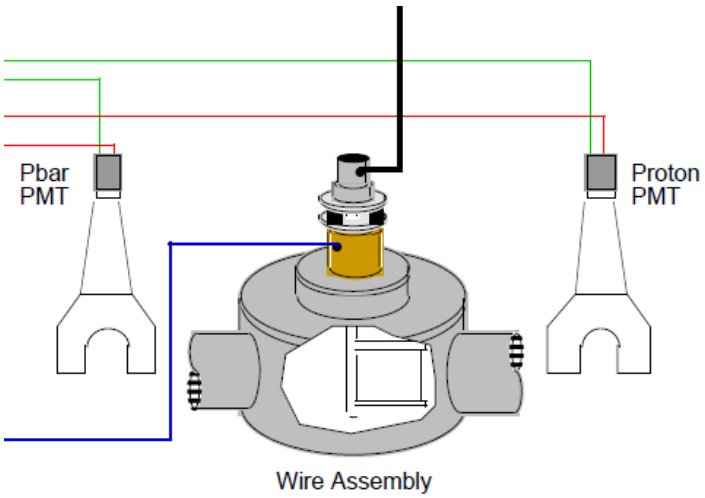

Figure 2.3: Illustration of the Tevatron wire scanner [5].

Figure 2.3 shows Tevatron wire tank assembly with the motor of top and two photomultiplier (PMT) to record secondary particles signal [5].

The latest publications related to wire scanner instruments shows that the scanners discussed by Gilpatrick [6], are currently in operation. For example, a more recent study (2009) by Shiraishi [7] shows that the conceptual design of Tevatron wire scanner are based on that described by Blokland [5] in 1997. The novel concept in [7] is that the scanner uses monofilament carbon wire of 5 um.

Igarashi [8] presents a good overview of the scanners operating at KEK PS main ring. According to Igarashi the technology used in this scanner is based on CERN fast wire scanners. This scanner belongs to the rotatory type and the wire crosses four times on the beam by scan cycle. The paper does not show clearly if the scan cycle consists of alternating movements back and forward or if each scan cycle is made by more than one complete tour (as it is the case on Tevatron).

In principle, crossing the beam twice (as is the case of Tevatron and KEK) has the advantage that the influence of vibration would be less important, since the wire could cross the beam in a less vibrating behavior. However this could also produce over heating of the wire [9].

The fact that CERN is a leading institute in the field of particle accelerators and beam instrumentation allows the assumption that the existing devices currently in operation at CERN can provide a good overview of the state of the art of the technology of wire scanner. This is confirmed by the literature researches which very often describe devices used at CERN.

CERN PS, and SPS wire scanner

Steinbach [10] presents a good overview of the scanners used until today at the PS and PSB accelerators of CERN. Since the design of this scanner (more than 25 year ago) some improvements have been made in the electronic card, the potentiometer and the motor, but the original design concept remains. A more detailed description is presented in the following paragraphs.

PS and SPS scanners can be classified as rotatory and fast wire scanners since the wire can reach a speed up to 6 m/s in the case of the SPS [13] and 20 m/s in the case of the PS scanner [14] (see Figure 2.4) .

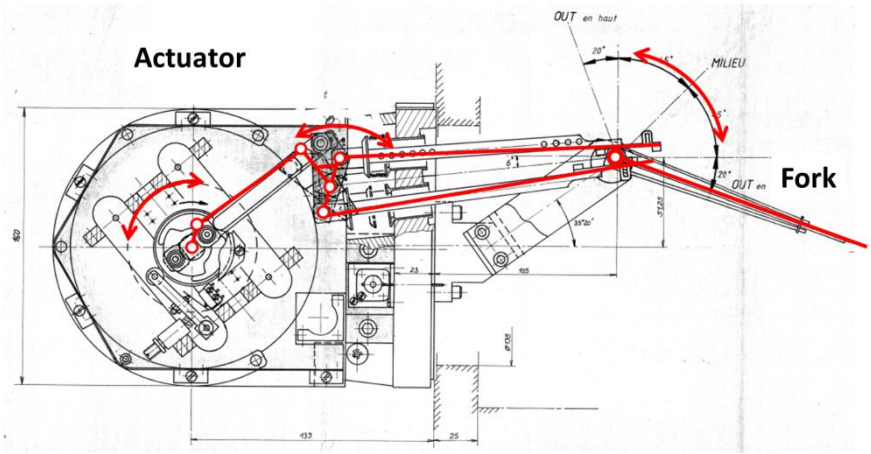

Figure 2.4: The mechanics of the PS wire scanner. In the figure the kinematic chain is represented in red.

Table 2.1: Rotation speed for operating wire scanner.

Laboratory/Accelerator	Peak Speed (m/s)	Remarks
Tevatron (US)	5	540 degrees, wire cross twice the beam
CERN / SPS	6	
CERN / PS & PSB	20	
KEK / PS	20	Wire crosses the beam twice
LANL / APLE & HPO	5	Wire is mounted in a disk

Table 2.1 summarizes the speed for the rotatory wire scanner presented in this section.

2.1.2. Carbon wire

The wire materials typically used in wire scanners are Carbon, Beryllium or Tungsten [4]. For the case of the new wire scanner design, it is anticipated that the choice of carbon as material for the wire will remain because of its properties.

Carbon is one of the materials for which many innovation and discoveries have been produced these last years; some examples of this are the carbon nanotubes or the graphene. However, carbon is still a material with a big potential for innovation and the discovery of new properties and applications over the coming years.

The properties of carbon make it one of the best candidates for use as target in fast wire scanner devices operating in high intensity proton beams. The carbon high melting point, its good thermal conductivity and relatively low density, make it resistant to the localized and intense heat produced at the moment of the wire-beam interaction [12].

As mentioned above, carbon wires are already used in the existing fast wire scanner in operation at CERN. In the existing scanner two carbon wire configurations are used, the *single wire configuration* and the twisted *multi strand wire*. These two configurations are detailed below.

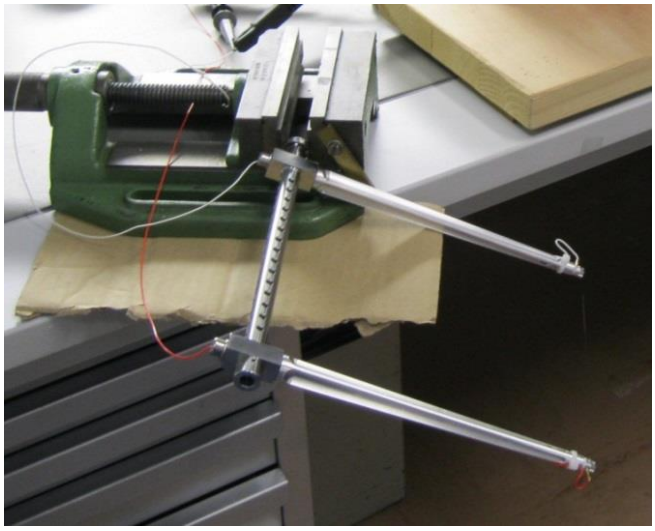

Figure 2.5: Rigid fork from a SPS fast wire scanner

Single carbon fibre wire

This type of wire configuration is used in the CERN SPS scanners [13] (see Figure 2.5). The wire, made of a single carbon fibre 34 µm in diameter is stretched in a rigid fork by means of a preload, typically between 0.05 and 0.3 N. As the fork is rigid, the stretch (tension) of the wire is maintained due to the elasticity of the wire itself.

Multi strand wire

This configuration is used in the case of the CERN PS and PSB scanners [14]. The wire is not a single wire but a multi strand wire made by several carbon fibres (typically 11) of 7 µm in diameter each. This assembly of fibres is twisted prior to be installed on the fork. The fork is flexible in the wire longitudinal direction (see Figure 2.6), thus the pre-deformation of the fork (by means of putting closer the two end of the fork) before fixing the wires is able to maintain the stretch on the wire.

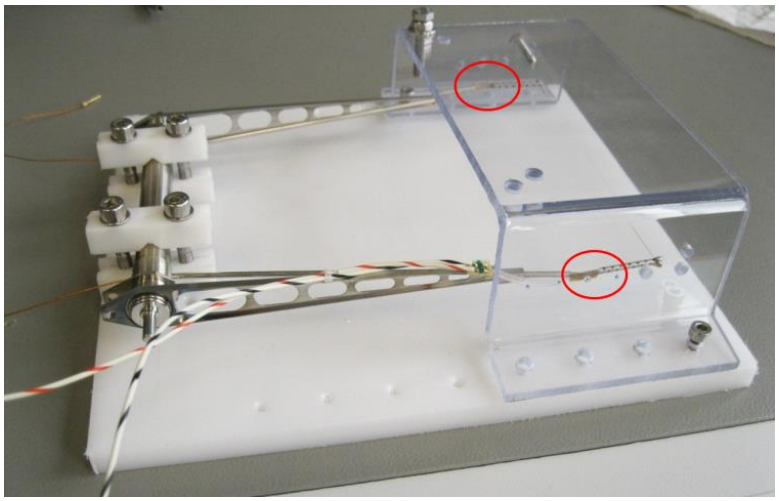

Figure 2.6: Flexible fork from a PS fast wire scanners. The red circles indicate the most flexible part of the fork.

Thin Carbon wire

Shiraishi [7] refers to a 5 micron carbon wires in Tevatron wire scanner. The use of such a thin wire may explain the fact that it is able to pass through beam of particles more than once without reaching the melting point of the carbon.

Microribbon

A new development is the work performed in the RHIC polarimeter instrument [15] where a carbon Microribbon is used as a fixed target. The advantage of this material configuration is that its interaction with the beam of particles could be very low and this allows smaller traveling speed and therefore less adverse effects, as vibrations or deflections due to the dynamic effects.

2.1.3. Precision issues

The accuracies achieved in the existing devices are limited by the motorization, the angular position measurement system located outside of the vacuum vessels, and the use of bellows to generate the movement into the vacuum tank. Furthermore, lever arm based mechanisms used to increase the speed of the wire introduce additional uncertainties.

Roncarolo [16] performed a thorough study around the accuracy of PS and SPS wire scanners. According to this study the range of uncertainty in the position is in the order of 0.2 mm. This value is in the same order as that presented by Koopman [17] for the PS and SPS scanners.

Blokland [5] presented a measured repeatability average error of 1% in the fast wire scanner operating in Tevatron. Blokland refers some error inflicted by vibration in the old wire scanner that they used, "The profile could also contain bad points due to, as later diagnosed, a vibration from the drive belt and the use of a soft coupler between the encoder and fork".

Bosser [3] comments that vibrations problems are not negligible in fast wire scanners instruments. He also developed [11] an experimental setup used in the PS and SPS scanner at CERN which could show the vibrations on the wire during scan process.

2.1.4. Current developments

The research performed so far, shows that beside the project where this thesis work is included (the New CERN Fast Wire Scanner) the following project is in phase of development in the field of wire scanners.

Cornell flying wire scanner

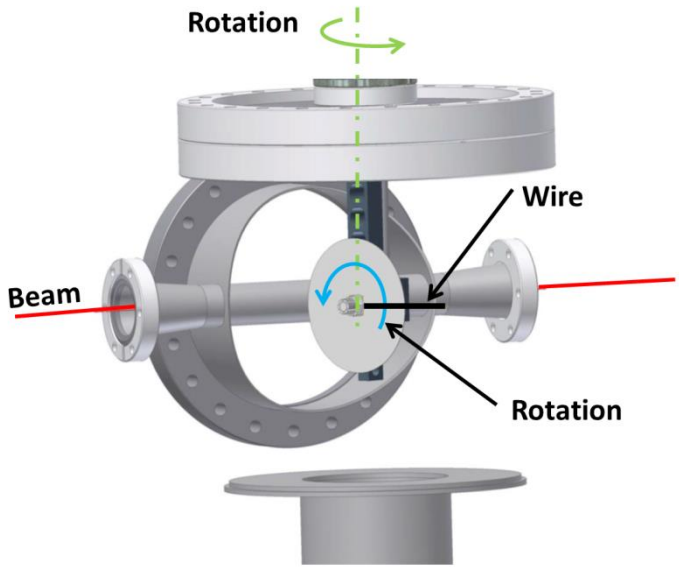

Figure 2.7: Digital mock-up of Cornell University flying wire [18].

This development will be used in the Electron Recovery Linac project (ERL). A digital mock-up of this device is shown Figure 2.7, where the beam is represented in red, the wire in black and the two combined rotations bringing the wire into the beam in by blue and green arrows. The system has two rotations axes, the first one is the disk rotation and the second one about the vertical axis defined by the black support which hold the disk. The operating principle consists of the rotation of the disk and the wire until the operating speed, then the rotation of this assembly (disk and wire) about the vertical axis in such a way that the wire crosses the beam of particles. The wire made of 20 micrometers carbon fibre crosses the beam at a speed of 20 m/s.

2.1.5. Conclusions

The main conclusion from this literature review is that the technology currently used in the existing wire scanner is quite consolidated and no substantial modifications have been performed in the last years.

With the exception of Bosser [3], [11] no special consideration has been addressed to the problem of position uncertainties produced by the residual vibrations.

Cornell flying wire design allows constant speed to be reached on the wire before crossing the beam of particles. This could minimize wire vibrations since the wire is rotating at a constant speed. However a transient movement is also needed in order to bring the wire into the beam at the suitable moment. Additionally, with this design two independent driver systems are required.

2.2. Vibration measurements

The number of accelerators and therefore research groups in beam instrumentation is quite low compared to the number of instrumentation groups in other fields. Consequently existing technologies for vibration measurement are usually not directly linked to the field of beam instrumentation. Due to this reason, since the beginning of this research, special attention has been given to find other fields of the technology having common points with the subject of this thesis work. Until now, a technology not directly linked to the field of beam instrumentation have been found, this technology is the Vibrating Wire Stain Gauge (VWSG), and is described on Section 2.2.2.

2.2.1. Measurements of vibration in wire scanner instrument

Two studies have been found in the literature related specifically to the measurement vibrations in a wire scanner. Iida [19] developed a method to measure vibrations in wire scanner instruments. Unlike that which is proposed in this thesis work (the study and measurement of the vibrations on the wire itself), this method measures the vibrations on the wire mount frame. The method is based in the use of a laser displacement meter located outside the vacuum tank and a reflective flag fixed in the wire holder (see Figure 2.8).

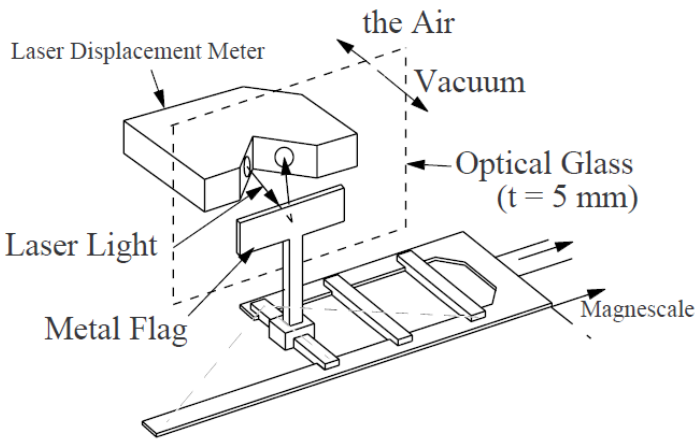

Figure 2.8: Iida vibration measurement system [19].

Bosser [11] performed some vibration measurements in fast wire scanner. The technique of measurement was based on the voltage induced in a conductor when it travels (moves at a certain speed) in a magnetic field and an example of the measurement results is show in Figure 2.9. In the measurement performed by Bosser, the main travel speed of the wire and the vibrations could be clearly identified. The paper does not show whether the measurement had been performed in vacuum or air environment. However the main conclusion of this test was that vibrations on the wire have to be taken into account as a source of position error.

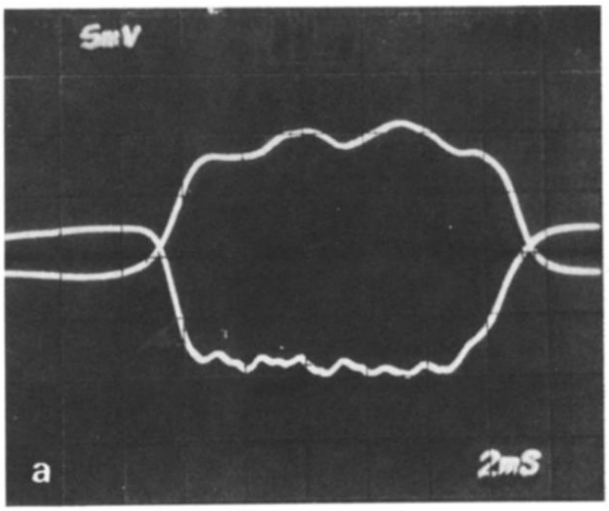

Figure 2.9: Measured induced voltage on a wire during two movements, forward and back [11].

So far no more studies or developments have been found in the literature related to the measurement vibrations in a wire scanner. However, devices relating different properties of thin wires to some aspects

of their vibratory behaviour characteristics exist. Even if the main goal of such devices is not the measurement of the wire vibrations (as they are somehow the tool to measure other parameters), the technology and knowledge to perform measurements in vibrating wires is included in these devices. Two of them are presented in the following section.

2.2.2. The vibrating wire strain gauge

The Vibrating Wire Stain Gauge (VWSG) is a well-known technology that uses the vibrational behaviour of a wire to perform strain measurements in structural elements. This technology can be considered today as a consolidated technology, and commercial products based in this technology can be found in the market [20], [21]. This device consists on a stretched wire and a sensor. The sensor part is composed of a permanent magnet and a plucking coil assembly (see Figure 2.10). When the wire is plucked by the sensor, it vibrates at its natural frequency, which is proportional to the tension on the wire. Any change in the strain of the wire directly affects the tension in the wire, resulting in a change in its natural frequency of vibration. Thus the VWSG can provide indirectly a stress measurement in a sample by means of multiplying the measured strain by the modulus of elasticity of the material of the sample.

According to Kuhinek [22], VWSG devices have at least one coil which stimulates the wire to vibrate and to pick up the resonance frequency signals. Kuhinek explains that some devices have two independent coils: one to provide stimulus and a second one to pick up the signal. Since the signal used to measure is in the form of a frequency, Kuhinek demonstrates that the signal can be transmitted over long distances without distortion.

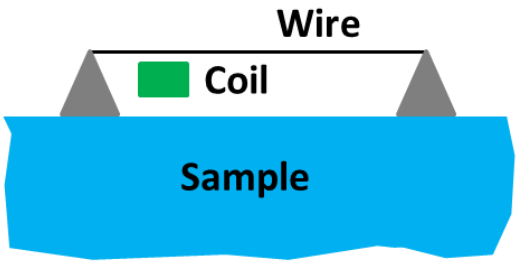

Figure 2.10: Illustration of a vibrating wire strain gauge [22].

As a drawback Kuhinek, shows that the effect of the temperature in the VWSG devices has a substantial influence on vibration frequency and this effect has to be taken into account to be compensated.

2.2.3. The vibrating wire scanner

The Vibrating Wire Scanner (VWS) is an instrument used to monitor the profile of a beam of particles; this is the same goal as a Fast Wire Scanner, but is based on a different technique for reconstructing the profile.

The operating principle in the VWS is based on the natural frequency change that a stretched wire has due to the increase of its temperature. This temperature increase results in a variation in the stretching of the wire which changes its natural frequency. When the wire moves across a beam of particles, its

temperature will change according to the density of particles in the beam. These temperature differences will be read as a change of its natural frequency. Looking at this frequency variation and the position of the wire, the profile of the beam of particles can be reconstructed.

Arutunian [23], based on the accumulated experience in the field of vibrating wire strain gauges, was able to develop techniques to measure spatial distribution of magnetic fields [24]. This accumulated experience was also used to develop vibration wire scanner instruments. Arutunian demonstrates that it is possible to use the natural frequency dependency on a thin stretched wire in order to reconstruct the beam profile. Arutunian [23] explains that pickups applied to vibrating wires are a wide-spread technology since this technology is used tensometry, gravimetry, and measurements of magnetic field and magnetic properties of materials.

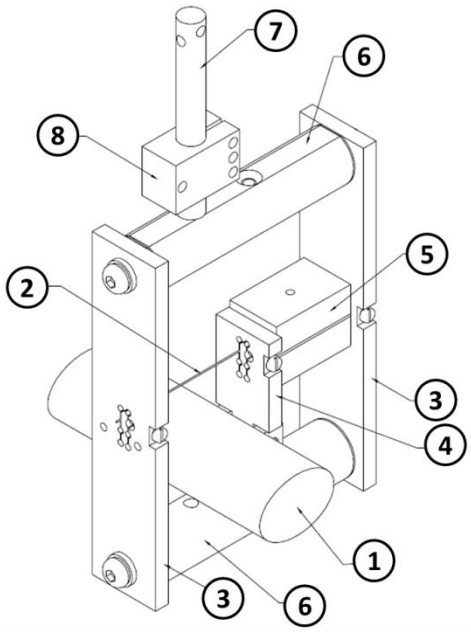

Figure 2.11: Illustration of a vibrating wire scanner [25].

Figure 2.11 shows a vibrating wire scanner mechanism, by numbers: 1 – measured beam, 2 – sensitive to temperature scanning wire, 3 - supporting plates with wire pinning, 4 – arm on the bearing axis, 5 – magnet system, 6 – rods from Invar, 7 – finger for VWM_LA support, 8 – brick for finger location."

In VWS the vibrations are induced onto the wire by means of interaction of the alternating current passing through the wire with the permanent magnetic field [26]. Strong samarium-cobalt magnets are used, which provide a field strength of order and higher than 8 kGs in the working range. Arutunian [26] also refers that the wire can be excited by special mechanical forcing.

In addition, he assesses that the VWS is very sensitive to the temperature of the base to which the wire is fastened, in order to solve this problem it was necessary to thermo-stabilize of the base.

2.2.4. Conclusions

This literature review shows that not too many studies have been performed in order to investigate the vibrational behavior of wire scanner instruments and the influence of these vibrations in the measurement error.

On the other hand it is shown that there are devices where the technology involves thin wires and measurement of vibrations, though the aim of such devices is not to measure of the vibrations of the wire itself (rather that measurements of vibrations of a wire are used to determine other parameters, for example, strain).

2.3. Review of vibration modelling

Considering the description and operation procedure of a rotating wire scanner device (see Introduction) it seems clear that the inertia forces (associated with the shaft rotation) will cause wire length changes. This complex phenomenon (triggered by the inertia forces) can be enhanced by the fork tips deflection resulting on parametric oscillations. Many scientific articles can be found where those phenomena are studied.

Parametric oscillations are encountered in many different fields. In civil engineering, they arise as a consequence of seismic excitation on long span cables in bridges and towers [27, 28]. In mechanical engineering, they appear in gear systems as a consequence of time-variable stiffness [29, 30, 31]. In naval engineering, the time-varying geometry of the submerged hull may generate dangerous parametric oscillations yielding instability [32]. In musical acoustics, any string-based instrument is prone to parametric vibrations: when a string is set into motion, its vibration is transmitted to the soundboard, whose vibration appears as a parametric excitation on the other strings [33]. In all cases, the equations of motion correspond to a linear Mathieu equation whenever the vibration amplitudes are moderate.

There are many scientific articles discussing parametric oscillations and cubic nonlinearities for the particular case of stretched strings. The cubic nonlinearities appear together with a parametric excitation whenever the oscillations reach high values (see for example [34, 35, 36]) or independent from it when tension changes associated with transverse vibrations are taken into account (see for instance [37, 38, 39]). In the latter case, the equations of motion take the general form of a Duffing equation.

Some articles propose continuous models which translate into partial differential equations. Their solutions are often explored assuming a reduced number of vibrating modes and using a multiple scale approximation [40, 41, 42]). In other cases, no analytical solution is proposed; instead a purely numerical solution is implemented [43, 44].

Mathieu and Duffing equations (or oscillators) have also received much attention because they may exhibit chaotic behaviours (see for example [45, 46]). However, this particular aspect is of no interest for our purpose.

2.3.1. Conclusions

After a thorough research in the literature, it does not appear that a dynamic model of a system with the same requirements as the fast wire scanner has been developed. The vibration problem presented in this thesis work is a classical one; thus the state of the art in this topic can provide the suitable tools to solve the problem satisfactorily. It is obvious that there is no need for innovative methods (or models) to solve this problem, that can be treated as problem of vibrations of coupled systems (the fork and the wire). A suitable model for each component should be considered; the choice of model depends not only on the particular geometry of the element but also on the complexity of its vibration pattern.

It should be noted that the current state of the art in Mechanics science provides the mathematical equations to accurately describe the vibrating behaviour of mechanical systems in general. In addition the mathematical tools to solve those equations have been well known for decades, and these mathematical tools range from pure analytical solutions to very accurate numerical methods.

3. Present design

This chapter deals with the sources of error when measuring with a rotating wire scanner. Analysing the origin of experimental imprecisions is a necessary step to undertake the improvement of both the device and its performance. The presentation of this work is divided in two parts. First, some general considerations about the sources of error which can affect the rotating wire scanner concept are presented. In the second part each specific error source is qualified for the particular case of the PS wire scanner.

3.1. General Considerations

In a general way, a rotating wire scanner consists of a shaft which supports a two-arm fork and a stretched thin wire between the fork tips. An angular position sensor, typically fixed to the shaft, provides the information about its angular position.

As mentioned in the introduction, the thin wire has to intersect the beam in an intermittent manner in order to generate secondary particles which provide the information, by means of the scintillator reading, to reconstruct the transverse beam density profile. This requires an actuator to generate and control the shaft rotation. The coupling between actuator and shaft may vary from one scanner design to another. Figure 3.1 shows two rotating wire scanner with different types of actuators. The left part of the figure shows the SPS rotating wire scanner, the actuator motor (M) and the sensor (S) are aligned with the same axis as the fork (F). The right part of the figure, shows the PS wire scanner, in this case, the axis of the actuator motor (M) and the sensor are not aligned with that of the fork (F), the actuator and the fork axis are linked through a crank mechanism.

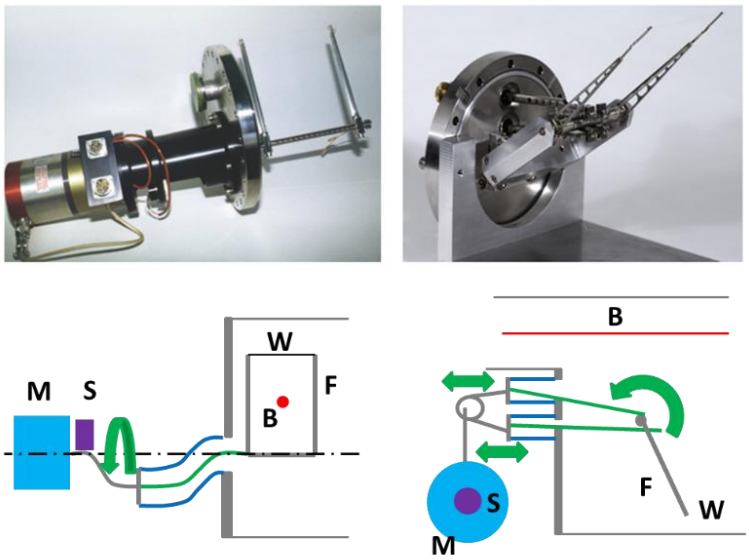

Figure 3.1: Two rotating wire scanners with different type of actuators SPS (left), PS (right).

3.1.1. Measurement chain

Let's define the measurement chain as a group of elements which link the position of the wire with the angular sensor intended to be used to determine that position. Typically a mechanical chain is made of different mechanical parts, connected between them (see Figure 3.2). In a perfect mechanical chain of rigid bodies, the wire location could be determined at any time instant from the angular position provided by the sensor, θ, and the length of the fork arms, L_f, as follows:

$$\text{Wire location} = f(\theta, L_f) \tag{3.1}$$

However, neither the mechanical chain is perfect, nor the constituting elements are rigid. Therefore, the measurement of the wire location will contain errors arising from different sources:

- misalignments between elements fixed together,
- kinematical play between elements (relative movement),
- elastic deformation of the elements,
- vibrations of the different elements,
- the particular position (in the direction of the shaft axis) where the wire intersects the beam.

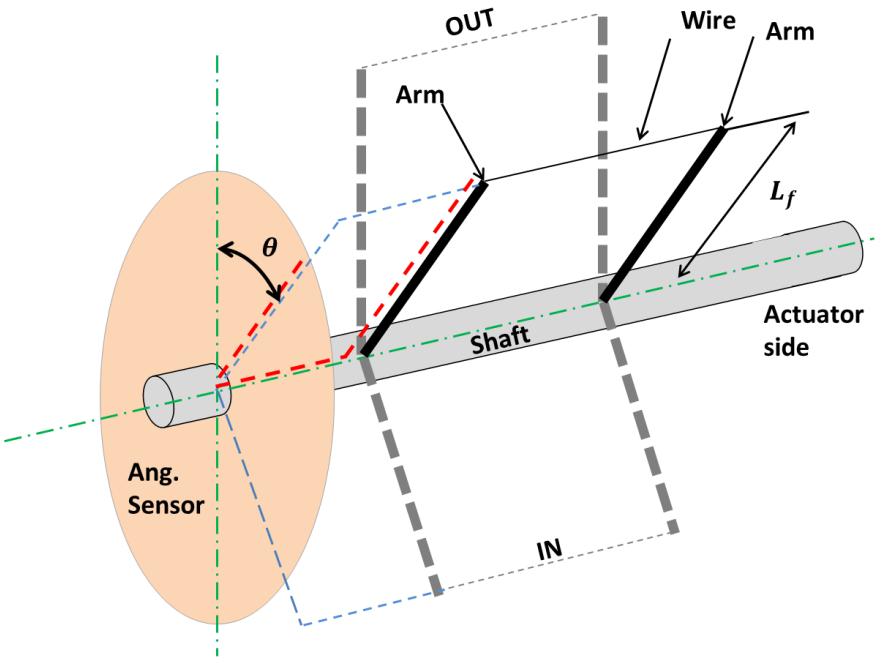

Figure 3.2: Schematic view of a rotating wire scanner; the chain linking the wire to the sensor is indicated with a dashed line in red.

Depending on the origin of the different errors induced by the measurement chain they can be classified as *systematic*, when various measurements taken under the same conditions always generate the same error, and *statistical*, where the error may vary between measurements made under identical conditions. The global error of a measurement is composed of these two types or errors.

3.1.2. Misalignment errors

These errors are due to a difference between the theoretical relative position of the elements involved in the wire position determination (kinematic chain) and their actual position. Misalignment errors appear during the mounting or manufacturing process, and generate systematic measurement errors.

3.1.3. Mechanical play errors

Mechanical play is required for a good functioning of the mechanisms. However for the case of mechanisms belonging to the kinematic chain involved in a measurement, that play introduces measurement errors.

In the case of the wire scanner, the measurements are performed in motion, and consequently the mechanical play may have a different impact on the measurement depending on type of motion: it will be different in measurements performed under constant acceleration and in measurements performed under variations of acceleration either in amplitude or direction.

Mechanical play errors can be considered as systematic errors whenever the motion of the system keeps the elements in contact all the time. Conversely if the mechanism is shaken due to the motion pattern, the error due to the mechanical play becomes less predictable and therefore has to be classed as statistical error.

3.1.4. Deflections

In order to reach the suitable speed in the wire at beam crossing, the actuator has to deliver a motion pattern which consists of an acceleration phase, a constant speed phase and a phase of deceleration (see Figure 3.3). Considering that the angular range is narrow (typically less than 360 deg., when the wire cannot cross the beam twice, and in most cases, less than 180 deg.,imposed by other design constrains), a strong acceleration is required. In the laboratory reference frame, this acceleration generates inertial forces which provoke deflections in the mechanical components of the system and in the wire. More precisely, they cause:

- twist of the different sections of the shaft,
- bending of the fork arms,
- bending of the wire (in two directions, tangential and radial to the rotation).

These deflections are schematically represented on Figure 3.4 for the case of rotating wire scanner concept.

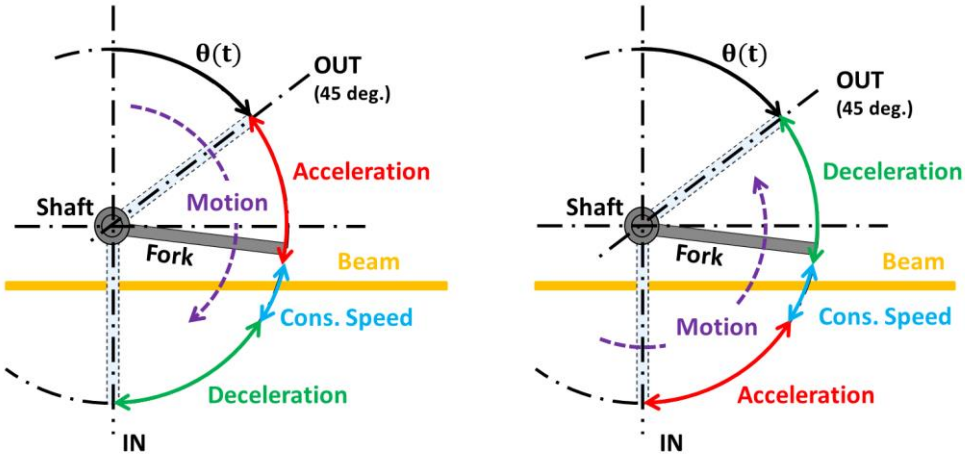

Figure 3.3: Illustration of the PS scanner scan cycle from OUT to IN (left) and from IN to OUT (right) positions.

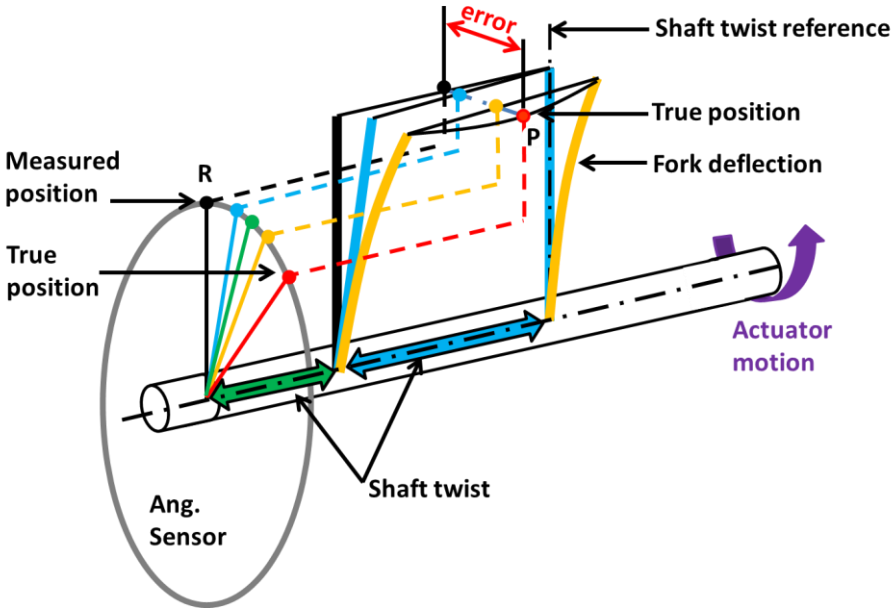

Figure 3.4: Deflections of the measurement chain for a rotating wire scanner.

3.1.5. Vibrations

As stated before, the acceleration applied to the system changes its amplitude and direction along a measurement cycle. Those variations are responsible for the oscillation of the different system elements. Therefore vibrations represent an additional source of error. Vibrations can be considered as a systematic or statistical source of error depending on their degree of reproducibility.

3.1.6. Uncertainty of the particular zone of the wire intersecting the beam

The fact that there is uncertainty of the particular zone of the wire intersecting the beam has to be considered as a source of error. Figure 3.5 represents a schematic view perpendicular to the beam axis at the instant in time of the wire-beam intersection, δmax and δmin respectively represents the maximum and minimum error due to the wire and arm deflections. As shown on the figure, depending on the region of the wire intersecting the beam and due to the uncertainty on the arm position and the actual wire shape, the difference between the actual beam position and the measured beam position may be non-negligible. The image shows one of the possible configurations that the wire and arms could take under motion. Even if the wire shape and arms position were perfectly known (which is generally not the case), the error due to this uncertainty would still persist. Therefore this error is due to three factors; the arm position error, the deformed wire shape and the uncertainty of the beam position along the wire longitudinal direction.

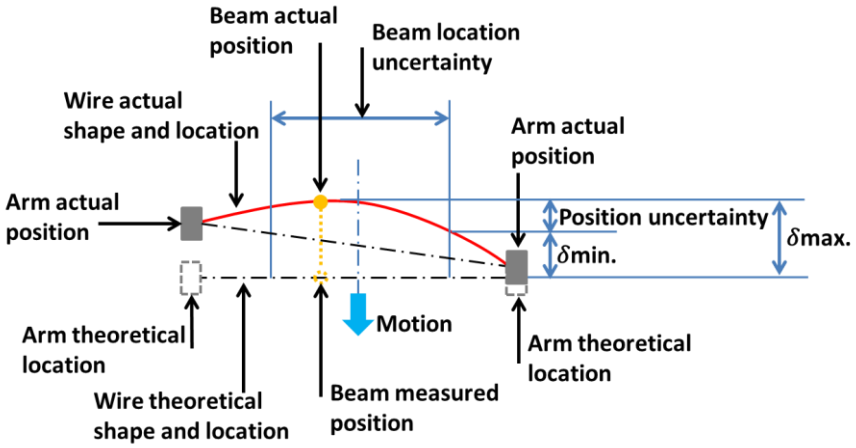

Figure 3.5: View in the direction of beam axis at the time instant of wire-beam intersection.

3.1.7. Error of measured beam width due to error of the detected angle

In order to provide information about the transverse beam profile, it is necessary to measure the beam width in a plane perpendicular to the beam axis. The transformation between the angular value provided by the sensor and the projected position of the wire has to be calculated. Figure 3.6 is presented to explain how the beam projection is calculated. The kinematic chain linking a point P of the wire to a reference mark R on the angular sensor is indicated by a red dashed line. The projection plane, perpendicular to the beam, and the projected position of P (P_p), are shown in green.

The quantity d gives the distance between the wire rotating axis and the projection of the point P in a plane perpendicular to the beam containing the wire rotation axis. Therefore:

$$d = L_f \cos(\theta) \tag{3.2}$$

where θ is the angle between the fork and the normal to the projection plane, and L_f is the fork length.

The beam profile is reconstructed by the synchronized recording the wire position d and the secondary particles intensity.

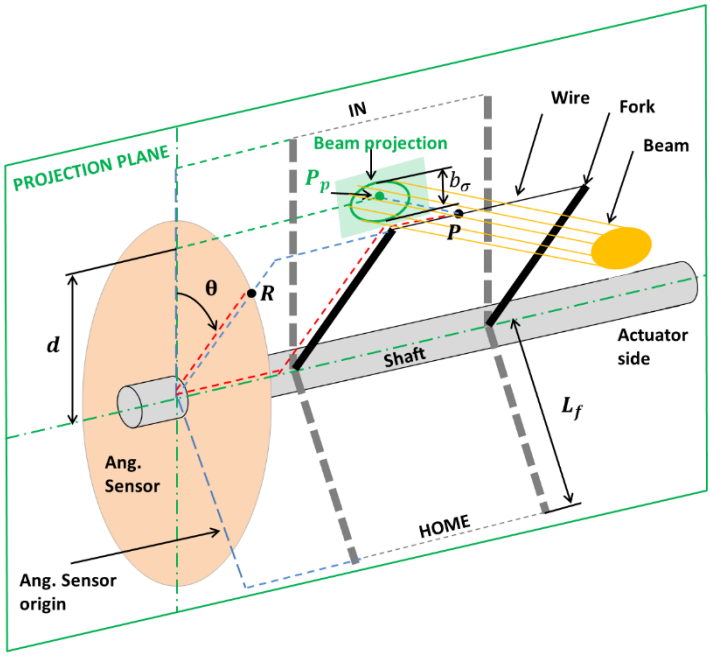

Figure 3.6: Schematic view of a rotating wire scanner.

The beam width can be calculated as follows (Figure 3.7):

$$b_\sigma = d(\theta(t_f)) - d(\theta(t_i)) \tag{3.3}$$

$$b_\sigma = L_f(\cos(\theta(t_f)) - \cos(\theta(t_i))) \tag{3.4}$$

Where t_i and t_f are the time instants when the wire starts and ends beam crossing, respectively.

Let us define

$$\theta_b = \frac{\theta(t_i) + \theta(t_f)}{2} \tag{3.5}$$

and

$$\theta_\sigma = \theta(t_f) - \theta(t_i) \tag{3.6}$$

Then, the beam width can be calculated as follows:

$$b_\sigma = -2L_f \sin\left(\frac{\theta(t_f)+\theta(t_i)}{2}\right)\sin\left(\frac{\theta(t_f)-\theta(t_i)}{2}\right) = -2L_f \sin(\theta_b)\sin(\frac{\theta_\sigma}{2}) \quad (3.7)$$

i.e. the width of the beam can be calculated as function of the angle between the initial and the final projected intersection points (θ_σ) and the angular absolute position of the beam (θ_b).

Let us define $E\theta_b$ as the error due to the angular position measurement, and $E\theta_\sigma$ the error in the angular measurement of the beam width (see Figure 3.7).

$$E\theta_\sigma = \theta_\sigma - \theta_{\sigma m} \quad (3.8)$$

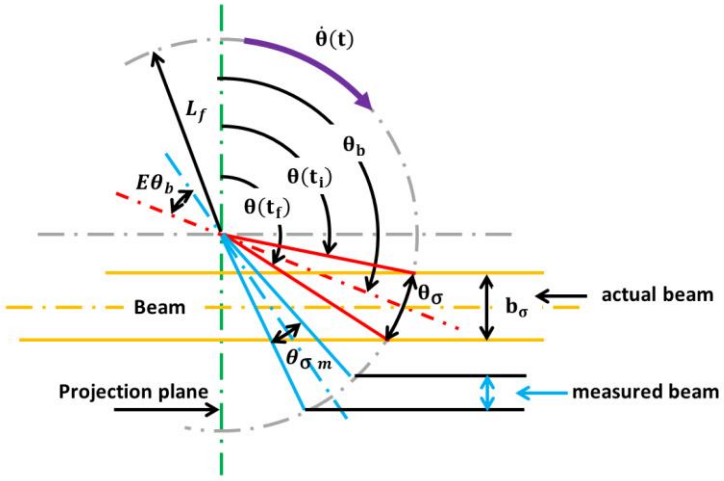

Figure 3.7: Actual (real) beam width (b_σ) and measured beam width.

Assuming that these two errors ($E\theta_b$ and $E\theta_\sigma$) are independent of each other, the total error in the width measurement ($b_{\sigma-error}$) can be calculated as follows using Eq. (3.7):

$$b_{\sigma-error} = \left|\frac{\partial b_\sigma}{\partial \theta_b} E\theta_b\right| + \left|\frac{\partial b_\sigma}{\partial \theta_\sigma} E\theta_\sigma\right| \quad (3.9)$$

$$b_{\sigma-error} = \left|-2L_f \cos(\theta_b)\sin\left(\frac{\theta_\sigma}{2}\right) E\theta_b\right| + \left|2L_f \sin(\theta_b)\cos(\frac{\theta_\sigma}{2})E\theta_\sigma\right| \quad (3.10)$$

Combining Eq. (3.7) and Eq. (3.10), the relative error can be expressed as

$$\frac{b_{\sigma-error}}{b_\sigma} = \frac{E\theta_b}{\tan(\theta_b)} + \frac{E\theta_\sigma}{\tan(\frac{\theta_\sigma}{2})} \tag{3.11}$$

Since the width of the beam is very small,

$$\tan\left(\frac{\theta_\sigma}{2}\right) \approx \frac{\theta_\sigma}{2} \tag{3.12}$$

and the relative error can be simplified as follows:

$$\frac{b_{\sigma-error}}{b_\sigma} = \left|\frac{E\theta_b}{\tan(\theta_b)}\right| + \left|-\frac{2E\theta_\sigma}{\theta_\sigma}\right| \tag{3.13}$$

This equation shows that the relative error on the beam width measurement depends on the error induced when measuring and also on the error in the measurement which determines the absolute position of the beam.

As can be seen from Eq. (3.13), the error is not constant along the beam width as it depends on $\tan(\theta)$, i.e. depends of the angular position of the measurement.

3.1.8. Error due to wire orientation error.

The orientation error of the wire with respect to the horizontal transverse coordinate of the beam (Z) for the vertical scans (or respect to the vertical transverse coordinate (Y) for the horizontal scans) may induce errors in the beam width measurement. This section is devoted to the analytical evaluation of that error.

The origin of the wire orientation error α_e is shown on Figure 3.8. In an ideal situation with no errors, points C_1 and C_2, defining the actual fork rotating axis, would have the same values of coordinates Y and Z, and the same could be said about points W_1 and W_2, which indicate the wire ends. In the real situation, misalignment errors result on different coordinates values for points C_1 and C_2, therefore the actual rotation axis of the fork is not collinear with the theoretical rotation axis. For points W_1 and W_2, the differences in the coordinate values come not only from the misalignment between points C_1 and C_2 but also from a possible difference in length between the two fork arms (L_{f1} and L_{f2}) and the angular misalignment $\Delta\theta$ between the fork arms. The consequence of all these errors is that the wire is not parallel to the beam horizontal plane. In principle, the wire orientation error is not constant along the complete fork cycle and depends on the fork angular position.

The previous explanation is based on the case of a vertical scanner, i.e., the scanner which provides information about the vertical beam profile. A similar explanation can be developed for the horizontal scanner, though the Y coordinate has to be replaced by Z as the rotation axis of the horizontal scanner is orthogonal to that of the vertical scanner. Therefore in the case of the vertical scanner, the value α_e corresponds to the wire orientation error respect to the beam vertical transverse coordinate (Y).

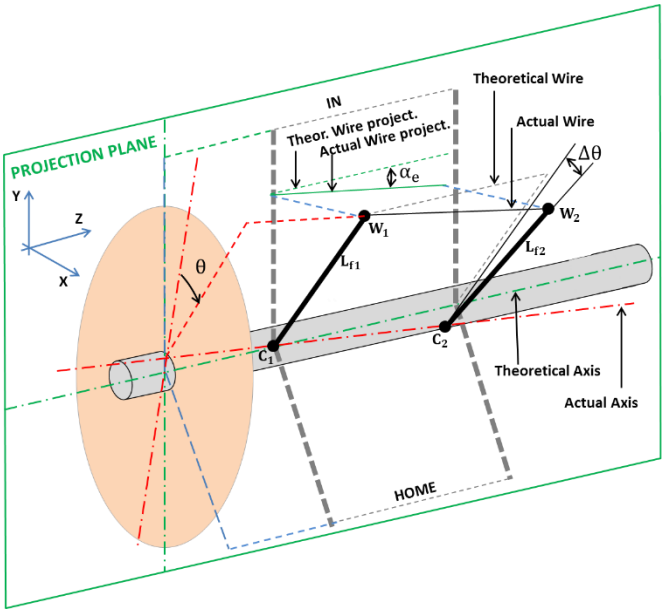

Figure 3.8: Schematic view of vertical scan. The value α_e stands for the wire orientation error respect to the beam horizontal transverse coordinate (Z).

Typically the scanner device is installed in a vacuum tank which in turn is installed in the suitable accelerator section. Thus, a fraction of the wire orientation error can be due to alignment errors in the tank. Consequently, the wire orientation error can be expressed as follows:

$$\alpha_e = \alpha_s + \alpha_t \tag{3.14}$$

where

α_s is the wire orientation error due to the scanner construction and misalignment errors,

α_t is the orientation error of the vacuum tank with respect to the beam.

The influence of the wire orientation error in the beam width measurement can be calculated for the vertical and horizontal scanner under the following assumptions:

- the transverse dimension of the beam is small enough; this allows to consider no variation on the wire orientation error while intersecting the beam, and therefore the wire orientation error can be considered as constant along the beam intersecting
- the beam transverse section corresponds to an elliptical shape located at the centre of the beam transverse coordinates system; therefore the transverse beam shape can then be described through the following equation:

$$\left(\frac{z}{a}\right)^2 + \left(\frac{y}{b}\right)^2 = 1 \tag{3.15}$$

where a and b are the two ellipse semi-axis in Z and Y direction respectively (see Figure 3.9 and Figure 3.11).

Vertical width relative error

In order to measure the vertical dimension of the beam width, the wire has to move in the direction of Y and must be orientated parallel to Z. According to Figure 3.9, the orientation and location of the wire at the moment of its first interaction with the beam is given by the following equation:

$$y = kz + y_t - kz_t \tag{3.16}$$

where

$$k = \tan(\pi - \alpha_e) \tag{3.17}$$

and α_e represents the orientation error of the wire respect to the horizontal transverse axis Z.

The point P of the ellipse with coordinates (z_t, y_t) is the first intersection between the wire and the ellipitical contour of the beam section. The tangent to the ellipse at point P has to have the same slope as the line which defines the wire at the moment of the interaction with the beam:

$$\left.\frac{dy}{dz}\right]_P = k \tag{3.18}$$

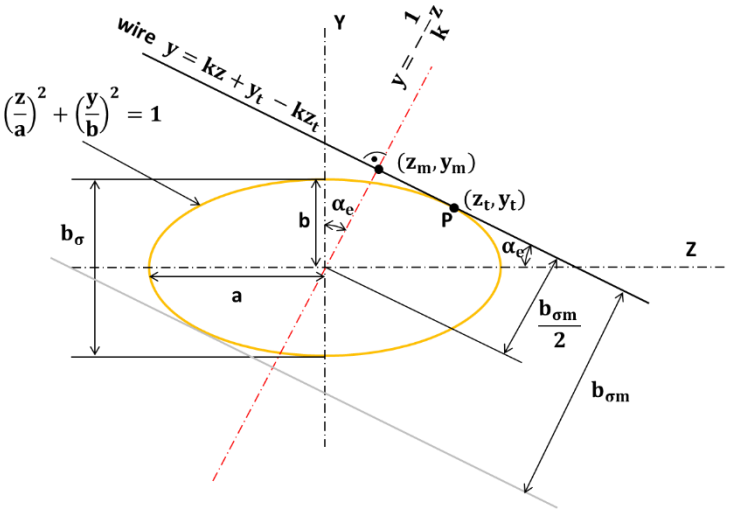

Figure 3.9: Vertical width measurement schematics (used to derivate the equations).

From Eq. (3.15),

$$y = b\sqrt{1-\left(\frac{z}{a}\right)^2} \Rightarrow \frac{dy}{dz} = -\frac{bz}{a^2\sqrt{1-\left(\frac{z}{a}\right)^2}} \tag{3.19}$$

and the coordinates (z_t, y_t) can be obtained solving the following system of equation

$$\begin{gathered}\frac{bz_t}{a^2\sqrt{1-\left(\frac{z_t}{a}\right)^2}} = -k \\ y_t = b\sqrt{1-\left(\frac{z_t}{a}\right)^2}\end{gathered} \tag{3.20}$$

The measured beam width $b_{\sigma m}$ can be calculated as follows:

$$b_{\sigma m} = 2\sqrt{(z_m^2 + y_m^2)} \tag{3.21}$$

where (z_m, y_m) are the coordinates of the intersection point between the line defining the wire location and a line perpendicular to it passing through the origin of coordinates (center of the beam). Therefore the values of (z_m, y_m) can be found through the solution of the following system of equations:

$$\begin{gathered}y_m = kz_m + y_t - kz_t \\ y_m = -\frac{1}{k}z_m\end{gathered} \tag{3.22}$$

The relative error in width REb_σ can be calculated as follows

$$REb_\sigma = \frac{b_{\sigma m}}{b_\sigma} - 1 \tag{3.23}$$

where b_σ represents the actual beam width along the vertical transverse coordinate and coincides with 2b (ellipse semiaxis).

Combining Eq. (3.22) and Eq. (3.20), the relative beam width error can be calculated as function of the wire orientation error α_e and the ratio between the horizontal and vertical beam transverse dimensions r:

$$r = \frac{a}{b} \tag{3.24}$$

The following plot (Figure 3.10) shows the values of the relative error under different orientation error values and semi-axis ratios.

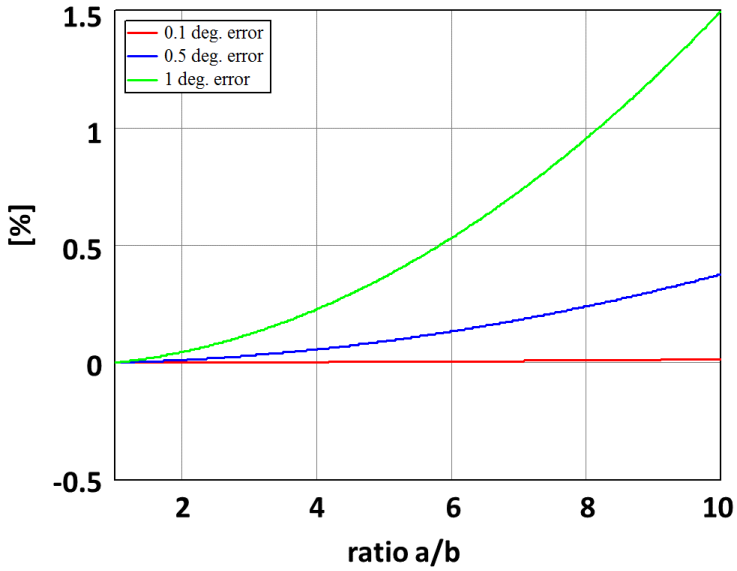

Figure 3.10: Relative vertical width error as function of the semi-axis ratio for different wire orientation errors.

Horizontal width relative error

A similar calculation can be developed to estimate the relative horizontal width error. Figure 3.11 describes the geometry in that case. Note that now,

$$k = \tan\left(\frac{\pi}{2} + \alpha_e\right) \tag{3.25}$$

and α_e is the orientation error of the wire respect to the horizontal transverse axis, Y.

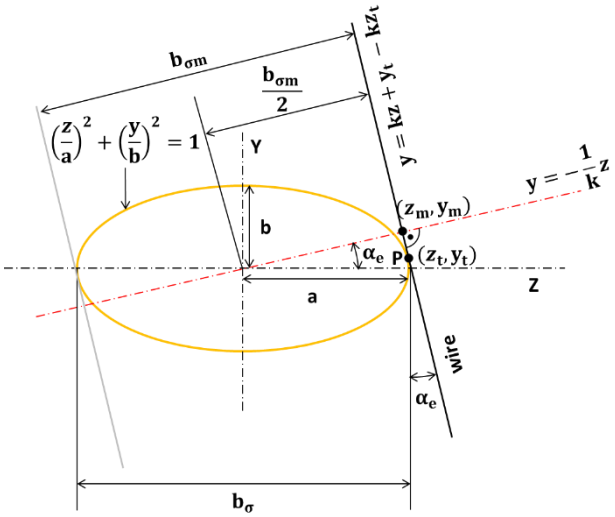

Figure 3.11: Horizontal width measurement schematics (used to derivate the equations).

The Figure 3.12 shows different values of relative beam width horizontal error for different values of wire orientation error and semi-axis ratios.

Figure 3.10 and Figure 3.12 are not united in one single figure because in the real accelerator the beam is always horizontally wider than vertically.

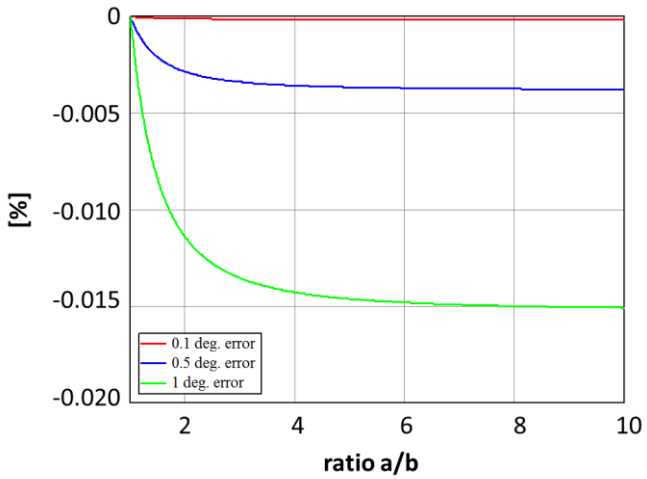

Figure 3.12: Relative horizontal width error as function of the semi-axis ratio for different wire orientation errors.

In view of the results it can be concluded that for the vertical scans, wire orientation errors until 1 deg. and values of r lower than 2 results on relative beam width error lower than 0.1%. For the horizontal scans, wire orientation errors until 1 deg. and values of r lower than 2, yields relative beam width error better than -0.012 %.

3.2. Precision assessment in PS wire scanner

In the previous section, the mechanical source of error affecting the measurement has been studied for the general concept of the rotating wire scanner instrument. The current section presents the quantification of this error for the particular case of the PS wire scanner. The quantification of the different sources of errors has been done experimentally in most of the cases, although in some cases the use of models has been necessary.

In principle, the wire orientation error is not constant along the complete fork cycle and depends on the fork angular position.

3.2.1. PS scanner description

The current design of the PS wire scanner was made more than 20 years ago and in principle was designed to reach a maximum speed of 20 m/s [10]. However until now, and due to some limitations in the control system, related to the length of the cables, its maximum safety operating speed has been limited to 15 m/s.

A digital mock-up of the PS scanner is shown in Figure 3.13. The device consists of a motor, a transmission system in air and in vacuum, and a fork with two arms welded on a shaft and a flange which supports the different parts of the system and allows the interface between air and vacuum.

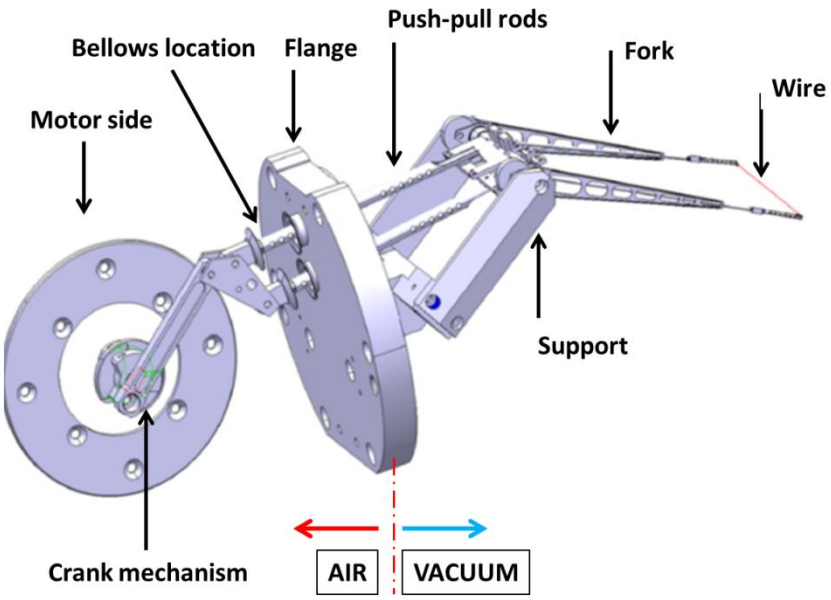

Figure 3.13: Digital mock-up of the PS wire scanner showing the main parts of the device.

The motor is a double shaft DC motor. One side of the motor is connected to a crank mechanism while the other part is directly connected to a potentiometer.

The crank mechanism transforms the rotation of the motor into a linear movement. Two push-pull rods transmit this linear movement from the air side into the vacuum. The air-vacuum tightness is performed by means of two bellows. On the vacuum side, the linear movement becomes a rotation on the fork axis by means of four tapes fixed to the push-pull rods and coiled around to the fork axis (see Figure 3.14). A more detailed explanation of this mechanism can be found in Appendix A.

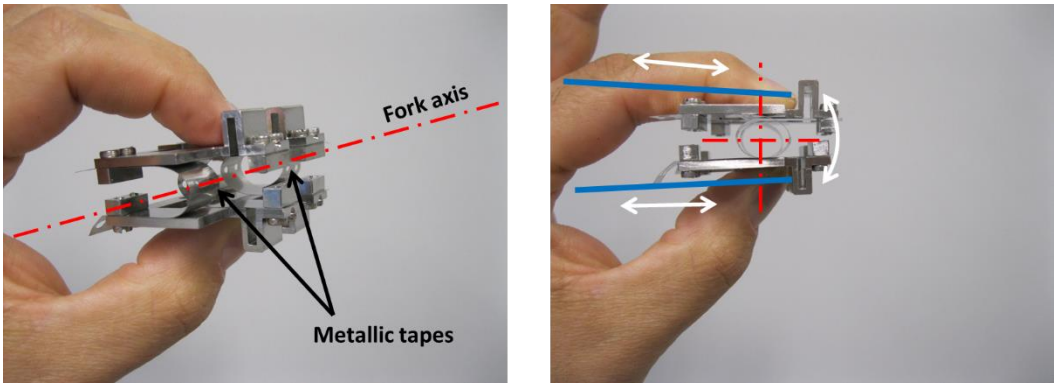

Figure 3.14: Detail of the four tapes assembly which transmit the linear movement of the push-pull rods in a rotation on the fork shaft.

The angular stroke of the fork, between the OUT and IN positions, is 130 deg. The two end positions of this stroke are defined by means of a cam directly connected to the motor shaft and two spring-loaded cam followers.

As previously mentioned, the fork consists on a shaft and two arms welded together; the end of each arm is built up of 2 mm external diameter tubes, a 0.25 mm wall lightened by drilling, and the very end of this tube is separated by a short flexible part (see Figure 3.15). A carbon wire made of 12 filaments of 7um diameter twisted together is stretched between the tips of the two flexible parts of the arm with a force of 0.2 to 0.3 N.

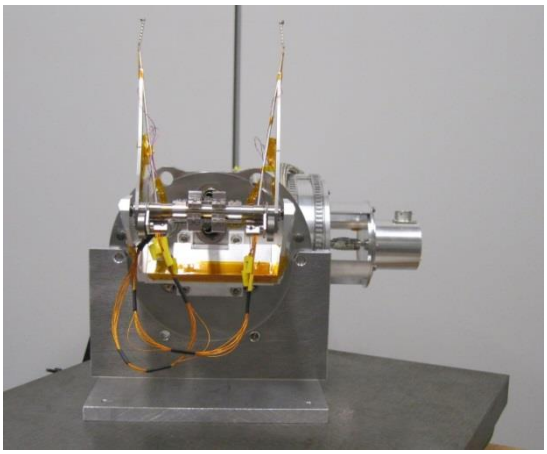

Figure 3.15: Image of the PS scanner; the geometry of the fork can be clearly appreciated.

3.2.2. Misalignment errors

Two types of misalignment errors have been considered. First, the misalignment directly affecting the angular positioning of the fork. Due to the design of the mechanism, small dimensional or mounting errors may result in variations on the full angular stroke of the fork and its offset respect to its theoretical initial position. Second, the misalignments affecting the orientation of the wire respect to the beam have been evaluated. These misalignments, due to mounting of the fork and its support on the flange, may induce errors resulting in a wire orientation error. The parallelism of the wire respect to the horizontal beam plane (for vertical scans) or to the vertical beam plane (for the horizontal scans) has an influence on the beam width measurement, as described in the previous section.

In order to evaluate these misalignments, a geometry control of different key points of the scanner has been performed. Figure 3.16 shows the experimental setup used for the geometry control. The results of this control have been compared with the theoretical geometry of the device in order to have a quantification of the error.

Figure 3.16: Experimental setup used for geometry control.

Methodology

In order to perform these measurements, the scanner has been installed in the maintenance support which consists of two orthogonal aluminium plates fixed together. The horizontal plate serves as a base for the support while the vertical allows the fixation of the scanner flange. The support is made in such a way that it allows the movement of the fork and the access to most of the parts of the device.

The maintenance support with the scanner mounted on it has been laid up on top of a flat reference surface. The assembly has been properly levelled so that the scanner flange is perpendicular to the

reference surface. The correct orientation of the scanner flange has been achieved by adjusting to the same value the vertical position of the two orientation pins on the flange whit respect to the reference surface. These two orientation pins are normally used to align the scanner on the vacuum tank and therefore they can be considered as a precise reference.

In order to know the location and orientation of the wire, the following measurements have been performed:

- distance between the two extremities of fork axis,
- length of the fork (distance from its axis to the wire), measured for both arms,
- wire ends position, measured for the both locations, IN and OUT.

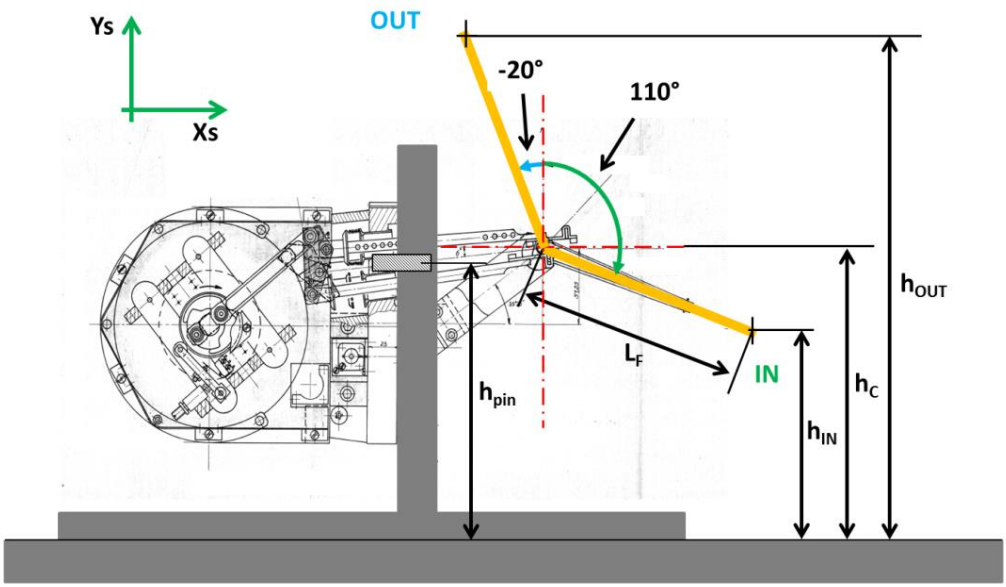

Figure 3.17: Schematic of the measured points.

The different measured points are shown in Figure 3.17; h_{pin} is the vertical distance from the reference surface to the orientation pins, h_{IN} and h_{OUT} are the vertical distances between the wire ends and the reference surface in the IN and the OUT configuration respectively, and h_C is the vertical distance between the fork axis and the reference surface.

Based on these measurements, the location and orientation of the wire has been calculated at IN and OUT locations.

Results

The results of the performed measurement are shown in Figure 3.18. The analysis of these measurements (summarized in Table 3.1) shows that the error in the fork angular stroke is in the range of 2.4 deg. The offset respect to the theoretical initial location of the fork (the OUT location) is in the range of 2 deg. and the offset respect to the IN position is in the range of 0.4 deg.

Table 3.1: PS wire scanner angular errors

	Theoretical (deg.)	**Measured (deg.)**	
		Opposite to Motor	Motor Side
θ_{OUT}	110	112.35	111.73
θ_{IN}	-20	-20.17	-20.61
θtotal	130	132.53	132.33
Offset_OUT	0	2.35	1.73
Offset_IN	0	-0.17	-0.61

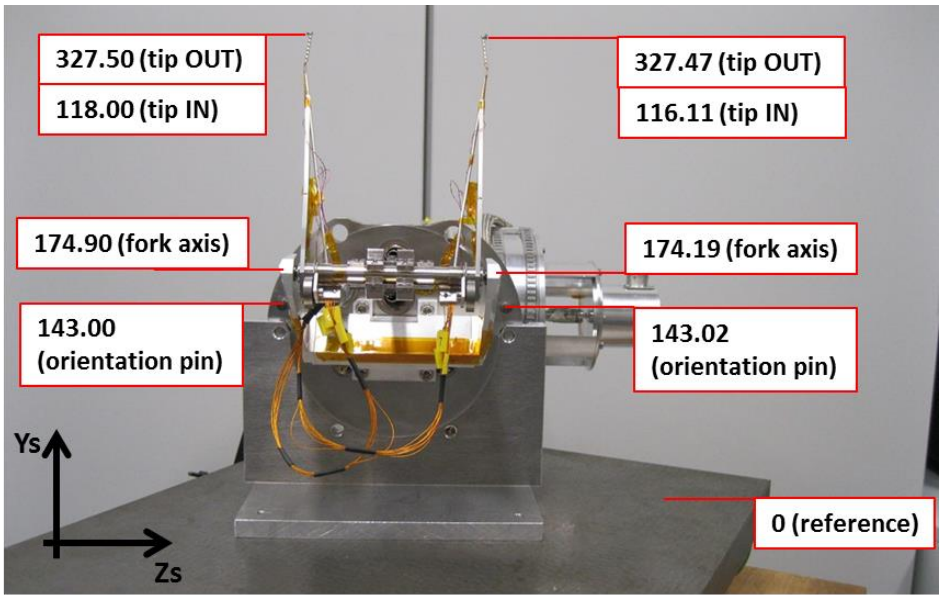

Figure 3.18: Result of the measurement performed on the test scanner.

As can be seen in Figure 3.19, the orientation of the scanner when it is in operation is rotated by 70 deg. with respect to the position where the measurements were taken. Therefore the measured values have been rotated by 70 deg. The angular location of the fork at the wire-beam intersection is 110 deg.

The performed measurements allow the calculation of the wire orientation error as a function of the angular location of the fork. Therefore, the wire orientation error in the wire-beam intersecting region (110 deg.) has been calculated and its value is in the range of 0.93 deg.

In accordance with the analytical equations in the previous section, the relative width error due to a wire orientation error of 0.93 deg. is shown in Figure 3.20.

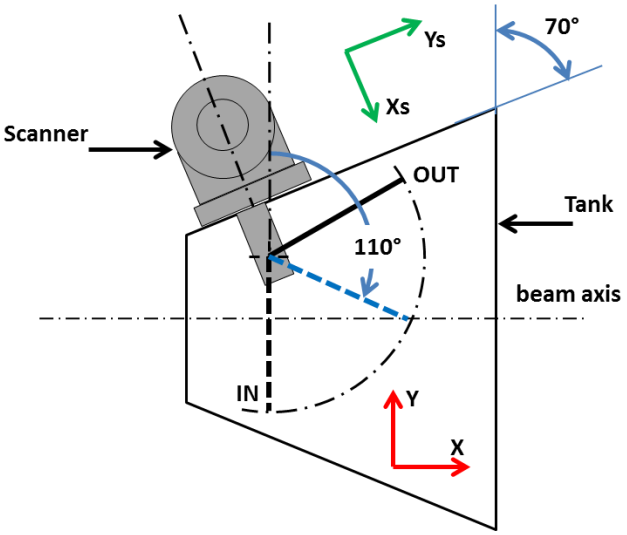

Figure 3.19: Schematic of the integration of the scanner in the vacuum tank; the beam coordinate system (in red) is rotated by 70 degrees respect to the scanner coordinate system (in green).

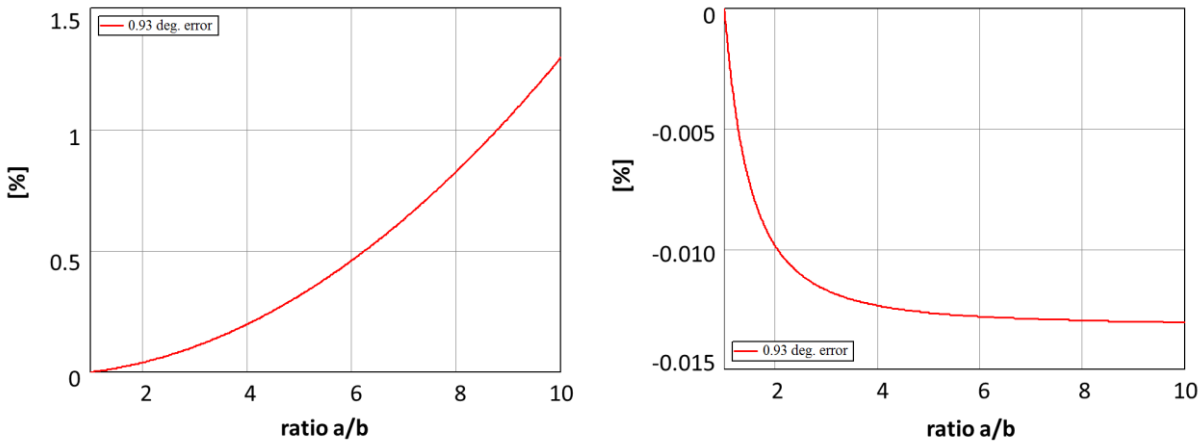

Figure 3.20: Vertical (left) and horizontal (right) width of measured relative error as function of the ellipse semi-axis ratio for a wire orientation error of 0.93 deg.

The orientation error thus calculated does not include any error due to any possible vacuum tank misalignment.

These values have been measured in a scanner dedicated to perform different types of test related to this thesis work. The fork has been manipulated several times in order to install the strain gauges used to perform the vibration measurements and therefore certain deformations have been unavoidable. However the scanners used in normal operation show lower values of wire orientation error, typically in

the range of 0.3 degrees. Concerning the misalignment errors that affect the angular positioning of the fork, the scanner used in operation shows equivalent values as those shown in Table 3.1.

3.2.3. Mechanical play

The mechanical play between the elements of the kinematic chain allows a certain angular displacement of the fork that also contributes to the beam size measurement error. The measurements shown in this section are intended to determine the amplitude of this error.

Methodology

The effect of the error due to the kinematic play is not homogenous along the whole travel of the fork because the kinematic chain behaviour is nonlinear; therefore the measurement of the mechanical play has been performed for different angular positions of the fork stroke, 13 in total, i.e. a measurement every 10 deg. approximately.

The experimental setup used to perform these measurements is shown in Figure 3.21. With the scanner properly mounted on the maintenance support, the fork arm was smoothly shaken in tangential direction and the amplitude of its tangential displacement was recorded by means of a dial comparator. At each measured position, the motor was locked by means of an *ad hoc* clamp installed in the motor-potentiometer coupling. Special care was taken throughout the measurements not to deform any mechanical element of the mechanism by means of the applied forces. Then the tangential value of displacement was derived to obtain the equivalent angular displacement at the fork axis.

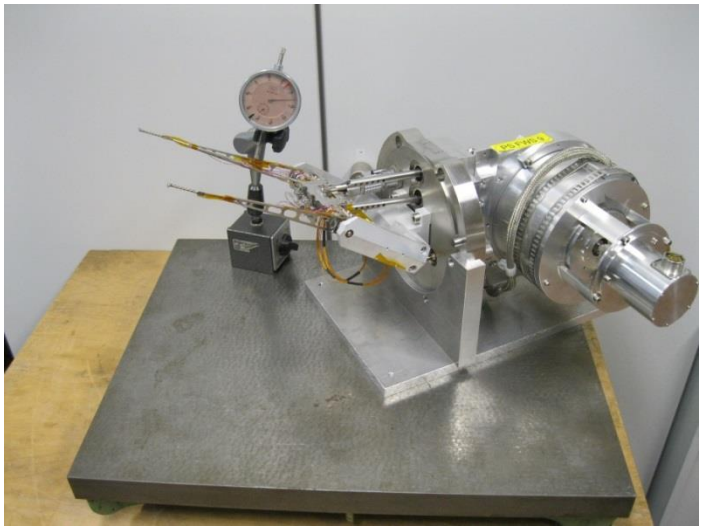

Figure 3.21: Experimental setup used to measure the mechanical play.

Results

The unrestricted angular displacement of the fork and the equivalent tangential displacement at the level of the fork tip are shown in Figure 3.22.

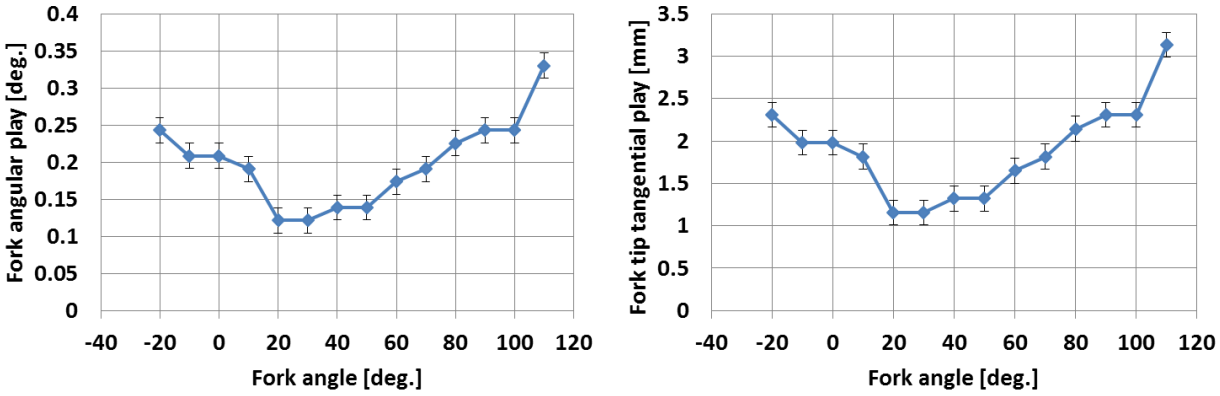

Figure 3.22: Angular play of the fork (left) and tangential play of the fork tip (right) along its angular stroke.

During the measurements to determine the backlash, it was observed that the bellows spring effect results in a non-constant force in the mechanism. When the mechanism is in the OUT position, i.e. the upper bellow is fully extended, the lower bellow, which is fully compressed, exerts a force that tends to drive the mechanism toward the IN position. Similarly, when the mechanism is in the IN position, the upper bellow, since fully compressed, exerts a force that tends to move the mechanism toward the OUT position. This phenomenon is schematically shown on Figure 3.23. In both configurations, the unbalanced force is compensated by the system of cams and springs, which ensures a stable position of the mechanism either at IN or OUT position. However, since this force depends on the length of the bellows, which changes along the full motion cycle, its value and direction are not constant (for example in the central region of travel the forces exerted by the bellows are mutually balanced).

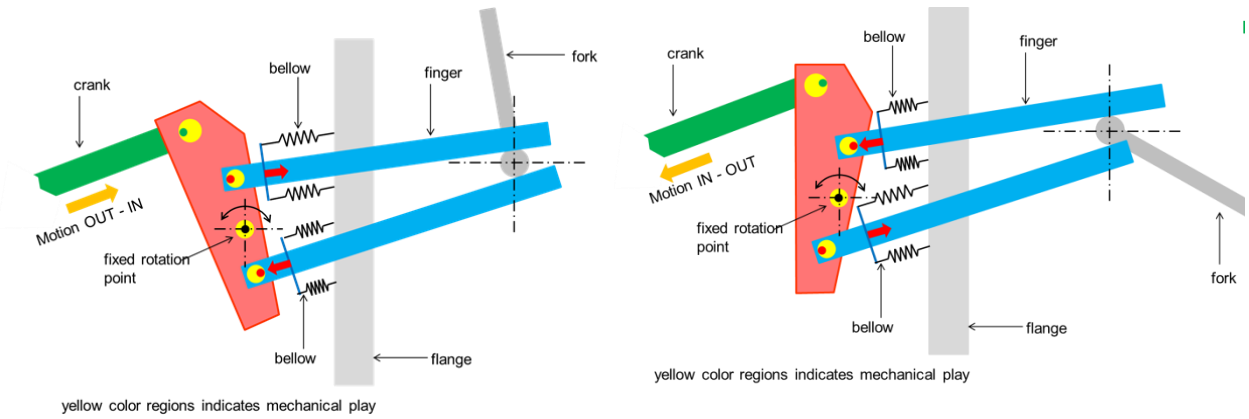

Figure 3.23: Illustration of the mechanical play and bellows spring effect.

On the other hand, the scanner used for this test had performed approximately 250000 scan cycles before being used for this work. Therefore the measured values of play are expected to be larger than in the operating scanner.

3.2.4. Error due to dynamics effects

The errors shown in the previous sections (misalignment and mechanical play errors) are independent of the movement performed by the device. Therefore these errors could be considered as static errors, which do not depend on the dynamics, i.e. regardless the type of movement, the error in the final measurement is the same. However, the influence of the motion in the measurement chain also induces errors. The action of the inertial forces in the elements of the measurement chain yields the following effects which contribute to the global measurement error:

- transversal deflection of the fork,
- transversal deflection of the wire,
- wire vibrations.

The estimation of these errors for the case of the PS wire scanner is based on the development of a *vibration measurement system*. A complete description and result of this part of work is presented in the following chapter. Hereinafter some of these results are used to estimate the maximum error in the profile and position measurements induced by the dynamic effects.

Transversal deflections of the fork tips

From observation of Figure 3.24 (extracted from the next chapter), which shows the transversal deflections (X-deflections) of the right and left tips (values Q_1^R and Q_1^L respectively) respect to the fork angular position, it is possible to make an assessment of the tip transversal deflections in the region of the beam-wire crossing, (110 deg). The tip X-deflections at the beam-wire crossing region, are around -200 µm for the OUT-IN 300 µm (considering the mean between the two arms) for the IN-OUT motion.

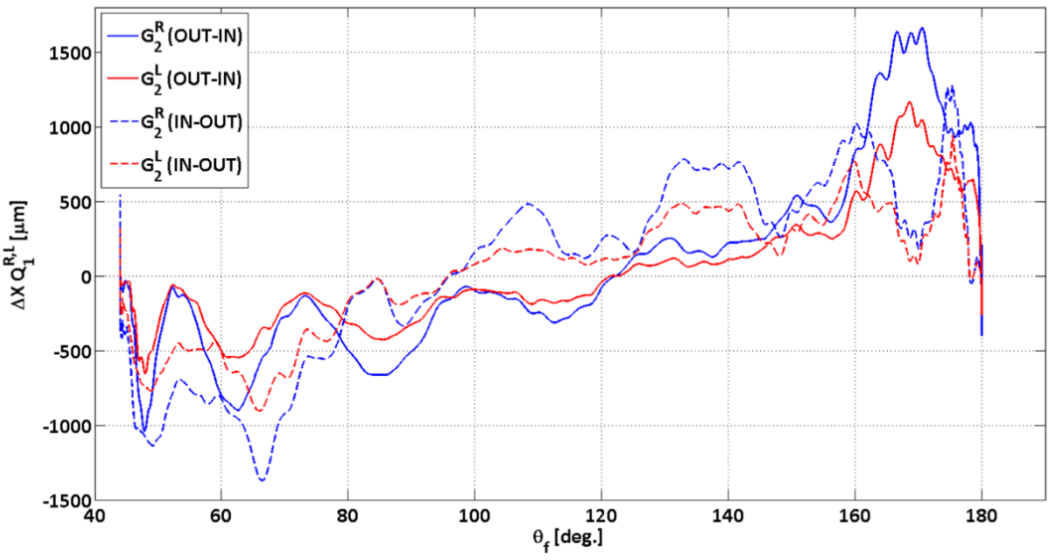

Figure 3.24: X-deflection of the fork tips (derived from the gauge measurements) for the two phases of the scan cycle as a function of the shaft angular coordinate.

Wire transversal deflections and vibrations

The assessment of the wire transversal vibrations requires further assumptions and analysis. Unfortunately the precision of the measurement system, which is detailed on the next chapter, does not allow a precise evaluation of the wire elongation. Figure 3.25 shows the wire oscillation amplitude ΔL and the tip distance variation ΔLz, as measured with the vibration measurement system. In principle the effective wire elongation could be calculated as ΔL-ΔLz. However, as shown in the plots, the value of ΔL is almost all the time lower than ΔLz, which is physically not possible. This could be due to a small calibration or offset error in the measurement system. Therefore, in order to estimate the wire transversal displacement, the result of the simulation models detailed on Chapter 5 have been used. Figure 3.26 has been extracted from Chapter 5 and shows the transversal wire displacement calculated from the parameters of and standard PS scanner. According to this figure it can be assumed a maximum wire transversal displacement of 0.150 mm.

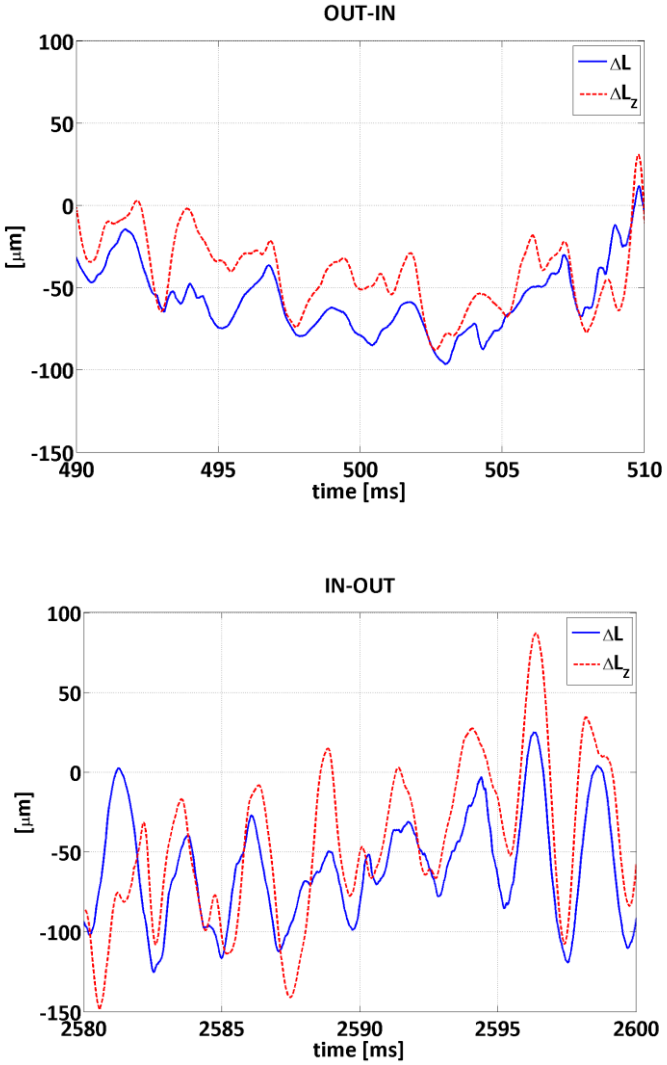

Figure 3.25: Wire elongation ΔL and the fork tips separation ΔL_z in the beam crossing region, extracted from Figure 4.16.

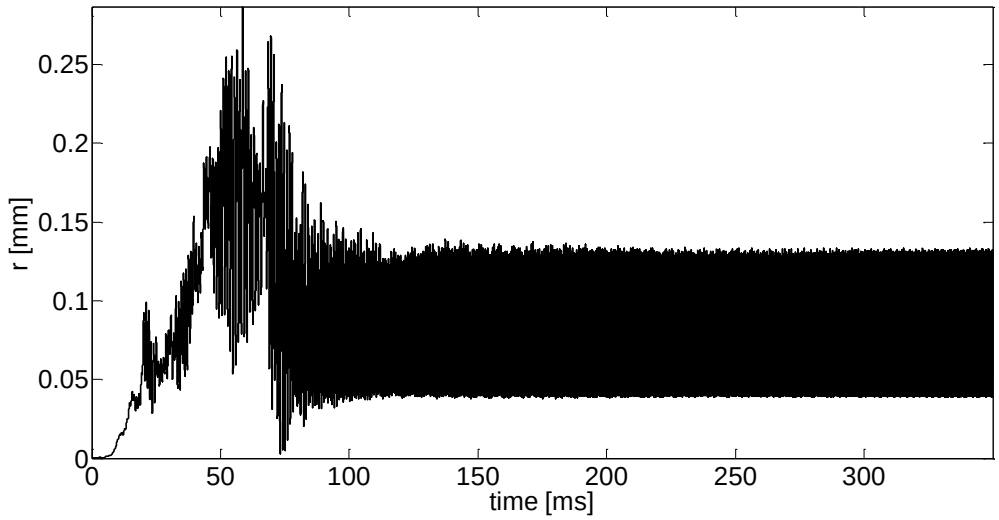

Figure 3.26: Wire transverse vibration results obtained with the hybrid approach during the OUT-to-IN phase of the scan cycle in Figure 1.23, and for a wire tension of 0.1 N.

Let's define E_x^F as the X-deflection of the fork tip and E_0^W as the maximum sag of the wire (which corresponds to the previous value named as s). Then, the maximum amplitude of a complete wire oscillation is $2E_0^W$. In order to determine the beam size and position, the values provided by the angular sensor have to be projected in a plane perpendicular to the beam, i.e. "the projection plane". From the performed wire elongation measurements it is not possible to determine the plane where the wire is oscillating. However the most unfavourable configuration is when the wire transversal oscillation plane is parallel to the projection plane (see Figure 3.27).

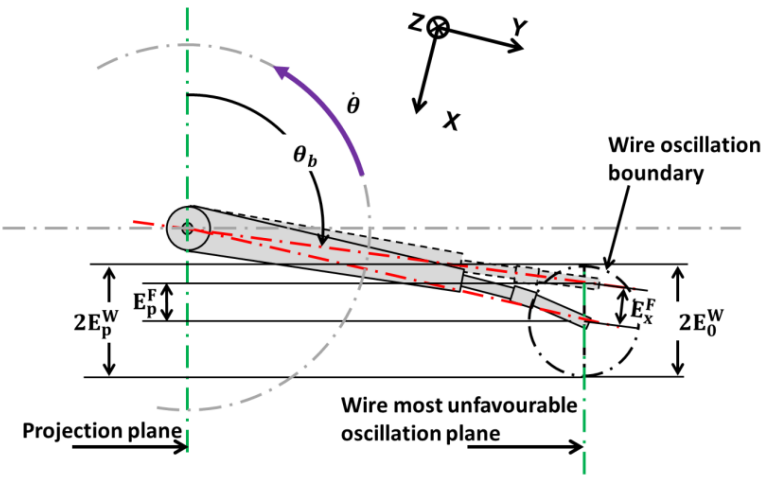

Figure 3.27: Illustration of the wire position error projection.

Due to the small size of the beam and the slow variation of E_x^F, this error can be considered to be constant along the whole beam crossing time. However the error due to the wire oscillation is not constant along this time. Let's assume that the time variation of the wire transversal deflection $E^W(t)$ obeys a sinusoidal function of the form:

$$E^W(t) = 2E_0^W \sin(\pi\omega t) \tag{3.26}$$

where ω stands for the wire oscillation frequency in Hz. The projection of the fork tip deflection E_p^F can be calculated as:

$$E_p^F = E_x^F \cos\left(\theta - \frac{\pi}{2}\right) \tag{3.27}$$

where θ is the angular measured position. Therefore the total projected error $E_p(t)$ due fork tip and wire deflections can be calculated as follows:

$$E_p(t) = E_p^F + E^W(t) = E_x^F \cos\left(\theta - \frac{\pi}{2}\right) + 2E_0^W \sin(\pi\omega t) \tag{3.28}$$

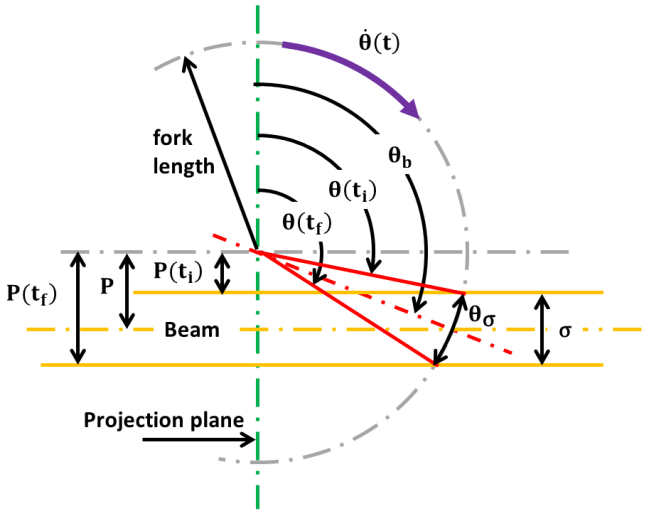

Figure 3.28: Illustration of the beam profile and position measurements.

As shown in Figure 3.28, t_i and t_f are defined as the initial and final crossing time instants of the wire with respect to a beam of size σ. Let's define t_σ as the time instant when a wire traveling at a certain angular speed $\dot{\theta}(t)$ needs to traverse this beam. Then:

$$t_\sigma = \frac{\theta(t_f) - \theta(t_i)}{\dot{\theta}(t)} \tag{3.29}$$

Beam position measurement

The measured position of the beam P_m is defined as:

$$P_m = \frac{P(t_i)+E_p(t_i) + P(t_f)+E_p(t_f)}{2} \tag{3.30}$$

which can be written as:

$$P_m = P + \frac{E_p(t_i) + E_p(t_f)}{2} \tag{3.31}$$

where P is the real position of the beam. Therefore the beam position error E_p^P is:

$$E_p^P = \frac{E_p(t_i) + E_p(t_f)}{2} \tag{3.32}$$

Introducing Eq. (3.28) into Eq. (3.32) results in:

$$E_p^P = \frac{2E_p^F + 2E_0^W (\sin(\pi\omega t_i) + \sin(\pi\omega t_f))}{2} \tag{3.33}$$

From Eq. (3.33) it can be shown that the maximum value of E_p^P does occur for a time interval $(t_f - t_i)$, such that $sin\left(\pi\omega\frac{(t_f-t_i)}{2}\right) = 1$, i.e, $\pi\omega\frac{(t_f-t_i)}{2} = \frac{\pi}{2}$. Therefore the maximum position error $E_{p\_max}^P$ can be calculated as follows:

$$E_{p\_max}^P = E_p^F + E_0^W \sin\left(\pi\omega\left(\frac{t_\sigma}{2}\right) + \frac{\pi}{2}\right) \tag{3.34}$$

Width measurement

The measured beam width σ_m can be calculated as the difference of the respective wire position projections $P(t_f)$ and $P(t_i)$ at times t_f and t_i,

$$\sigma_m = P(t_f)+E_p(t_f) - P(t_i)-E_p(t_i) \tag{3.35}$$

$$\sigma_m = \sigma + E_p(t_f) - E_p(t_i) \tag{3.36}$$

Therefore the beam size error E_p^{σ} is:

$$E_p^{\sigma} = E_p(t_f) - E_p(t_i) \tag{3.37}$$

Introducing Eq. (3.28) into Eq. (3.37) and considering that E_p^F can be treated as constant along the beam crossing, results in:

$$E_p^{\sigma} = 2E_0^W \left(\sin(\pi\omega t_f) - \sin(\pi\omega t_i)\right) \tag{3.38}$$

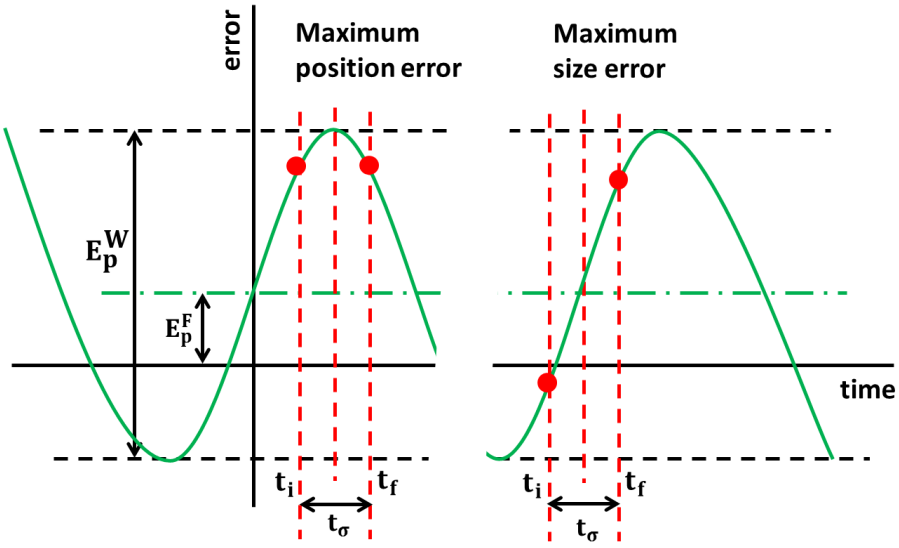

Figure 3.29: Time interval schematic for the maximum position and size error locations.

Again, according to Eq. (3.38), the maximum value of E_p^{σ} does occur for a time interval $(t_f - t_i)$, such that $\sin\left(\pi\omega\frac{(t_f - t_i)}{2}\right) = 0$, i.e, $\pi\omega\frac{(t_f - t_i)}{2} = (0, \pi)$, as shown in Figure 3.29. In this case, the maximum error for the beam size measurement $E_{p\_max}^{\sigma}$ is:

$$E_p^{\sigma} = 4E_0^W \sin\left(\pi\omega\left(\frac{t_\sigma}{2}\right)\right) \tag{3.39}$$

Table 3.2 shows the beam position and beam width maximum errors calculated for different beam sizes. For this calculation, the value of the angular speed at the beam crossing time interval was considered to be constant, and its value obtained from Figure 4.14 (see subsequent chapter).

Table 3.2: maximum calculated error in size and position due to dynamic effects

		OUT - IN			**IN - OUT**			
σ	Beam size	2	1	0.2	2	1	0.2	[mm]
$\dot{\theta}$	Beam cross. speed	100	100	100	110	110	110	[rad/s]
θ_b	Beam cross. ang.	110	110	110	110	110	110	[deg.]
t_σ	Beam cross. interval	0.129	0.065	0.013	0.118	0.059	0.018	[ms]
$E^P_{p\_max}$	Max. pos. error	-0.350	-0.350	-0.350	0.450	0.450	0.450	[mm]
$\delta E^P_{p\_max}$	Relative max. pos. error	0.623	0.624	0.624	-0.802	-0.802	-0.802	[%]
$E^\sigma_{p\_max}$	Max. size error	0.049	0.024	0.005	0.044	0.022	0.004	[mm]
$\delta E^\sigma_{p\_max}$	Relative max. size error	2.44	2.45	2.45	2.22	2.22	2.22	[%]

3.3. Summary

The sources of error that can affect a rotating wire scanner instrument have been identified. These errors have been estimated for the case of the PS wire scanner. A direct error quantification is not possible in all cases, so the vibration measurement system was used to determine the deflection and vibration amplitude values. It has also been necessary to use the wire-fork dynamic model to estimate the transversal wire oscillation amplitude.

The aim of this part of the work was not to find precise values of vibration amplitude, but to analyse the vibrational behaviour of the system. In fact the measurements performed by the strain gauges do not provide accurate values concerning the amplitude of the oscillations. However this measurement clearly indicates that oscillations occur during the motion and the frequencies involved in these oscillations can be accurately determined in the frequency domain analysis.

4. Vibration measurements system

This chapter is devoted to the description of the vibration measurement system which represent one of the most relevant parts of this work. The system has been used both to understand the vibrational behaviour of the PS scanner and to adjust the dynamic models of the wire-fork assembly. Furthermore the most innovative part of this system, that allows to measure the wire vibrations based on the piezoresistive effect of the wire itself, will be included in the design of the new wire scanner system (see Chapter 6) to monitor its vibrations during operation and provide on-line corrections of the measurements.

The chapter is organized as follows:

- Section 1 describes the measurement system.
- Section 2 describes the calibration procedures.
- Section 3 is devoted to the measurements of fork and wire vibrations.
- Section 4 presents some qualitative comments on the dynamics of the wire.
- Section 5 contains the relevant conclusions.

4.1. Measurement System

The vibration measurement system has been developed for an existing fast wire scanner used in the PS [47, 48]. The experimental setup consists basically of seven elements (Figure 4.1):

- a wire scanner actuator,
- a wire scanner fork equipped with semiconductor strain gauges,
- an electronic readout system based on a Wheatstone bridge to measure the resistance variation on the strain gauges,
- an electronic readout system based on a Wheatstone bridge to measure the wire resistance variations,
- an oscilloscope,
- a vacuum tank,
- a vacuum pump.

During the scan cycle, the following variables are measured:

- actuator angular position,
- tension on the strain gauges bonded to the fork,
- changes of electrical tension in the carbon wire.

The actuator angular position is measured by means of a precision rotary potentiometer and a 16 bits ADC. This allows an angular resolution of 95 µrad.

The four channels available in the oscilloscope limited the simultaneously acquired quantities to two strain gauges, the wire resistance variation and the motor angular sensor. Hence, to cover the eight strain gauges available in the setup it was necessary to perform multiple measurements.

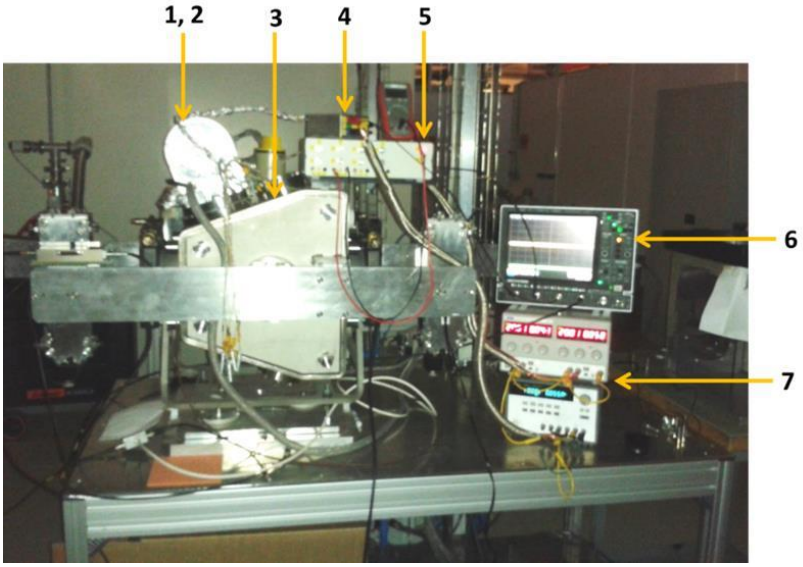

Figure 4.1: Experimental setup for vibration measurements:

actuator (1), fork (2), vacuum tank (3), Wheatstone bridge and amplifier for wire resistance variations (4), Wheatstone bridge and amplifier for strain gauges (5), oscilloscope (6), power supplies (7).

Although standard resistive strain gauges were used initially, their resolution was not high enough to show the deflections of the fork arms and were replaced by P type silicon (111) semiconductor strain gauges. The gauges have been bonded to some strategic parts of the fork arms using 3M™ Scotch-Weld™ General Purpose Instant Adhesive EC2500. Figure 4.2 show a typical strain gauge bonded to the fork arm. The dimensions and performances of the gauge bonded to the fork are shown in Table 4.1.

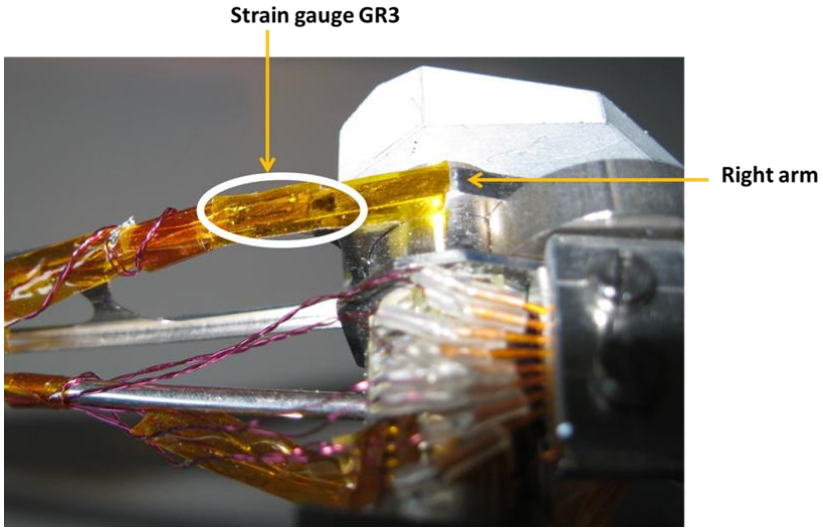

Figure 4.2: Semiconductor strain gauge detail bonded to the PS scanner arm.

Table 4.1: Dimension and performances of semiconductor strain gauges.

Resistance [Ohm]	350
Dimension naked, length x width x thickness [mm]	3.8 x 0.2 x 0.04
Dimension baking, length x width x thickness [mm]	5 x 3.7 x 0.05
Gauge factor (GF)	130 ± 5%
TCR [1/°C]	< 0.35 %
TCGF [1/°C]	< 0.28 %
Maximum working current [mA]	10
Operating temperature range [°C]	- 50 ~ +80
Fatigue life time [cycles]	$2 \cdot 10^6$
Strain limit [με]	6000

Figure 4.3 shows the coordinate system and the location of the sensors (strain gauges) on the fork. The Z axis is the shaft longitudinal direction and coincides with the wire longitudinal direction in the rest configuration; the Y correspond to the fork longitudinal direction, and the X axis is transversal to both elements. Gauges GR2, GR3, GL2 and GL3 are sensitive to deflections in the X direction ("transversal direction"); gauges GR1 and GL1 are mainly sensitive to the deflections in Z direction ("longitudinal direction"). In fact gauges GR1 and GL1 are sensitive to the deflections both in the X and Z directions. However, as they are bonded in the neutral bending axis of the X deflections, even if X deflections do occur, their contribution to the total strain variation would be negligible.

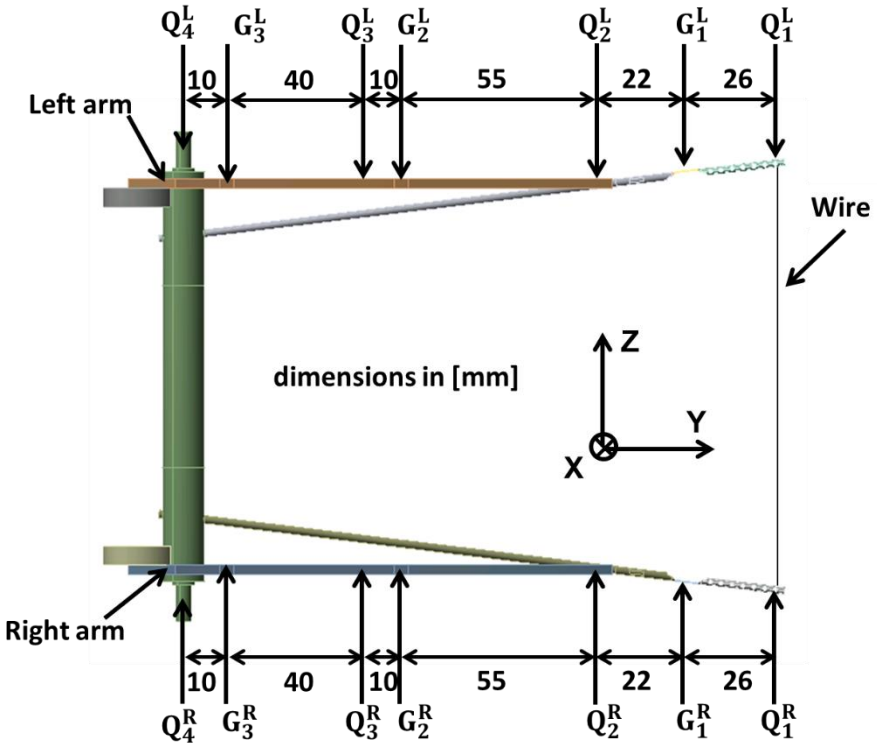

Figure 4.3: Location of the semiconductor strain gauges on the PS fork ($G_n^{R,L}$), location of points whose deflection has been measured ($Q_n^{R,L}$), and definition of the coordinate system.

An electronic circuit based on a Wheatstone bridge and an amplifier has been developed to measure the strain gauge and wire resistance variations. The amplified tension is read by the oscilloscope. This acquisition system records also the angular position of the fork by means of the actuator angular sensor.

The electronic readout system for the strain gauges consists of four identical circuits so the strain gauges can be measured simultaneously. A similar system, that consist of a single Wheatstone bridge and a single amplifier, has been developed for the wire resistance variation. The schematics of this electronic circuit can be seen in Appendix B.

4.2. Calibration procedures

The final goal of the calibration procedure is to quantify the X- and Z-deflections of the fork arm and the changes of the wire length (wire elongation) ΔL, from the measurement of the electrical tension variations [ΔU] recorded by the acquisition system during the scan cycle.

The gauges G_n^R/G_n^L record strain mean values in the region of 3.8 mm where they are located. Those mean values, expressed as electrical tension changes ΔU, will be identified as the values at locations G_n^R/G_n^L.

Gauges GR1 and GL1 are mounted on the fork flexible hinges (locations G_1^R and G_1^L). Consequently they are mainly sensitive to the wire elongation changes (and so to the Z-deflections of the fork). Their calibration should provide the following coefficients to determine fork tip position changes and change of distance between the two tips:

$$Cz_{GR1} = \frac{\Delta Z\left(Q_1^R\right)}{\Delta U(GR1)} \quad , \quad Cz_{GL1} = \frac{\Delta Z\left(Q_1^L\right)}{\Delta U(GL1)} \quad . \tag{4.1}$$

Gauges GR2 and GL2 are mounted on the fork middle zone (points G_2^R and G_2^L respectively), whereas gauges GR3 and GL3 are mounted on fork zones close to the shaft (points G_3^R and G_3^L respectively). The four are mainly sensitive to the X-transversal deflections of the fork. Their calibration should provide the following coefficients:

$$\frac{\Delta X\left(Q_1^R\right)}{\Delta U(GR2)} \quad , \quad \frac{\Delta X\left(Q_1^R\right)}{\Delta U(GR3)} \quad , \quad \frac{\Delta X\left(Q_1^L\right)}{\Delta U(GL2)} \quad , \quad \frac{\Delta X\left(Q_1^L\right)}{\Delta U(GL3)} \quad . \tag{4.2}$$

It is not straightforward to obtain those calibration coefficients under real dynamical conditions (the fork deflections and the wire elongation during the scan cycle are generated by the inertia forces associated with the rotation of the shaft). In the present case, less demanding conditions have been adopted and are presented in the following three subsections.

For the sake of simplicity, some calibration coefficients have been obtained through separate static measurements on the fork and on the wire (those two elements were not assembled together during the calibration process).

The measurements have to be complemented by a Finite Elements (FE) simulation of the fork deflections. This FE model will also be used to assess the influence of the dynamic conditions, associated with the fork rotation during the scan cycle, on the calibration coefficients. The model will have to be tuned to properly match the measurements.

4.2.1. Calibration coefficient for the wire elongation

Measuring the wire resistance elongation coefficient is done by recording the resistance variation (ΔR) as a function of the elongation changes (ΔL). The procedure has consisted on increasing the wire length progressively and measuring simultaneously the resistance variation. Figure 4.4 shows the experimental setup, which includes a 10 µm resolution linear stage equipped with an electrically isolated clamp, a fixed point with another clamp (each wire end is attached to a clamp), and two electrical cables to connect the multimeter.

The gauge factor (GF) can be determined through $GF = (\Delta R/R_0)/(\Delta L/L_u)$, where R_0 and L_u are the initial resistance and length of the wire respectively. The wire tension elongation coefficient (CL_W) has been obtained using the same experimental setup replacing the multimeter by the Wheatstone bridge circuit. Figure 4.5 shows the measured curve for the case of the 34µm diameter carbon wire typically mounted on the fork tips.

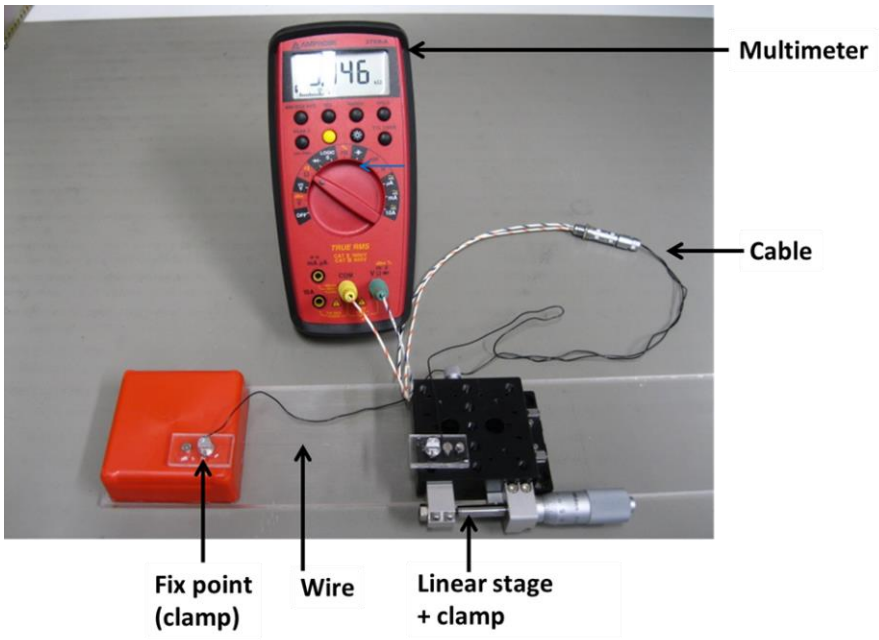

Figure 4.4: Experimental setup used to measure the wire resistance variation as a function of the wire elongation.

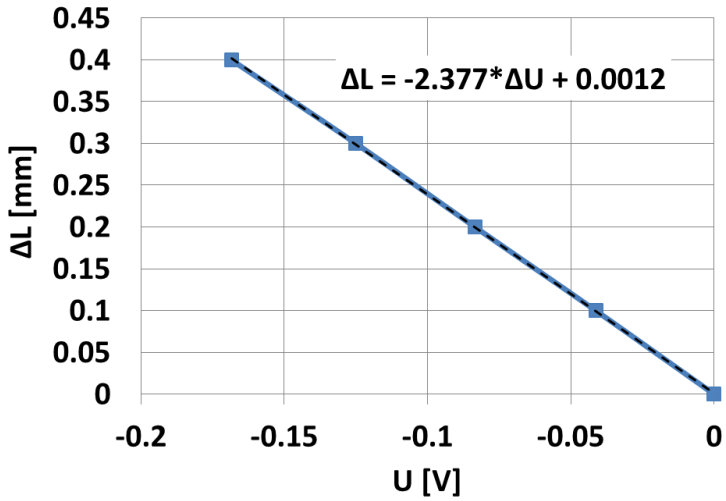

Figure 4.5: Change of wire elongation as function of voltage change.

The measurement of the wire axial stiffness was performed by means of an experimental setup consisting in a calibrated dynamometer and a calliper (to measure the wire elongation). The wire ends are attached to a fixed point and to the dynamometer. The procedure consisted in pulling the wire by means of the calibrated dynamometer and measuring simultaneously the wire length L and the applied force F. The wire axial stiffness k_w is determined through $k_w = F/(L - L_u)$.

Table 4.2 summarizes the main characteristics of the carbon wire and the result of the calibration.

Table 4.2: Wire characteristics and calibration coefficients

Ø	Wire diameter	34	[µm]
ρ	Density	1800	[kg/m^3]
L_U	Wire length	115	[mm]
k_W	Axial stiffness	344	[N/m]
F_{max}	Breaking force	0.5	[N]
R	Resistance	31	[Ohm/mm]
CL_W	Tension elongation coefficient	-2.377	[mm/V]
GF	Gauge factor	0.64	

4.2.2. Calibration coefficients for the fork Z-deflections

The calibration of gauges GR1 and GL1 (sensitive to the Z deflections) has been achieved through a simple procedure consisting of imposing controlled progressive deflections on the fork tips in the Z direction $\left(\Delta Z\left(Q_1^R\right), \Delta Z\left(Q_1^L\right)\right)$ and recording simultaneously the tension changes $\left(\Delta U(GR1), \Delta U(GL1)\right)$ using the Wheatstone bridge circuit.

Figure 4.6 shows two typical curves (for the left and right fork tips). Their slope represents the calibration coefficient. Table 4.3 summarizes the results.

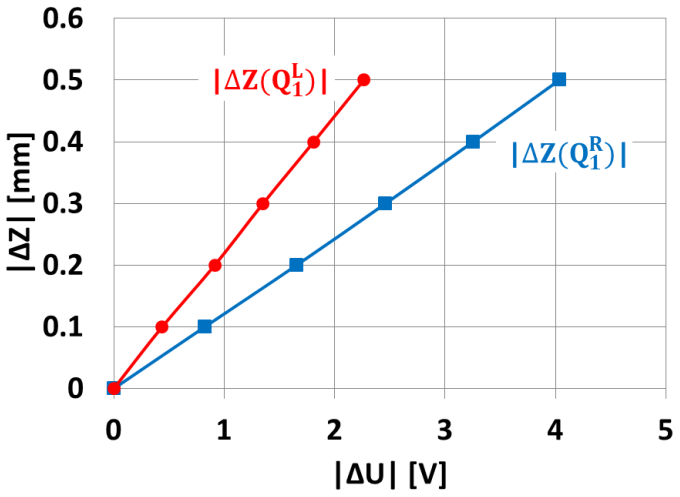

Figure 4.6: Typical result of fork tip deflections $\Delta z\left(Q_1^R\right)$ and $\Delta z\left(Q_1^L\right)$ vs. tension variations on GL1 and GR1, respectively.

Table 4.3: Z-deflection calibration coefficients

Coefficient	**[mm/V]**
Cz_{GR1}	-0.124
Cz_{GL1}	0.221

4.2.3. Calibration coefficients for the fork X-deflections

This calibration is also based on static measurements but, unlike the preceding ones, the possible influence of the dynamical conditions on the deflection has been taken into account through FE simulations. The whole procedure can be described as a hybrid one and can be split into four steps:

- Calibration of the strain gauges under static loads.
- FE simulation of the fork under static loads.
- FE simulation of the fork under dynamic loads.
- Correlation of the previous results.

<u>Calibration of the Z-strain gauges under static loads</u>

For the static calibration, the fork is mounted on a rigid and stable support (in the same configuration as when mounted on the actuator) and subjected to a progressive load P_{exp}^{st} at a point Q (Q_R and Q_L for the right and left fork arms respectively) close to the fork tips (Figure 4.7). For each particular load, the tension variations $\left(\Delta U_{exp}^{st}(GRn), \Delta U_{exp}^{st}(GLn)\right)$ in the strain gauges sensitive to the X-deflections (n =

2,3) are recorded together with the fork deflections x_{exp}^{st} at the $Q_2^{R,L}$ and $Q_3^{R,L}$ locations by means of dial comparators.

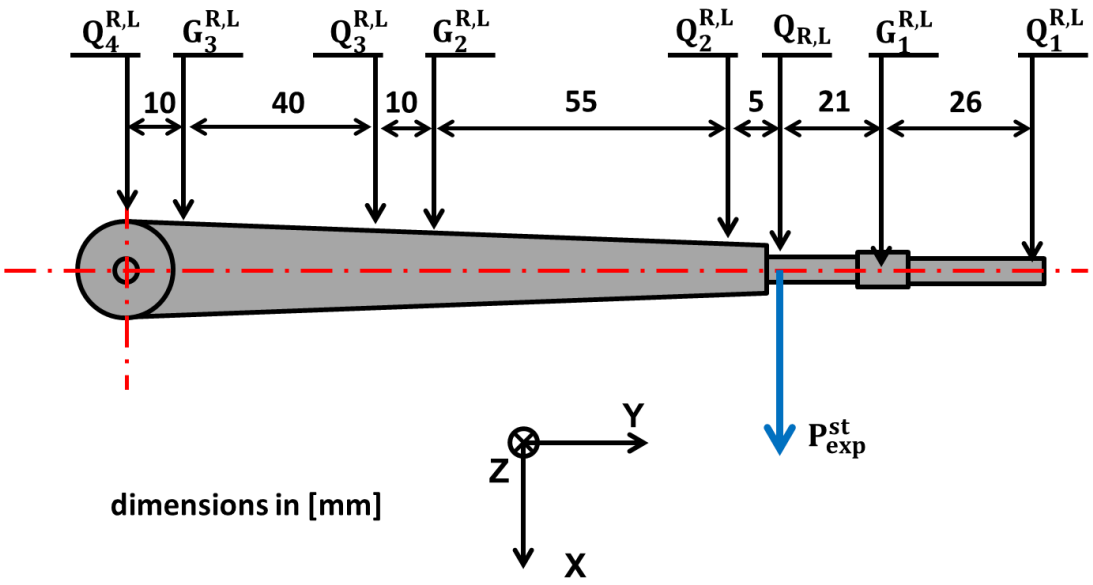

Figure 4.7: PS fork and applied load at $Q_{R,L}$ locations. $Q_n^{R,L}$ and $G_n^{R,L}$ are the measurement points and the gauge locations (as in Figure 4.3).

The correlation coefficient between the applied loads and the strain gauge tension variations and that between load and fork deflection is thus obtained for each location:

$$\frac{\Delta U_{exp}^{st}(GRn)}{P_{exp}^{st}(Q_R)} \quad , \quad \frac{x_{exp}^{st}\left(Q_n^R\right)}{P_{exp}^{st}(Q_R)} \quad , \quad \frac{\Delta U_{exp}^{st}(GLn)}{P_{exp}^{st}(Q_L)} \quad , \quad \frac{x_{exp}^{st}\left(Q_n^L\right)}{P_{exp}^{st}(Q_L)} \quad , \; n = 2,3 \quad . \tag{4.3}$$

FE static and dynamic simulations of the fork

The same conditions as described in the previous paragraphs (boundary conditions and applied loads) have been used to simulate the static fork deflections x_{FE}^{st} and the strain values ε_{FE}^{st} at points $G_2^{R,L}$ and $G_3^{R,L}$ through a FE model.

The wire was described by an analytical spring (preloaded with a tension of 0.3 N) tensioned between the two tips with the same axial stiffness as the real wire, k = 340 N/m (see Figure 4.8). The mass of wire soldering spots has been introduced as two mass points analytically modelled and located on the fork tips, with value m = 0.06 grs.

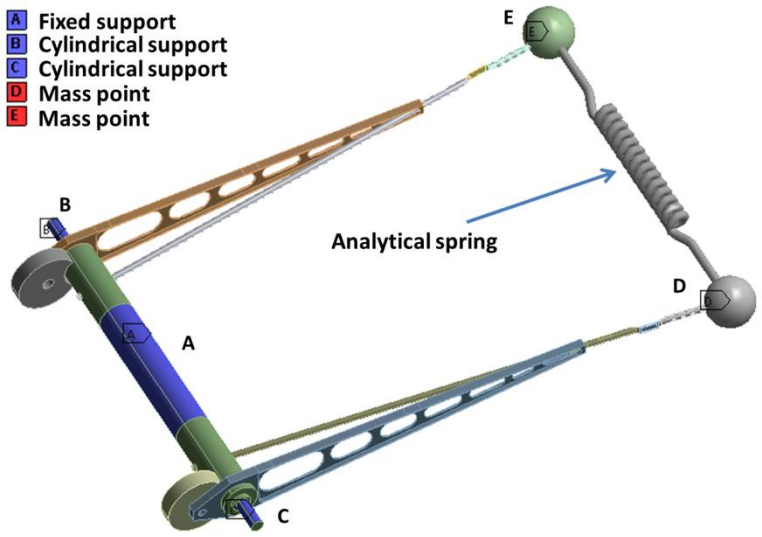

Figure 4.8: Finite Element model of the fork wire arrangement.

Figure 4.9 shows the results of the displacement at locations $Q_2^{R,L}$. As the FE model is perfectly symmetrical, $x_{FE}^{st}\left(Q_2^R\right) = x_{FE}^{st}\left(Q_2^L\right)$. Of course this is not the case for the real system, and consequently the measured X-deflections are not equal: $x_{exp}^{st}\left(Q_2^R\right) \neq x_{exp}^{st}\left(Q_2^L\right)$.

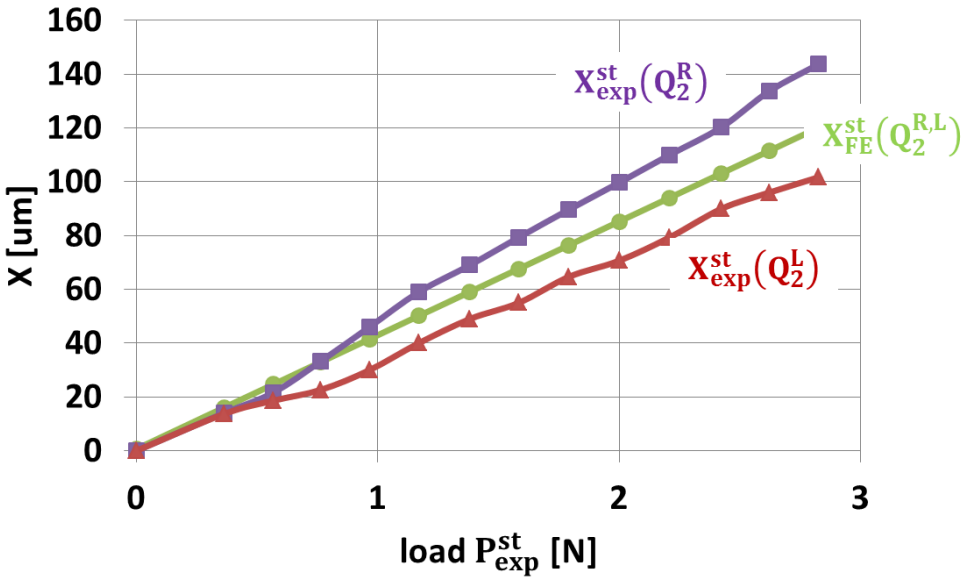

Figure 4.9: Measured (exp) and calculated (FE) static deflections at locations $Q_2^{R,L}$.

The correlation coefficients between loads and the resulting strains at points $G_2^{R,L}$ and $G_3^{R,L}$ are obtained based on the measurements:

$$\frac{\varepsilon_{FE}^{st}\left(G_n^R\right)}{P_{exp}^{st}\left(Q_L\right)} \quad , \quad \frac{\varepsilon_{FE}^{st}\left(G_n^L\right)}{P_{exp}^{st}\left(Q_R\right)} \quad , \; n = 2,3 \quad . \tag{4.4}$$

Finally, the fork has been subjected to different values of angular acceleration $\ddot{\theta}$ (from 0 to 12000 rad/s^2), and the corresponding deflections of the fork tips $x_{FE}^{dyn}\left(Q_1^R,\ddot{\theta}\right)$, $x_{FE}^{dyn}\left(Q_1^L,\ddot{\theta}\right)$ and the strain values $\varepsilon_{FE}^{dyn}\left(G_2^{R,L},\ddot{\theta}\right)$, $\varepsilon_{FE}^{dyn}\left(G_3^{R,L},\ddot{\theta}\right)$ have been calculated through the FE analysis (Figure 4.10). The corresponding correlation coefficients are:

$$\frac{x_{FE}^{dyn}\left(Q_1^R,\ddot{\theta}\right)}{\varepsilon_{FE}^{dyn}\left(G_n^R,\ddot{\theta}\right)} \quad , \quad \frac{x_{FE}^{dyn}\left(Q_1^L,\ddot{\theta}\right)}{\varepsilon_{FE}^{dyn}\left(G_n^L,\ddot{\theta}\right)} \quad , \; n = 2,3 \quad . \tag{4.5}$$

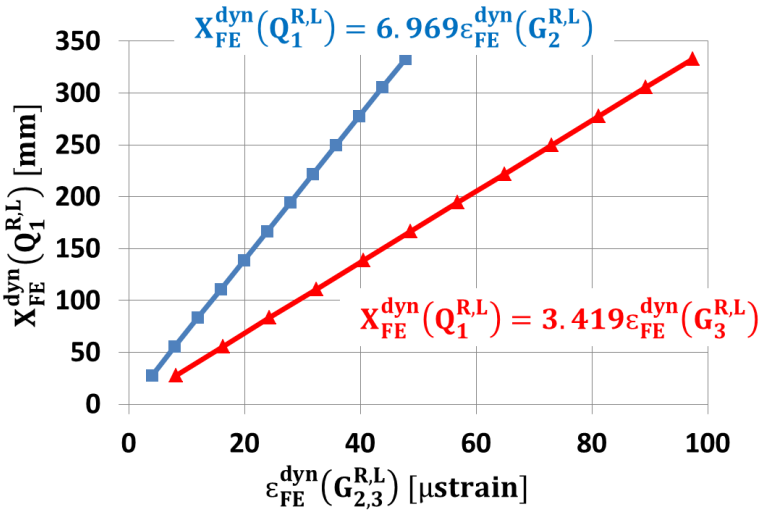

Figure 4.10: Typical result of calculated fork tip deflection vs. calculated strain for values of angular acceleration in the range $(0-12000)\,rad/s^2$.

Comparisons between the FE results and the measurements yield the calibration coefficients relating the X-deflection of the fork tips under dynamic conditions, $x_{FE}^{dyn}\left(Q_1^{R,L},\ddot{\theta}\right)$, and the electrical tension variation recorded by the X-strain gauges (also under dynamic conditions):

$$\frac{x_{FE}^{dyn}\left(Q_1^R,\ddot{\theta}\right)}{\Delta U_{exp}^{dyn}\left(G_n^R,\ddot{\theta}\right)}\ ,\quad \frac{x_{FE}^{dyn}\left(Q_1^L,\ddot{\theta}\right)}{\Delta U_{exp}^{dyn}\left(G_n^L,\ddot{\theta}\right)}\ ,\ n=2,3\ . \tag{4.6}$$

An example is given in Figure 4.11. The calibration procedure is summarized in Figure 4.12, and the detailed results are shown in Table 4.4.

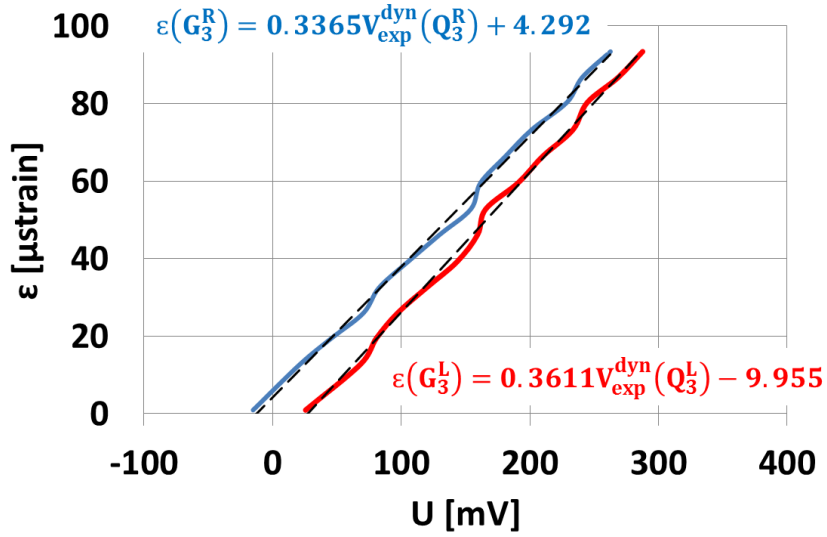

Figure 4.11: Typical result of correlation between the tension recorded by gauges GR3 and GL3, and the strain at points $G_3^{R,L}$ calculated with the FE model.

Table 4.4: Z-deflection dynamic calibration coefficients

Coefficient	$x_{FE}^{dyn}(\ddot{\theta})/\Delta U_{exp}^{dyn}(\ddot{\theta})$ $[mm/V]$
Cx_{GR2}	-2.658
Cx_{GL2}	-2.658
Cx_{GR3}	-1.304
Cx_{GL3}	-1.304

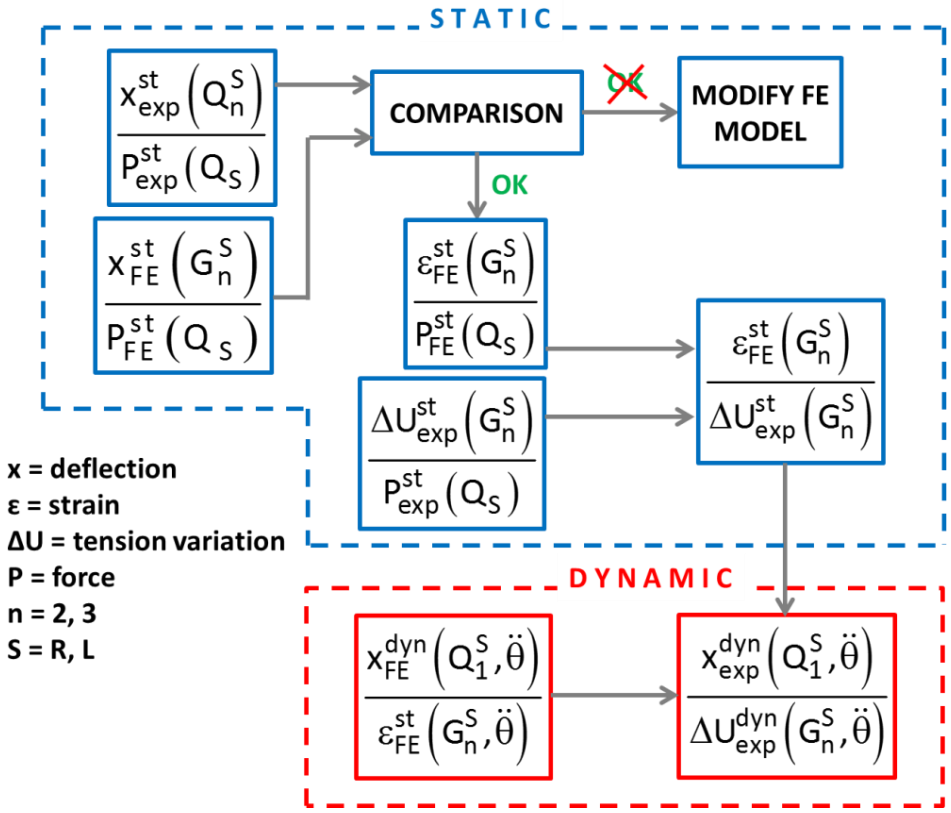

Figure 4.12: Flow diagram showing the calibration procedure. The diagram is subdivided in a static part (measurements and FE) and a dynamic part (only FE based).

4.3. Vibration measurements

Figure 4.13 shows a schematic drawing of the three variables that have been measured in dynamic conditions (during a whole scan cycle): X and Z deflections of the fork ("transversal" and "longitudinal" deflections, respectively) and wire elongation ΔL. As explained in the previous section, the fork longitudinal deflections and the wire elongation are computed from the records of the GR1 and GL1 gauges. The calculation of the fork transversal deflections is done from the records of the GR2 and GR3 gauges for one arm, and of the GL2 and GL3 gauges for the other one.

As mentioned above, the scan cycle consists of a rotational fork and wire motion, and can be divided into three phases:

- Motion from OUT to IN: the wire intersects the beam for the first time on the cycle. The main constraint is the wire speed at the beam crossing instant.
- Waiting time at IN position: both fork and wire are retained at the IN position during a certain time, long compared with the cycle duration.
- Motion from IN to OUT: similar to the first phase but in opposite direction; the wire intersects the beam a second time. Again the main kinematic constraint is given by the required minimum wire speed.

The minimum speed requirement is given by the maximum heat deposition of the beam in the wire (high temperature provokes wire material sublimation) and subsequent breakage due to the inertial forces or an instantaneous partial sublimation of the wire.

Typical motion patterns of the OUT-IN and IN-OUT phases as function of time are shown in Figure 4.14. As every scan cycle has to follow the same motion pattern, a unique predefined motion pattern can be used as reference to be followed by the scanner actuator. This predefined motion pattern has to be designed in such a way that it matches the requirements of the scan cycle. The requirements concern the full travel length, the beam crossing region and the wire speed at the beam crossing region.

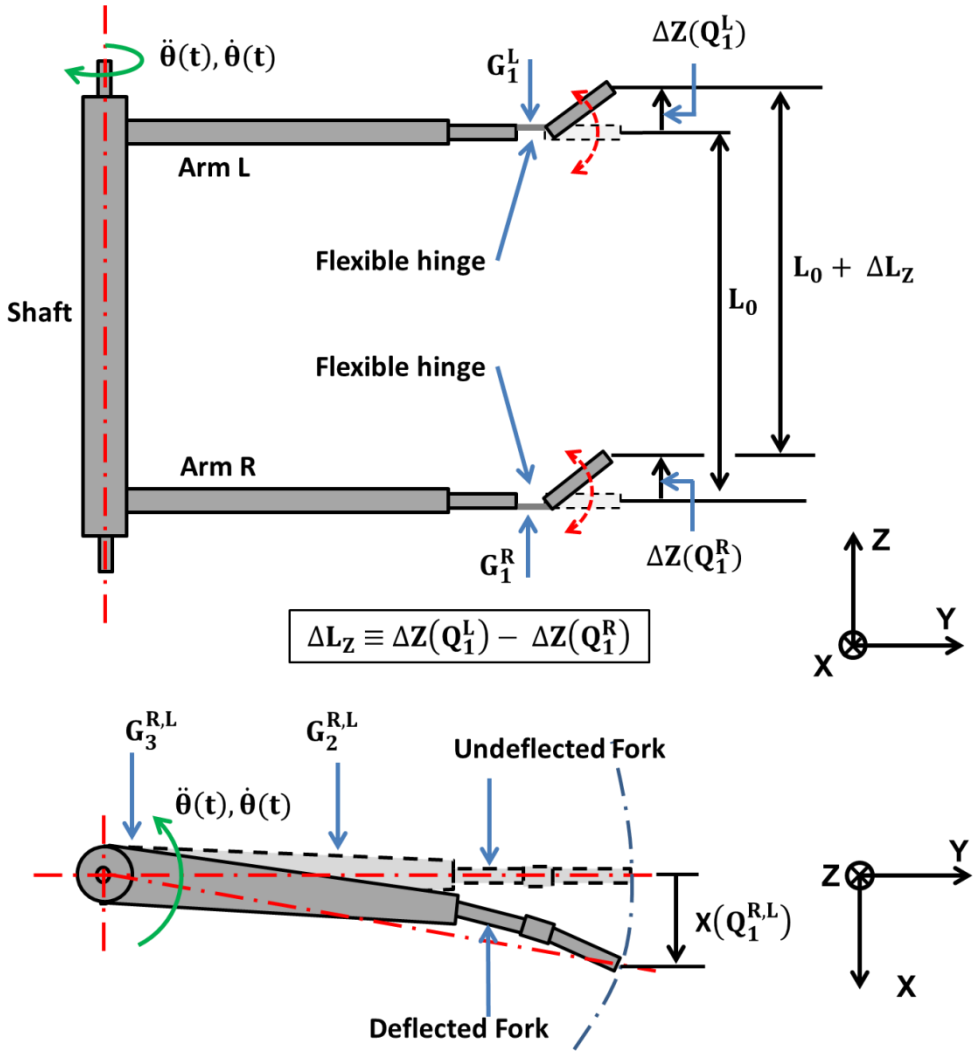

Figure 4.13: Schematic of the fork deflections with resulting wire elongation and location of the strain gauges.

The peak acceleration values can vary depending on the required peak speed, the fork length, the angular travel and the motion pattern design. Typical values for the PS wire scanner are shown in Table 4.5.

Table 4.5: Performances of the PS CERN vacuum wire scanner.

Peak speed [m/s]	16.4
Fork length [mm]	164
Peak angular speed [rad/s]	100
Peak angular acceleration [rad/s^2]	12700
Peak tangential acceleration [g]	212
Peak normal acceleration [g]	203

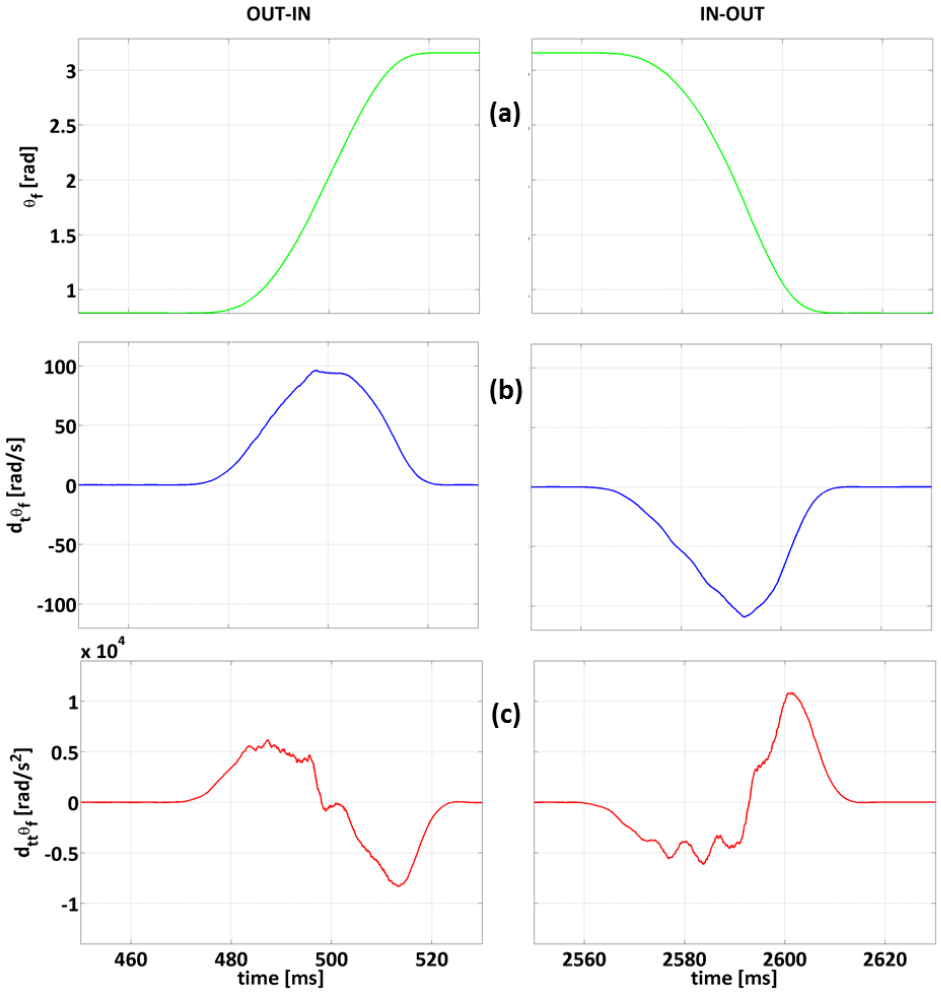

Figure 4.14: Typical measured motion patterns for a full scan motion cycle: angular position (a), velocity (b) and acceleration (c).

4.3.1. Z-deflections

Figure 4.15 shows the Z-deflections of the fork tips, $\Delta z\left(Q_1^{R,L}\right)$, calculated from the measured tension variations ΔU_{exp}^{dyn} at gauges GR1 and GL1 and the corresponding calibration coefficients.

As far as vibrations are concerned, the Z-deflection behaviour is rather similar for both tips, but with different phase. Both the OUT-to-IN and the IN-to-OUT motion show an oscillation of the fork tips with the same frequency and phase.

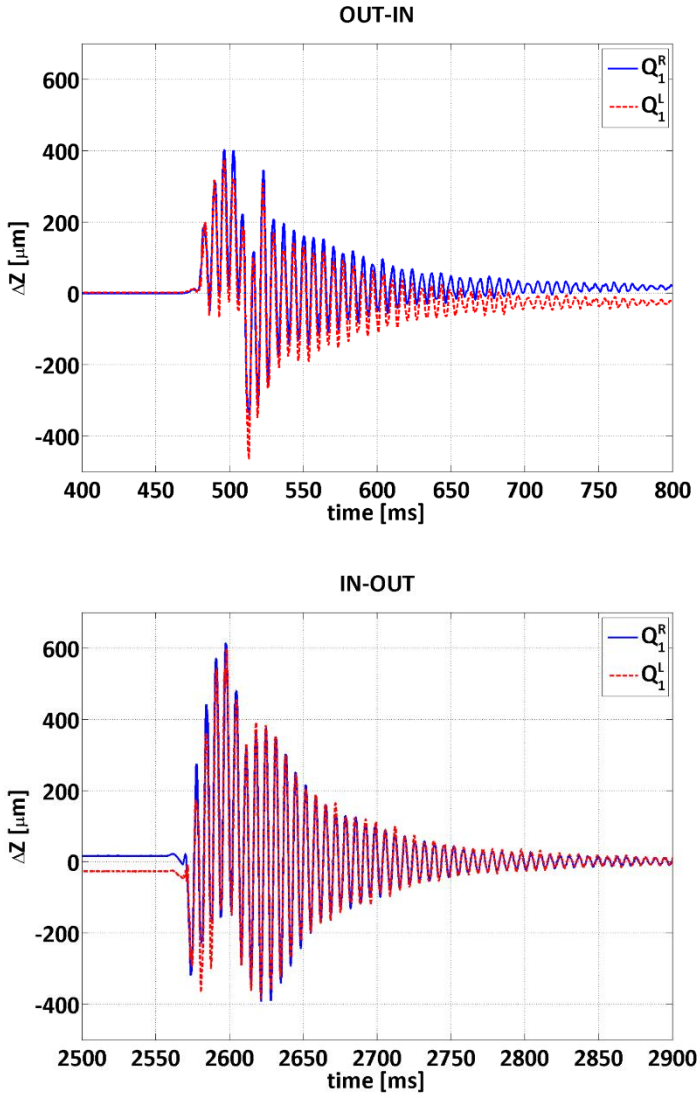

Figure 4.15: Z-deflection of the fork tips (locations $Q_1^{R,L}$) for the OUT-IN (top) and the IN-OUT (bottom) phases, calculated from the electric tension variations at gauges GR1 and GL2.

Wire elongation

Figure 4.16 compares the wire elongation ΔL assessed from the electric tension variations due to its resistance and the fork tips separation change ΔL_Z. Suppressing the oscillations with appropriate running sum value, ΔL and ΔL_Z show the same trend.

Although the absolute value of ΔL should always be equal or greater than the absolute value of ΔL_Z, this is not always the case. The differences are primarily due to the uncertainty of the calibration factors and to the noise of the wire resistance read-out electronics.

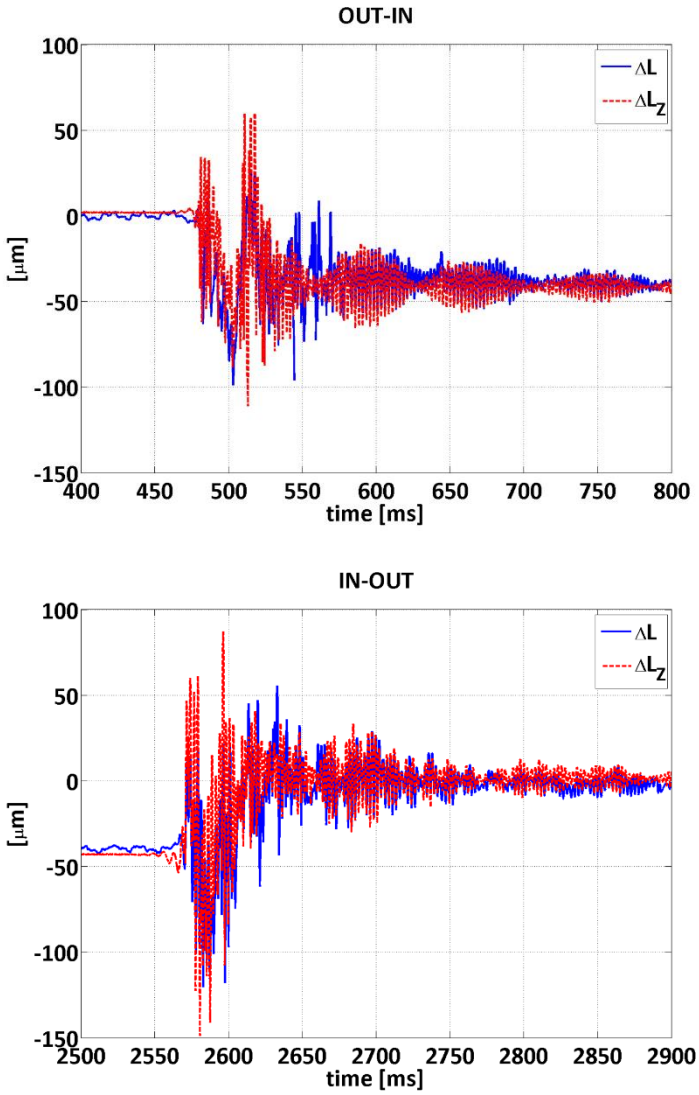

Figure 4.16: Comparison between the wire elongation ΔL and the fork tips separation ΔL_Z during the OUT-IN (top) and the IN-OUT (bottom) phases.

The comparison between the initial and final values shown in Figure 4.16 (both OUT-IN and IN-OUT motions) shows an offset of approximately 40 um between OUT and IN positions. A test consisting on a very gentle manual rotation from OUT to IN has been performed. The results of the test, where the wire,

the strain gauges signals and potentiometer position have been recorded are shown in Figure 4.17. Such a result can be well explained by a fork deformation as shown in Figure 4.18. Due to this deformation (defect), the fork tips tend to approach each other. However, as they are preloaded by the wire, this results in an increasing of the hinges outward bending, which is measured by the gauges (GR1 and GL1 provide a relative measurement between the tip and the fork arm) as if there were a tip separation of approximately 300 µm. However the wire elongation which is an absolute measurement, shows that what occurs is an approaching between the tips of around 40 um.

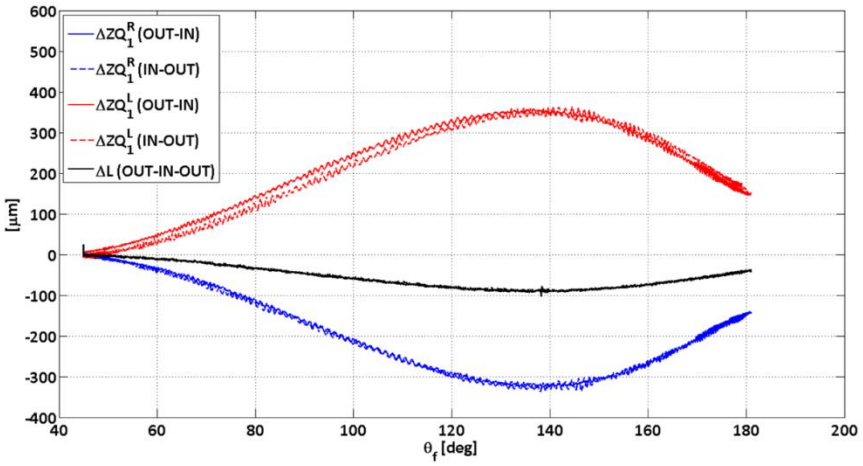

Figure 4.17: Values of the tip deflection for a gentle manual rotation.

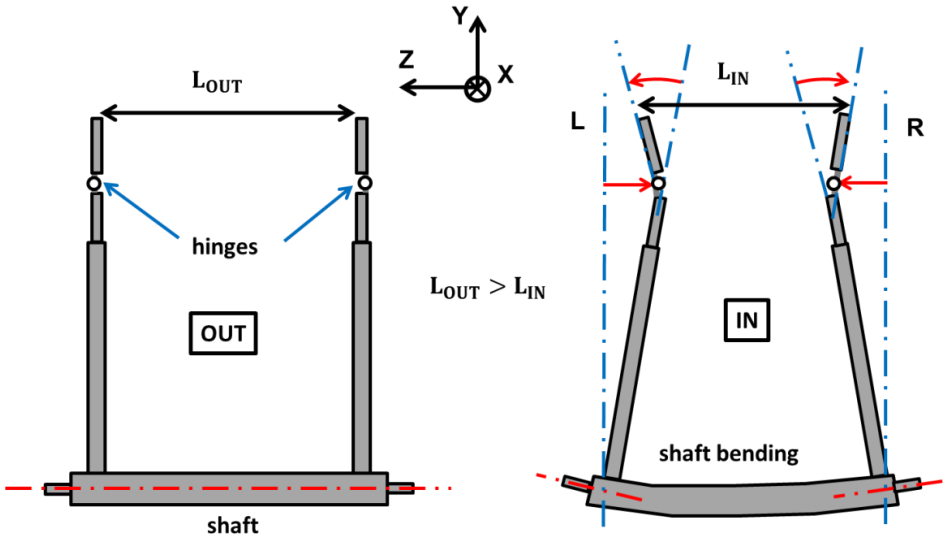

Figure 4.18: Illustration of the phenomenon causing the offset signals between OUT and IN.

4.3.2. X-deflections

The measured Z-deflections at the locations Q_4^R and Q_4^L were zero for all load values applied at the location Q_R and Q_L. Therefore these loads do not produce any bending on the shaft along the Y axis which could distort the measurements of the static deflections performed on the location $Q_2^{R,L}$ and $Q_3^{R,L}$.

Figure 4.19 shows the X-deflections at the location Q_1^R and Q_1^L obtained from the tension variations of the transversally sensitive strain gauges (GR2, GR3) and (GL2, GL3), respectively using the corresponding calibration coefficients for the two phases of the scan cycle. If all gauges were correctly calibrated, $x\left(Q_1^R\right)$ should have the same value whether gauge GR2 or gauge GR3 is used. This should also be the case for $x\left(Q_1^L\right)$.

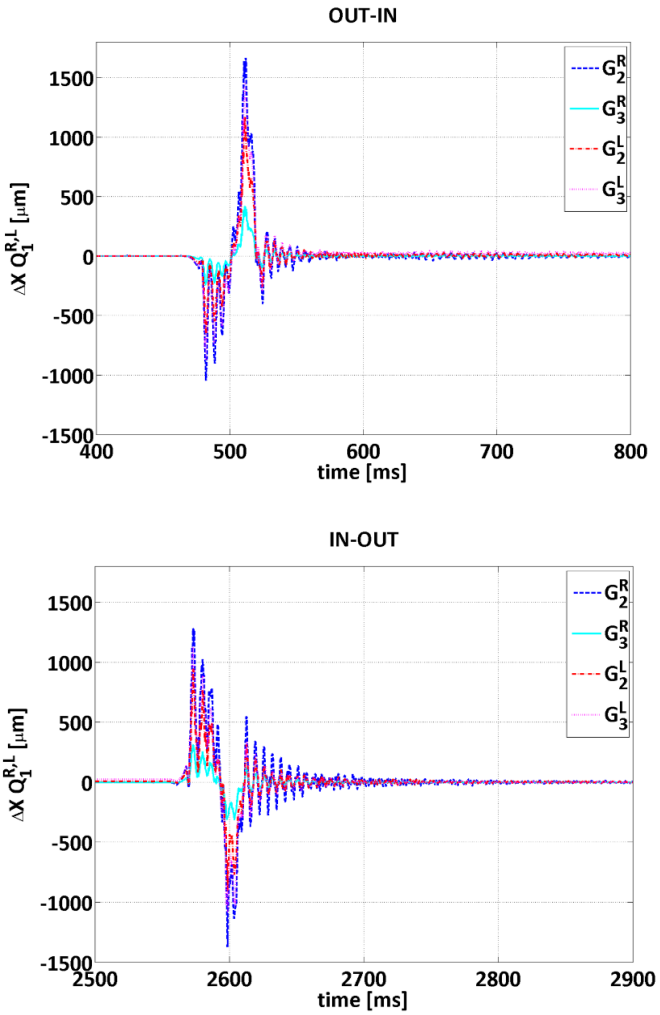

Figure 4.19: X-deflection at locations $Q_1^{R,L}$ calculated from the tension variations in the transversally sensitive strain gauges (G2, G3) during the OUT -IN phase (top) and the IN -OUT (bottom) phases.

A close inspection of the measurements of Figure 4.19 yield the following conclusions:

- $x\left(Q_1^L\right)$ obtained from gauges GL2 and GL3 respectively are very close in both shape and amplitude. This consistency of the two independent measurements for the same arm indicates the relative accuracy of the measurement system.
- Conversely $x\left(Q_1^R\right)$ obtained from GR3 shows the same increasing and decreasing tendency as all the other curves but its amplitude is not as similar to that of $x\left(Q_2^L\right)$ obtained from GR2 as it should be. This probably indicates a defective bond between GR3 and the fork arm.
- Differences of amplitude between $x\left(Q_1^R\right)$ and $x\left(Q_1^L\right)$ are attributed to small differences on the stiffness of the two fork arms.
- The vibrational behaviour shown by all gauges is centrally due to the mechanical play between the push pull rod (fingers) and the spring effect due to the vacuum bellow, see section 3.2.3.

Figure 4.20 shows the X-deflections at points Q_1^R and Q_1^L, obtained from the GR2 and GL2 gauges respectively, as a function of the shaft angular position along the two phases of the scan cycle. Both the right and the left fork arms show close deflectional behaviour, which is a proof of the consistency of the calibration coefficients.

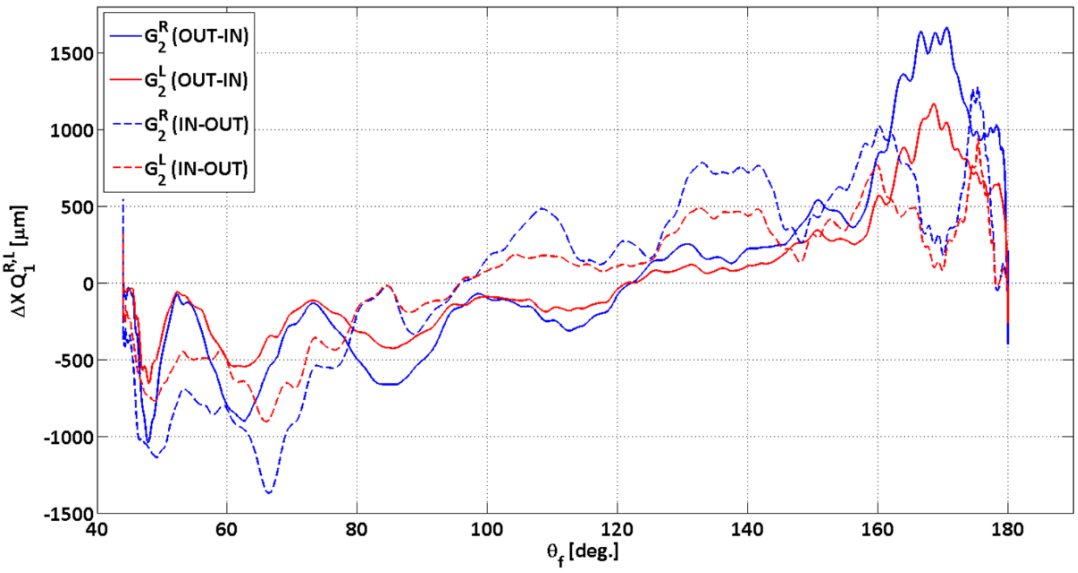

Figure 4.20: Z-deflection of the fork tips (derived from the gauge measurements) for the two phases of the scan cycle as a function of the shaft angular coordinate.

Typically the wire crosses the beam in the region of 110 degrees. The maximum tip deflection on the region of the measurement for the OUT-IN motion is in the range of 250 um for both arm, while for the IN-OUT the value show an important variation between the right arm (500µm) and the left (200µm). This

different behaviour of the right arm depending on the rotation direction would be due to building imperfection resulting on a non-symmetric stiffens of the arm respect to the shaft.

4.4. Comments on the dynamics

As mentioned in the previous section, the wire oscillation and deflection are driven by the inertia forces associated with shaft rotation, and the likely parametric oscillations are associated with the wire tension changes caused by the fork tips deflections in the Z direction.

In order to highlight the causes of the wire oscillations, a modal analysis of the (fork+wire) system has been performed through the FE model. The two first natural vibration modes associated with the fork Z-deflection are shown in Figure 4.21. The first Z-mode has a frequency of 151 Hz and consists on the symmetrical Z-deflection of the fork tips (SZ-mode). In that case, the wire keeps its length constant.

The second Z-mode is located at 382 Hz and consists on an antisymmetrical Z-deflection of the tips (AZ-mode). This mode may lead to instability of the wire straight shape thus generating transverse parametrically-driven oscillations on the wire.

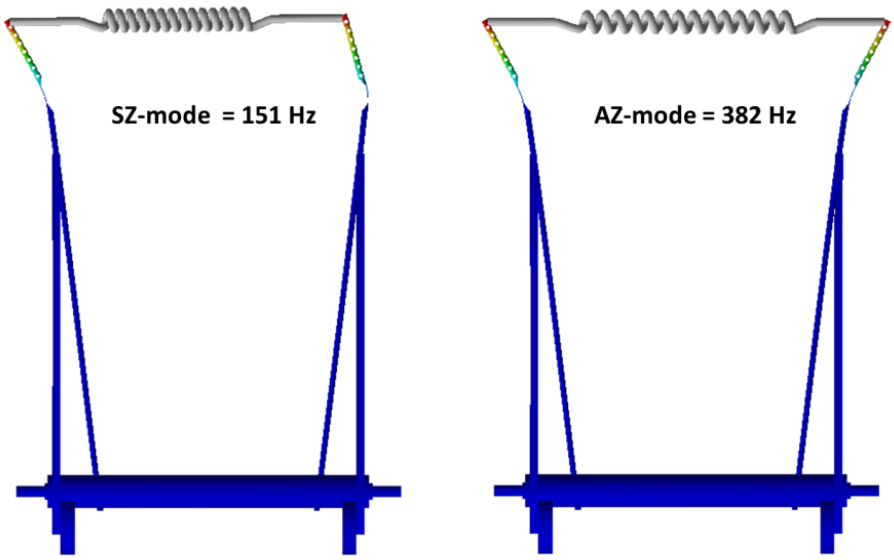

Figure 4.21: Symmetric (left) and Antisymmetric (right) Z-modes of vibration obtained through the modal analysis performed with the FE model.

Figure 4.22 shows the FFT performed on the X-deflections at the location Q_1^R and Q_1^L (plotted in Figure 4.15). The two peaks appear at frequencies 154 Hz and 404 Hz match the two frequencies (151 Hz and 382 Hz) shown by the modal analysis performed on the FE simulations with a relative error of 1.9% and 5.7% respectively. Such a relatively small disagreement can be explained by the uncertainty on the wire soldering material mass, that in the model is likely heavier than in reality.

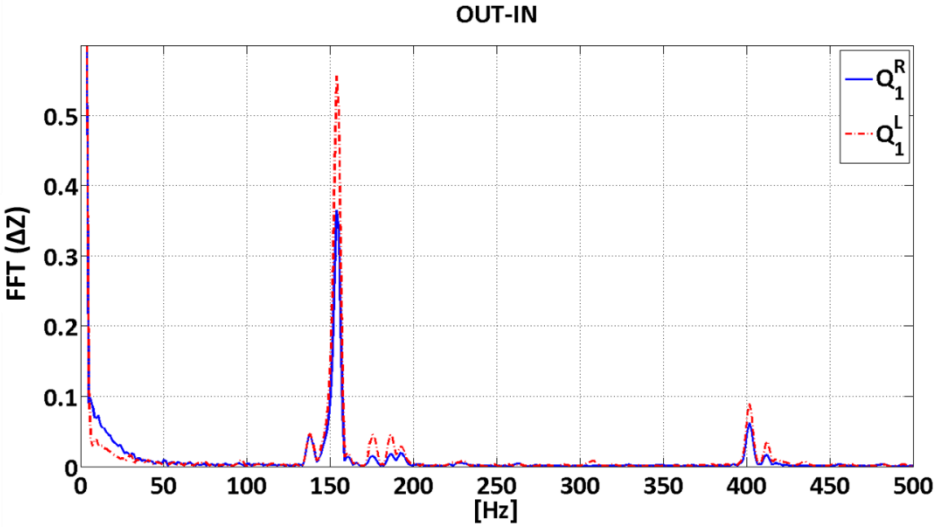

Figure 4.22: Spectra of the Z-deflections of the fork tips shown in Figure 4.15.

Figure 4.23 shows the FFT performed on the wire elongation signal plotted in Figure 4.16. The high-amplitude peak appears around 400 Hz confirms the hypothesis of a parametric vibration of the wire generated by the AZ-mode.

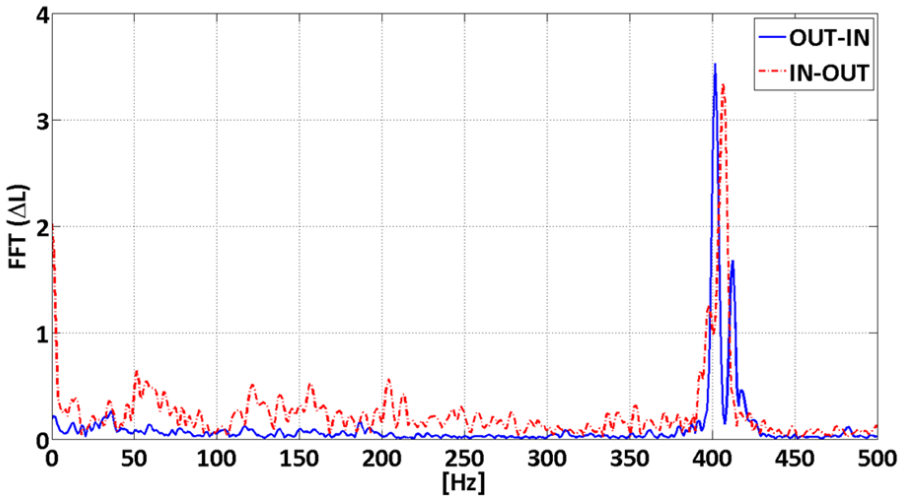

Figure 4.23: Spectrum of the wire elongation ΔL plotted in Figure 4.16.

4.5. Summary

A vibration measurement system has been developed and tested. A hybrid calibration procedure using experimental measurements and FE simulations has been developed in order to overcome the challenges of a calibration under a dynamic and non-linear acceleration field.

The results of the measurements show that this system allows the visualization of the vibrational behaviour of the existing PS wire scanner. It has been demonstrated that the measurements based on the wire piezoresistive effect provide consistent information and allow the determination of the vibrational behaviour of such a system. The FE model and the experimental results showed a remarkable agreement in terms of the two first natural modes frequency. As seen on the previous chapter, the measurement of the longitudinal and transversal amplitudes of the fork and the wire vibrations allows a preliminary quantification of the induced error due to the dynamic effects on the PS wire scanner.

5. Dynamic models

The main purpose of this part of the work is the development of a suitable dynamic model in order to understand the vibrational behaviour of the rotating wire scanner concept. The development and tuning of these dynamic models has been based on the measurements and tests performed on one of the PS scanners [49]. The vibration measurement has been performed by means of the vibration measurement system presented in Chapter 4.

The design of the PS fork, which is very flexible in the wire longitudinal direction, introduces a relative level of complexity to the model. It is clear that there will be changes in the wire length associated with the mutual approaching/separating motion of the fork tips (in the fork plane) and also with the transverse wire vibrations (provided their amplitude is important). The quality of the match between simulation and measurement has been evaluated in order to decide how suitable the models are to predict the wire elongation given a particular fork and a particular rotation pattern.

The chapter is structured as follows:

- Section 1 presents two physical models for the wire (a discrete model and a continuous one).
- Section 2 proposes a simple 2 Degrees of Freedom (DoF) fork model.
- Section 3 is devoted to the assessment of the parameters appearing in the models.
- Section 4 compares measurements and simulated results for the case of free behavior of the (fork+wire) system with no shaft rotation, and proposes modifications to the fork model accordingly.
- Section 5 compares measurements and simulated results under rotation of the fork.
- Section 6 contains the partial conclusions.

5.1. Wire model

The dynamics of the wire have been described in the coordinate system RF (or reference frame) shown in Figure 5.1. It is a moving frame (with constant orientation and acceleration equal to that of the fork tips), and consequently inertia drag forces have to be taken into account. They are independent from the wire configuration as they are proportional to the acceleration of the fork tips in the laboratory frame (LF):

$$\overline{a}_{LF}(\text{fork tips}) = \begin{Bmatrix} H\left(-\dot{\theta}^2(t)\sin\theta(t) + \ddot{\theta}(t)\cos\theta(t)\right) \\ H\left(-\dot{\theta}^2(t)\cos\theta(t) - \ddot{\theta}(t)\sin\theta(t)\right) \\ \ddot{z}(\text{tips}) \end{Bmatrix} . \tag{5.1}$$

The wire will be represented through a discrete or lumped-parameter model (DM). Appendix C shows a continuous model (CM) where the wire is represented as a taut spring. We show that, under the

assumption that the wire moves mainly according to the first string mode, the resulting equations are exactly the same as in the DM.

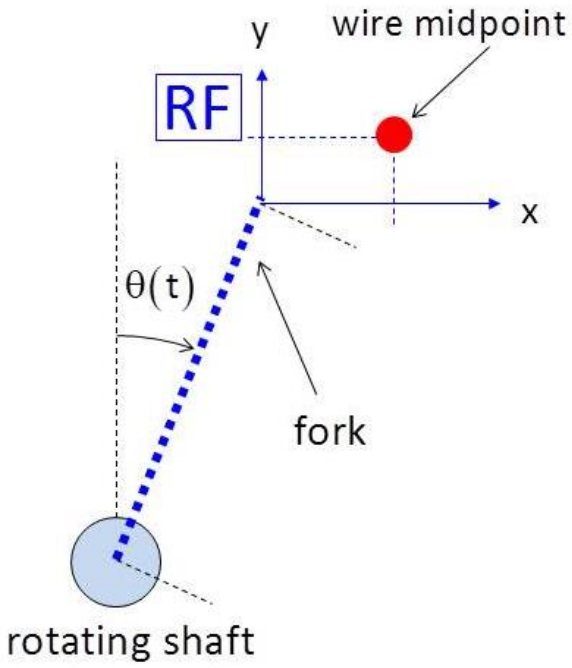

Figure 5.1: Coordinate system used to formulate the wire dynamics.

In the discrete model, the wire is represented as two identical linear springs with stiffness k and connected through a mass point m (Figure 5.2).

In the general case, the point mass may have up to 3 DoF, two associated with transverse motion and a third one associated with longitudinal motion. Assuming an antisymmetrical motion of the fork tips (that is, they move with a same amplitude either inwards or outwards, $z_R = z_L = z_0 f(t)$), the mass longitudinal motion can be disregarded and so the model is reduced to 2 DoF.

Newton's second law applied to the mass point P states:

$$\bar{F}_R + \bar{F}_L + \bar{F}_{drag} = m\,\bar{a}_{RF}(P) \qquad (5.2)$$

where F_{drag} is the drag inertia force, and $F_{R,L}$ are the forces associated with the springs systems at both sides of the mass point (the weight is negligible compared to all the other forces appearing in Eq.(5.2).

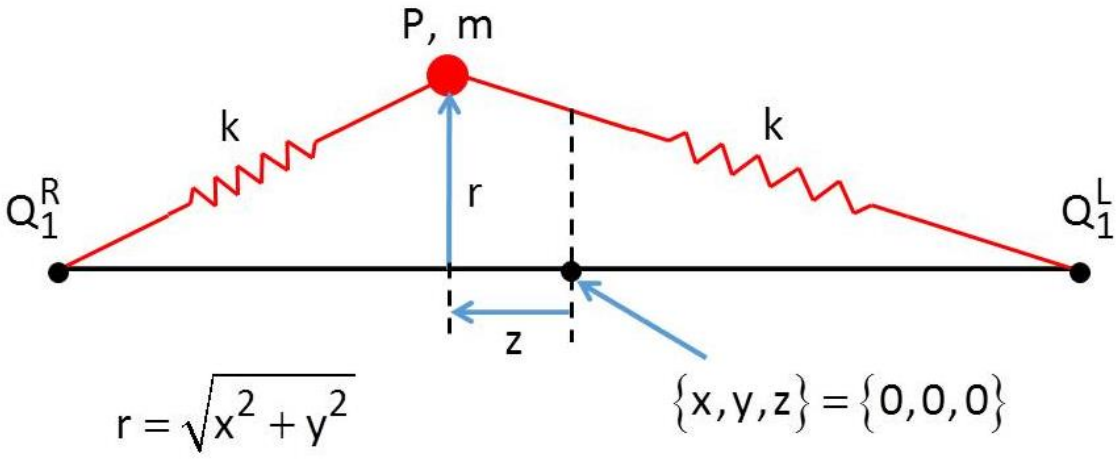

Figure 5.2: Lumped-parameter model (DM) in a general configuration. Points Q_1^R and Q_1^L are the fork end points.

As the fork is flexible, the wire length depends on both the wire and the fork tips coordinates. As mentioned before, the approaching/separating motion of the fork tips causes a non-negligible change in the wire length. Figure 5.3 shows the general configuration of the wire and the fork tips in that case. The fork tips motion is described through an angular coordinate.

Taking the tips motion into account, the variable wire length L becomes:

$$L = \rho_R + \rho_L \quad , \text{ with } \quad \rho_{R,L} = \sqrt{\left(r - r_{R,L}\right)^2 + \left(\frac{L_0}{2} + z_{R,L}\right)^2} \quad . \tag{5.3}$$

It is clear that $r_{R,L} << z_{R,L}$ always, so from now on the simplification $r_{R,L} \simeq 0$ will be assumed.

The spring forces in the general configuration are calculated as:

$$F_{R,L} = T_0 + k\left(\rho_{R,L} - \frac{L_0}{2}\right) = T_0 + k\left(\sqrt{r^2 + \left(\frac{L_0}{2} + z_{R,L}\right)^2} - \frac{L_0}{2}\right) \quad , \tag{5.4}$$

where T_0 and L_0 are the initial spring tension and spring length, respectively.

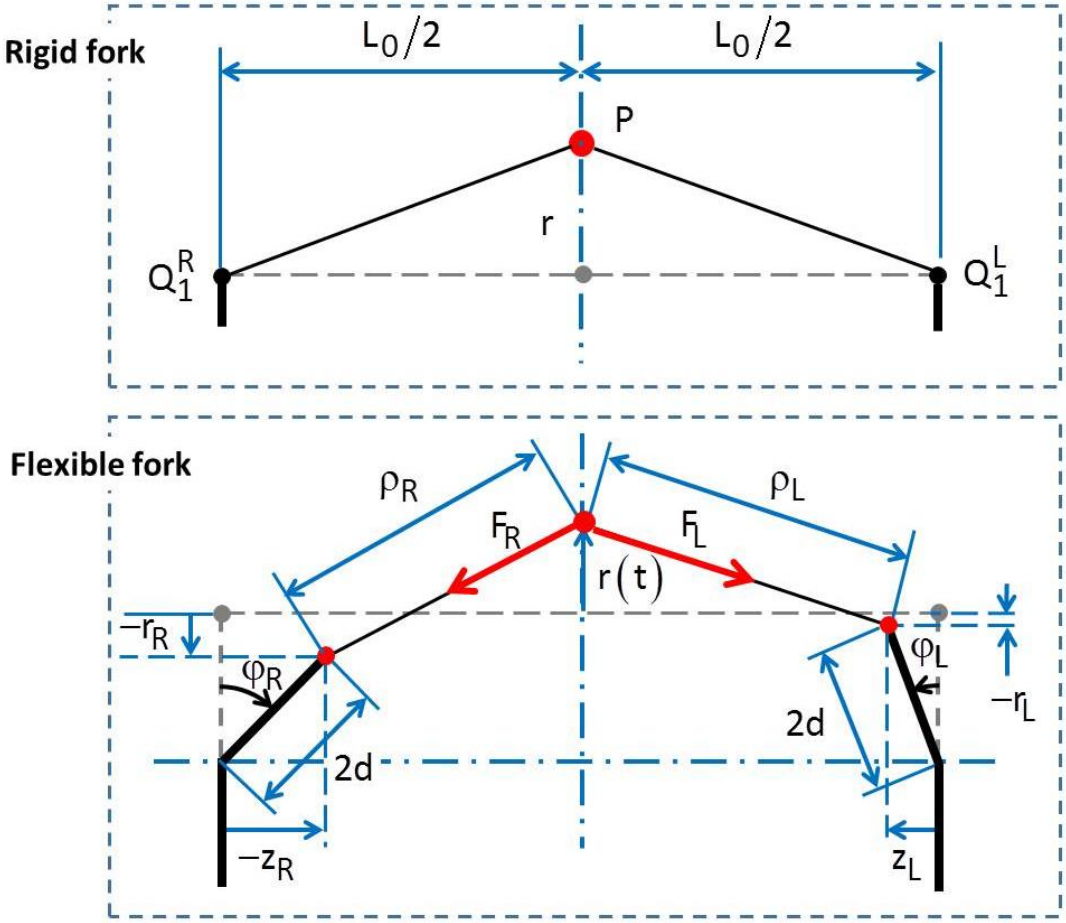

Figure 5.3: DM in a general configuration with (down) and without (up) deflection in the fork tips.

Note that k does not correspond to the carbon wire stiffness k_w . As the wire is represented through two series springs, $k = 2k_w = 2\left(E \cdot A / L_u\right)$, where E is the Young modulus, A is the area of the wire cross section and L_u is the unstressed wire length. The initial tension T_0 can be written as a function of those last parameters:

$$T_0 = (E \cdot A)\frac{L_0 - L_u}{L_u} \equiv (E \cdot A)\varepsilon \quad , \quad \text{with} \quad \varepsilon(\text{strain}) << 1 \quad . \tag{5.5}$$

Projection of Eq.(5.2) in the (x, y) directions yields:

$$
\begin{aligned}
m\ddot{x} + \left(\frac{F_R}{\rho_R} + \frac{F_L}{\rho_L}\right) x &= mH\left(\dot{\theta}^2 \sin\theta - \ddot{\theta}\cos\theta\right) \ , \\
m\ddot{y} + \left(\frac{F_R}{\rho_R} + \frac{F_L}{\rho_L}\right) y &= mH\left(\dot{\theta}^2 \cos\theta + \ddot{\theta}\sin\theta\right) \ .
\end{aligned}
\tag{5.6}
$$

These two equations are highly nonlinear. However, it is possible to discover in them the main phenomena provoking the wire vibrations by just retaining the nonlinear terms up to the cubic order. Taking into account that $z_{R,L} << (L_0/2)$:

$$
\frac{F_{R,L}}{\rho_{R,L}} \simeq \left(\frac{2T_0}{L_0} - k\right)\left[1 - \frac{1}{2}\left(\frac{2}{L_0}\right)^2 r^2 + \left(\frac{2}{L_0}\right)^2 z_{R,L}^2 - \left(\frac{2}{L_0}\right) z_{R,L}\right] + k \ . \tag{5.7}
$$

Introducing Eq.(5.7) into Eqs.(5.6) results in:

$$
\begin{aligned}
\ddot{x} + \omega_T^2 x + \frac{\omega_L^2 - \omega_T^2}{L_0}\left[\frac{1}{L_0}\left(2r^2 - 2(z_R^2 + z_L^2)\right) + \Delta z_{tips}\right] x &= H\left(\dot{\theta}^2 \sin\theta - \ddot{\theta}\cos\theta\right) \ , \\
\ddot{y} + \omega_T^2 y + \frac{\omega_L^2 - \omega_T^2}{L_0}\left[\frac{1}{L_0}\left(2r^2 - 2(z_R^2 + z_L^2)\right) + \Delta z_{tips}\right] y &= H\left(\dot{\theta}^2 \cos\theta + \ddot{\theta}\sin\theta\right) \ ,
\end{aligned}
\tag{5.8}
$$

where $\Delta z_{tips} = z_R + z_L$, $\omega_T = \sqrt{4T_0/mL_0}$ and $\omega_L = \sqrt{4k_w/m}$. Note that $\left(\omega_T^2/\omega_L^2\right) \approx \varepsilon << 1$.

Eqs.(5.8) correspond to a coupled complex vibration: the wire plane of oscillation will be a rotating one (in other words, the vibration is not polarized). The coupling is associated to the cubic nonlinearity (remember that $r^2 = x^2 + y^2$).

Let's follow the build-up of the wire oscillation from an initial rest position. When the scan cycle begins, the inertia forces appearing on the right hand side (rhs) of Eqs.(5.8) are responsible for an initial vibration. The problem is a forced one: only if those forces contain frequencies close to any multiple of ω_T (that is, if a resonance occurs) will the wire amplitude attain high values.

For the case of a rigid fork, two different scenarios may appear:

1. No resonance: it is a case of a linear uncoupled oscillation driven by the inertia forces.
2. Resonance: the magnitude of wire amplitude becomes significant and the nonlinear terms have to be taken into account. The corresponding equations describe two coupled Duffing-type oscillators. Once the shaft has come to a rest, their general expression is

$$\ddot{q} + \omega_T^2 \left(1 + \frac{2}{\varepsilon} \frac{1}{L_0^2} \left(q^2 + p^2 \right) \right) q = 0 \quad . \tag{5.9}$$

As $\varepsilon > 0$, the cubic terms will be responsible for a saturation of the vibration amplitude.

The case of a flexible fork adds complexity to the problem. Let's assume that the fork tips have an antisymmetric harmonic motion $\Delta z_{tips} = z_R + z_L = 2 z_0 \cos(\Omega t)$. If the frequency of the fork deflections is close to a subharmonic of two times the wire frequency (if $\Omega \simeq (2/n)\omega_T$, with n=1,2,3…) [34], a parametric resonance appears. The inertia forces provide the "initial conditions" which are amplified by that resonance. For low amplitudes, the equation describing that situation reads:

$$\ddot{q} + \omega_T^2 \left(1 - \frac{1}{L_0} \frac{2}{\varepsilon} 2 z_0 \cos(\Omega t) \right) q = 0 \quad , \tag{5.10}$$

which is a Mathieu equation. Depending on the values of the coefficients, the behaviour may be stable or unstable [45]. In the latter case, the increasing amplitude would eventually be saturated by the cubic nonlinearity:

$$\ddot{q} + \omega_T^2 \left(1 + \frac{1}{L_0} \frac{2}{\varepsilon} \left(\frac{1}{L_0} \left(q^2 + p^2 \right) - 2 z_0 \cos(\Omega t) \right) \right) q = 0 \quad . \tag{5.11}$$

This situation can be described as a Mathieu-Duffing problem.

Eqs.(5.8) can be used to calculate the wire elongation in two different ways:

- Experimental values for the fork deflections Δz_{tips} can be directly used as inputs (together with the rotation pattern). In this case, the problem has just the 2 DoF of the wire. This will be called "hybrid approach".
- The fork deflections are generated from an analytical model. Two more differential equations have to be solved simultaneously with Eqs.(5.8). We will call this procedure "analytical approach".

In the hybrid approach, the fork tips motion will never be totally antisymmetric (as the measured z_R and z_L will never be equal). This is not compatible with a zero longitudinal vibration of the wire but, as that motion does not generate changes in the wire length, the hypothesis $z = 0$ will be maintained.

In the analytical approach, if the two fork arms are considered to be identical, the number of differential equations (or DoF) can be reduced to three. Maintaining 4 DoF will allow for breaking of that symmetry.

Both approaches will be used, and the results will be presented in Section 5.5.

5.2. Fork model

The word "fork" is used to describe a system which contains several elements: the actual metallic fork plus the mass of the wire fixation system (Figure 5.4) and that of the electrical cable.

As explained in section 3.2.1, the fork tips are cylindrical and connected to the arm through a flexible short segment behaving as a hinge. Thus, the deflections of the fork tips can be studied through a model consisting of two 1 DoF linear systems coupled through a spring. Figure 5.5 shows a detail for those tips and their idealized model, consisting of a rod connected to the rigid part of the fork through a hinge with torsional stiffness k_φ. Some torsional damping c_φ is also associated with that hinge. The hinges have a 1-DoF motion associated with shaft bending described at page 67. Any other deformations of the fork arm (with length H-2d) are neglected in this model.

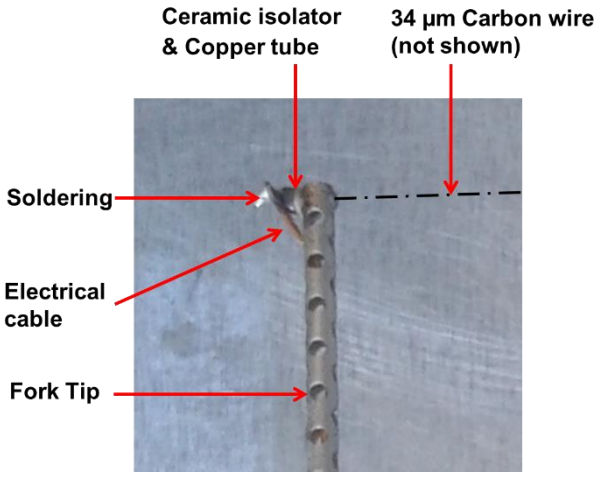

Figure 5.4: Detail of the wire fixation system.

Figure 5.6 shows the forces and torques acting on one fork tip. Note that the wire force F is not in the same plane as the fork: the dotted conical surface shows the different orientations of that force. Thus, there are in general two components of that force yielding a nonzero moment about the hinge. The axial component $(F\cos\psi)$ is always responsible for a moment about the hinge with value $(F\cos\psi)(2d\cos\varphi)$ which tends to unstabilize the fork tips deflection. However, the radial component $(F\sin\psi)$ may yield a moment with either sign whose maximum value would be $(F\sin\psi)(2d\sin\varphi)$. It is clear that this contribution is much smaller than that of the radial one, and for this reason it was neglected.

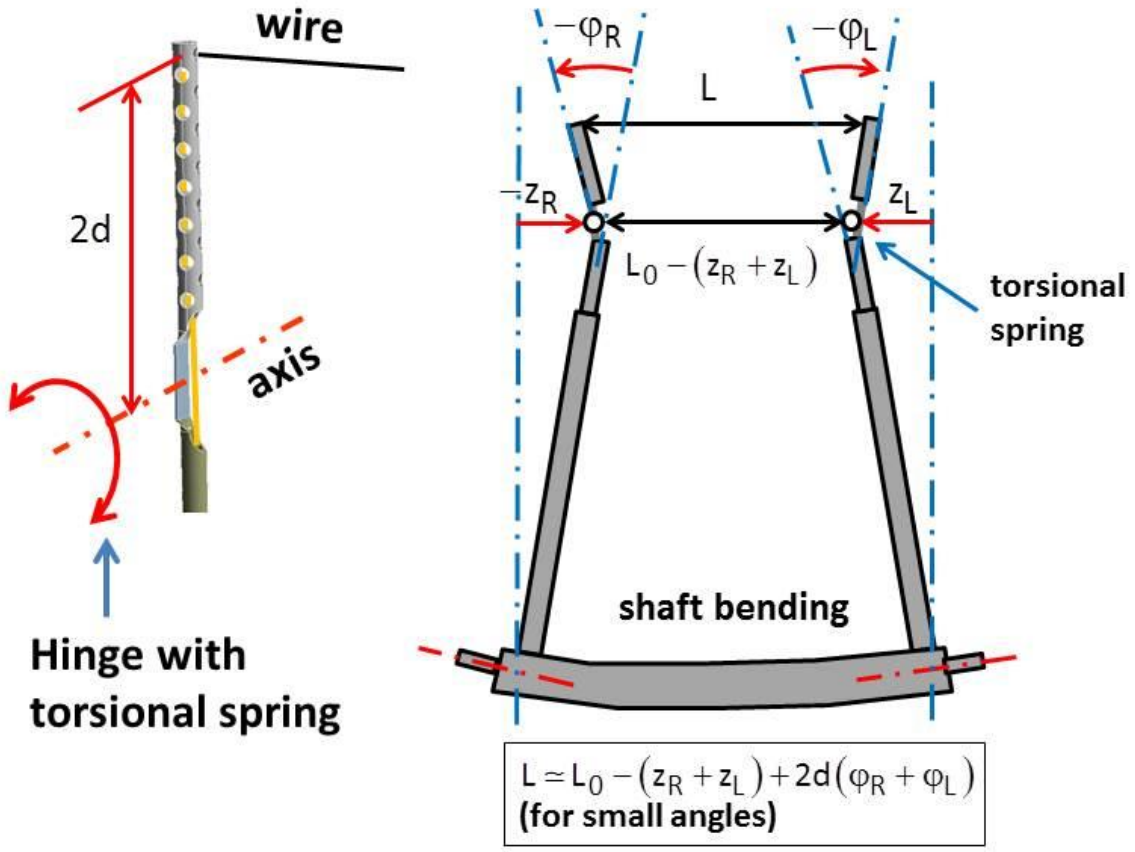

Figure 5.5: Flexible fork tip (left) and its representation through a hinged joint (right).

Under this simplification and assuming that the problem is symmetrical, the equations of motion for the fork tips are:

$$I_\varphi \ddot{\varphi}_{R,L} = -M_0 - m_{tip}(H-2d)\dot{\theta}^2(d\sin\varphi_{R,L}) - m_{tip}\ddot{z}(O_{R,L})(d\cos\varphi_{R,L}) - k_\varphi(\varphi_{R,L}-\varphi_0) - c_\varphi\dot{\varphi} + \frac{F_{R,L}}{\rho_{R,L}}\left(\frac{L_0}{2}-2d\sin\varphi_{R,L}\right)(2d\cos\varphi_{R,L}) \quad , \tag{5.12}$$

where I_φ is the inertia moment about the hinge, and $M_0 = -2dT_0$ is the initial torsional momentum associated with the hinge in the rest initial configuration φ_0. The first term in the right hand side of Eq.(5.12) corresponds to the momentum of the inertia force associated with the shaft rotation (the fork tip center of masses has been considered to be halfway between the hinge and the fork end point).

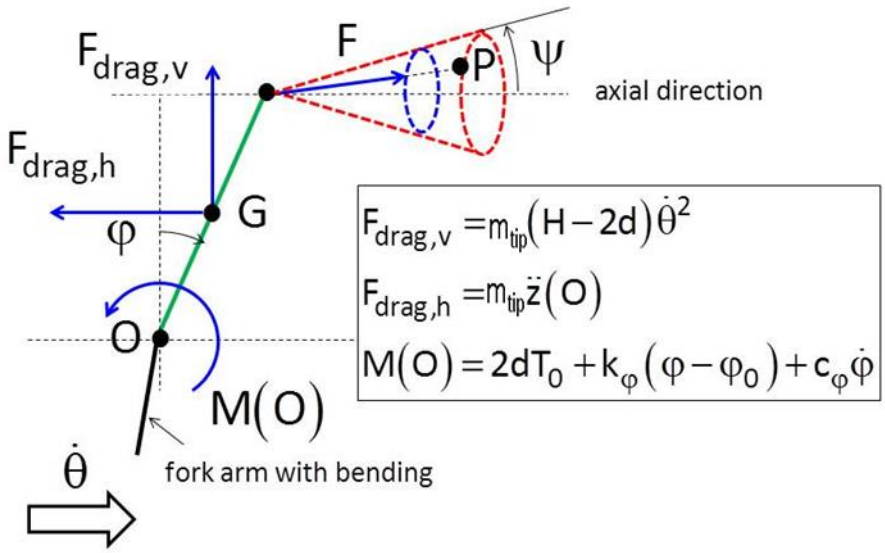

Figure 5.6: Forces and torques on the fork tips. F is the wire tension, which is not constrained to the fork plane in general.

As the wire mass is much lower than that of the fork tips, the wire force F can be formulated as that of a massless linear spring:

$$F_{R,L} = T_0 - 2dk_w\left(\sin\varphi_R + \sin\varphi_L\right) . \tag{5.13}$$

Consistency with the simplifications applied to the wire equations (consisting of neglecting the longitudinal motion of the mass point P and approximating the wire tension according to Eq.(5.7)) and the hypothesis of small tip deflections ($r_{R,L} \cong 0$ and $z_{R,L} << \left(L_0/2\right)$, or what is the same, $\sin\varphi_{R,L} \cong \varphi_{R,L}$ and $\cos\varphi_{R,L} \cong 1$) transform Eq.(5.12)into

$$I_\varphi \ddot{\varphi}_{R,L} = -m_{tip}d\left(H-2d\right)\dot{\theta}^2\varphi_{R,L} - m_{tip}d\ddot{z}\left(O_{R,L}\right) - k_\varphi\varphi_{R,L} - c_\varphi\dot{\varphi}_{R,L} - 4d^2k_w\left(\varphi_R + \varphi_L\right), \tag{5.14}$$

Unlike the wire equations of motion, only the linear terms were retained.

According to this model, and for the case of a nonrotating shaft and low damping, the fork system has two natural vibration modes with frequencies

$$f_S = \frac{1}{2\pi}\sqrt{\frac{k_\varphi}{I_\varphi}} \quad , \quad f_A = \frac{1}{2\pi}\sqrt{\frac{k_\varphi + 8d^2k_w}{I_\varphi}} \quad . \tag{5.15}$$

Frequency f_S corresponds to the symmetrical mode (SZ-mode), where the tips move simultaneously to the right or to the left (the wire has no effect on the tips motion), and f_A to the antisymmetrical one (AZ-mode), where the tips move simultaneously inwards or outwards due to the coupling through the wire.

Note that blocking one tip (always with no shaft rotation) would result in a single DoF system whose natural frequency f_{1DoF} would be located between f_S and f_A :

$$f_{1DoF} = \frac{1}{2\pi}\sqrt{\frac{k_\varphi + 4d^2 k_w}{I_\varphi}} \quad , \quad f_S < f_{1DoF} < f_A \quad . \tag{5.16}$$

Alternatively, Eq.(5.14) can be expressed through the $z_{R,L}$ variables $\left(z_{R,L} \simeq -2d\varphi_{R,L}\right)$:

$$\frac{I_\varphi}{4d^2}\ddot{z}_{R,L} = -\frac{m_{tip}}{4d}(H-2d)\dot{\theta}^2 z_{R,L} + \frac{m_{tip}}{2}\ddot{z}(O_{R,L}) - \frac{k_\varphi}{4d^2}z_{R,L} - \frac{c_\varphi}{4d^2}\dot{z}_{R,L} - k_w(z_R + z_L) \quad , \tag{5.17}$$

and the fork model represented as shown in Figure 5.7, where $m_z = I_\varphi \big/ 4d^2$, $k_z = k_\varphi \big/ 4d^2$, and $c_z = c_\varphi \big/ 4d^2$.

Introducing $\omega_{S,A} = 2\pi f_{S,A}$, Eq. (5.17) can also be written as:

$$\ddot{z}_{R,L} = -\frac{m_{tip}d(H-2d)}{I_\varphi}\dot{\theta}^2 z_{R,L} + \frac{2m_{tip}d^2}{I_\varphi}\ddot{z}(O_{R,L}) - \omega_S^2 z_{R,L} - \frac{1}{2}\left(\omega_A^2 - \omega_S^2\right)(z_R + z_L) - \frac{c_z}{m_z}\dot{z}_{R,L} \, . \tag{5.18}$$

Introducing $f_{R,L}(t) = \left(2m_{tip}d^2 \big/ I_\varphi\right)\ddot{z}(O_{R,L})$ and $\omega^2(t) = \left(m_{tip}d(H-2d) \big/ I_\varphi\right)\dot{\theta}^2$, these equations can be written as

$$\ddot{z}_{R,L} + 2\varsigma_0\omega_S\dot{z}_{R,L} + \frac{1}{2}\left(\omega_A^2 + \omega_S^2 + \omega^2(t)\right)z_{R,L} + \frac{1}{2}\left(\omega_A^2 - \omega_S^2\right)z_{L,R} = f_{R,L}(t) \quad , \tag{5.19}$$

which correspond to a driven parametric oscillator.

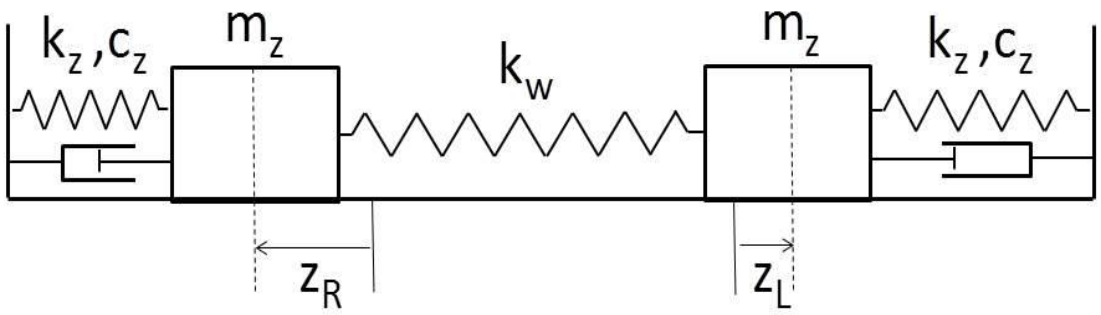

Figure 5.7: Alternative representation for the fork model.

5.3. Assessment of model parameters

The model parametrization was obtained either through direct measurements or indirectly from simulations.

The geometrical ones (L_0 and d) come from straightforward measurements, and the linear mass μ_0 for a specific carbon wire is well-known.

The measurement of the wire axial stiffness k_w was described in section 4.2.1. Figure 5.8 shows the plot of the force F versus the elongation $\Delta L = L - L_u$. The measurements show a fairly linear dependence on the elongation, and its slope yields the wire axial stiffness: $k_w = 344\ N\ m^{-1}$.

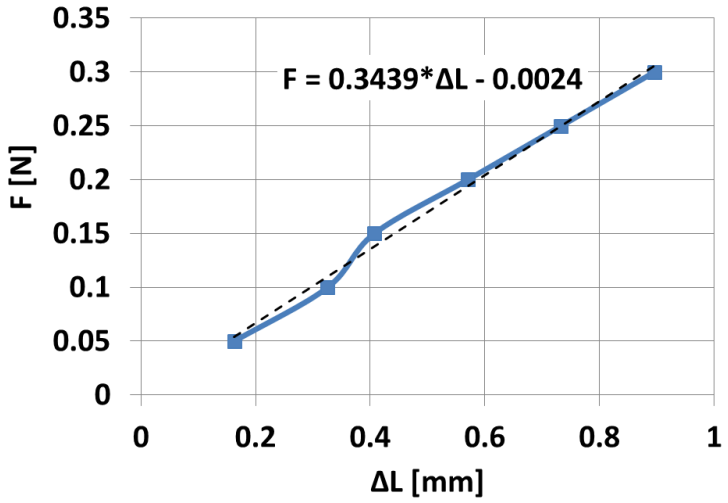

Figure 5.8: Experimental curve of tangential force F versus the wire elongation $\Delta L = L - L_u$.

The initial wire tension T_0 is a variable parameter which depends strongly on the accuracy of the wire installation and its direct and precise measurement is not simple. In general, the order of magnitude is 0.1 N.

From the values of μ_0, k_w and T_0, the lumped parameter m is readily obtained through a frequency consistency match:

$$\omega_T = \frac{\pi}{L_0}\sqrt{\frac{T_0}{\mu_0}} = \sqrt{\frac{4T_0}{mL_0}} \Rightarrow m = \frac{4}{\pi^2}\mu_0 L_0 \quad . \tag{5.20}$$

Fork tips mass

The fork tip consists of three parts with different geometry and mass: a flat part (acting as flexible hinge), a transition element between the flat part and the cylinder ("bellow") and a hollow cylinder lightened by drilling (Figure 5.9(a)). Their volumes were measured from a digital mock-up of the fork. Their corresponding masses (m_{flat}, m_{bell}, m_{cyl} respectively) were calculated assuming a density of $7800\ kg\ m^{-3}$ (which corresponds to the density of the fork material: stainless steel).

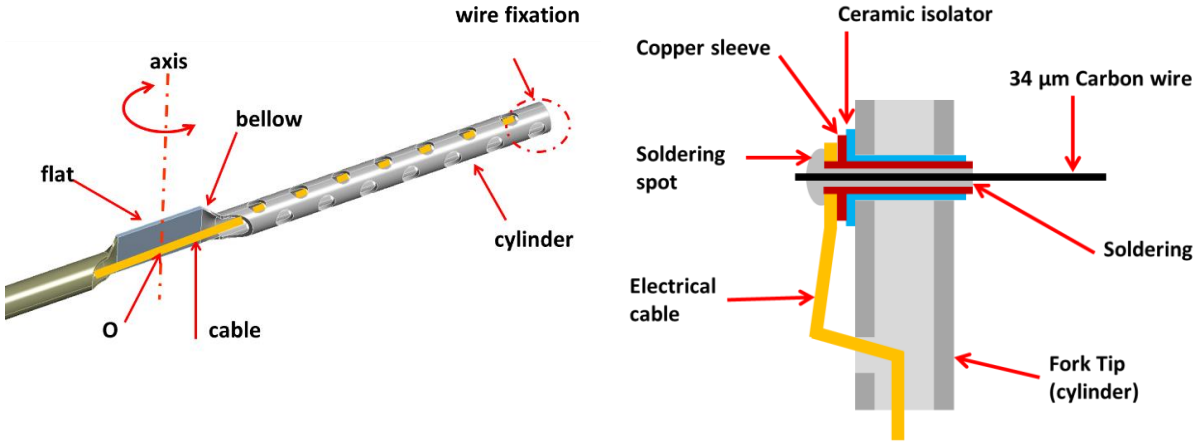

Figure 5.9: Detail of the fork tip (left); Illustration of the wire fixation system (right).

Inside the cylinder, there is a driven 0.45 mm diameter insulated cable of copper electrically connected to a copper sleeve and to the carbon wire by means of soldering performed with tin alloy 96SC. The copper sleeve and the fork are electrically isolated by means of another sleeve in ceramic (Figure 5.9(b)).

As the geometry of the wire fixation parts and the electrical cable is very simple, their volume was calculated analytically, while that of the soldering spot was calculated under the assumption that it is a hemisphere of diameter 2.4 mm. The following densities were used:

copper = 8960 kg m^{-3}, ceramic = 3690 kg m^{-3}, tin alloy 96SC = 10000 kg m^{-3}.

Fork tips torsional stiffness

The fragility of the fork tips discouraged the measurements of its torsional stiffness in the real fork (that could provoke its damage or even break this part of the fork). Therefore the tips torsional stiffness was evaluated using a FE model. For the sake of simplicity, a force F is applied at the same point where the wire is attached (the soldering spot), and then the FE model simulates the tangential displacement Δz of that point. From this, it is possible to calculate the moment $M(O)$ about the hinge and the fork tip rotated angle $\Delta\varphi$ according to:

$$M(O) = 2d \cdot F = k_{\varphi}\Delta\varphi \quad , \text{ with } \Delta\varphi = \tan^{-1}(\Delta z/2d) \quad . \tag{5.21}$$

The torsional stiffness was obtained through $k_{\varphi} = 2dF/\Delta\varphi$. Figure 5.10 shows the plot of F versus Δz (top) and that of the total momentum M versus the rotated angle $\Delta\varphi$ (bottom). This lower one shows a fairly linear dependence on the angle, and its slope yields the torsional stiffness $k_{\varphi} = 0.0848 \text{ N m rad}^{-1}$.

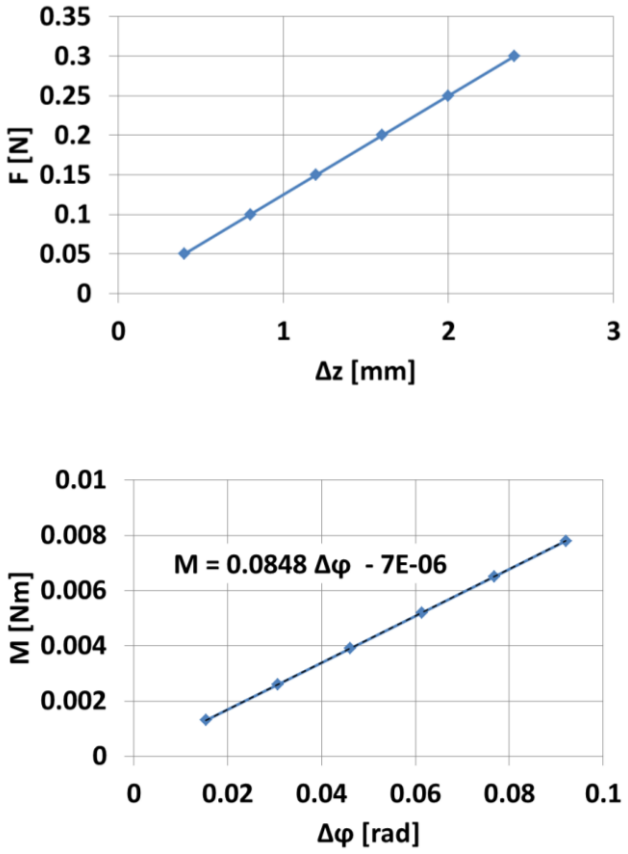

Figure 5.10: Experimental curve of tangential force F versus tangential displacement Δz (top) and total momentum $M(O)$ versus rotated angle $\Delta\varphi$ (bottom).

Finally, the fork torsional damping c_φ was assessed from a measurement. Figure 5.11 shows the measured free response of the right fork tip without the carbon wire (that of the left tip is similar). The tips were slightly deflected in the Z direction and then released. The subsequent motion was measured through properly calibrated strain gauges.

That result fits a damped sinusoidal function expressed as

$$z(t) = z_0 e^{-\varsigma\omega_0 t} \sin(\omega_n t + \phi), \tag{5.22}$$

where ω_0 is the natural angular frequency of the fork tips $\omega_F^{\text{no wire}}$ given in Eq.(5.16), ς is the damping ratio and $\omega_n = \omega_0\sqrt{1-\varsigma^2}$. The values of ω_n and ς assessed from the results in Figure 5.11 are $(2\pi\cdot 154)\,\text{rad}\,\text{s}^{-1}$ and 0.018 respectively.

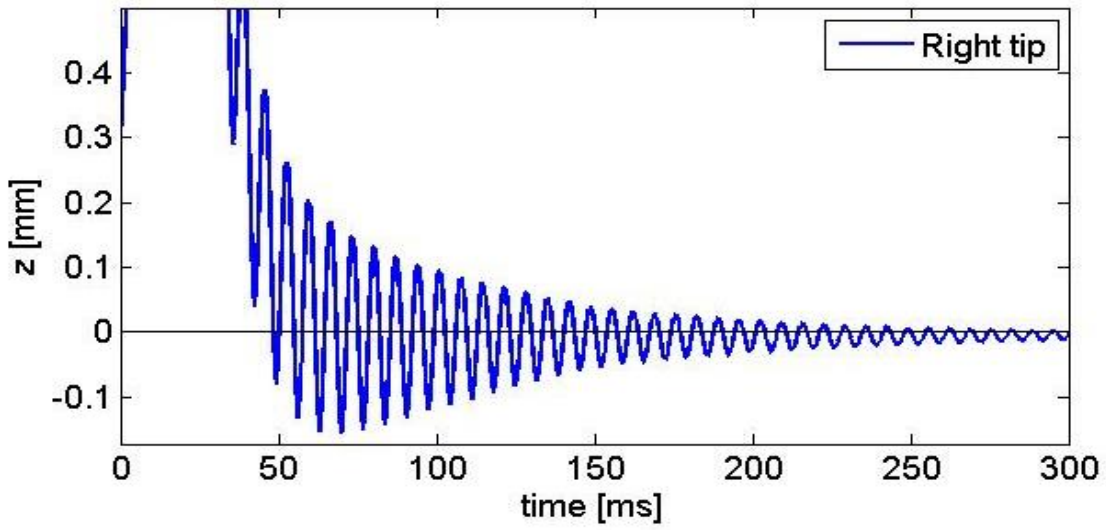

Figure 5.11: Free response of the right fork tip associated with the first Z-vibration mode.

From ω_n and ς, I_φ and c_φ are readily obtained:

$$\begin{aligned} I_\varphi &= k_\varphi\left(1-\varsigma^2\right)\Big/\omega_n^2 = 9.05428\cdot 10^{-8}\,\text{kg}\,\text{m}^{-2}, \\ c_\varphi &= 2\varsigma\sqrt{I_\varphi k_\varphi} = 3.1545\cdot 10^{-6}\,\text{kg}\,\text{m}^{-2}\text{s}^{-1}. \end{aligned} \tag{5.23}$$

Table 5.1 summarizes the DM and the CM parameters.

Table 5.1: DM and CM parameters

Discrete (DM)	Continuous (CM)
wire rest length $L_0 = 0.115$ m	
lumped mass $m = 7.597 \cdot 10^{-8}$ kg	wire linear mass $\mu_0 = 1.63 \cdot 10^{-6}$ kg m^{-1}
springs stiffness $k = 688$ N m^{-1}	wire axial stiffness $\left(E \cdot A / L_u\right) = 344$ N m^{-1}
fork tips length $2d = 0.026$ m	
fork arms length $H = 0.142$ m	
fork tip mass $m_{tip} = 3 \cdot 10^{-4}$ kg	
moment of inertia about the hinge $I_\varphi = 9.05428 \cdot 10^{-8}$ kg m^2	
hinge torsional stiffness $k_\varphi = 0.0848$ N m rad^{-1}	
hinge torsional damping $c_\varphi = 3.1545 \cdot 10^{-6}$ N m s^{-2}rad^{-1}	

With these values, the fork natural frequencies given in Eqs. (5.15) and (5.16) take the following values:

$$f_S = 154.02 \text{ Hz}, \; f_A = 392.22 \text{ Hz}, \; f_{1DoF} = 297.96 \text{ Hz} \quad . \tag{5.24}$$

A complementary validation of these parameters was done through a FE modal analysis of the fork. The geometry implemented in this analysis was obtained from the manufacturing drawings of the fork. The wire was modelled by means of an analytical spring tensioned between the two tips with an unstressed length $L_u = 115.68$ mm and preloaded with a tension of 0.3 N. In order to simulate the fork plus the wire and the fork on its own, two different spring stiffness have been used in the model: $k_w = 344$ N m^{-1} (axial stiffness of the real wire) and $k_w^0 = 344 \cdot 10^{-3}$ N m^{-1} (very elastic wire equivalent to “no wire”). The mass of the wire fixation system (already shown in Figure 5.9) and the mass of the electrical cable were included in the FE model trough two analytically modelled mass points of 0.06 g each, located at the very end of the fork tips.

The configuration without the wire yields a frequency of 151.02 Hz while that obtained for the configuration with wire is 382.82 Hz. These two values match those given in Eq.(5.1)(5.20) with a relative error of 1.9 % and 2.5 % respectively.

5.4. Simulation Results: Free vibrations

The analytical models were checked first through comparison with free vibration measurements (that is, with no shaft rotation). The main purpose was to investigate the match between the calculated vibration frequencies and the measured ones.

Two different sets of measurements were performed. In the first one (called free-fixed set from now on), one fork tip was blocked between two aluminium blocks, while the other one was slightly displaced from its equilibrium position and then released (this initial displacement was not acurately measured as only qualitative behaviour was to be analysed; the order of magnitude was 1 mm).

In the second set (free-free set), one tip is slightly displaced and then released while the other one is free. Because of the wire coupling through the wire, the latter will also be displaced from its equilibrium position, but its initial deformation will be less than that of the directly displaced tip.

Free-fixed set: measurements

Figure 5.12(a,b) show the left tip displacement z_L and the wire elongation ΔL, corresponding to the free-fixed set ($z_R = 0$). The z_L initial amplitude is about twice the one of ΔL and both quantities exhibit a rather linear damping with time. The slight differences between ΔL and z_L are associated with some transverse motion of the wire. As the initial condition on z_L is imposed manually, an initial transverse displacement of the wire is unavoidable. Compared to the fork tip deflection, this transverse wire motion is hardly damped, and it is responsible for the fairly constant amplitude of ΔL during the last 150 ms of the plotted signal.

The corresponding spectra (FFT) are very similar, and only that of ΔL is shown (Figure 5.12(c)). As we are only concerned by the resonance frequencies, the spectrum amplitude was normalized to the highest peak. One single resonance appears in the spectrum. This is perfectly consistent with the boundary condition imposed on one tip: under such circumstances, we expect the fork to behave as a 1-DoF system. The peak is located roughly at 320 Hz, that is, 7% higher than the 298 Hz predicted by the model (Eq.(5.16)). At this stage, this difference is acceptable.

The proportionality between $z_L(t)$ and $\Delta_L(t)$ plus the fact of having a similar spectrum suggests that the wire is behaving linearly, basically driven by the tip motion.

The same kind of measurement was performed inverting the conditions on the fork tips. Figure 5.13(a,b) show the measured right tip motion z_R and wire elongation ΔL, respectively, having fixed the left tip. For the same reasons pointed out before, just the ΔL spectrum is shown in Figure 5.13(c).

(a)

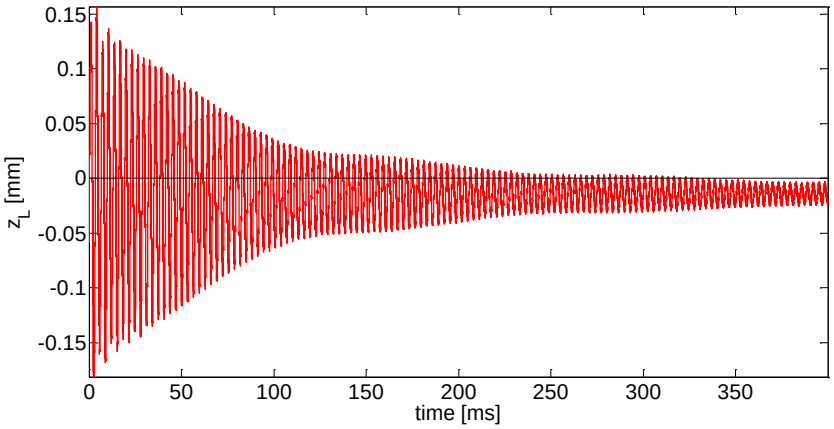

(b)

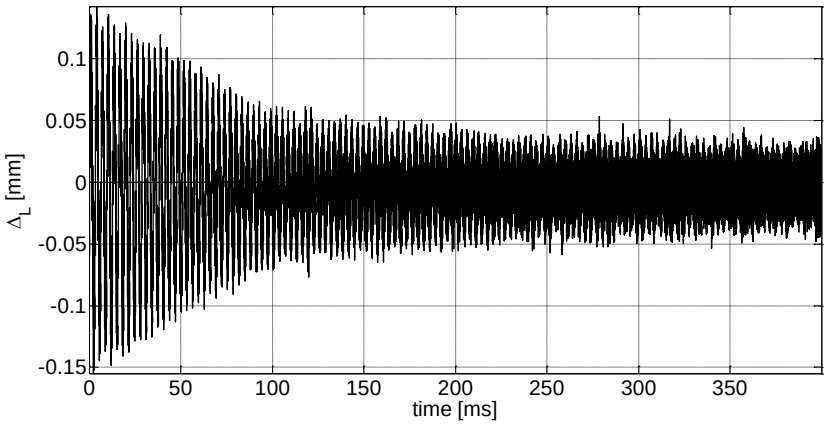

(c)

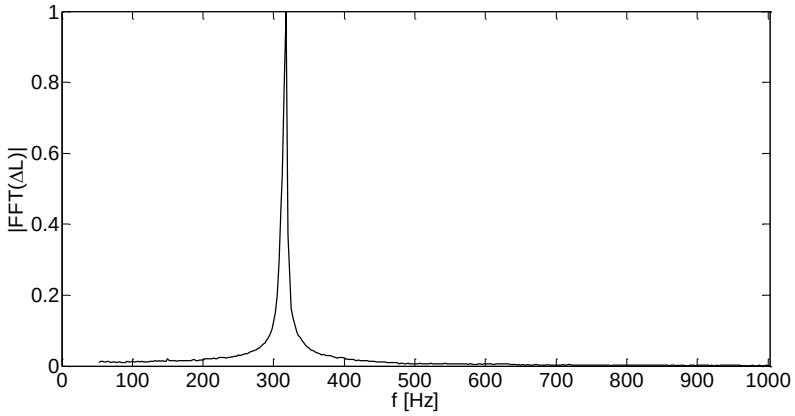

Figure 5.12: Free-fixed measurement (with $z_R = 0$): (a) left tip displacement z_L, (b) wire elongation ΔL, (c) normalized spectrum amplitude of the wire elongation $|FFT(\Delta L)|$.

Surprisingly, there is a non-negligible difference as compared to the results in Figure 5.12(c): the single peak in the spectrum of the preceding measurements has split into two peaks. The small difference between them is responsible for the amplitude modulation appearing in Figure 5.13(a,b). Now, the fork seems to behave as a 2-DoF system. Besides this striking feature, the wire elongation responds linearly to the fork tip motion (as before).

The first hypothesis was that this second DoF is associated with the motion of the mass of the wire fixation system, which was probably not totally fixed to the fork. However, a closer inspection showed that this was not the case. At that point, we decided to add that second DoF in an *ad hoc* way in order to obtain similar results through the analytical models. Though the first fork model was a physical one (based on a physical description of the real system), this new model is a phenomenological one.

Before presenting that *ad hoc* modification, the free-fixed set of measurements will be analysed.

Free-free set: measurements

Figure 5.14(a,b) show the left tip displacement z_L and its normalized spectrum, respectively, corresponding to the free-free set where the manually displaced tip is the left one (the z_R is not shown as it is qualitatively very similar to the z_L though with lower amplitude). In this case, two peaks appear in the z_L spectrum, which suggest that the fork is evolving according to 2 DoF. The lower frequency is around 150 Hz while the upper one is roughly 400 Hz. These frequencies are very close to those of the symmetric and antisymmetric modes given in Eq.(5.16. As both tips may move and the initial condition imposed in z_L (<0) generates immediately a $(z_R > 0, \text{ with } |z_R| < |z_L|)$, both modes appear necessarily.

Figure 5.15(a,b) show the time evolution and the normalized spectrum, respectively, of the corresponding wire elongation ΔL. As in the free-fixed set, $\Delta L(t)$ is roughly proportional to $z_L(t)$ during the first part of the plot, but maintains a fairly constant amplitude during the second one associated with the transverse wire oscillation. Regarding the ΔL spectrum, only one peak located around 400 Hz appears. This is logical as the tips symmetric mode does not generate any wire elongation.

Imposing the initial condition on the right tip and letting the left one be free to move leads to the measured results shown in Figure 5.16 (right tip displacement z_R) and Figure 5.17 (wire elongation ΔL). The main difference (as compared to the results shown in Figure 5.14 and Figure 5.15) is the splitting of the peak associated to the antisymmetric tips motion. The *ad hoc* modification suggested earlier must be able to reproduce this feature.

(a)

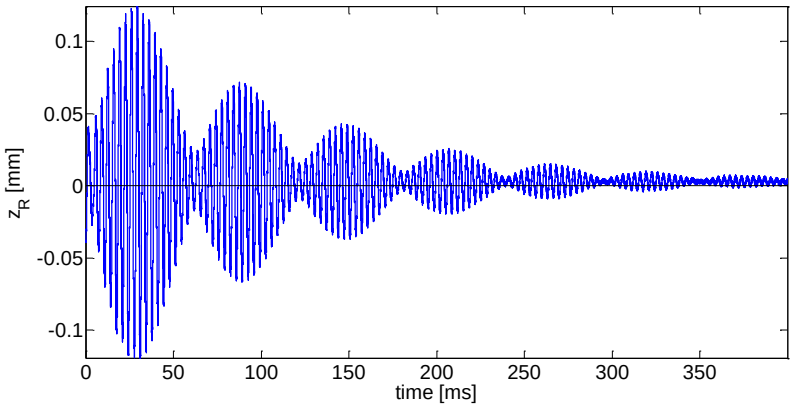

(b)

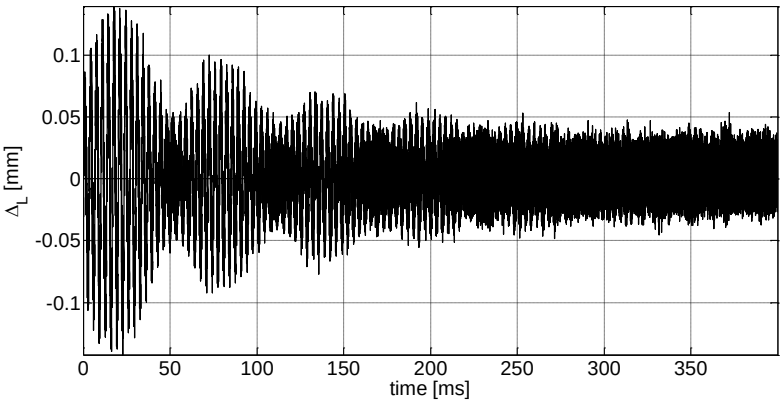

(c)

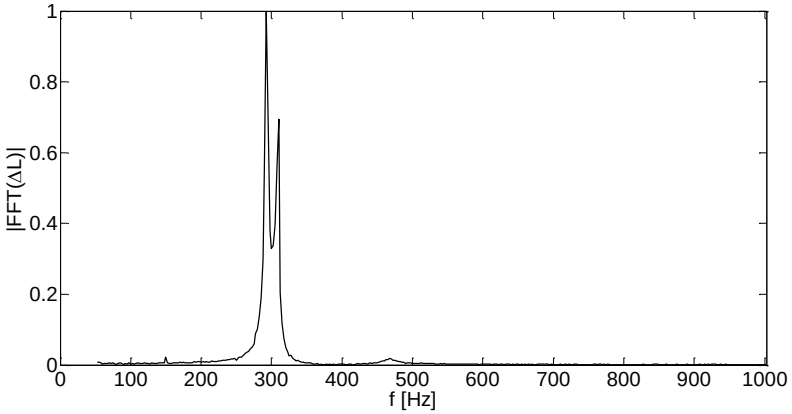

Figure 5.13: Free-fixed measurement (with $z_L = 0$): (a) right tip displacement z_R, (b) wire elongation ΔL, (c) normalized spectrum amplitude of the wire elongation $\left|FFT(\Delta L)\right|$.

(a)

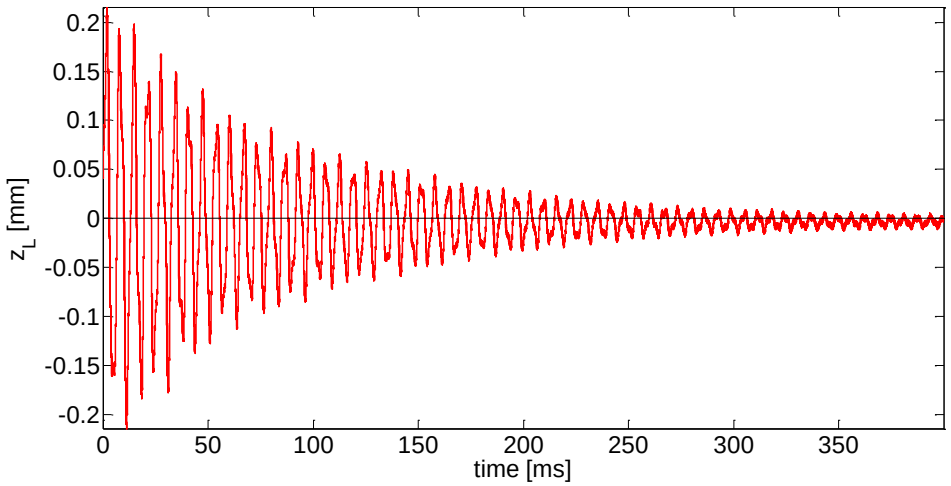

(b)

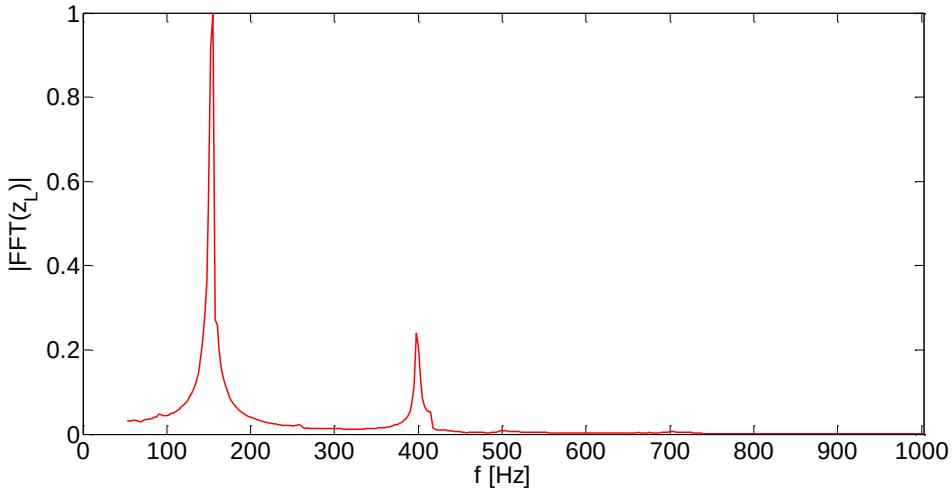

Figure 5.14: Displacement of the left tip (z_L) in a free-free measurement: (a) time evolution, (b) normalized spectrum.

(a)

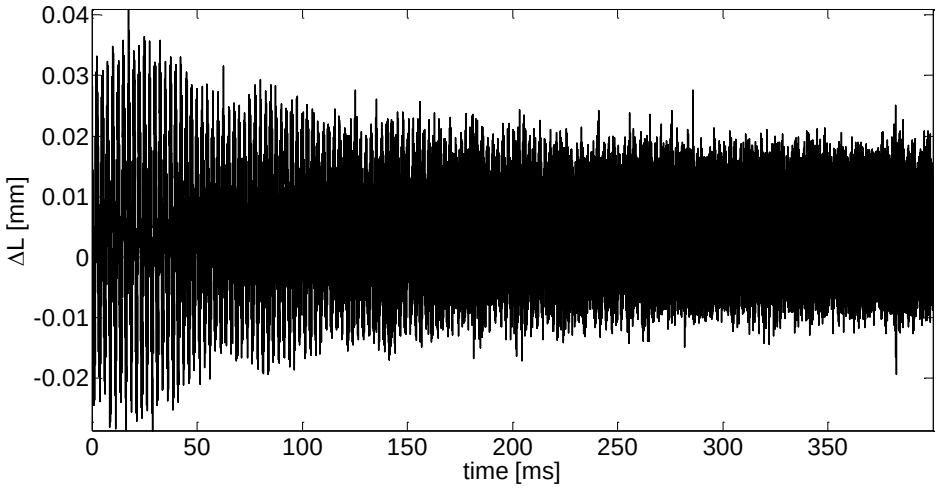

(b)

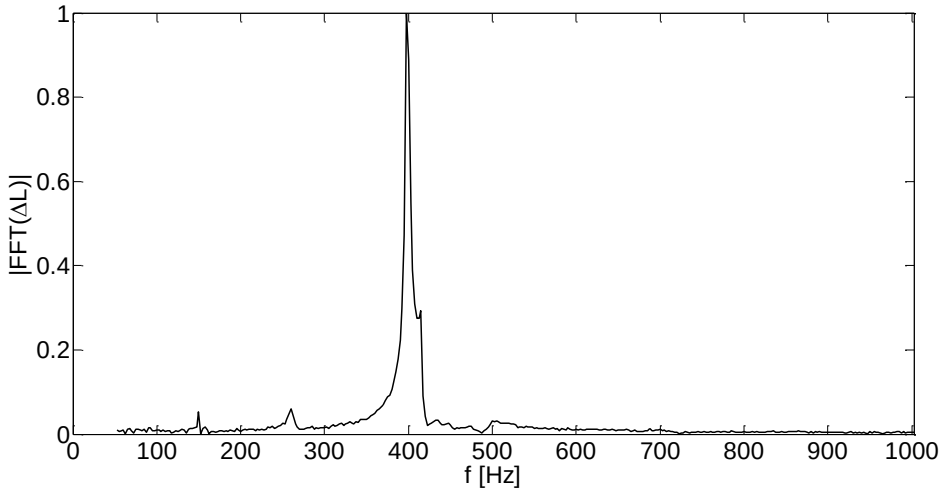

Figure 5.15: Wire elongation (ΔL) associated with the free-free measurement in Figure 5.14: (a) time evolution, (b) amplitude of the normalized spectrum.

(a)

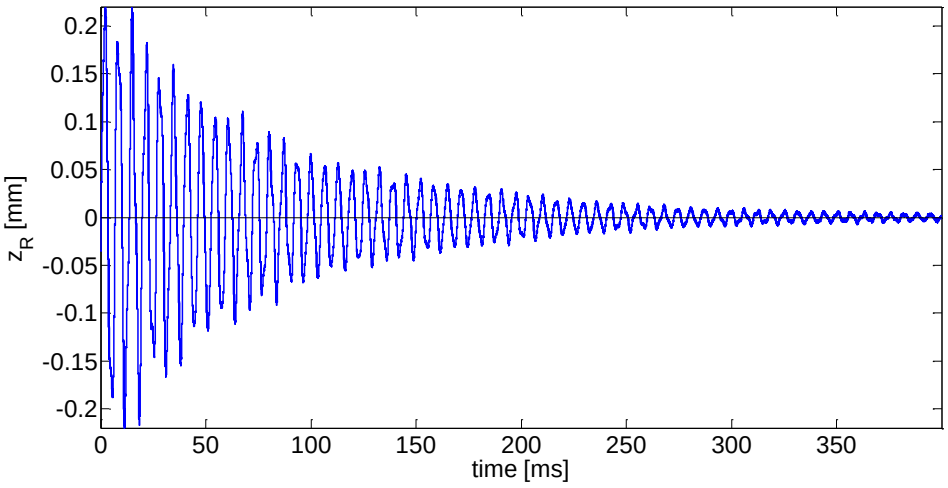

(b)

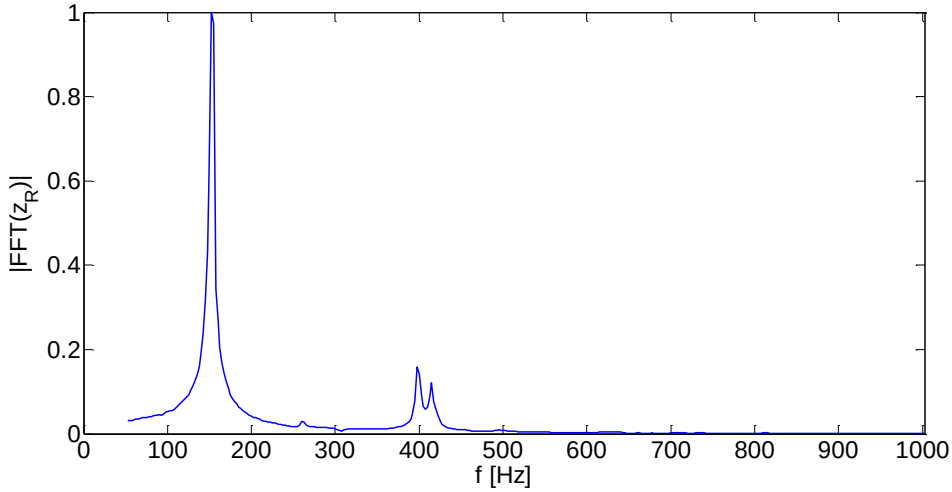

Figure 5.16: Displacement of the right tip (z_R) in a free-free measurement: (a) time evolution, (b) amplitude of the normalized spectrum.

Fork phenomenological model (*ad hoc* modification)

The *ad hoc* modification is based on a well-known fact: when you couple two 1-DoF systems with exactly the same natural frequency f, the coupled systems exhibits two natural frequencies $f_{\pm}$ whose values are $f_{\pm} = f \pm \Delta$, with Δ very small. Thus, coupling a 1-DoF system with a natural frequency of 300 Hz to a moving tip would yield the observed peak splitting in Figure 5.13(c). Coupling a second 1-DoF system with a natural frequency of 400 Hz would generate the splitting in Figure 5.16(b) and Figure 5.17(b).

(a)

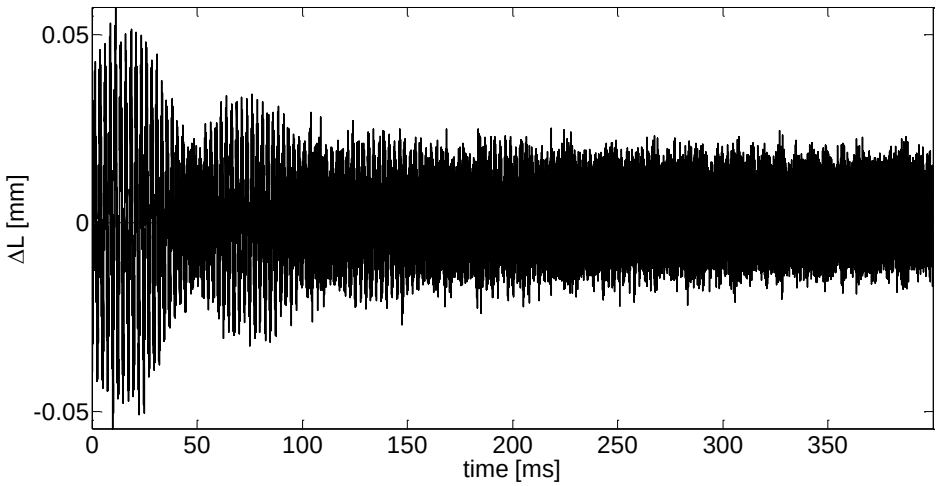

(b)

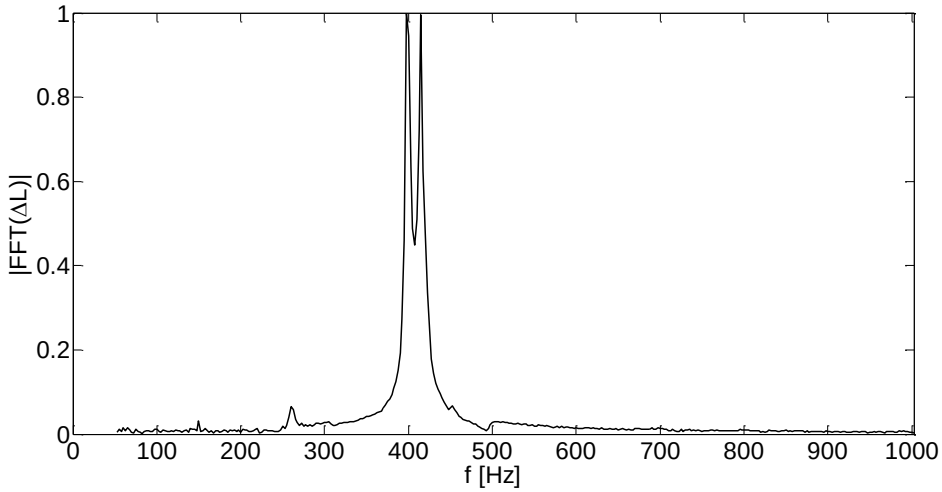

Figure 5.17: Wire elongation (ΔL) associated with the free-free measurement in Figure 5.16: (a) time evolution, (b) amplitude of the normalized spectrum.

Figure 5.18 shows the new fork model including those two additional 1-DoF systems. The new equations for the fork tips become:

$$\begin{aligned} \tilde{m}_{R,L}\ddot{\tilde{z}}_{R,L} &= -\tilde{k}_{R,L}\tilde{z}_{R,L} - \tilde{k}_{cR,cL}\left(\tilde{z}_{R,L} + z_{R,L}\right) , \\ m_z\ddot{z}_{R,L} &= -k_z z_{R,L} - c_z\dot{z}_{R,L} - k_w\left(z_{R,L} + z_{L,R}\right) - \tilde{k}_{cR,cL}\left(\tilde{z}_{R,L} + z_{R,L}\right) . \end{aligned} \tag{5.25}$$

Another expression for Eqs.(5.25) is:

$$\begin{aligned} \ddot{\tilde{z}}_{R,L} &= -\tilde{\omega}^2_{R,L}\tilde{z}_{R,L} - \tilde{\omega}^2_{cR,cL}z_{R,L} , \\ \ddot{z}_{R,L} &= -\omega_S^2 z_{R,L} - \frac{1}{2}\left(\omega_A^2 - \omega_S^2\right)\left(z_R + z_L\right) - \tilde{\omega}^2_{cR,cL}\frac{\tilde{m}_{R,L}}{m_z}\left(\tilde{z}_{R,L} + z_{R,L}\right) - \frac{c_z}{m_z}\dot{z}_{R,L} , \end{aligned} \tag{5.26}$$

with $\tilde{\omega}^2_{R,L} = \left(\tilde{k}_{R,L} + \tilde{k}_{cR,cL}\right)\Big/\tilde{m}_{R,L}$, $\tilde{\omega}^2_{cR,cL} = \tilde{k}_{cR,cL}\Big/\tilde{m}_{R,L}$.

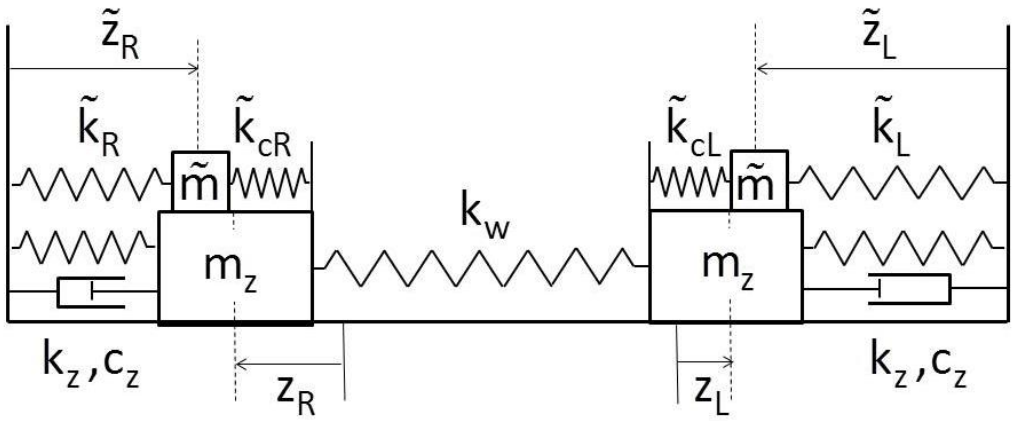

Figure 5.18: Fork modified model. $\tilde{m}$, $\tilde{k}_{R,L}$, $\tilde{k}_{cR,cL}$ represents the ad-hoc masses and springs respectively.

Simulations: free-free and free-fixed sets

Figure 5.19 to Figure 5.22 show the simulations obtained from Eqs.(5.8) (with no inertia forces) and Eqs.(5.25). The initial conditions and new parameters' values are shown in Table 5.2.

(a)

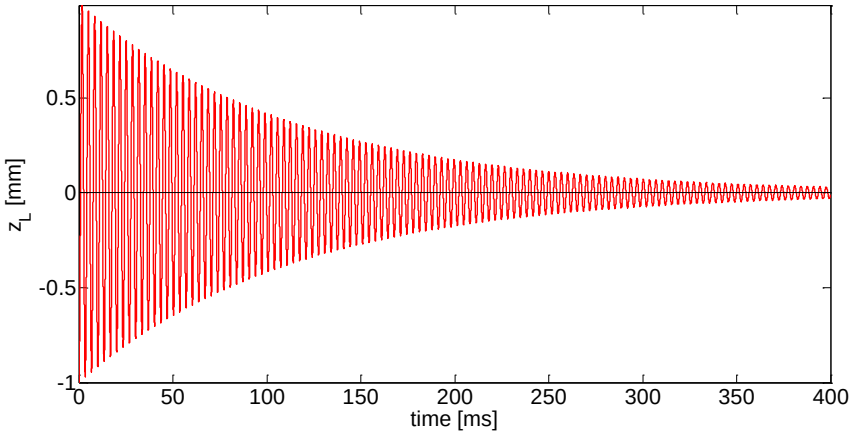

(b)

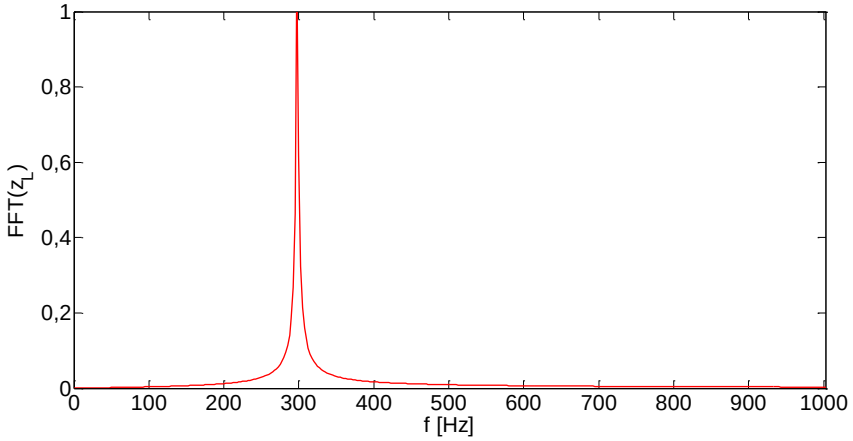

Figure 5.19: Displacement of the left tip (z_L) in a free-fixed simulation $(z_R = 0)$: (a) time evolution, (b) normalized spectrum.

(a)

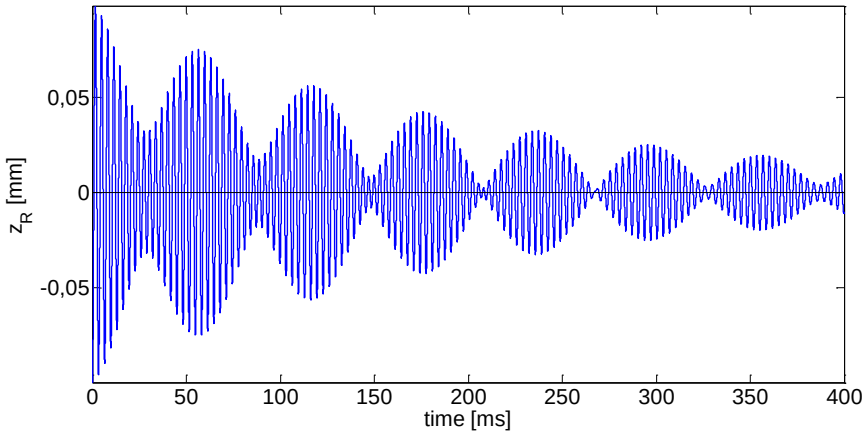

(b)

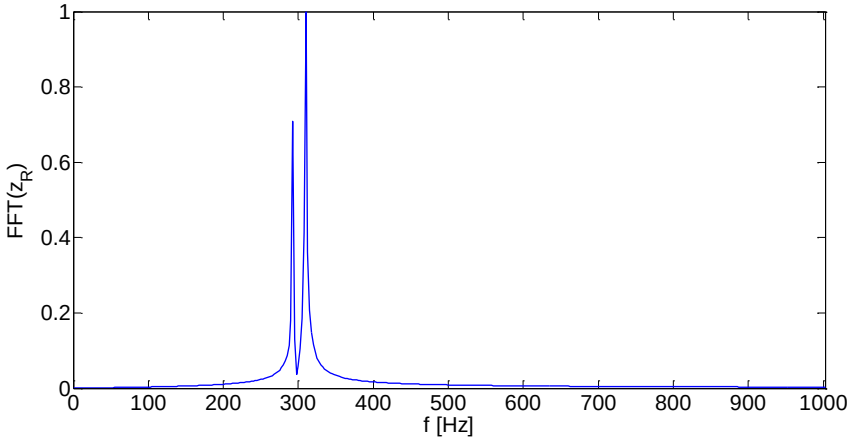

Figure 5.20: Displacement of the left tip (z_R) in a free-fixed simulation $(z_L = 0)$: (a) time evolution, (b) normalized spectrum.

(a)

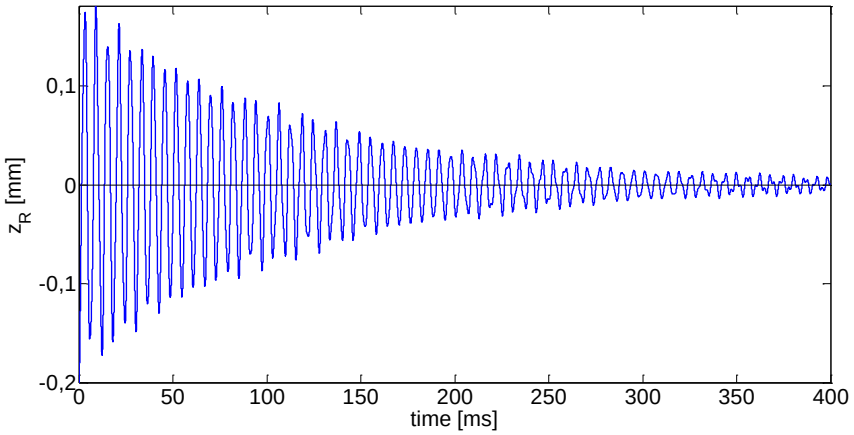

(b)

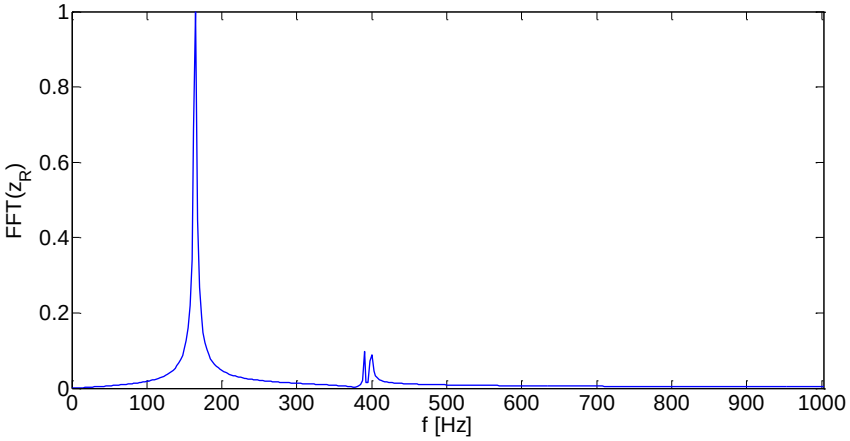

Figure 5.21: Displacement of the right tip (z_R) in a free-free simulation: (a) time evolution, (b) normalized spectrum.

(a)

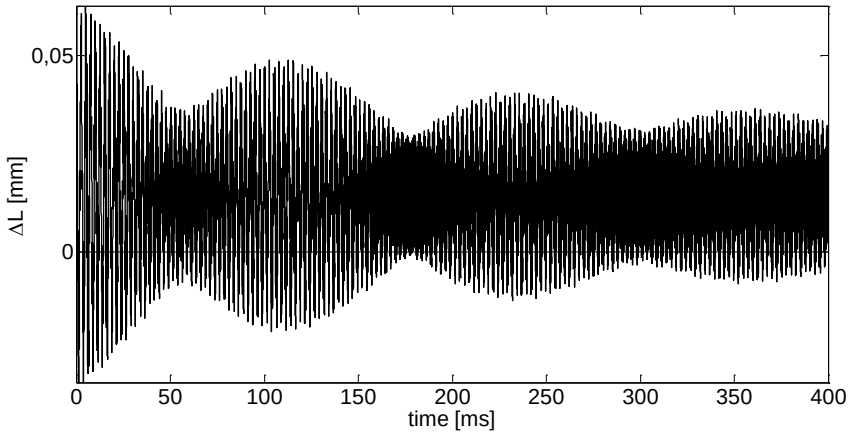

(b)

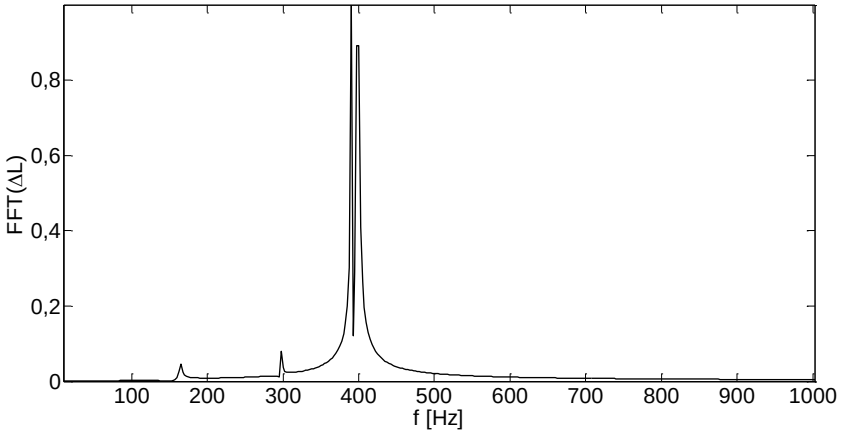

Figure 5.22: Wire elongation (ΔL) associated with the free-free simulation in Figure 5.21: (a) time evolution, (b) normalized spectrum.

Table 5.2: Initial condition and parameters

Figure	Initial conditions	Parameters' values
Figure 5.19 **(free-fixed)** (compare to Figure 5.12)	$x = 0,\ y = 0.1\ mm$ $z_L = -1\ mm\ (z_R = 0\ permanently)$	$\tilde{\omega}_R = \omega_{1DoF}$, $\tilde{\omega}_L = \omega_A$ $\tilde{\omega}_{cR} = \tilde{\omega}_{cL} = 450\ s^{-1}$ $\frac{\tilde{m}_R}{m_z} = 0.8$, $\frac{\tilde{m}_L}{m_z} = 0.5$
Figure 5.20 **(free-fixed)** (compare to Figure 5.13)	$x = 0,\ y = 0.1\ mm$ $z_R = -1\ mm\ (z_L = 0\ permanently)$	
Figure 5.21**,** Figure 5.22 **(free-free)** (compare to Figure 5.16, Figure 5.17)	$x = 0,\ y = 1\ mm$ $z_L = 0.8\ mm,\ z_R = -1\ mm$	

The results are remarkably similar to the experimental ones (Figure 5.12 to Figure 5.17). The main difference appears in Figure 5.22(a): its mean value is much higher than that of the corresponding measurement in Figure 5.17(a). This is due to a higher initial condition in the wire transverse displacement.

With these simulations we consider that the model with no shaft rotation has been validated. The next one will explore the effect of the inertia forces associated with the scan cycle.

5.5. Simulation results under shaft rotation

The wire behaviour during a scan cycle was first simulated with the "hybrid approach". In that case, the governing equations were just those of the wire motion (Eqs.(5.8)). The tips motion was introduced as a boundary condition. Thus, the simulations allowed to check whether the inertia forces appearing in the wire model were able to generate reasonable wire transverse vibrations.

Figure 5.23 shows the motion pattern for the OUT-to-IN phase of a scan cycle (the IN-to-OUT phase is very similar and will be omitted). The measured fork tips deflections $z_{R,L}$ and wire elongation during that phase are shown in Figure 5.24.

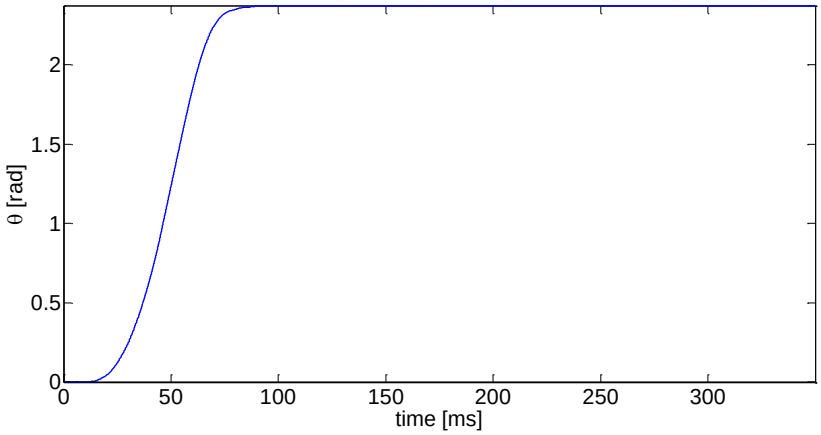

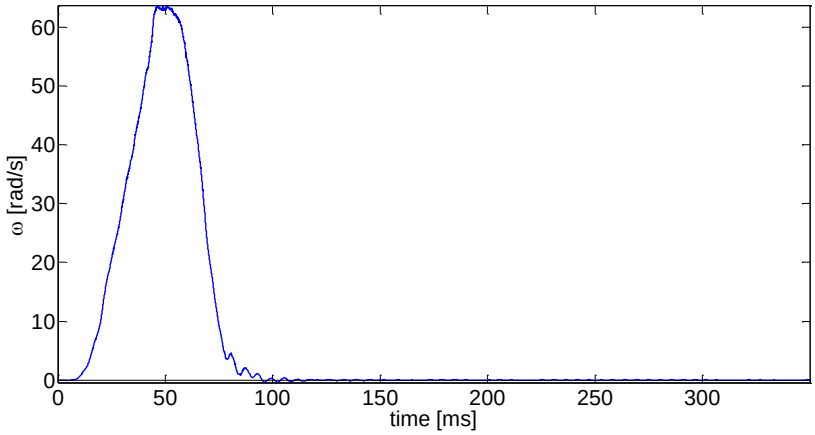

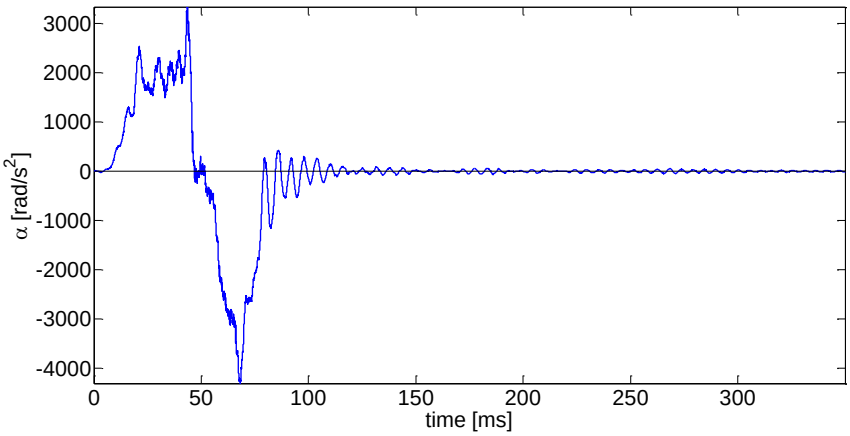

Figure 5.23: Measured time evolution of the angle, the angular velocity and the angular acceleration of the shaft during an OUT-to-IN scan cycle.

(a)

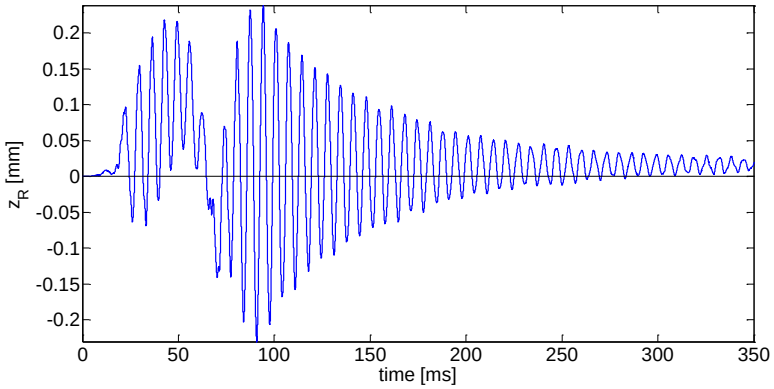

(b)

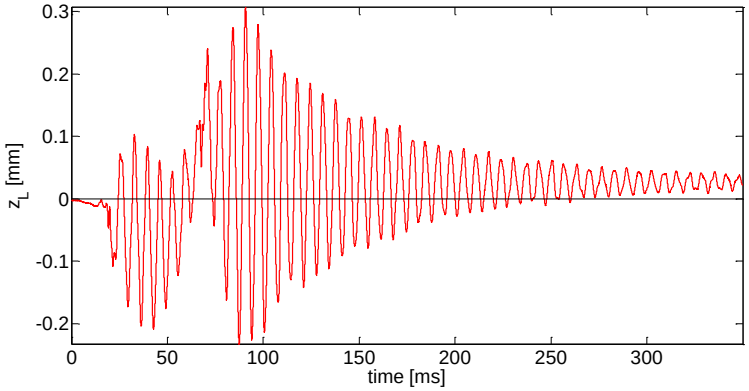

(c)

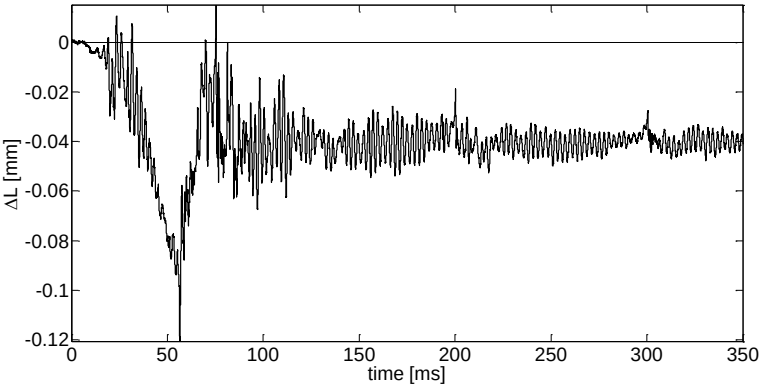

Figure 5.24: Measured behaviour of fork tips and wire during the OUT-to-IN phase of the scan cycle shown in Figure 5.23: (a) right tip deflection; (b) left tip deflection; (c) wire elongation.

From Figure 5.23, it is clear that the inertia forces triggering the fork tips and wire vibrations appear only during roughly 70 ms. From that time instant, the system vibrates freely. This is consistent with the tips motion shown in Figure 5.24 (a,b): both are damped quasilinear oscillations once the scan cycle is over. As for the starting transient, both show similar trends but are not identical.

Simulations with the hybrid approach

The hybrid simulation was first run for a wire tension of 0.1 N (which is the average tension in all the measurements). Figure 5.25 (a,b) show the wire transverse amplitude r and the wire elongation ΔL (called "active" elongation from now on), respectively, calculated as

$$\Delta L = \sqrt{r^2 + \left(\frac{L_0}{2} + z_R\right)^2} + \sqrt{r^2 + \left(\frac{L_0}{2} + z_L\right)^2} - L_0 \quad . \tag{5.27}$$

Figure 5.25(c) shows the difference between ΔL and the wire elongation if there was no wire transversal vibration ("passive" elongation).

Note that the tips motion alone would not generate any wire transverse oscillation, as it appears multiplied by the transverse coordinate r in Eqs.(5.8) governing the wire motion, and the variables were all initialized with a zero value. The transverse vibration in Figure 5.25(a) was triggered by the inertia forces and further enhanced by the tips motion. However, they have nearly no effect on the wire length: the difference between the active and the passive elongation (Figure 5.25(c)) is very small.

There are discrepancies between the simulated active elongation shown in Figure 5.25(b) and the measured one (Figure 5.24(c)). The reason is twofold: the wire model is an idealization, and the measurements are not free from measurement errors. Nevertheless, we consider that those results constitute an acceptable validation of the wire model as both the order of magnitude and the mean value are correct.

In order to assess the consequences of a parametric resonance, simulations with different wire tension values (leading to transverse wire frequencies ω_T related to the antisymmetric tips motion frequency ω_A through $\omega_A = (2/n)\omega_T$) were run. Figure 5.26 shows the result for the case $n = 2$ $(T_0 = 0.013\ N)$. The transverse wire displacement is ten times higher than that in Figure 5.25(a), and the consequence on the wire elongation is that not only the oscillations about the mean value are much higher but also the overall elongation is positive. This was not the case in the first simulation: the fork hinges deformations (associated with the shaft bending) were responsible for a global decrease in the wire length. In the present case, the transverse oscillation is high enough to compensate for the hinges approaching motion.

(a)

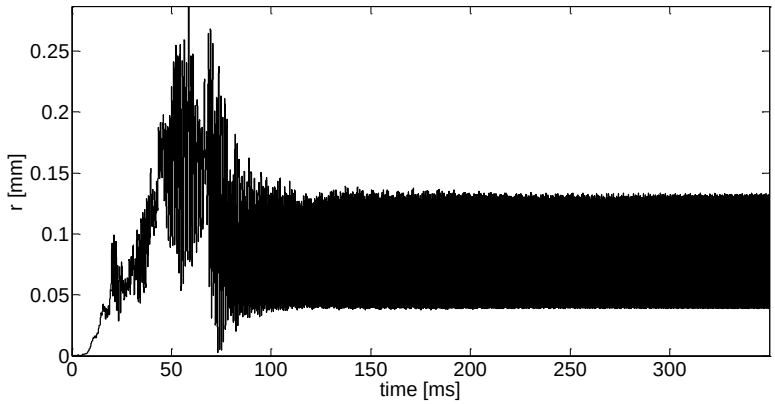

(b)

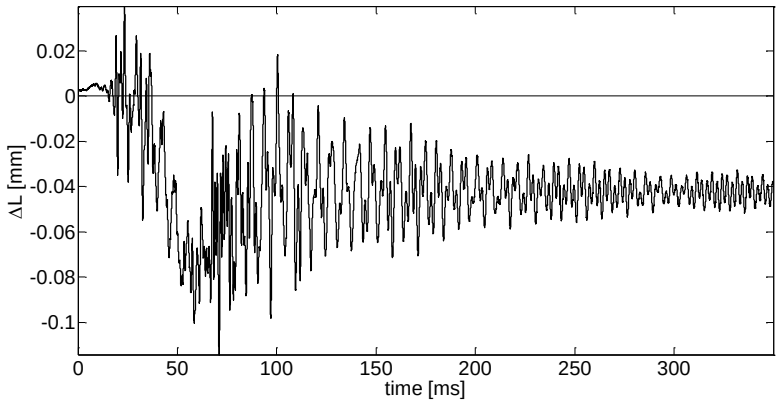

(c)

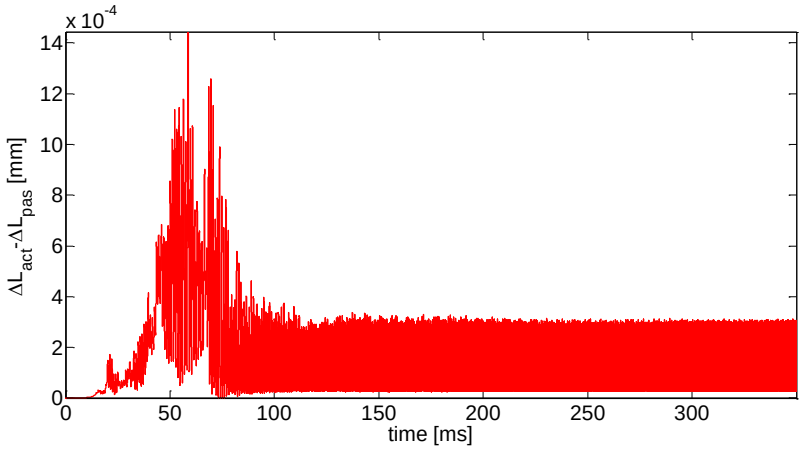

Figure 5.25: Results obtained with the hybrid approach during the OUT-to-IN phase of the scan cycle in Figure 5.23, and for a wire tension of 0.1 N: (a) wire transverse vibration; (b) wire elongation; (c) comparison between the active and the passive wire elongations.

(a)

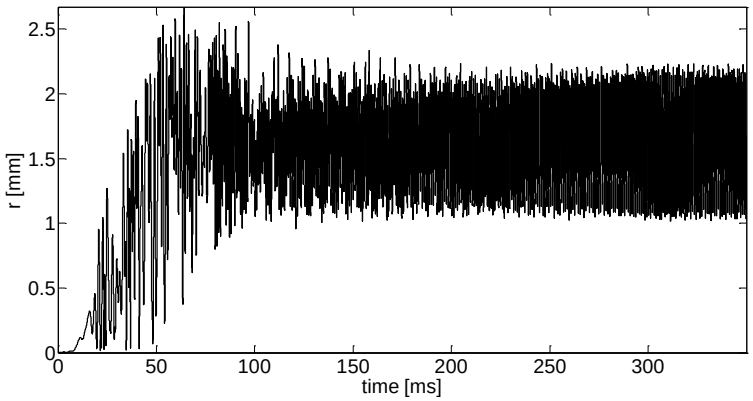

(b)

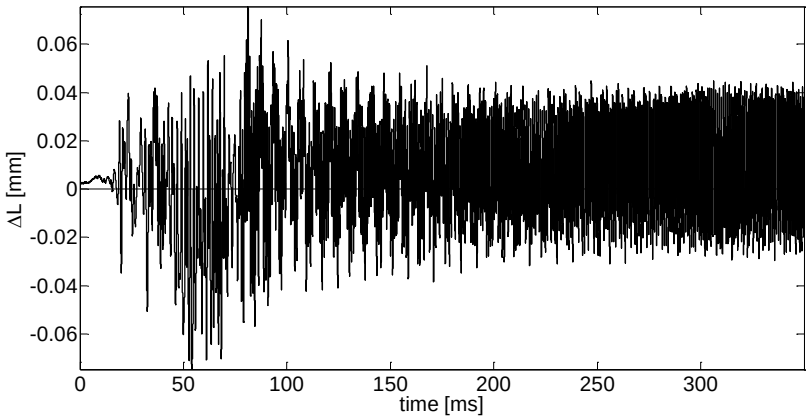

(c)

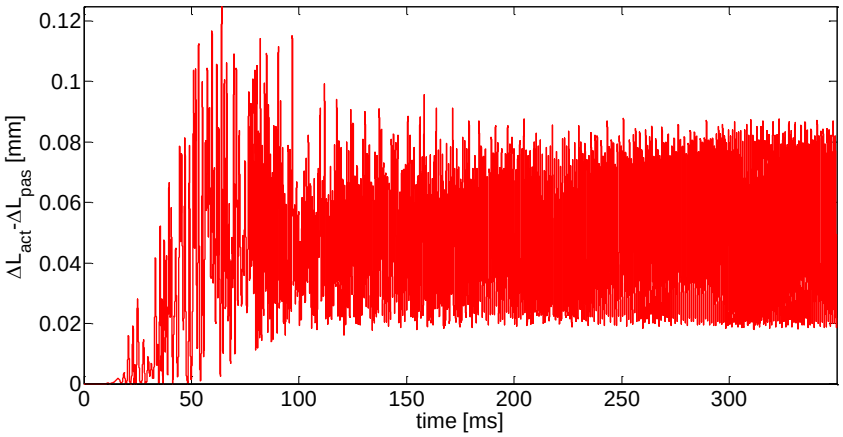

Figure 5.26: Results obtained with the hybrid approach during the OUT-to-IN phase of the scan cycle in Figure 5.23, and for a wire tension of 0.013 N: (a) wire transverse vibration; (b) wire elongation; (c) comparison between the active and the passive wire elongations.

Simulations with the analytic approach

In the analytical approach, the effect of shaft bending is introduced directly as a boundary condition on the fork tips hinges. As mentioned at page 67, the hinges displacements as a function of the shaft angular configuration were measured in a quasi-static test. The time-evolution of the hinges' displacements was obtained combining those data with the time-evolution of the shaft angular coordinate in Figure 5.23. The result for the right hinge ($z(o_R)$) is shown in Figure 5.27(a). A numerical time derivative of $z(o_R)$ lead to the time-evolution acceleration $\ddot{z}(o_R)$ (Figure 5.27(b)). That of the left hinge is not shown. It is qualitatively very similar though higher in amplitude.

Being the result of a quasi-static test, it is not surprising that both plots are smooth. For that reason, the terms on $\ddot{z}(o_{R,L})$ appearing in the model will never provoke any resonance effects. However, real accelerations under shaft rotation may differ from those smooth curves. It is most probable that the hinges undergo vibrations and consequently that the spectrum of the accelerations $\ddot{z}(o_{R,L})$ shows different resonance peaks. As we were not able to measure the bending effect on the hinges under rotation conditions, we may expect substantial differences between measured and simulated tips vibrations.

The analytical approach (based on Eqs.(5.8) and Eqs.(5.26)) was run also for a wire tension of 0.1 N and assuming the scan cycle pattern in Figure 5.23 and the hinge acceleration in Figure 5.27(b). The initial conditions were zero velocity and zero displacement for the wire and the tips. From that rest configuration, the inertia force associated to shaft bending provided a nonzero initial condition for the fork tips, while the inertia forces associated to the shaft rotation triggered the wire transverse oscillation.

The resulting right and left tip oscillations are shown in Figure 5.28 (a) and (b), respectively. They have a rather different starting transient but both exhibit a damped linear behaviour during the last 250 ms. The initial differences come from the different amplitudes of the hinges accelerations used in the simulation.

The main difference between simulations (Figure 5.28 (a,b)) and measurements (Figure 5.24 (a,b)) happens during the first 50 ms of the motion. The mean values are very similar, but the oscillations in the measurement do not appear in the simulated plot.

It is difficult to say whether this is the result of an oversimplification of the model or if the measurement is contaminated with other phenomena. Strain gauges used to measure deflections along the fork arms might be registering not only the motion in the fork plane but also capturing part of the motion in the transverse plane.

On the other hand, those initial oscillations might be associated with hinge vibrations due to shaft bending. At this stage, the measurement method does not allow more precision, so we have not been able to reach a definite conclusion.

(a)

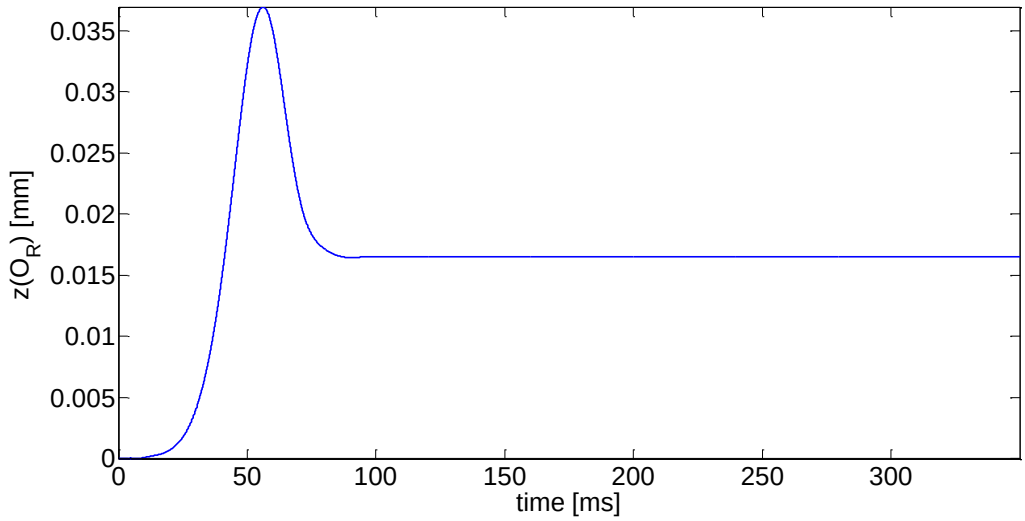

(b)

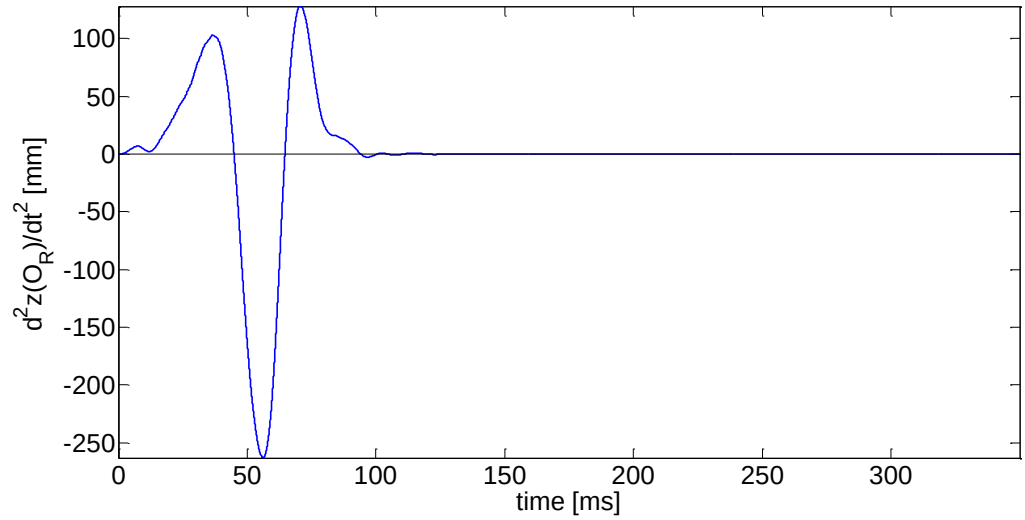

Figure 5.27: Displacement (a) and acceleration (b) of the right fork tip obtained through combination of a quasi-static test and the angular pattern in Figure 5.23.

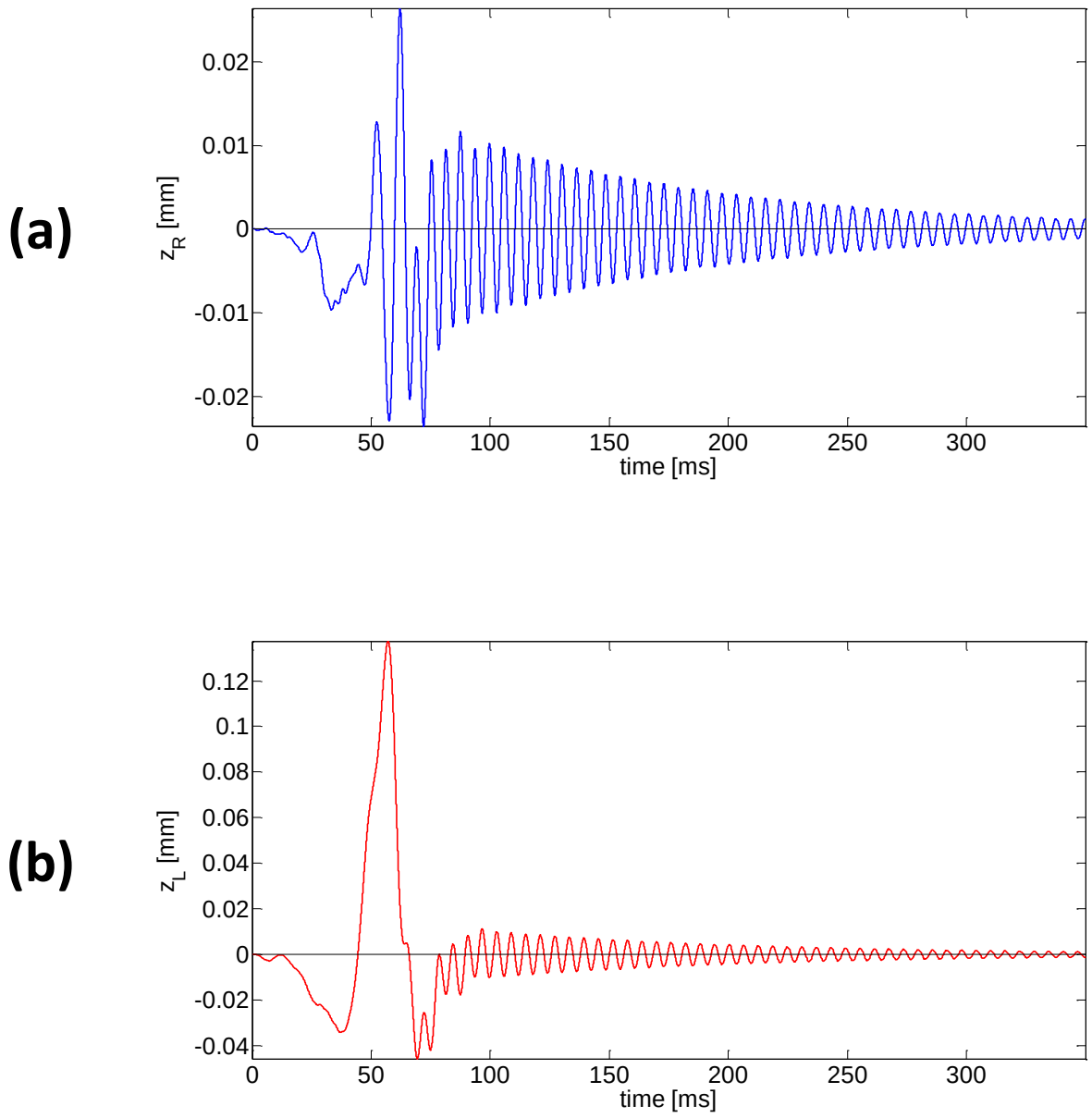

Figure 5.28: Oscillation of the right (a) and left (b) fork tips obtained with the analytical approach. The inertia forces considered in the simulation are those associated with the scan cycle shown in Figure 5.23 and the hinge acceleration shown in Figure 5.27(b).

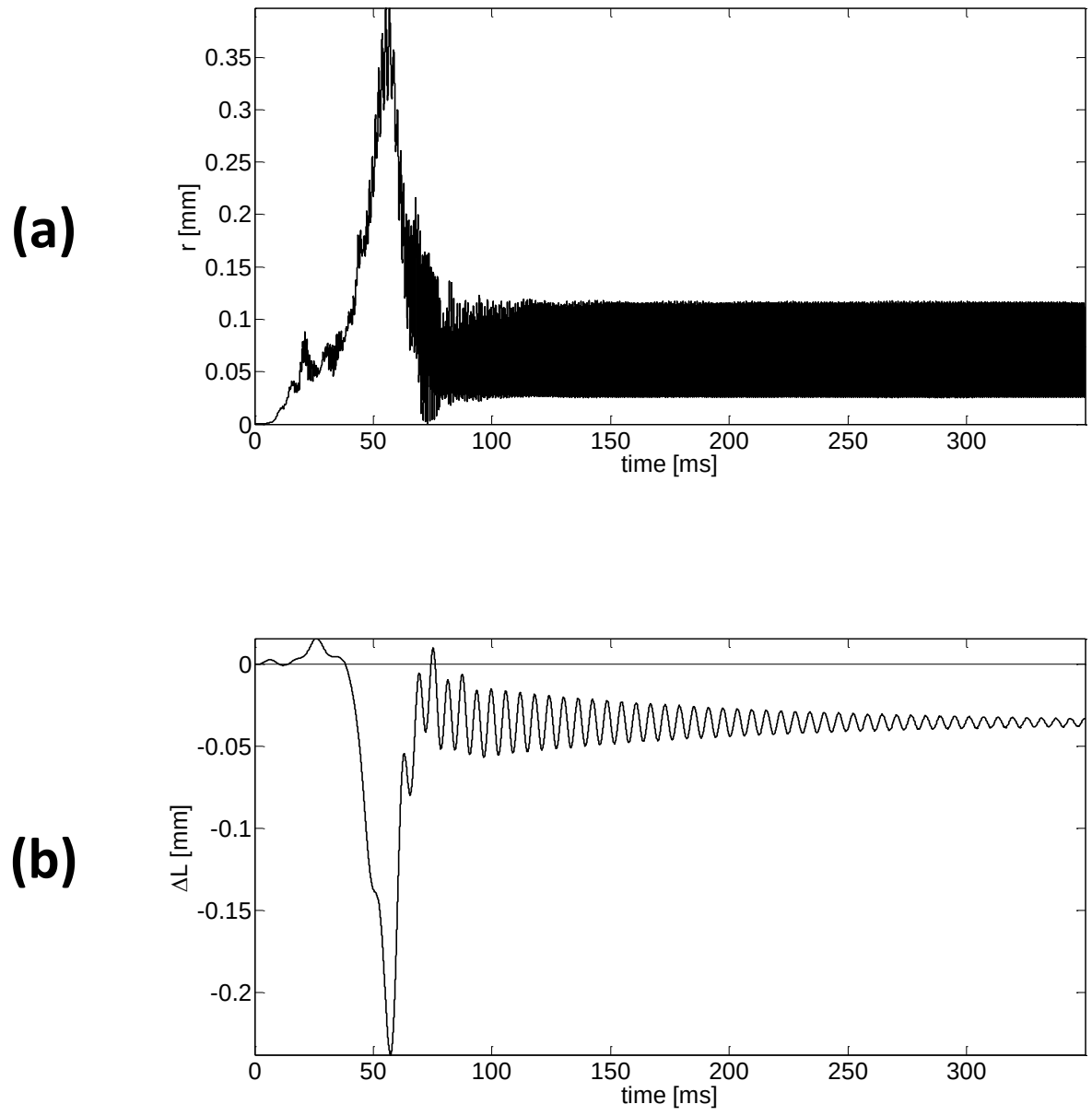

Figure 5.29: Results obtained with the analytical approach during the OUT-to-IN phase of the scan cycle in Figure 5.23, and for a wire tension of 0.1 N: (a) wire transverse vibration; (b) wire elongation.

The wire transverse coordinate is shown in Figure 5.29(a). As compared to that obtained with the hybrid approach (Figure 5.25(a)), the peak in the initial transient is higher (though with the same order of magnitude) but the oscillation stabilizes again from t=100 ms and keeps the same amplitude. As for the wire elongation (shown in Figure 5.29(b)), though exhibiting a mean value close to that of the measured one (Figure 5.24(c)), its frequency content is far too simple. The high frequency and the modulation in Figure 5.24(c) are missing in the simulated result. Reproducing those features through an analytical model is not simple. *Ad hoc* modifications in this case are not easy to find, as we are dealing here with a highly nonlinear problem.

(a)

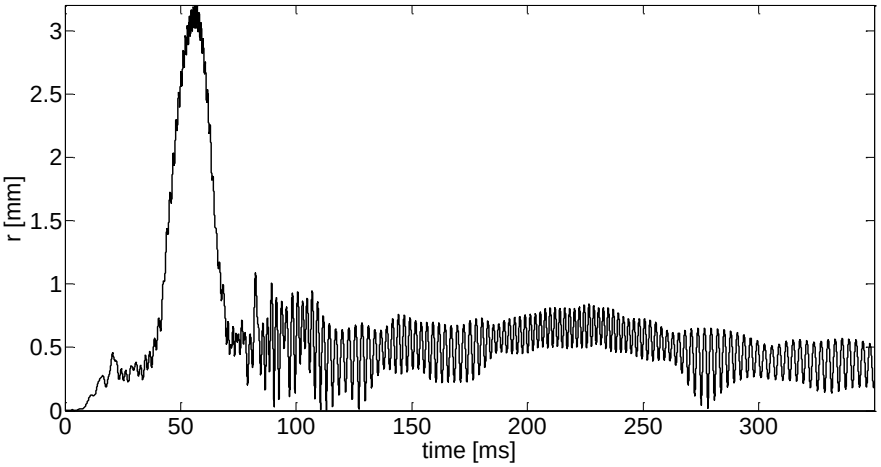

(b)

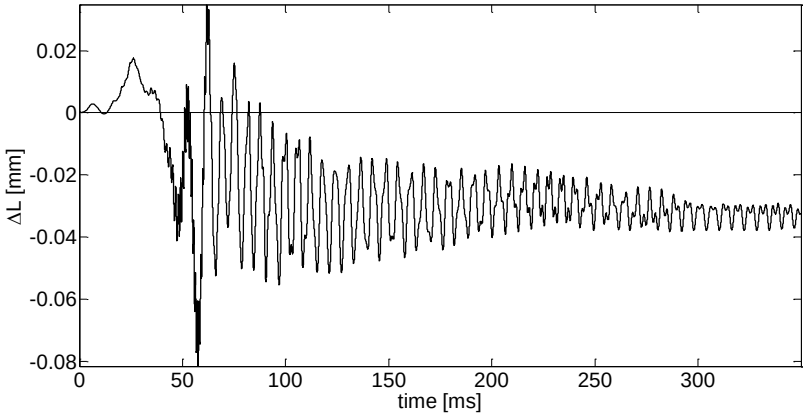

Figure 5.30: Results obtained with the analytical approach during the OUT-to-IN phase of the scan cycle in Figure 5.23, and for a wire tension of 0.013 N: (a) wire transverse vibration; (b) wire elongation.

However, we consider that the model is sufficient valid to test again its behaviour when confronted with a possible parametric resonance. The analytical approach was run again for a wire tension of 0.013 N. The results are shown in Figure 5.30. As in the hybrid approach, the wire transverse oscillation is ten times higher, and there is a positive shift in the wire elongation (though it stays negative). After the initial transient, a more complex oscillation is shown as compared to the 0.1 N case: not only the frequency content is richer but some sort of modulation can also be observed.

5.6. Summary

This part of the work presented an analytical model which allows the study and simulation of the wire vibrational behaviour in rotating wire scanner devices. The model has been developed for the PS wire scanner. The model robustness and accuracy was demonstrated by the good agreement with experimental vibration measurements.

Two different models were built: a discrete model, where the wire is a point-mass attached to the fork tips through linear springs and dampers, and a continuous one, where the wire was treated as a taut string. We proved that the continuous model is qualitatively equal to the discrete one when a single string vibration mode is considered. Under this hypothesis, both wire models present parametric and nonlinear terms.

The fork flexibility was taken into account at first through a single DoF linear model corresponding to an antisymmetrical motion of the tips. Comparison between simulation and measurement for the case of free oscillations (with no shaft rotation) suggested the addition of extra DoF for the fork tips.

Simulations including shaft rotation were run with two different approaches: a hybrid approach (were the fork tips motion was taken from measurements) and a purely analytical one (were fork tips were modelled analytically). Some differences appear between the simulated results and the measured ones. At this stage, we were not able to establish whether the measurements were not accurate enough or whether the models oversimplified the reality.

Nevertheless, the general trends are satisfactory. Different wire tension values were assumed in order to check the sensitivity of the system to possible parametric resonances. As expected, whenever the tension leads to a transverse wire frequency equal to that of the fork antisymmentric vibration, the wire oscillations and the wire elongation increased.

6. New design

The aim of this chapter is to describe and evaluate the design of the new wire scanner. The chapter presents (1) the concept of the new design and (2) the optimization strategy guidelines of the most critical and sensitive elements.

The technical solutions introduced in this new design are intended to avoid or minimize the drawbacks of the existing designs. These improvements are the result of the studies performed on the existing wire scanner, thus most of the conclusions of the previous parts of the work have been used as the starting point for the new design. Although those improvements concern different aspects (maintenance, reliability, accuracy), the discussion will mainly focus on the improvements which have an impact on the accuracy of the measurements.

The accuracy improvements of the new design are organized in three parts: conceptual improvements, design improvements and operation improvements. An example of conceptual improvement is the suppression of the error due to the motion transmission play, since the new design does not require any mechanical transmission susceptible to mechanical play. An example of design improvement is the minimization of the fork tip deflection achieved by the fork design optimization. Concerning operating improvements, an example is the vibration minimization by means of the motion pattern optimization.

6.1. Conceptual design description

The most remarkable feature of the new wire scanner concept is that all the movable components of the system are under vacuum. Although the rotating elements (actuator, angular sensor, shaft, fork and wire) remain the same as in the existing design (i.e. a fork holding the wire is mounted on a rotating shaft), the mechanical complexity of the system is highly reduced since no kinematical links are required to transmit the motion from the pressure side to the vacuum side. Additionally, all movable parts are mounted in the same shaft, which implies the suppression of the kinematic chain which typically links the wire measuring point to the angular position sensor. Avoiding these kinematic chains represents a conceptual improvement compared to the existing devices from the precision point of view, as there is no mechanical play between the different parts of the measurement chain. Therefore, the position determination of the measuring chain is much more accurate.

The main parts of this new wire scanner concept are (Figure 6.1):

- Actuator
- Shaft
- Fork
- Wire
- Angular sensor
- Magnetic restrain system
- Bearings

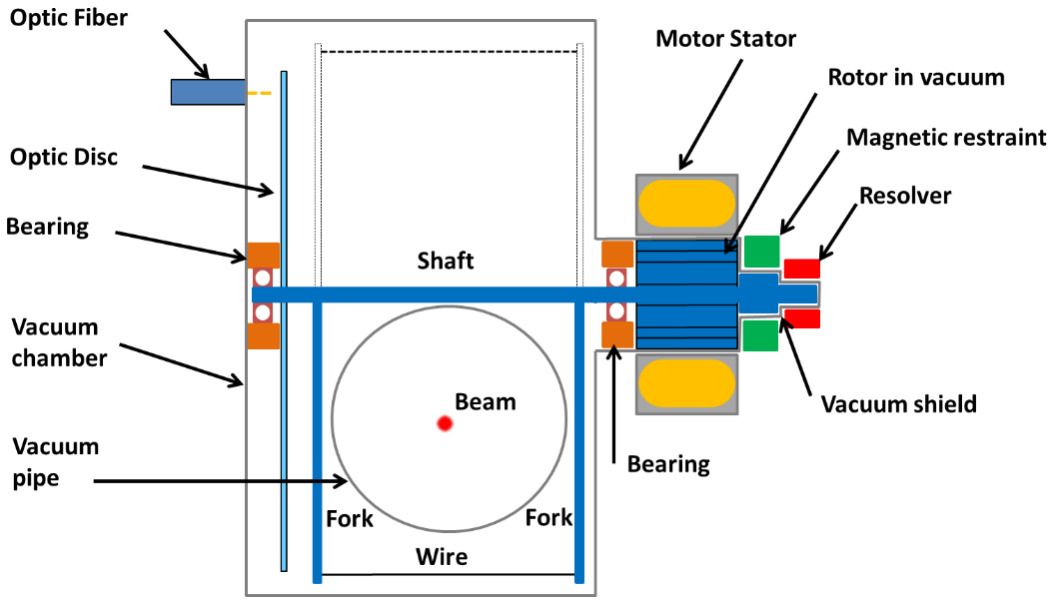

Figure 6.1: New wire scanner conceptual design.

6.1.1. Actuator

The actuator consists of a frameless electrical motor. In this type of motor, the rotor and stator are independent, which allows a proper embedding of the motor in the system. In the case of the new wire scanner, this type of motor has been chosen because it allows the rotor to be installed in vacuum while the stator remains outside vacuum. In the typical air gap between rotor and stator is located the vacuum barrier, which is a very thin cylindrical shell made from stainless steel. As in a standard motor, the rotor is driven by the rotating magnetic field generated by the stator. The advantage of this configuration is that the rotor (already in vacuum) is connected directly to the shaft. Therefore no mechanical transmission is required, thus avoiding elements which are fatigue-prone.

6.1.2. Shaft

The shaft is the element driving the rotational motion of the system. The rotation torque delivered by the actuator is transmitted to the shaft by the rotor, and provokes its rotation as well as that of all the elements mounted on it.

The following elements are directly mounted on the shaft:

- resolver
- magnetic restrain system
- the motor rotor
- the two fork arms (mechanically bonded to the shaft)
- the optical encoder disk

The shaft is supported in two opposite vacuum compatible ball bearings.

6.1.3. Fork

In the new design, the concept of the fork consists of a fork which is rigid in both directions (longitudinal and transversal). The PS scanner fork could be considered rigid in the transversal direction but it showed flexibility in the longitudinal direction (because of the flexible hinges). As already mentioned, the flexible hinges of the PS fork maintain the tension of the carbon wire and also provide a constant and homogeneous tension during the scan process. However, the measurements and the dynamic models show that this longitudinal flexibility on the fork tips may enhance the transversal vibration amplitude of the wire. Therefore, for the new design it has been decided to use a fork concept which is also rigid in the wire longitudinal direction. Consequently, the wire tension is guaranteed only by the wire elasticity and the initial preload tension applied at the first mounting. It is expected that this initial preload and the elasticity of the wire will be enough to absorb the potential deformation of the fork over time. This deformation would induce wire tension variations which (in case of a tension drop) would yield an increase in the wire deflection amplitude.

6.1.4. Wire

Even though the fork assembly (a wire or cable fixed on the two fork tips) and the wire material (Carbon) are very similar to the existing design, all the studies presented in the previous chapters can be used to define the best wire-fork assembly configuration.

Type of wire

Nowadays, CERN wire scanners are equipped with two different types of wires: 34um diameter single carbon wires and multi strand carbon wires made of 12 twisted fibers each 7um in diameter. The strength of the multi-strand carbon wire is higher than that of the single wire. Several tests to compare performances of these two wires are planned during the commissioning of the new wire scanner. These tests are intended to evaluate which wire has the best performance with respect to parameters such as initial wire tension, deflection and vibration amplitudes, breaking probability and ageing.

Fixation system

In the PS wire fixation system, the wire is not mechanically fixed to the fork, but is fixed by soldering to the copper sleeve. However, the copper sleeve can move axially on the ceramic isolator, which in turn can move axially on its housing on the fork tip (Figure 5.9). Therefore, the wire tension can be affected by the stiffness of the electrical cable. To avoid this source of uncertainty (which could cause unpredictable wire tension variation and even unexpected breakages), the wire fixation system for the new design mechanically links the wire to the fork.

A suitable brazing will be applied between the ceramic isolator and the fork, as well as between the copper sleeve and the ceramic isolator (see Figure 6.2). Thus, the extremities of the carbon wire will be properly bonded to the fork tips but electrically isolated.

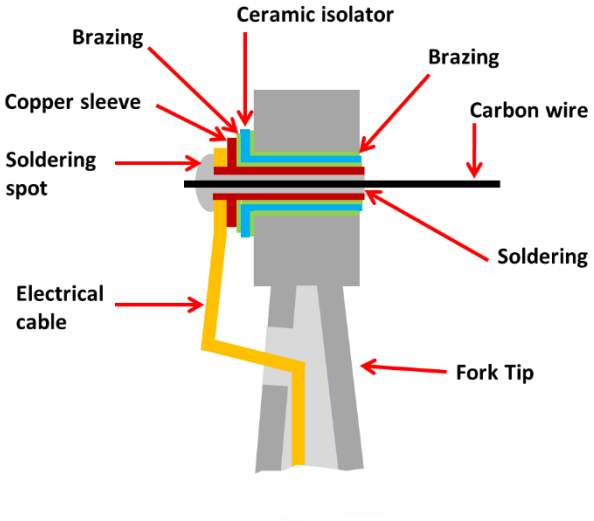

Figure 6.2: Wire fixation system concept.

Wire initial tension

The initial wire tension should be such that deflection and vibrations are minimized, while not causing an early breakage of the wire.

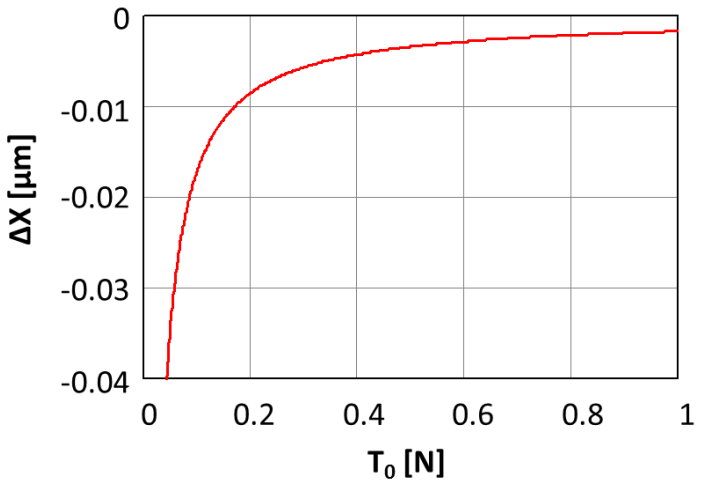

Figure 6.3: Central wire deflection versus tension for a fixed acceleration value of 1560 m/s^2.

As an example of the influence of the initial wire tension on the wire deflection, Figure 6.3 shows the central sag for a 34um diameter carbon wire, spanning 115 mm, supported in two fixed points under a constant acceleration field of 1560 m/s^2, for different values of the initial tension. The plot shows that the higher the initial tension, the lower the wire central deflection. An interesting feature is that the deflection amplitude on the initial tension is highly nonlinear: the amplitude variation with respect to the initial

tension variation is lower for higher values of tension. Depending on the strength of the wire to be used, the value of the initial tension should be optimized according to this criterion. For the particular case of the 34 um carbon wire, it has been found experimentally that its breaking force is between 0.3 N and 0.5 N.

6.1.5. Angular sensor

The angular sensor is the element which serves to determine the angular position of the shaft and therefore the absolute position of the fork. This information is required to perform the beam profile reconstruction (see in the introduction chapter the functional description of the wire scanner). Moreover, the information provided by the angular sensor is needed to feedback the control system in order that the scan follows the suitable motion pattern. In the new design, the function of this angular sensor is achieved by means of two independent angular sensors, a solid rotor resolver for the motor feedback loop and an optical encoder for the beam projection reconstruction.

Resolver (motor feedback)

This device measures the absolute angular position of the shaft and provides this information to the feedback control loop.

This device is relatively robust and provides angular absolute position without having to go to a home position, i.e., it provides continuous absolute angular position. The resolver device consists of a solid rotor without windings fixed to the shaft and therefore under vacuum. The stator is located on the air side. As in the actuator, a very thin cylindrical shell made of high magnetic permeability stainless steel allows this configuration.

Although the accuracy of this device is relatively low (17 mrad), it shows a high reproducibility, which allows to improve the accuracy by means of a calibration procedure.

Optical disk

This part of the angular sensor is based in the incremental angle optical encoder technology and consists of a glass disk with a pattern made of high reflectivity chrome directly mounted on the shaft. An optical fiber drives the light from a laser diode to the optical disk. Using the reflectivity of the chrome pattern, the reflected light is coupled back into the same fiber, and directed to a photodiode through an optical circulator. After proper calibration, this sensor provides a resolution in the range of the requirements, i.e. 2.8 μm at the fork tip.

6.1.6. Magnetic restrain system

The new conceptual design does not integrate any kind of mechanical link between the rotating parts and any other element that could block the unwanted rotation of the shaft. Bearing friction would not be enough to restrict the rotational momentum produced by the unbalanced weight of the fork. The only way to guarantie the grip of the shaft would be by means of the holding torque provided by the stator. However, in case of an electrical failure (the stator would be unpowered), the shaft could eventually rotate out of control. That situation could bring the wire in front of the beam causing the wire melting or, in the worst case, beam losses that could oblige to dump (or stop) the beam.

The conceptual design of the magnetic restraint system, show in Figure 6.4, consists on a dipolar magnetic field generated by a permanent magnet, a magnetic frame or yoke located outside the vacuum, and a ferromagnetic piece fixed to the shaft. The magnetic field (circuit) thus produced guaranties a resistive torque which avoids unwanted rotations. This resistive torque is very low compared to the torque that can be provided by the motor, therefore this magnetic restriction cannot stop the rotation of the shaft under the action of the motor.

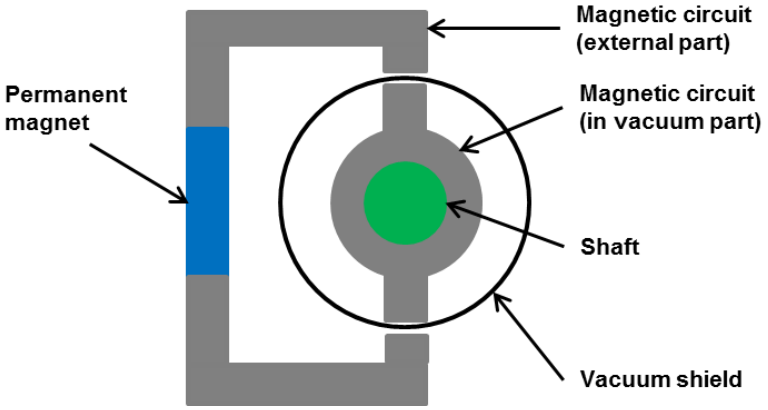

Figure 6.4: Illustration of the magnetic restrain system.

6.2. Sources of errors: review

This section presents a qualitative review of the sources of error, already defined in the first part of Chapter 3, for the case of the new design.

6.2.1. Measurement chain

As already discussed above, even if the components of the mechanical assembly of the new system (wire, fork, shaft, angular position sensor) are the same as in the past, the design has been significantly simplified. The angular position sensor is now located on the same mechanical shaft as the fork and the actuator, consequently the measurement position is not affected by any mechanical play. Therefore, the impact on the error due to the mechanical chain is only related to the deflections and vibrations of the parts of this chain. Thus, minimization of the error due to the measurement chain consists of the minimization of deflections and vibrations of its component parts.

6.2.2. Misalignment errors

The misalignment errors affecting the new conceptual design can be reduced to:

- Differential misalignment between arms
- Angular sensor misalignment

The concept of the new design may show this type of errors as it is made of different parts which can have manufacturing errors or misalignment between them during the mounting process.

The minimization of these errors can be achieved by adjusting the manufacturing tolerances and conceiving a design which minimizes these potential mounting errors.

6.2.3. Mechanical play

As has been already mentioned, the mechanical play has been eliminated in the new design. Therefore this error source does not have any impact on the new design.

6.2.4. Deflections

The measurement chain of the new conceptual design will also be affected by the deflection of its different components caused by the inertial forces, i.e., the shaft twist, the forks bending and the sag of the carbon wire. The minimization of the error due to these deflections can typically be achieved by minimizing mass and increasing stiffness in the design.

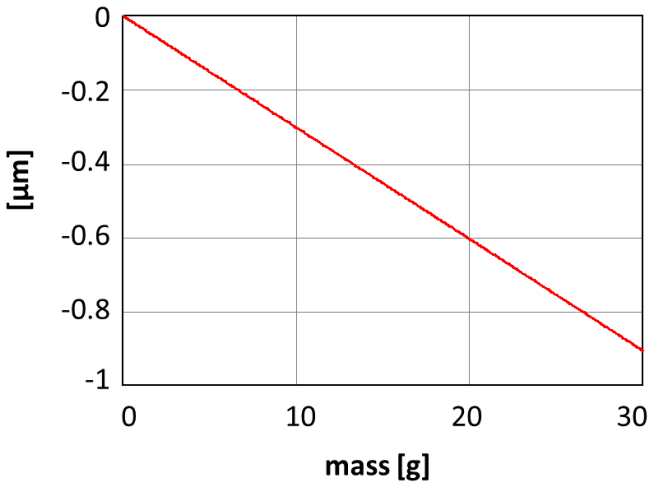

Figure 6.5: Central wire deflection versus wire mass for a fixed acceleration value of 1560 m/s^2 and initial tension T_0 = 0.3 N.

The minimization of the wire sag can be achieved through the increase of the initial stretching tension. The limiting factor which determines the maximum wire initial tension is the wire breaking force. In principle thicker wires show larger breaking forces and therefore can be stretched under a bigger initial tension. However, the thicker the wire, the larger its mass and therefore its sag. Figure 6.5 shows different values of wire sag as a function of the wire mass for the same initial tension and the same constant acceleration field.

6.2.5. Vibrations

From the conceptual point of view, the error due to vibrations is minimized because of the simplification of the measurement chain. The higher simplicity of the measurement chain reduces the number of components which may vibrate. However, the vibrations of the measurement chain components remains a major issue of the new design. Minimization of error produced by the vibrations has not been totally

removed by the new conceptual design and relies in the design optimization of the measurement chain components.

6.2.6. Uncertainty of the particular zone of the wire intersecting the beam

This kind of uncertainty also appears on the new wire scanner concept. As already explained in Chapter 3, this uncertainty is due to the fact that the position where along the wire the beam intersects is unknown. This means that something that would be considered as a systematic error becomes a statistical error. The minimization of this source of error relies on the minimization of the deflection errors.

6.2.7. Error of measured beam width due to error of the detected angle

As has been shown in eq. (3.13), the error on the beam projection is related to the beam position determination and to the beam width measurement. These two errors are related to the measurement chain. Therefore, the minimization of the error on the beam projection is directly related to the accuracy of the measurement chain.

6.2.8. Error due to the wire orientation error

The source of this error is the wrong wire orientation relative to the plane perpendicular to the beam projection. Therefore, this error is affected by the shaft orientation and the potential shaft twist which would provoke an offset between the two fork tips and the consequent wire orientation error. This source of error has not been eliminated at the conceptual level, however the shaft design optimization has contributed to the minimization of this error, see Section 6.4.1.

Conclusion:

After this analysis of the error sources, it can be concluded that the conceptual design for the new wire scanner eliminates the errors due to the mechanical play, but those associated with misalignment and deflections remain. Therefore, some optimization criteria have to be defined and applied to the design in order to minimize those error sources.

6.3. Design optimization

After discussing the conceptual design simplifications (see previous section) conceived to minimize or eliminate errors (e.g. elimination of mechanical plays), this section will cover the optimization of the mechanical components (that are unavoidably present) and their assembly and way of operation.

More in particular, this section will discuss the optimization of the following parts:

- Shaft
- Fork
- Wire
- Motion pattern

6.3.1. Optimization strategy for rotating parts

The general strategy applied in the design of the rotating parts of the measurement chain consists of minimizing the deflections produced by the inertial forces, thus reducing both errors due to deflections and errors due to vibrations.

This strategy basically results in maximizing the stiffness while minimizing the mass. Such an approach has in addition a positive side effect of increasing the natural frequencies of these elements. This allows larger variation on the motion pattern acceleration profile which finally results in the capability of the system to reach higher speed values with smaller angular travel.

Additionally, from the functionality point of view, the lower the inertia of rotating parts of the system, the lower the torque required from the actuator.

Shaft

The optimization of the shaft consists in enhancing its torsional stiffness and minimizing inertia of the shaft itself together with the rotating elements fixed to it. This results in a reduction of the shaft twist under the effect of the inertial forces.

Fork

The optimization of the fork is intended to minimize the tip deflections produced by the inertial forces by increasing the fork flexural stiffness and minimizing its mass. Minimizing fork mass also contributes to a reduction of the moment of inertia about the rotating axis and therefore minimizes the shaft torsion which in its turn induces an error.

As in the new design, the initial wire tension it is not guaranteed by the flexibility of the fork tip, as was the case in the PS scanner design maintaining the initial wire tension relies on the wire pre-elongation applied at the first installation. However, the stiffness and stability of the fork have to be guaranteed since small variations on the tip distance can reduce the initial wire tension and therefore increase the wire sag under the inertial forces.

Wire

The wire optimization consists in minimizing its mass and increasing its initial tension. However, this strategy has to be carefully implemented since in principle a mass decrease would also provoke a decrease of the wire strength.

The initial tension of the wire has to be such that the natural frequency of the wire is not close to some other natural frequencies of the fork, otherwise parametric oscillations of the wire could appear.

The design optimization criteria defined in this section of the work have been implemented in another work [51] and their results are shown in section 6.4 (New design performances).

Concerning the motion pattern optimization, a detailed strategy will be implemented for the motion pattern design and the commissioning of the system will be presented below.

6.3.2. Motion pattern

The second part of the design optimization strategy deals with the motion pattern optimization. The acceleration motion pattern has a direct impact on the deflections induced by the inertial forces, while the variation of the acceleration (jerk) has a direct impact on the production of vibrations and therefore on the wire position determination.

In the framework of this work, optimization can be defined as the selection of the set of parameters from different available options that, when introduced in the system, provides the best result for a given variable according to some criteria. These criteria are implemented by means of a cost function.

The goal of this section is to summarize the different topics related to the motion pattern optimization for the particular case of the wire scanner. To introduce the subject, the section covers also the basic description of the wire scanner control system and the discussion of different optimization strategies.

Moreover, this part of the work is intended to provide information in order to evaluate the feasibility of the integration of an automated optimization structure which could be launched at any time during the operation of the scanner. This would allow to identify and modify some of the predefined parameters that could become out of tune due to the ageing of the system or other environmental effects affecting the system.

6.3.2.1. Control system description

Before presenting the different optimization strategies, some comments on the wire scanner operation procedure, the predefined motion pattern and the control system are necessary.

The description of the control system designed for the wire scanner includes the following parts:

- Wire scanner operation procedure,
- Predefined motion pattern,
- Control system description.

Wire scanner operation procedure

The scan cycle is performed under demand when a beam profile measurement is required. The scan cycle consists of a rotational motion of the fork and wire, and can be divided into the following phases:

- Motion from OUT to IN,
- Waiting time at IN position,
- Motion from IN to OUT.

Motion from OUT to IN

This first phase of the cycle drives the wire from the OUT position to the IN position. This part requires an acceleration sub-phase followed by a deceleration one. Eventually a constant speed sub-phase can be included between the two (see figure Figure 6.6).

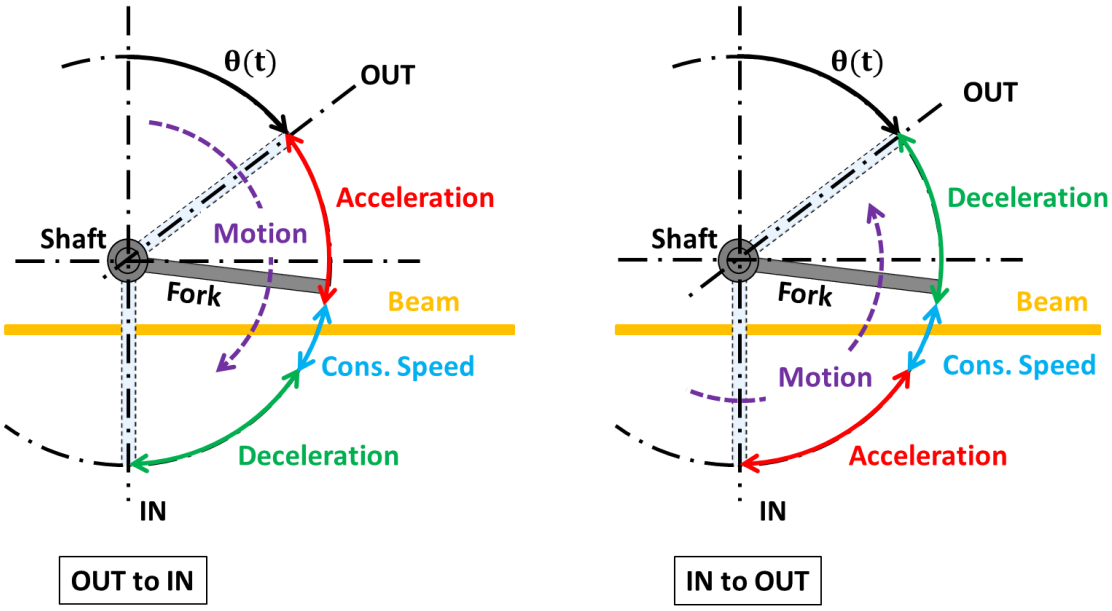

Figure 6.6: Phases of the motion cycle.

During this OUT-to-IN motion, the wire crosses the beam for the first time on the cycle. The main requirement for this phase is the speed of the wire at the moment of beam crossing, which must attain a minimum value in order to minimize the energy deposition on the wire which could otherwise melt it and in the case of LHC scanners minimize the number of secondary particles which could quench the magnets downstream of the scanner.

Waiting time at IN position

This phase consists in the holding of the fork and wire at the IN position during a certain time. The waiting time phase can be more or less long, and is required for synchronization purposes

Motion from IN to OUT

In the third phase of the scan cycle the wire and fork are brought from the IN to the OUT location following an equivalent motion schema to that of the OUT-to-IN phase (i.e, acceleration, constant speed and deceleration), though in opposite direction. During this IN-to-OUT motion phase the wire crosses a second time the beam (see Figure 6.6) with the main kinematic constrain on the wire speed.

Motion pattern

As the scan cycle remains constant from one scan to the other (i.e., every scan cycle has to follow the same motion pattern), a unique predefined motion pattern can be used as reference motion to be followed by the scanner actuator (motor). This predefined motion pattern determines the different positions that the actuator (motor) has to reach as a function of time (see Figure 6.7) in order to fulfil the scan cycle requirements.

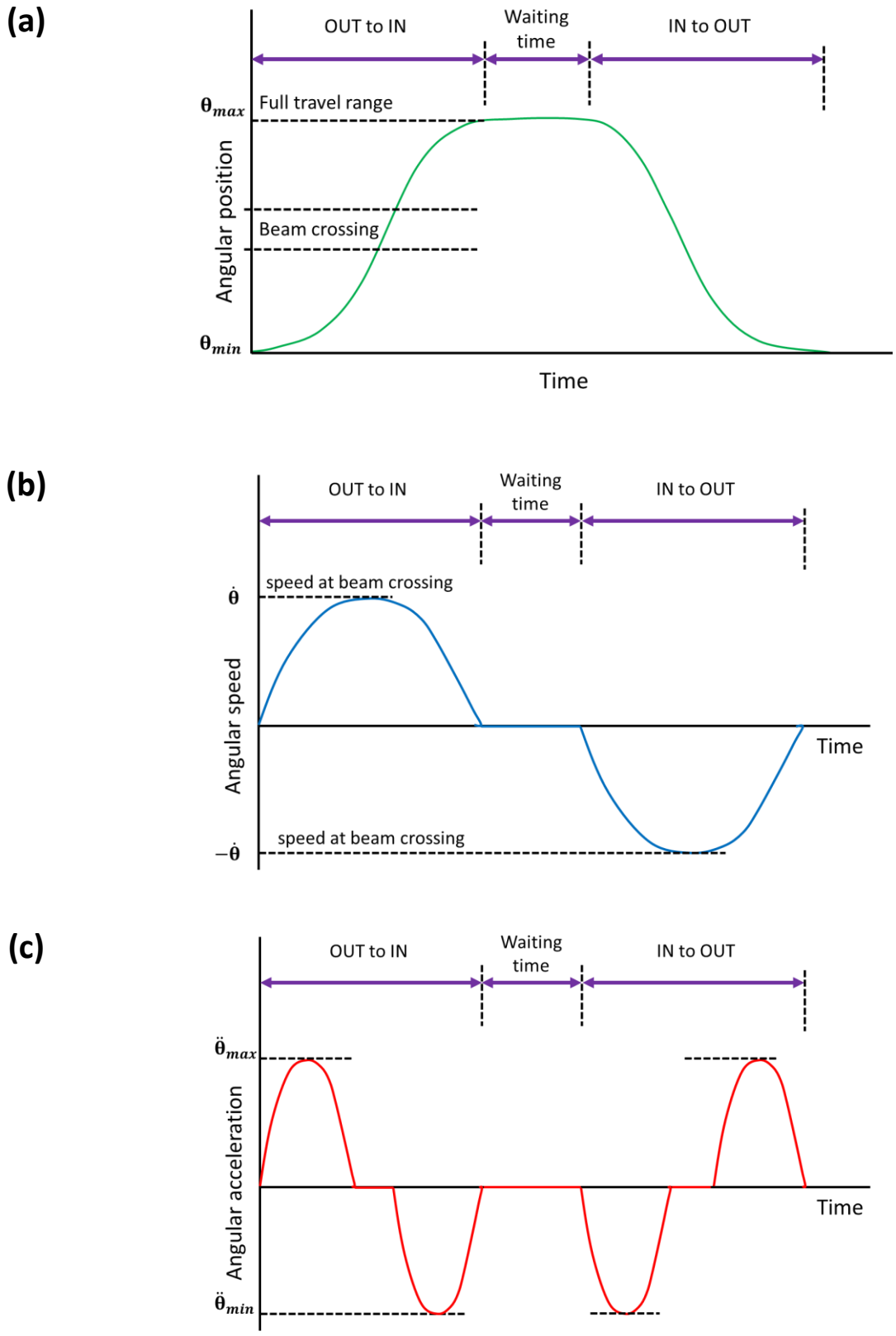

Figure 6.7: Typical motion pattern, (a) position, (b) speed and (c) acceleration vs. time for a full scan motion cycle.

The requirements to be considered in the design of the motion pattern concern:

- the full travel range,
- the beam crossing region,
- the wire speed at the beam crossing region,
- the maximum allowable acceleration.

Control system

A control system is required in order to guarantee that the actuator follows the predefined motion pattern. In the particular case of the new wire scanner, the system controls the motor current and consists in a cascade of 3 proportional-integral (PI) controllers. This triple closed loop control system (Figure 6.8) compares the measured values of position, speed and torque (the torque is proportional to the acceleration and to current) to the reference (input) values provided by the reference motion pattern. From that comparison, the right value of current to be provided to the motor at every time instant is determined. Position and speed are measured by means of a resolver, while the current value (used to determine the torque) is measured by means of a three Hall-effect transducer.

In each of the three control loops, the error between the actual measurement and the setpoint at every time instant is multiplied by a predefined gain factor, Kp (for the proportional part) and a factor Ki (for the integral part). Therefore, this control system requires 6 factors (a single Kp and a single Ki factor for each of the 3 controllers) to be predefined and also a suitable motion pattern. Hence, those gain factors and the motion patterns are the elements that can be modified in order to change the dynamic behaviour of the system and optimize its performance.

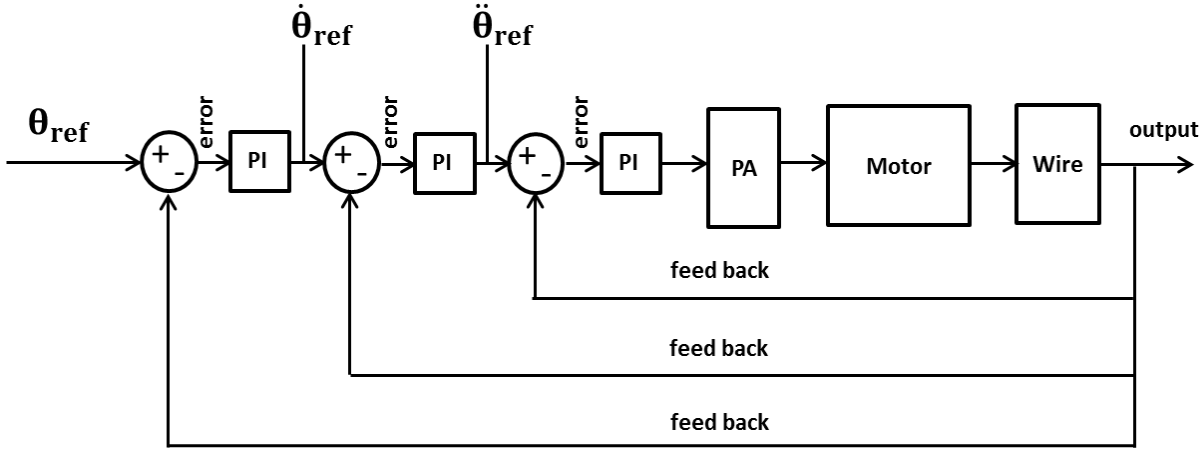

Figure 6.8: Control system schematics, PI stand for proportional integral controller, PA represents the power amplifier

6.3.2.2. Optimization strategies

Under the assumption that the mechanical parameters of the system have already been optimized at this stage of the work, the only parameters left to be optimized are those of the control system and those describing the motion pattern.

Different optimization strategies are presented in this section. The following topics will be described and commented:

- Optimization criteria
- System model
- Control system feedback loop
- Cost function definition
- Number of parameters

Optimization criteria

Two optimization criteria have been considered:

- Match the scan cycle requirements (in that case, the cost function does not take into account the vibrational behaviour of the wire).
- Minimize the tangential wire displacement on the beam crossing region (obviously the corresponding cost function does take into account the wire vibrations).

The main difference between these two approaches is that, in order to match the scan cycle requirements, an optimization procedure which does not take into account the wire model would be enough. However, in order to minimize the tangential wire displacement, the wire model has to be integrated as a part of the model of the system to be optimized.

System model

As already mentioned the full wire scanner system can be divided into the following subsystems:

- **The control system**, which includes the controller with the sensors, the power amplifier and the electrical part of the motor,
- **The motor or actuator**, which includes the mechanical rotating components of the system,
- **The wire**.

Depending on whether the sub-system used in the optimization process is a theoretical model or the real subsystem, the following configurations are possible:

- MODEL: in this configuration, the three sub-systems are theoretical models.
- HYBRID: in this case, the control system and the motor used in the optimization are real, while the wire is taken into account through a theoretical model.
- REAL: the three sub-systems are the real ones. This solution requires a vibration measurement system in order to determine the wire oscillations.

The following table (Table 6.1) summarizes those options.

Table 6.1: Different options according to the type of description considered in the optimization process.

Name	Control system	Motor (actuator)	Wire
MODEL	model	model	model
HYBRID	real	real	model
REAL	real	real	real

Control system feedback loop

As explained above, each of the three controllers needs the information about the actual value of the controlled parameter in order to compare it with the set (nominal) value and calculate the instantaneous error, which is used to calculate the suitable gain by means of the corresponding predefined gain factor.

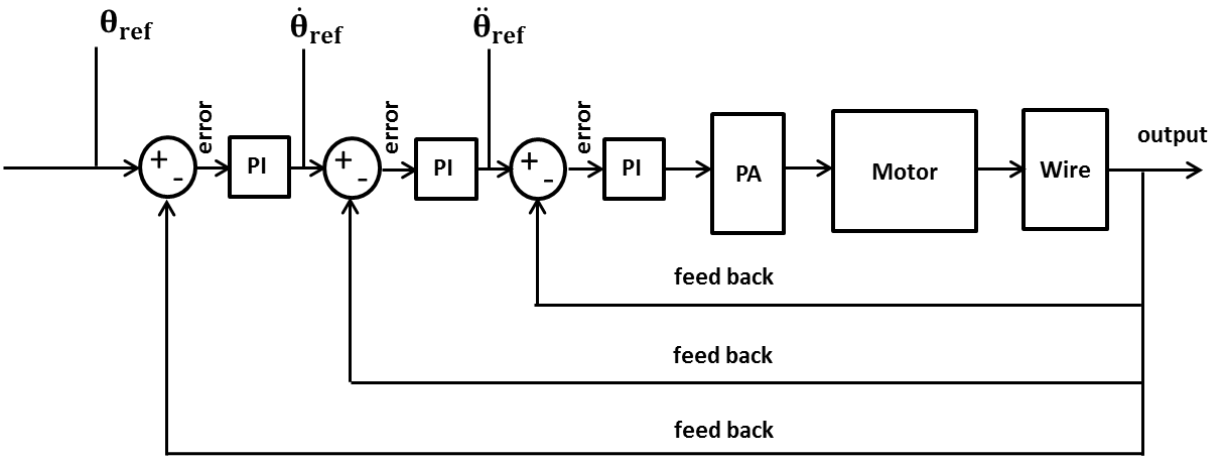

Figure 6.9: Control system schematics including the wire.

Figure 6.8 shows the schematic of a system whose last element is the motor. The wire is not included. Figure 6.9 shows the complete schematics of the system (including the wire).

As mentioned above, the predefined motion pattern is a function which defines the angular position of the motor shaft as function of the time (see Figure 6.7). In order to evaluate the error, this motion pattern has to be compared with the equivalent output value from the system.

There are two possibilities for the feedback of the control system:

- Use the output provided by the motor (“feedback from the motor”)
- Use the output related to the wire behaviour (“feedback from the wire”)

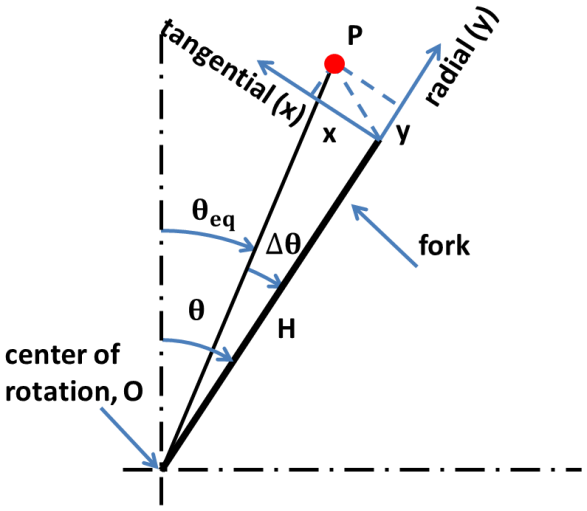

Figure 6.10: Schematic showing the equivalent angle θ_{eq}; P is the wire midpoint.

There is an important difference between these two approaches. In the first case, the input and output consist of the same physical quantity (either position or speed or acceleration). In the second case, the final output generated by the system, at the wire level, is a linear displacement (typically the wire transversal displacement) which is not directly comparable with the input (an angular parameter). Therefore an equivalent angular value from the transversal wire displacement has to be calculated in order to use the output generated from the wire in the feedback loop.

From Figure 6.10, the equivalent angle θ_{eq} can be calculated as follows:

$$\theta_{eq} = \theta - \Delta\theta, \tag{6.1}$$

where $\Delta\theta$ represents the difference between the actual instantaneous angle of the shaft and the angle defined by the line OP and the fork (Figure 6.10). This difference is related to the coordinates (x, y) of the wire midpoint, P, through

$$\Delta\theta = \operatorname{atan}\left(\frac{x}{H + y}\right). \tag{6.2}$$

Consequently,

$$\theta_{eq.} = \theta - \operatorname{atan}\left(\frac{x}{H + y}\right), \tag{6.3}$$

and

$$\dot{\theta}_{eq.} = \dot{\theta} - \frac{d}{dt}\left[\text{atan}(\frac{x}{H+y})\right], \tag{6.4}$$

and

$$\ddot{\theta}_{eq} = \ddot{\theta} - \frac{d^2}{dt^2}\left[\text{atan}(\frac{x}{H+y})\right]. \tag{6.5}$$

Therefore, this procedure allows to find an angular parameter (value) which take into account the wire dynamic behaviour to be compared with the predefined motion pattern.

Cost function definition

In any optimization process the cost function quantifies how good a given set of parameters is according to the optimization criteria. Two different cost functions have been considered in this study, each one associated with one optimization criterion defined above (control system feedback loop section):

- Integral absolute error (IAE)
- Maximum vibration amplitude (MDA)

Integral absolute cost function

The cost function is based on the integral absolute error (IAE) between the input motion pattern, and the output of the system (Figure 1.12).

The cost function (J) is calculated as follows:

$$J = IAE_{\theta} + IAE_{\dot{\theta}} + IAE_{\ddot{\theta}} \tag{6.6}$$

Where

$IAE_{\theta}, IAE_{\dot{\theta}}$ and $IAE_{\ddot{\theta}}$ are the integrate absolute errors for the angular position, speed and acceleration respectively.

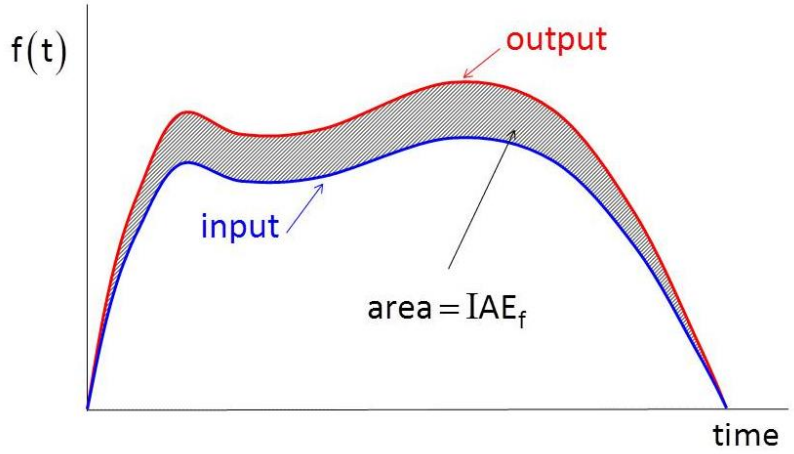

Figure 6.11: Illustration to define IAE, which is the absolute value of area between the input and the output functions. In the figure the generic function f(t) denotes the quantity used in the cost function.

The optimization goal is to minimize the cost function.

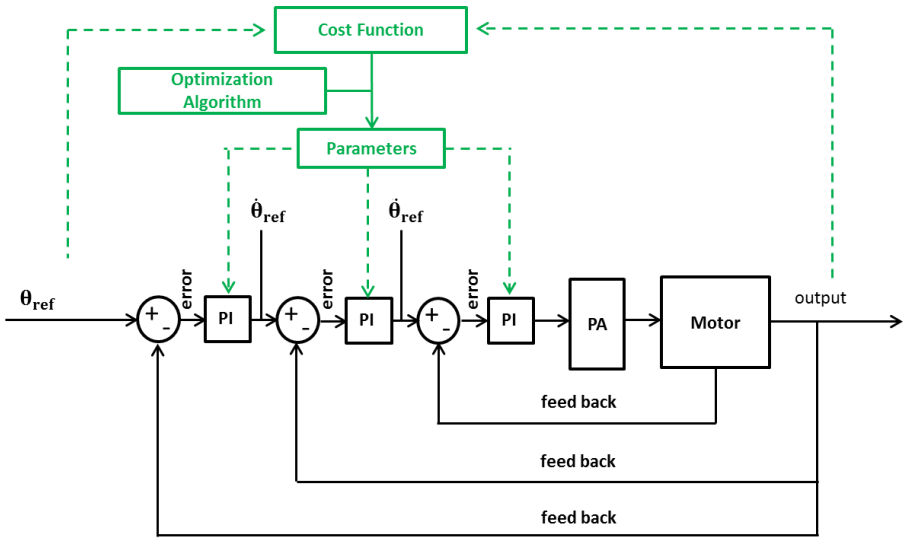

Figure 6.12: Control system schematics including the cost function loop (highlighted in green)

As for the case of the feedback there are two possibilities, depending on which output is used to evaluate the cost function:

- If the output is provided by the motor position sensor (angular position sensor), the corresponding cost function will be called “CF-M” (see Figure 6.12).
- If the output is related to the wire behaviour, the corresponding cost function will be called “CF-W” (see Figure 6.13).

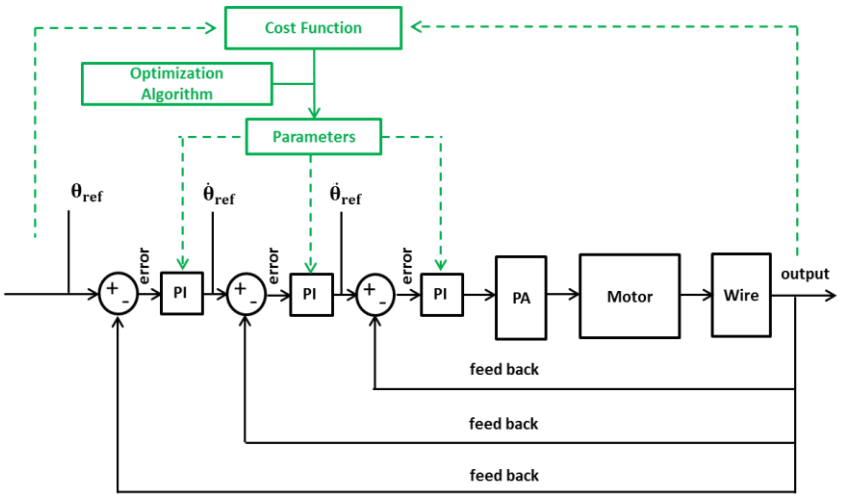

Figure 6.13: Control system schematics including the wire model and the cost function loop (highlighted in green)

Vibration amplitude approach

In this approach, the cost function is directly calculated from the amplitude of the wire oscillations:

$$J = |x_{max}]_b|, \tag{6.7}$$

where $|x_{max}]_b|$ stands for the maximum absolute value of wire tangential deflection in the beam crossing region.

Unlike the previous case, here the cost function is independent from the input of the system (Figure 6.14). Thus, only the output at the level of the wire model has to be used.

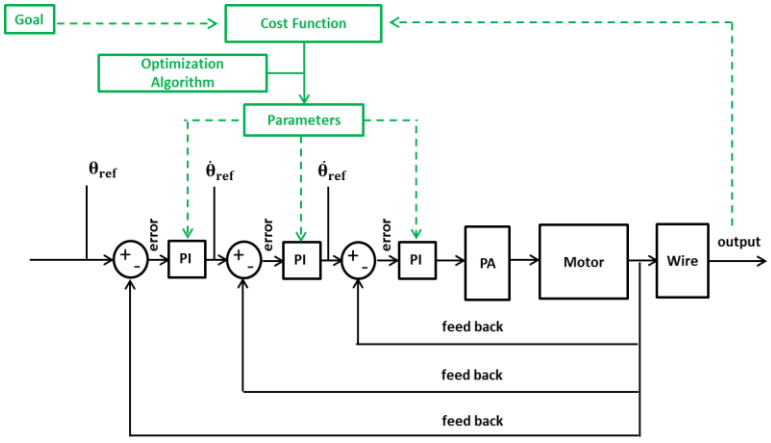

Figure 6.14: Control system schematics including the wire model; the cost function loop is highlighted in green.

Number of parameter

In the following the quantity of parameters to be included in the optimization is discussed. As explained above, the parameters which define the control system are the 6 gain factors. However, it is also possible to parameterize the predefined motion pattern in such a way that the motion pattern parameters can also be included in the optimization procedure.

Therefore there are two possibilities in the parameter definitions:

- Consider as optimization parameters only the 6 gains factors required by the controllers.
- Consider as optimization parameters the 6 gains plus an additional set of parameters which define the motion pattern.

The second option (which includes the parameterization of the motion pattern) brings the advantage that the resulting motion takes into account the influence of the elements of the system located between the reference pattern and the wire. It is also important to take into account that just the implementation of an optimal trajectory reference pattern on the control system, does not guarantee the optimal dynamic behaviour of the system, since the performances of the control system will also play a role in its final dynamic behaviour. Therefore the second option would bring the advantage that both, motion pattern and gain factors, are optimized at the same time, therefore the resulting motion pattern would integrate and correct the effects that the controller have in the final dynamic behaviour of the system.

Somehow this first option would be a sort of calibration of parameters intended to force the wire to follow a pattern which, is the most suitable for the requirements of the system. However in the second option the fact that the motion pattern is not fully predefined (a parameterized motion pattern is used) brings a potential improvement respect to a simple calibration as the final motion pattern takes into account the full characteristics of the system including the controller characteristics.

The number of parameters to be optimized does not increase as a result of including the dynamic model of the system in the optimization procedure. Just using the motor output in the optimization loop (Figure 6.12) or the dynamic model output (Figure 6.14) does not change the number of parameters to be optimized (i.e., the 6 gain factors required by the controller). This case would be a standard controller parameters tuning. However in case that a parameterizes motion pattern is included in the optimization procedure, the 6 parameters required by the controller will be increased by the number of parameters which are required to define the motion pattern.

Optimization strategies

In order to discuss the various optimization strategies, let's summarize the different options mentioned earlier.

- Concerning the model of the system there are 3 options -> MODEL, HYBRID and REAL
- Concerning the feedback for the controllers there are 2 options -> MOTOR and WIRE
- Concerning the cost function type there are 2 options -> IAE and MDV
- Concerning the cost function value there are 2 options -> CF-M and CF-W

- Concerning the optimization parameter there are 2 options -> GF (gain factors) and PP (parameterized pattern)
- Concerning the dynamic model to be use there are 2 options -> DISCRETE and CONTINUOUS

The following table (Table 6.2) summarizes all those options.

Table 6.2: Summary of the optimization strategies.

ELEMENT	**OPTION NAME**			**OPTIONS QTY.**
MODEL	MODEL	HYBRID	REAL	3
FEEDBACK	MOTOR	WIRE		2
CF TYPE	IAE	MDV		2
CF VALUE	CF-M	CF-W		2
PARAMETERS	GF	GF + PP		2
DYNAMIC M.	DISCRETE	CONTINUOUS		2

The combination of all these possibilities yields 96 potential optimization strategies. This is too high a number, of strategies to be implemented and compared, especially considering that each optimization strategy would have to optimize at minimum 6 parameters. Therefore a careful study of the optimization strategies is required in order to reduce de number of possibilities in an efficient way.

The following table shows a different arrangement of the optimization strategies organized by the type of dynamic model.

Table 6.3: Summary of the optimization strategies.

MODEL	MODEL		HYBRID		REAL	
FEEDBACK	MOTOR	WIRE	MOTOR	WIRE	MOTOR	WIRE
CF TYPE	IAE	MDV	IAE	MDV	IAE	MDV
CF VALUE	MOTOR	WIRE	MOTOR	WIRE	MOTOR	WIRE
PARAMETERS	GF	GF + PP	GF	GF + PP	GF	GF + PP
DYNAMIC M.	DISCRETE	CONTINUOUS	DISCRETE	CONTINUOUS	DISCRETE	CONTINUOUS

Some combinations are not possible at the present time (though they may be possible in the future), because any strategy based on the real wire behaviour (not the simulated one), as accurate measurements of tangential deflection of the real wire are still not possible.

Some justified options of simplification can be proposed:

- MODEL: at this moment the option REAL would not be implemented because some work is still needed in order to quantify the amplitude of the wire vibrations.
- FEEDBACK: the proposal is to base it only on the MOTOR as it is more realistic at this moment since, as mentioned before, it would not be possible to quantify properly the measures of wire vibration amplitude.
- CF TYPE: the proposal uses the IAE type and the feasibility to implement the cost function MDV is still under discussion, since the former is broadly used in optimization, and the implementation

of the latter would need some test in order to verify whether its implementation would be effective,

- CF VALUE: the cost function based on the wire, CF-W, is preferable since it is more sensitive to the error,
- PARAMETERS: the option GF (only the gain factors parameters) is avoided as the other option (GF + PP) includes both groups of parameters. However it would be interesting to have the possibility to perform both strategies in order to compare results.
- DYNAMIC MODEL: only the discrete model will be used in view of both (discrete and continuous) are qualitatively equivalent and discrete model implementation is simpler.

Table 6.4: Summary of the simplified optimization strategies; the eliminated options are crossed out.

ELEMENT	OPTIONS NAME			OPTIONS QTY.
MODEL	MODEL	HYBRID	~~REAL~~	2
FEEDBACK	MOTOR	~~WIRE~~		1
CF TYPE	IAE	MDV		2
CF VALUE	~~MOTOR~~	WIRE		1
PARAMETERS	~~GF~~	GF + PP		1
DYNAMIC M.	DISCRETE	~~CONTINUOUS~~		1

Therefore a total of 4 options remain after this simplification procedure (see Table 6.4). Further work could include some of the options which are not implemented in the present work, in particular the optimization based on the model REAL.

6.3.2.3.Motion pattern parametrization

In the following, a motion pattern parametrization approach based on a fourth order strategy inspired by the one described by Lambrechts P. [52] is shown. The motion pattern is defined by the derivative of the jerk, which is integrated four times in order to obtain the jerk, acceleration speed and position pattern.

Lambrechts's approach is intended to provide a motion pattern with low vibrations at the end of the trajectory. However in our case it is more important to minimize the vibrations at the end of the acceleration sub-phase. Therefore the second part of the motion pattern (the deceleration sub-phase) is less critical and its design can be simpler.

In order to build a full four order position pattern (Figure 6.15, left side), a total of 23 parameters are necessary: from t_1 to t_{15} to define the different time spans and from dj_1 to dj_8 to define the amplitude of the jerk derivative.

For the construction of the "simplified" four orders position pattern (only the acceleration sub-phase is based in a four order position pattern), the proposed simplified motion consists on (Figure 6.15, right side):

- a fourth order position pattern for the acceleration sub-phase,
- a first order position pattern for the constant speed sub-phase,
- a second order position pattern for the deceleration sub-phase.

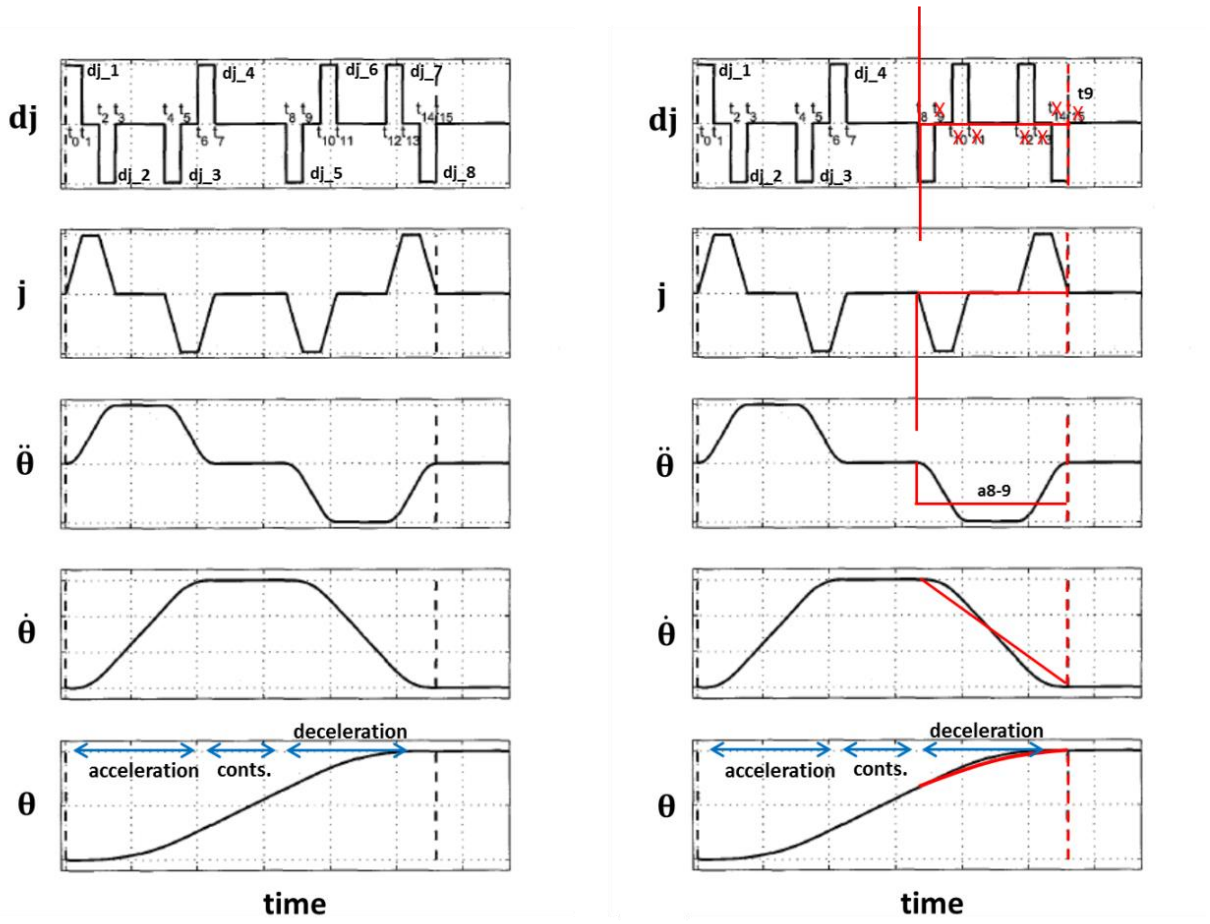

Figure 6.15: Fourth order position motion pattern (left); proposed simplification in red (right)

As the deceleration sub-phase consists on a lower order position pattern, the total number of parameters needed to build this simplified motion pattern are: 8 time steps parameters (from t_1 to t_8), 4 parameters to define the amplitude of the jerk derivative (from dj_1 to dj_4) and the parameter defining the constant acceleration value of the deceleration sub-phase ($\ddot{\theta}_{8-9}$); therefore a total of 13 parameters.

Additionally, the number of parameters can be reduced due to the constraints that have to be fulfilled by the motion pattern:

θ_a = acceleration angle [rad]

θ_c = constant speed angle [rad]

θ_d = deceleration angle [rad]

$\dot{\theta}_c$ = speed at θ_c [rad/s]

$\ddot{\theta}_{max}$ = maximum allowed acceleration [rad/s^2]

Imposing that the constant speed angle (θ_c) and the speed value in the constant speed region ($\dot{\theta}_c$) determine the time span at constant speed ($t_8 - t_7$) yields:

$$t_8 - t_7 = \frac{\dot{\theta}_c}{\theta_c} \tag{6.8}$$

Under the assumption that the maximum allowed acceleration is applied during the deceleration sub-phase,

$$\ddot{\theta}_{max} = -\ddot{\theta}_{8-9} \tag{6.9}$$

The value of the deceleration angle (θ_d), the speed value in the constant speed region (θ_c) and maximum allowed acceleration ($\ddot{\theta}_{max}$) determine the final time span ($t_9 - t_8$),

$$-\frac{1}{2}\ddot{\theta}_{max}(t_9 - t_8)^2 + \dot{\theta}_c(t_9 - t_8) = \theta_d \tag{6.10}$$

$$(t_9 - t_8) = \frac{-\dot{\theta}_c \pm \sqrt{\dot{\theta}_c{}^2 - 2\ddot{\theta}_{max}\theta_d}}{\ddot{\theta}_{max}} \tag{6.11}$$

Therefore the constraints determine 3 of the parameters of the motion pattern, and consequently the total number of parameters to define the motion pattern is reduced to 10.

For the remaining parameters, the constraints impose that

$$\iiint_0^{t7} dj(t)dt = \dot{\theta}_c \tag{6.12}$$

and,

$$\int \iiint_0^{t7} dj(t)dt = \theta_a \tag{6.13}$$

Indeed multiple set of parameters could match these criteria. However the optimization process select those which match the requirements (constraints) and minimize the cost function.

6.4. New design performances

This section provides an overview of the expected performances for the new wire scanner design (see Figure 6.16) regarding the measurement accuracy. The evaluation of the new design performances is based in the following:

- FE transient simulation of the fork-shaft assembly,
- modal analysis,
- control system behaviour,

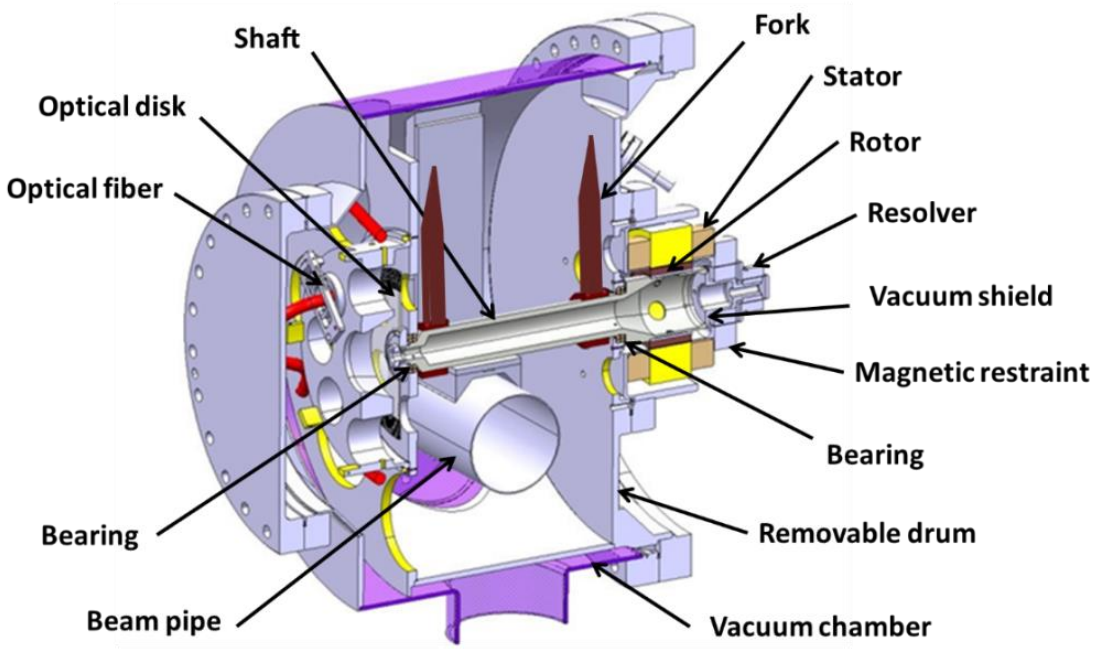

Figure 6.16 Digital mock-up of the new wire scanner.

6.4.1. FEA transient simulations results

The design and dimensioning optimization strategy defined in previous sections have been implemented [51]. Based on the results of this optimization process, it was possible to define in detail the new system mechanical design, as shown in Figure 6.16. In order to evaluate the dynamic behaviour of the rotating parts of this design, a dedicated FE transient simulation has been performed.

The simulation consisted in applying two different acceleration motion patterns to a model of the rotation part of the system (see Figure 6.17). Thus it was possible to evaluate the performances of the new device and compare its response under two different motion patterns (Figure 6.18).

The two motion patterns used in these transient simulations provide the same maximum angular speed and angular travel. The main difference between them lies on the variation of acceleration: the first one (Figure 6.18(a)) shows less smooth acceleration transitions, while the second one (Figure 6.18(b)) shows smoother acceleration transitions.

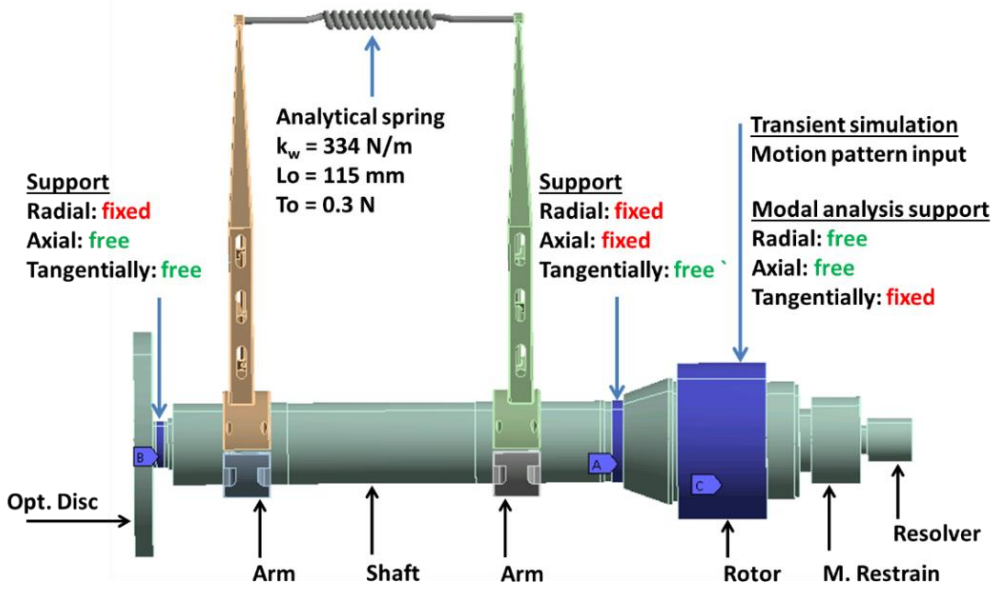

Figure 6.17: Boundary condition applied in the transient simulations and modal analysis.

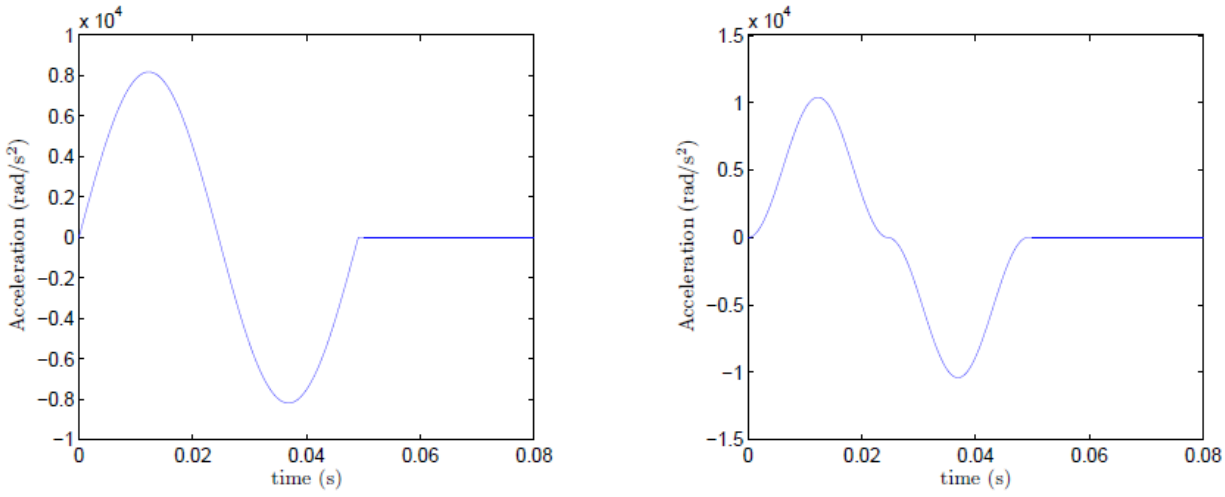

(a) less smooth (b) smoother

Figure 6.18: Acceleration profile for the two motion patterns used as input of the FE simulations.

Transversal tip deflection and transversal tip oscillation results are shown in Figure 6.19. The maximum tip deflection on the beam crossing region is around +/- 30 um using the less smooth motion pattern (Figure 6.19(a)) and around +/- 20 um for the smoother motion pattern (Figure 6.19(b)).

Concerning the tip oscillations, the results based in the smoother motion pattern clearly show lower tip oscillations.

Figure 6.20 shows the difference between the transversal deflection of the two tips, which are directly related to the wire orientation with respect to the beam. Considering that the distance between the tips is 115 mm, this wire orientation error (defined in section 3.1.8) would be in the worst case (for the less smooth motion pattern) in the range of 8.5 µrad, which is a very low value. The transversal tip deflection differences shown in Figure 6.20(a) display a ripple behaviour with a frequency of 900 Hz. This frequency could match one of the natural frequencies of the system (see bellow). Because of the more gentle transition shown by the smoother motion pattern, this ripple behaviour does not appear in the transversal tip deflection difference when using the smoother motion pattern Figure 6.20(b).

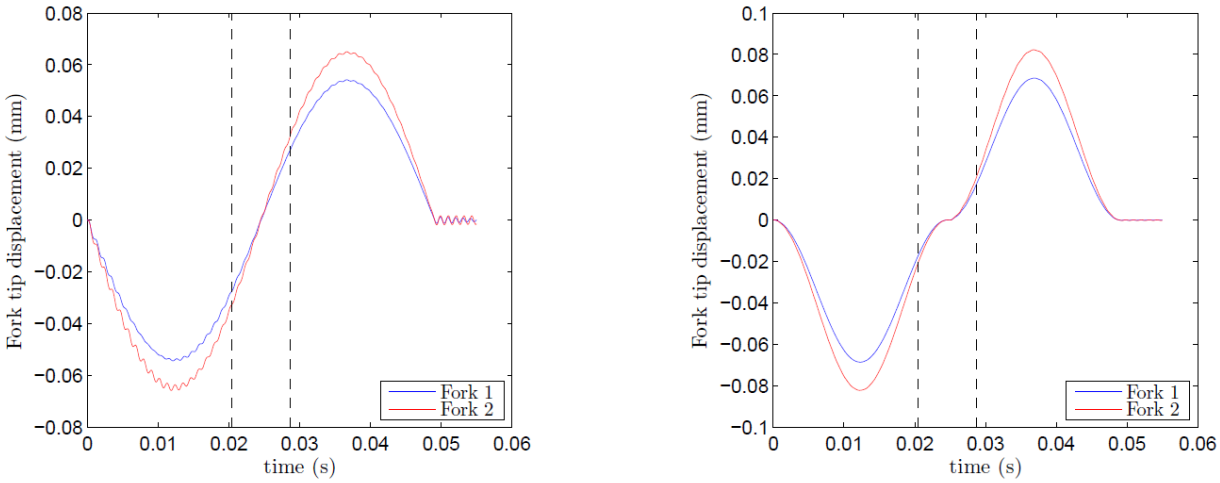

(a) less smooth (b) smoother

Figure 6.19: Fork tip transversal deflection result under the two motion patterns shown in Figure 6.18. Beam crossing region is indicated by two dotted vertical lines [51].

Besides the evaluation of the dynamic behaviour of the system, the results of this simulation show that the motion pattern has an important influence on the fork tip deflections. The motion pattern shown in Figure 6.18(b) has smoother acceleration transition and therefore the tip oscillations are much lower than using the motion pattern shown in Figure 6.18(a). However, because of the smoother transitions, larger peak acceleration values are required, which result in large tip defections. The maximum deflection with the smoother motion pattern is 80 µm while with the less smooth is only 60 µm.

Although the peak acceleration is higher in the smoother patterns, they are preferable since they generate fewer oscillations. In principle, oscillations become part of the statistical error of the system and therefore their correction is difficult. Conversely the deflection induced by the peak accelerations falls within systematic errors and its correction can be performed by mean of calibration processes as this error is highly repetitive.

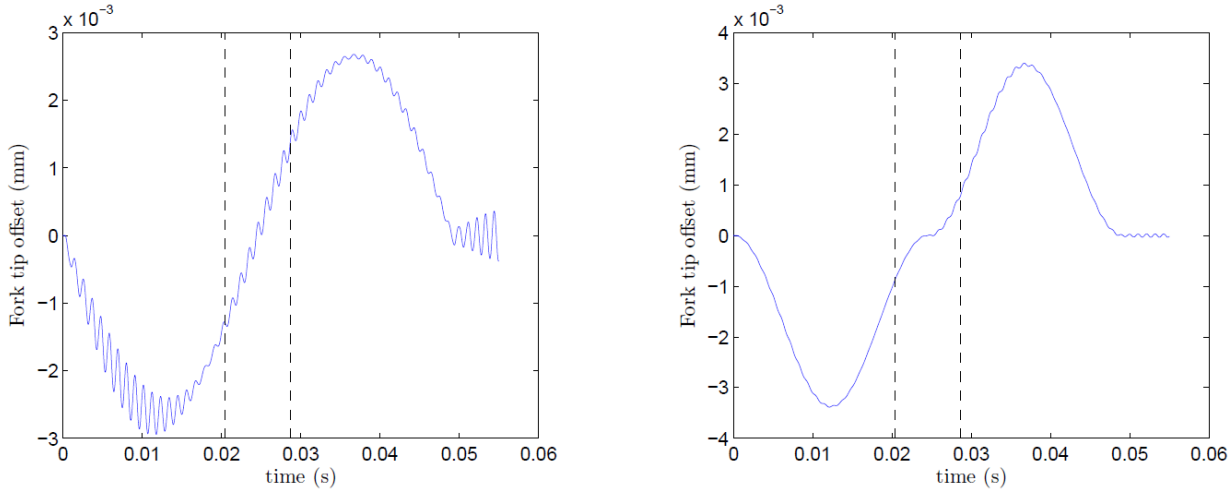

Figure 6.20: Transversal tip deflection difference [51].

6.4.2. Modal analysis

A FE modal analysis of the shaft-fork assembly has been performed. The boundary conditions are shown in Figure 6.17, and the first six modes resulting from the analysis are shown in Figure 6.21.

These results allow to evaluate the potential performance of the system under different motion patterns. Larger natural frequencies of the system grant less restrictive motion patterns because larger acceleration variations on the motion pattern would not excite the system. This modal analysis also provides information about what would be the most suitable wire initial tension in order to avoid wire parametric resonances.

The first mode consists on a symmetric mode of the two fork tips in the same Z direction (SZ) with a frequency of 371 Hz. In principle, this mode would not be excited by the motion, which consists on angular rotation, while the mode consists in deflection along Z direction. This mode would not affect the wire length as the distance between the tips remains constant and the mode does not include transversal oscillations.

The second mode consists on the shaft for which both arms rotate in a symmetric direction (ST) with a frequency of 855 Hz. This mode would cause both elongation and transversal oscillation of the wire, and can be triggered by a motion pattern including such frequency.

The third model could be defined as an antisymmetric mode is Z direction (AZ) with a frequency of 872 Hz. This mode would only cause wire longitudinal elongations and is not expected to appear as consequence of the rotational motion of the system.

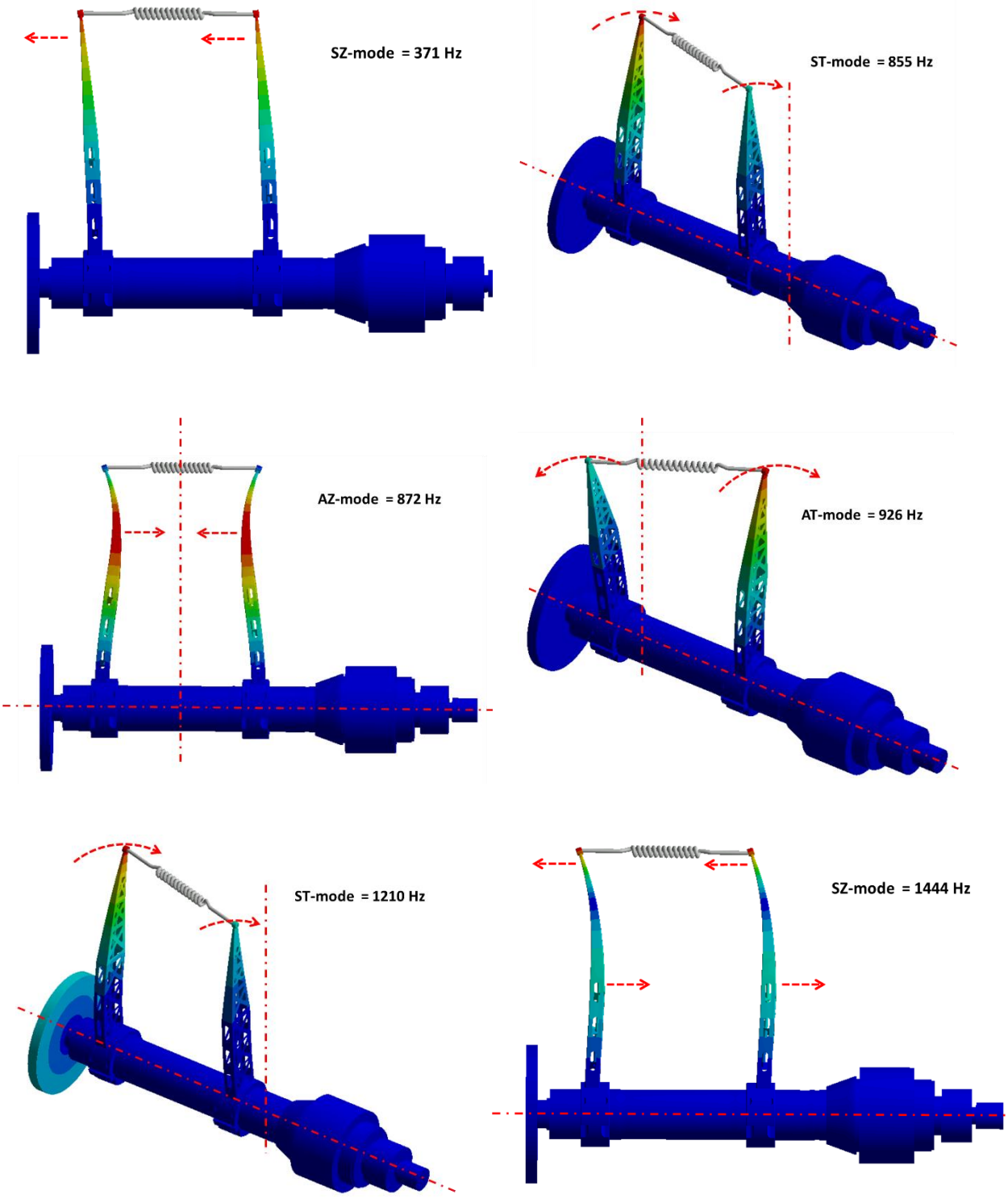

Figure 6.21: First six modes of the shaft-fork assembly.

The fourth mode can be defined as antisymmetric twist of the shaft (AT) as the fork arms rotate in opposite directions at 926 Hz. This mode would only cause wire oscillating elongations and can be triggered by the motion pattern.

The fifth mode is again a symmetric twist of the shaft (ST) with a frequency of 1210 Hz. Therefore this mode would cause elongation and transversal deflections of the wire, and can also be triggered by the motion pattern.

The sixth mode is a symmetric mode in Z direction, its frequency is 1444 Hz. Like the first SZ mode, this mode would no cause wire elongations.

Unlike the PS scanner, where the AZ-mode and SZ-mode could be easily excited due to the large flexibility of the fork tips in this direction, in the new design it is not expected to excite Z-modes because of the greater rigidity of the fork and the good cylindricity and stiffness of the shaft. The modes consisting on shaft twist that could cause also wire parametric resonances are relatively high, allowing to use a wire initial tension high enough to minimize the wire transversal deflections and oscillations.

Table 6.5 summarizes the six first modes of the new wire scanner. The modes that could be triggered by the rotational motion of the system are underlined.

Because of the different transversal amplitude between the two tips the frequency shaft torsional frequencies either symmetric or antisymmetric have the same effect on the wire, i.e., each single oscillation cause that the wire stretches or shrinks twice.

Table 6.5: first six modes of the system.

Mode	Description	Frequency [Hz]
1	SZ	371
2	ST	855
3	AZ	872
4	AT	926
5	ST	1210
6	SZ	1444

6.4.3. Control system behaviour

The evolution of the performances of the control system along the different modelling steps has been compared in [53]. One of the strategies used in these comparisons is based on the discrete dynamic model presented in Chapter 5. The parameters of the dynamic model have been modified in order to represent a rigid fork, as foreseen in the new design.

The procedure consisted in applying an identical predefined motion pattern as input on the four modelling steps of the control system (see Figure 6.22). The effective angular motion pattern resulting from each model has been used as input in the wire dynamic model. The dynamic model provides the dynamic behaviour of the wire central point. The results are shown in Figure 6.23. The comparison of the four plots allows performing a qualitative evaluation of the modelling steps performances. Simulink and Modelsim

models show an important vibrational behaviour of the wire, especially on the central region of the motion. The FPGA model also shows a vibrational behaviour, even if the oscillation amplitude is noticeably lower. This enhanced behaviour shown by the FPGA would be due to the filtering effect that the real system inertia plays on it dynamic behaviour. DSpace model shows a similar behaviour to the latter, but it is much more unstable as evidenced by the different amplitude peaks.

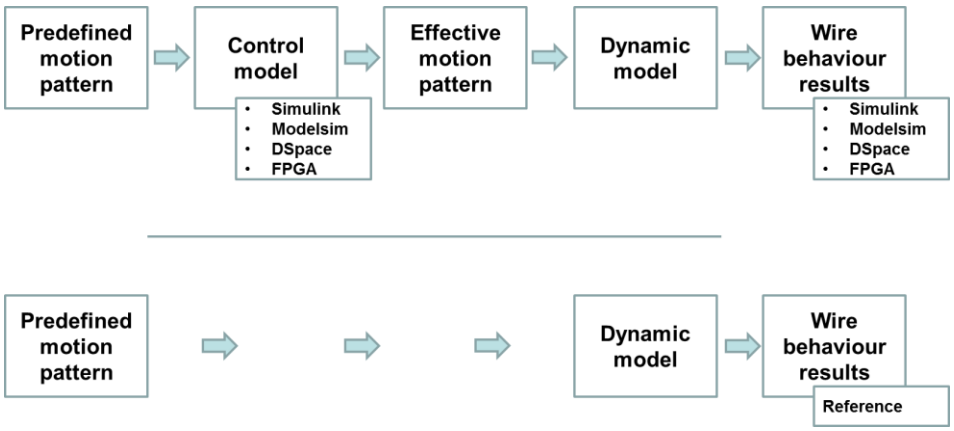

Figure 6.22: Schematic of the control system evaluation

The plot named as “reference” in Figure 6.23 results from directly applying the motion pattern to the dynamic model. The qualitative comparison among the result of each different modelling step and the reference plot evidences the influence of the control system which worsens the wire dynamic behaviour for a given motion pattern.

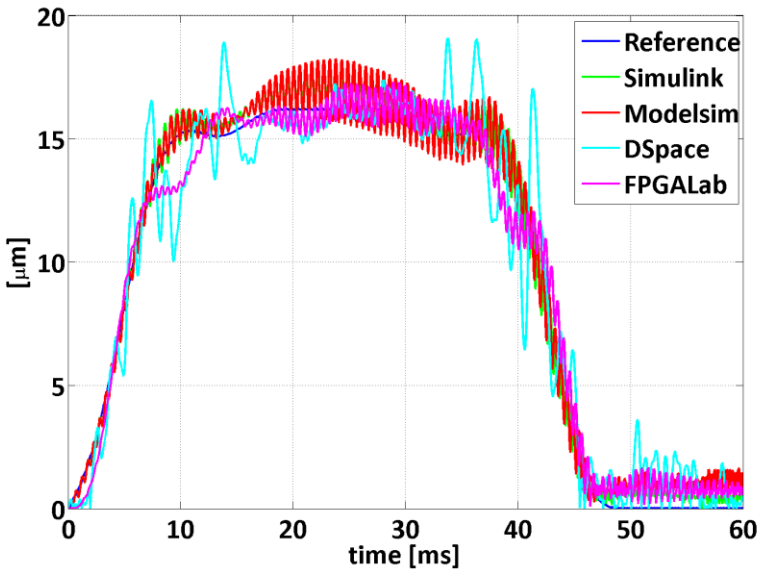

Figure 6.23: Maximum wire central point displacement.

6.5. Calibration test bench design proposal

Besides the performance improvements achieved through the conceptual design and the design optimization of some critical parts of the system, a calibration process is still needed in order to minimize systematic errors of the system. The typical systematic errors are the repetitive ones due to deflections or misalignment of the elements of the measurement chain. Calibration also allows improving the performances of the angular sensors since these components have a very good repeatability. Based on these arguments, a conceptual design of a calibration test bench is shown in this section.

As explained before, the final goal of the wire scanner instrument is to determine the beam profile projection (width and position) from the angular sensor signals. Therefore it is desirable that the calibration system provides the information to improve the correlation between the angular signal provided by the angular sensor and the effective projection of the wire in the beam perpendicular plane.

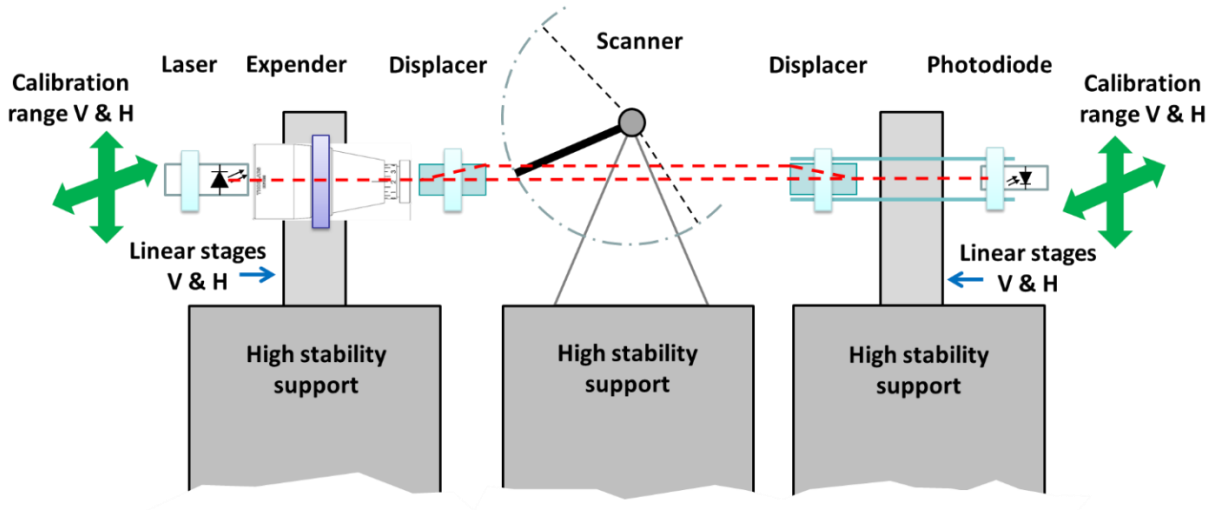

Figure 6.24: Illustration of the calibration system proposal.

The calibration test bench concept, shown in Figure 6.24, consists of 3 independent high stability supports. The scanner to be calibrated is installed on the central support. The other 2 supports are equipped, in the upper part, with a set of two orthogonal precision linear stages. One linear stage set, supports a laser while the other one supports a diode. Laser and diode are perfectly aligned, and their linear stages can move in a synchronized manner. The independent high stability supports guarantee that the motion of the scanner does not induce displacements or vibrations either on the laser or the diode.

When a scan motion is performed, the photodiode detects the time instant at which the wire crosses the laser beam since a signal variation occurs. The calibration process consists on positioning laser and diode on different vertical (V) and horizontal (H) positions. For each single position V, H, a scan is performed;

the signal variation seen by the diode is used as a trigger to record the signal of the angular sensors. V and H values plus the angular sensor signal are recorded in order to generate a table with the following values:

- Laser/diode position V & H
- Resolver signal
- Optical disk signal

The travel range for V and H has to be determined depending on where the calibrated scanner will operate. Scanners operating on wide or off-centered beams require larger calibration ranges than scanners operating in regions of the machine where the beam is smaller and well centered on the beam pipe.

The resulting calibration table can then be loaded in the scanner operational software to determine the wire projected position as function of the angular sensor signal. The wire position combined to the photomultiplier signal allows reconstruction the transverse beam profile.

6.6. Correction factors proposal

In addition to the calibration table discussed above, other correction factors and strategies can be implemented based on the gained experience with the test on the existing devices, the vibration measurement and the dynamic models.

This includes two kinds of approaches:

- improving the measurement data by means of suitable post-processing.
- providing information about the system dynamic behaviour to be used in order to adjust critical operating parameters.

System status monitoring

When properly implemented on the new device, the system to measure the wire vibration behaviour based on the piezoresistive effect of the wire itself (shown in chapter 4) can provide valuable information about the device vibrational behaviour. This information can be combined with the profile measurement in order to apply suitable experimental correction factors to the measurement. Additionally, monitoring the wire vibrations along the scanner lifetime allows evaluating the aging of the system (especially wire, fork and bearings) and preventing unexpected failures. Vibration monitoring would also serve as an indicator to modify initial motion pattern parameters according to the wear or aging of the system and therefore minimize the wire position uncertainty. Moreover, any unexpected change on the wire configuration (like a tension variation) would be easily detected and corrective actions could be applied.

Wire frequency monitoring

It is expected that, along the time, the aging of the system modifies some critical parameters as the wire mass and the wire initial tension. As these parameters affect directly the wire dynamic behaviour (for example the wire vibration amplitude), it is important to know them along the scanner operation lifetime.

This would enable the possibility to apply the optimal operating condition and correction factors at each given time.

The procedure to measure the wire tension could consist on exciting the wire by means of an abrupt motion (abrupt motion pattern acceleration variation) similar to a step function. A FFT analysis of the resulting wire vibrations would serve to determine the wire natural frequency. This information could then be compared with previous values in order determine whether the wire mass or its initial tension have changed.

This procedure has been validated by experimental measurements. An elastic element has been installed between the two arms to simulate a variation of the wire tension (see Figure 6.25 left). The position of the elastic element has been changed from the bottom part of the fork towards the tips. As the elastic element tends to generate an inward deformation of the fork tips, the closer the elastic element to the tips, the higher wire tension decrease. The shaft has been shaken and the wire vibrations recorded for each position of the elastic element.

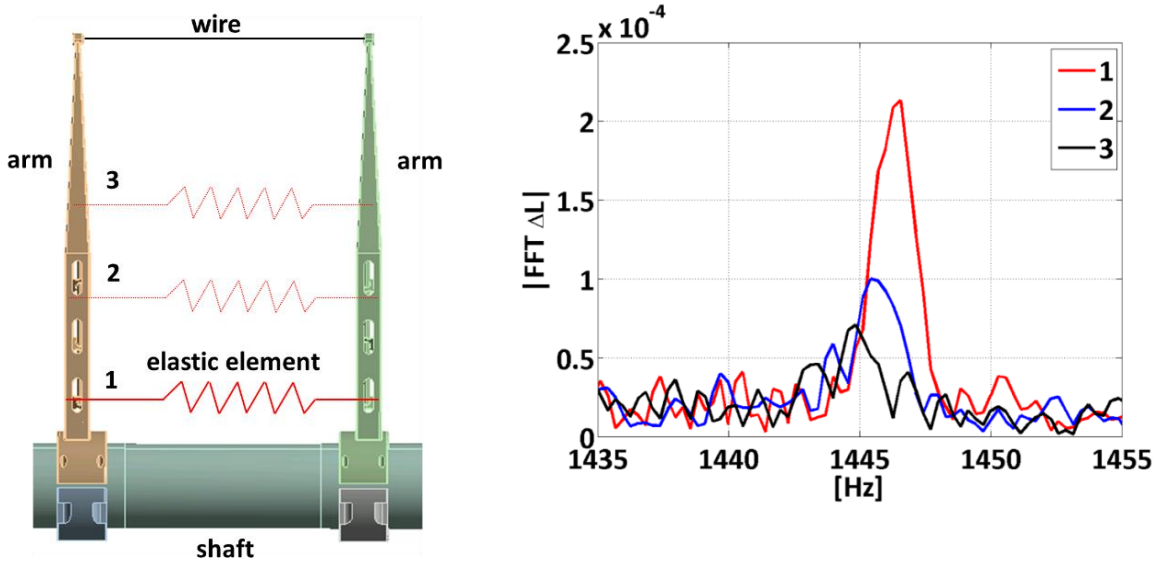

Figure 6.25: Schematic of the different positions of the elastic (left), measured FFT results (right).

The results of this experimental test (see Figure 6.25 right) clearly shows a variation on the recorded transversal frequency of the wire (ω_T), from 1446 Hz in position 1, to 1445 in position 2 and 1444 in position 3. As the wire length (L_0 = 115 mm) and mass (m = 2.26 mg) are known, the initial tension (T_0) can be calculated from ω_T using the following equation,

$$\omega_T = \sqrt{4 T_0 / m L_0} \qquad (6.14)$$

Table 6.6: wire tension results as function of the elastic element position.

position	Freq. [Hz]	T_0 [N]
1	1446	0.13557
2	1445	0.13538
3	1444	0.13520

Table 6.6 shows the wire tension values calculated form Eq. (6.14), the resolution on the tension variation is better than the mN.

Wire transversal deflection simulation

This strategy would correct the error due to the wire transversal oscillation. The procedure consists on introducing the effective motion pattern recorded from the angular position sensor for a given scan in the wire dynamic model. As a result, the dynamic model can provide the wire transversal deflections as shown in Figure 6.23. From those simulated values, the effective error affecting the measurement can be calculated and used to perform the suitable on-line correction on the beam width measurement.

6.7. Summary

A new rotating wire scanner design has been achieved. A thorough design process has been conducted from the conceptual design to the proposal of specific measurement correction factors, through the optimization of the critical parts involved of the measurement chain and the procedure to optimize the motion pattern. The design profited significantly from the comprehensive set of studies (simulations and experiments) based on the existing PS scanners.

The new design concept eliminates some typical sources of error as the mechanical play. In addition, the optimization of the main component of the mechanical chain gives very low values of deflection and vibration amplitude.

The dynamic models and the vibration measurements presented in this thesis work will serve to improve the new system reliability, accuracy and performance monitoring. This includes the definition and implementation of the proper calibration procedures to correct for systematic errors.

The influence of the control system on the final device performances has been shown. In order to minimize this influence, a motion pattern optimization strategy integrating the controls system model has been proposed.

Despite not having performed any tests on the final device, the simulation using a non-optimized smooth motion pattern shows that the performances of the new device are much better than those of the operating PS device used as reference. The optimization of the motion pattern together with the calibration of the devices will allow to meet the requirements.

Future work will be focused on the implementation of the motion pattern optimization in order to mitigate the influence of the control system. The construction and implementation of the calibration test bench is also part of the forthcoming work. Finally, during the first operation time it is foreseen the test and tuning of the correction factors described above. It is expected that this will require a learning process of some cycles of operation to understand the evolution of the device behavior along time.

7. Conclusions

Wire scanner instruments are used to measure beam profile in particle accelerators. The main requirement for this type of instrument is the accuracy on wire position determination. Errors on the wire position when intersecting the beam have a direct consequence on the profile and position measurement accuracy. Thus, identifying and minimizing the uncertainties and error sources was the main goal of this thesis work.

In this work the sources of error affecting the rotating wire scanner instrument are clearly identified. This identification is based on two concepts described in this document; the *measurement chain* and the *dynamic effect errors.* The error sources identification represents central part of this work from which the analysis of the performance of the existing PS scanners has been achieved. Additionally these error sources have been used as the main indicators to define the new wire scanner concept and their design optimization strategies.

A *vibration measurement system* has been developed which allows the monitoring of wire scanner vibrational behaviour. In addition, several *dynamic models* have been built which has enabled the vibrational behaviour of the wire scanner to be understood.

The vibration measurement system allowed showing the temporal vibrational behaviour of the PS fork-wire assembly and identifying the main frequencies involved in the vibrations. Furthermore the measurement of vibrations based on the wire piezo-resistive effect has been tested and its efficacy has been shown. This technique allows evaluating the vibrational behaviour of a wire scanner instrument without the need to include any external sensor on the device, the thin carbon wire is the sensor in itself. Therefore measurement of vibrations based on the wire piezo-resistive effect can be easily implemented in existing wire scanner devices because only an external signal measurement system is required.

Further it has been shown that a combination of vibration measurement and dynamic models allows profile and position error estimation. For the PS scanner the error due to the dynamic effect is responsible for up to 0.8 % relative position error position and 2.45 % relative beam width error measurement.

The results of the vibration measurement and analytical simulation performed on the PS wire scanner show that the tips separation has a direct consequence on the initial wire tension. Thus, the wire is actually a mechanical system with a variable parameter, which may result in parametric oscillations, that can reach very detrimental high values. On the other hand, the inertia forces associated with the accelerated rotation of the fork may also contribute to wire oscillations in the transverse dimension. Thus, the real behaviour of the wire can be viewed as a result of a driven oscillation (associated with the inertia forces) and a parametric oscillation (associated with the wire tension changes). These studies performed on the PS wire scanner, whose fork is extremely flexible in the wire longitudinal direction, clearly demonstrate that parametric wire oscillations can occur in such type of devices. Therefore it has been decided to avoid the use of a flexible fork in the new design, and thus keep the wire tension as constant as possible. Nevertheless the performed FE modal analysis on the new design shows vibration modes that could yield parametric resonances. As a consequence, also for the new design, it is recommended to carefully study the initial wire tension in order to minimize the effect of parametric oscillations on the wire position determination.

In summary, the performance of the new wire scanner system has been improved on three levels: conceptual level, design level and operation level. Although the new prototype has not been fully tested yet, we show in this work that the new design represents a significant improvement over the existing PS scanner. For example the contribution to the error from the mechanical play in the former design could reach values of 1.2 mm, on the fork tip, while in the new design the mechanical play contribution error is zero. The design optimization strategy performed on the most critical parts of the new system has contributed to minimize the error from dynamic effects. The deflection on the fork tips due to the dynamic effects is in the range 1.5 mm for the PS scanner, whereas in the new design this deflection is in the range of 0.08 mm. In regard to the operation of this new design, a motion pattern optimization strategy has been proposed which will allow to optimize the operation of the device from the vibration point of view. Finally, several post-processing correction strategies have been suggested to minimize the remaining measurement errors, which cannot be eliminated through design, calibration or operation.

The implementation of the motion pattern optimization for the new devices can be considered as one of the most promising strategies to minimize the remaining vibration. Section 6.4.3 shows that the final behaviour of the new system is very sensitive to the control system performances. Therefore the integration of the control system into the pattern optimization process can improve the global behaviour of the system.

Additional further work will focus on the implementation of the vibrational measurement based on the wire piezo-resistive effect in the new wire scanner design. This has not been possible during the thesis work, as the available prototype was not under vacuum and this kind of measurements is highly influenced by the air environment.

The implementation of the off-line correction factors strategy presented on Section 6.6 is another of the relevant topics. Also the implementation of this strategy needs the prototype to be in realistic operation conditions. Additionally the evaluation of some of the correction factors will require real beam profile measurement and therefore measurements performed with beam.

A first prototype on the new scanner has been already installed on the SPS accelerator and will be tested along 2016. The optimization strategies, not yet implemented, as the motion pattern optimization or the off-line correction factor will be also implemented and evaluated at this time.

A. Appendix - PS scanner motor-fork kinematic chain

The transmission of the rotational movement between the motor shaft and the fork is achieved through a kinematical chain which introduces a non-linear relationship between the motor angular rotation and that of the fork. This appendix is devoted to the study of that kinematical chain in order to obtain the equations relating the motor and the fork motions. Figure A.1 shows a cross section of the PS wire scanner where the main parts of the kinematical chain are highlighted. Figure A.2 shows a simplified scheme of the chain and the notation that will be used in the equations.

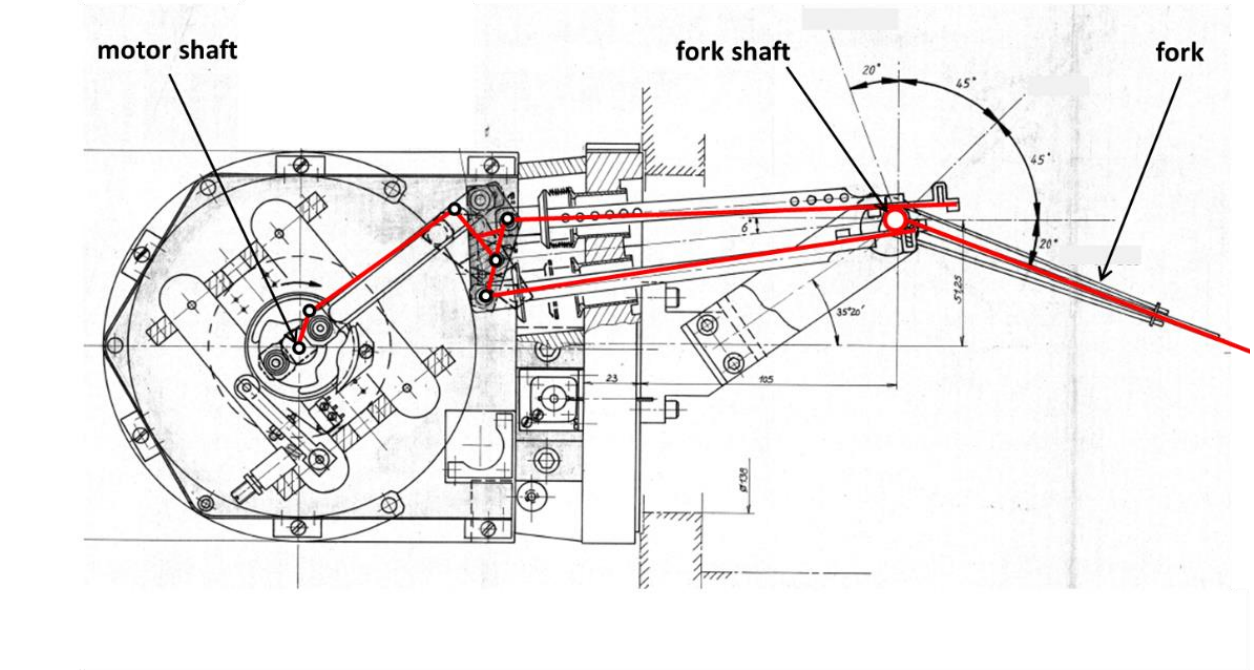

Figure A.1: Motor-fork kinematical chain of the PS wire scanner

The mechanism can be divided in two parts. The first part consists on a four-bar mechanism. The second part is made by two push-pull roads which transform the linear motion from the four-bar mechanism on a rotation at the fork axis. Four metallic bands attached to the push-pull rods and surrounding the fork shaft transmits the motion from the rods to the fork shaft (see Figure 3.14).

The relationship between the motor rotation angle θ_m and that of the fork θ $\left(\theta = \theta(\theta_m)\right)$, has been obtained in two stages: we first determine $\varphi_1 = \varphi_1(\theta_m)$, then $\varphi_2 = \varphi_2(\varphi_1)$ and then $\theta = \theta(\varphi_1)$. The combination of these results yields $\theta = \theta(\theta_m)$.

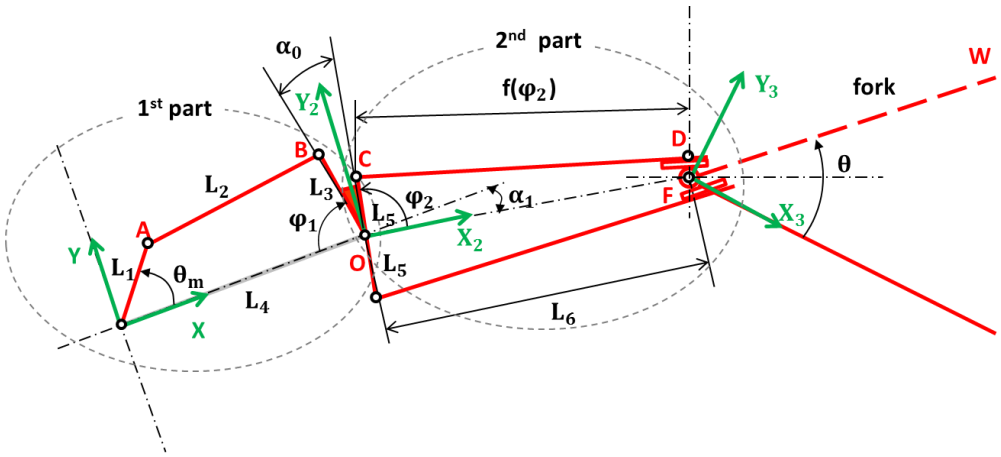

Figure A.2: Motor-fork kinematical chain

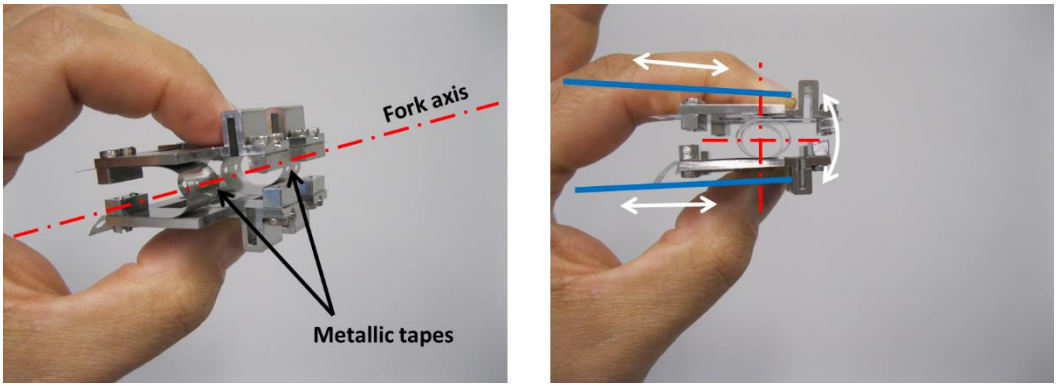

Figure A.3: Detail of the four tapes assembly which transmit the linear movement of the push-pull rods in a rotation on the fork shaft.

The first part of the mechanism is governed by the following equation:

$$L_2^2 = (B_x - A_x)^2 + (B_y - A_y)^2 = ((L_4 - L_3\cos\varphi_1) - L_1\cos\theta_m)^2 + (L_3\sin\varphi_1 - L_1\sin\theta_m)^2, \quad \text{(A.1)}$$

where the (X_1, Y_1) coordinate system has been used and from which $\varphi_1 = \varphi_1(\theta_m)$ is obtained.

The relationship $\varphi_2 = \varphi_2(\varphi_1)$ is straightforward:

$$\varphi_2 = \pi + \alpha_1 - \alpha_0 - \varphi_1 \quad \text{(A.2)}$$

Figure A.4 shows a more detailed description of the second part of the mechanism. Note that the distances between points C and D and between points C and F are not constant but a function of angle φ_2.

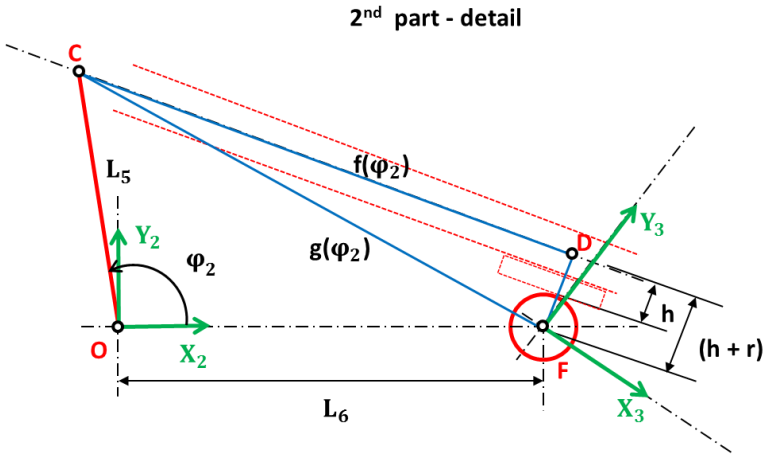

Figure A.4: Detailed description of the second part of the mechanism

The second part of the kinematic chain obeys the following equations:

$$g^2(\varphi_2) = (F_x - C_x)^2 + (F_y - C_y)^2 = (L_6 - L_5\cos\varphi_2)^2 + (L_5\sin\varphi_2)^2,$$
$$f^2(\varphi_2) = g^2(\varphi_2) - (r+h)^2, \qquad \text{(A.3)}$$

where the (X_2, Y_2) coordinate system has been used.

The relationship $\theta = \theta(\varphi_2)$ is obtained from

$$\theta = \frac{f(\varphi_2) - f(\varphi_2)_{min}}{r+h}, \qquad \text{(A.4)}$$

where $f(\varphi_2)_{min}$ is the minimum value of the distance between C and D, and corresponds to a configuration where the fork is aligned with the X_3 axis.

Finally, since φ_2 is function of φ_1 and φ_1 is function of θ_m, we have the relationship between θ, and θ_m is obtained.

The numerical solution of the previous set of equations is presented in Figure A.5 and Figure A.6.

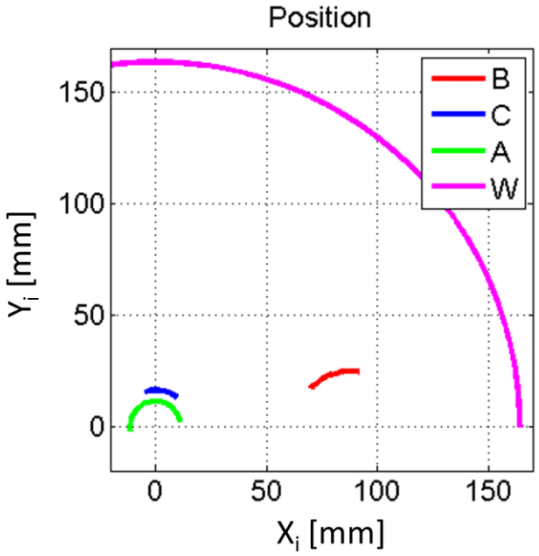

Figure A.5: Trajectories of several points of the mechanism.

Figure A.5 shows the trajectories of different points of the mechanism. Different coordinates systems have been used: (X_1, Y_1) for points A and C, (X_2, Y_2) for point E, and (X_3, Y_3) for point W (representing the fork tip).

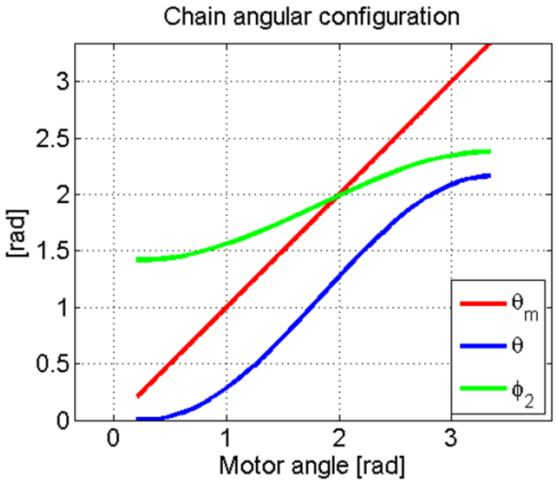

Figure A.6 : Mechanism angles as a function of the motor angle.

Figure A.6 shows the $\theta_f = \theta_f(\theta_m)$ $\theta_f = \theta_f(\theta_m)$ and $\varphi_2 = \varphi_2(\theta_m)$ relationships. The trivial one $\theta_m = \theta_m$ has been included as a reference.

B. Appendix – Electronic circuits

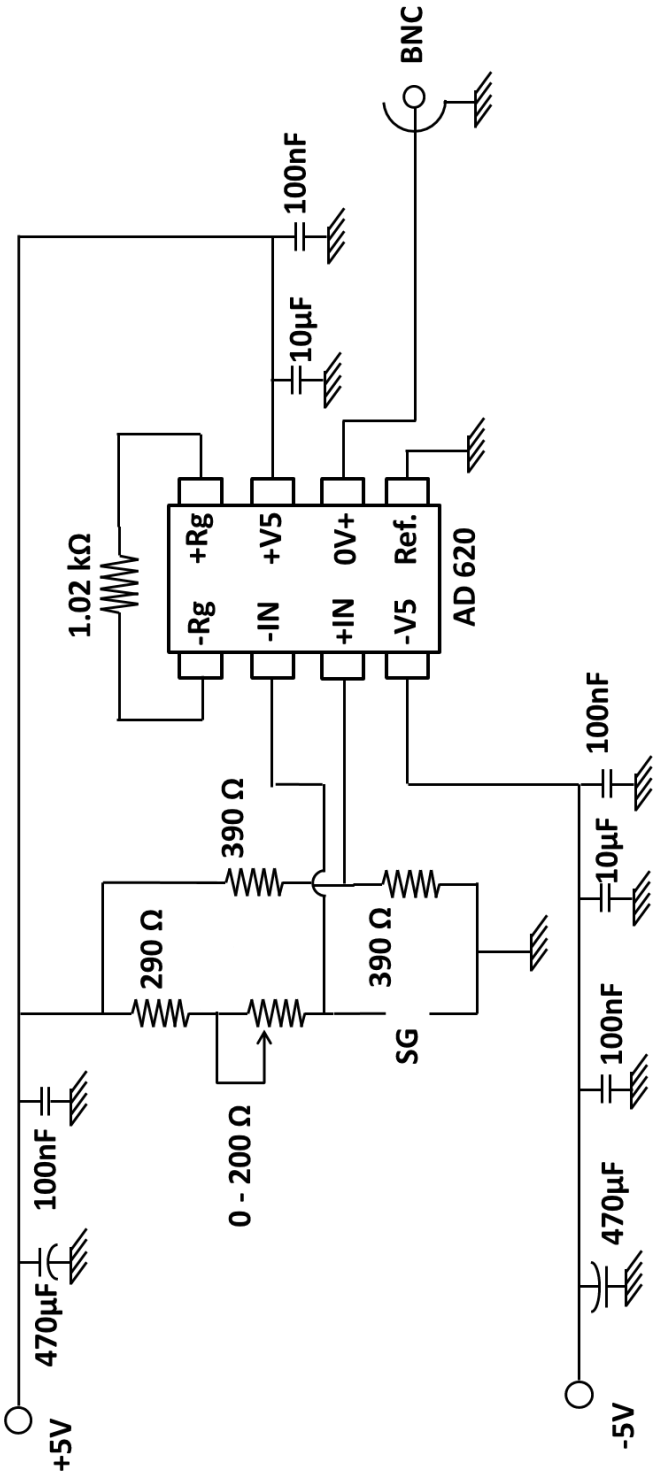

Figure B.1: Strain gauges electronic circuit.

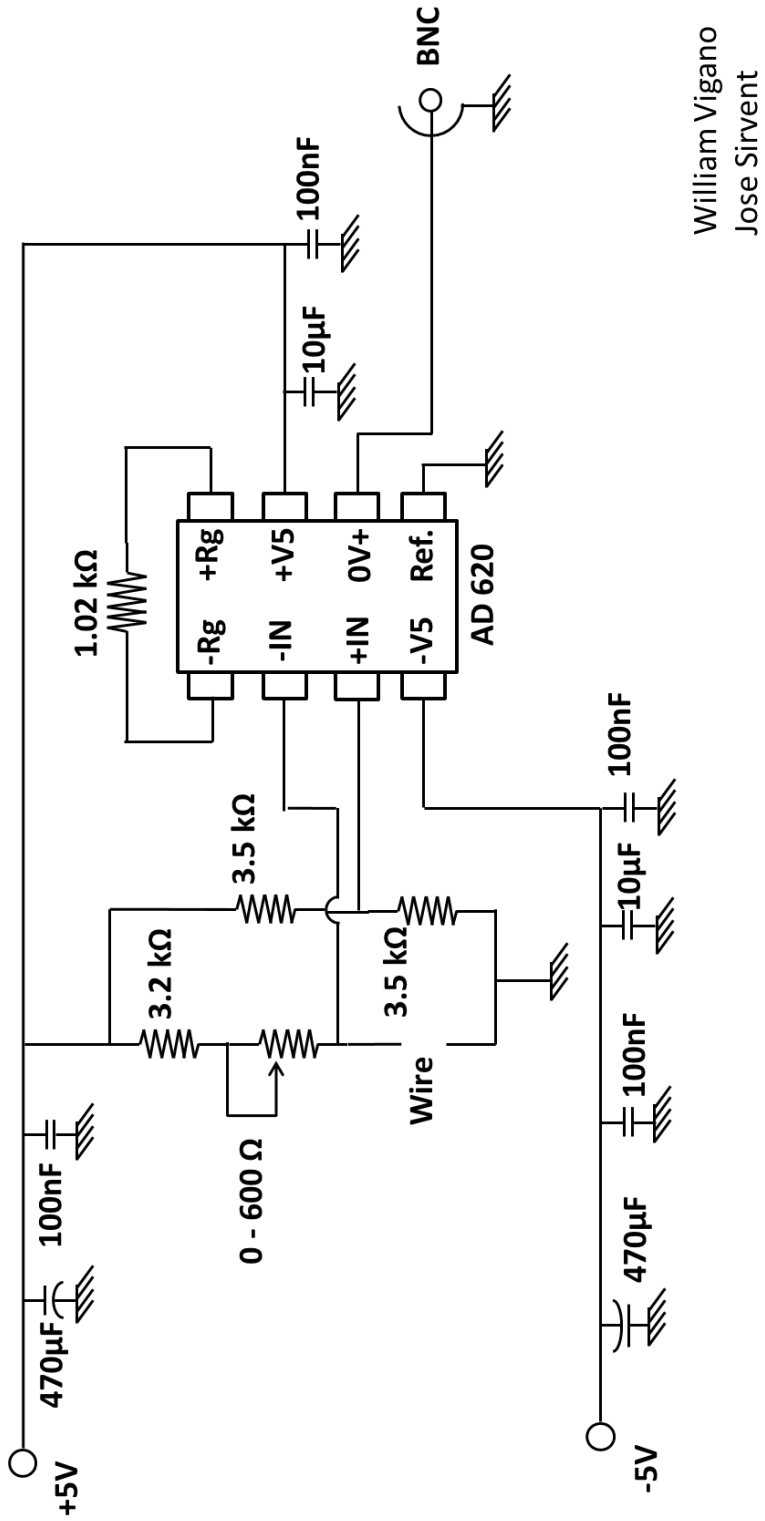

Figure B.2: Wire electronic circuit.

C. Appendix - Wire continuous model (CM)

A continuous model for the wire was studied and compared to the discrete one. We will prove that, under the hypothesis that the wire moves according to its first natural mode, the equations are equivalent to those of the DM.

In the CM model, the wire is treated as a uniform taut string. Under the hypothesis of small vibration amplitude and neglecting the longitudinal motion (for consistency with the DM), its free behaviour is described through the classical wave equation:

$$\frac{\partial^2 r(\xi,t)}{\partial t^2} = c_T^2 \frac{\partial^2 r(\xi,t)}{\partial \xi^2} \quad , \tag{C.1}$$

where c_T is the propagation speed of the transversal waves ($c_T = \sqrt{T_0 / \mu_0}$, with μ_0 = linear string density) and ξ is the wire longitudinal coordinate (the fork tips correspond to $\xi = 0$ and $\xi = L_0$).

When the scan cycle begins, the drag forces per unit mass (forcing terms) have to be added in the rhs of Eq.(C.1):

$$\frac{\partial^2}{\partial t^2}\begin{Bmatrix} x \\ y \end{Bmatrix} - c_T^2 \frac{\partial^2}{\partial \xi^2}\begin{Bmatrix} x \\ y \end{Bmatrix} = H \begin{Bmatrix} \dot{\theta}^2 \sin\theta - \ddot{\theta}\cos\theta \\ \dot{\theta}^2 \cos\theta + \ddot{\theta}\sin\theta \end{Bmatrix} \quad . \tag{C.2}$$

The analytical solution of the transverse free vibration of a string with fixed ends is well known. It can be described in the time domain through the impulse responses $h_q(\xi,t)$ (in our case, $q = x, y$). The general vibration of a string under general forcing terms $dF_q(\xi,t)$ is then obtained through a convolution product:

$$q(\xi,t) = h_q(\xi,t) * dF_q(\xi,t) = \int_0^t h_q(\xi, t-\tau) * dF_q(\xi,\tau)\, d\tau \quad . \tag{C.3}$$

The impulse responses can be either described as global function or through the superposition of the modal impulse responses. In that case, the forcing terms have to be projected on the modal basis and convolved with the corresponding modal responses:

$$h_q(\xi,t) = \sum_{n=1}^{\infty} h_n(\xi,t) = \sum_{n=1}^{\infty} \Psi_n(\xi) T_n(t) \Rightarrow q(\xi,t) = \sum_{n=1}^{\infty} \Psi_n(\xi) T_n(t) * Q_n^q(\xi,t) \quad , \tag{C.4}$$

where $\Psi_n(\xi)$ are the string eigenmodes, ω_n are the angular eigenfrequencies and

$$T_n(t) = \frac{1}{m_n \omega_n} \sin(\omega_n t) \quad , \text{with} \quad m_n = \int_0^{L_0} \mu_0 \sin^2\left(n \frac{\pi}{L_0} \xi\right) d\xi = \frac{1}{2} \mu_0 L_0 \quad . \tag{C.5}$$

The boundary conditions (fixed ends in our case, $x(0,t) = x(L_0,t) = y(0,t) = y(L_0,t) = 0$) determine the eigenfrequencies and the eigenmodes:

$$\omega_n = n\left(\pi \frac{c_T}{L_0}\right), \; \Psi_n(\xi) = \sin\left(n \frac{\pi}{L_0} \xi\right) \quad . \tag{C.6}$$

The modal excitations are calculated as:

$$Q_n^q(t) = \mu_0 \int_0^{L_0} \frac{dF_q}{dm} \Psi_n(\xi) d\xi = \mu_0 \int_0^{L_0} \frac{dF_q}{dm} \sin\left(n \frac{\pi}{L_0} \xi\right) d\xi \quad . \tag{C.7}$$

As in our case $\left(dF_{x,y} / dm\right)$ do not depend on ξ, the integral is straightforward:

$$Q_n^q(t) = \frac{\mu_0 L_0}{n\pi} \frac{dF_q(t)}{dm} \left(\cos(n\pi) - 1\right) \Rightarrow \begin{cases} Q_{2n}^q(t) = 0 \\ Q_{2n+1}^q(t) = -\dfrac{2\mu_0 L_0}{(2n+1)\pi} \dfrac{dF_q(t)}{dm} \end{cases} \quad . \tag{C.8}$$

As expected, only the uneven modes participate in the total vibration.

Putting everything together:

$$\begin{Bmatrix} x(\xi,t) \\ y(\xi,t) \end{Bmatrix} = -\frac{4HL_0}{\pi^2 c_T} \sum_{n=0}^{\infty} \frac{1}{(2n+1)^2} \sin\left((2n+1)\frac{\pi}{L_0}\xi\right) \sin\left((2n+1)\frac{\pi c_T}{L_0} t\right) * \begin{Bmatrix} \dot{\theta}^2 \sin\theta - \ddot{\theta}\cos\theta \\ \dot{\theta}^2 \cos\theta + \ddot{\theta}\sin\theta \end{Bmatrix} \quad . \tag{C.9}$$

The symmetry of the problem is responsible for the fact that only the uneven modes participate in the motion. For the sake of simplicity, just the first one was considered. Thus comparisons between DM and CM were straightforward.

Under this hypothesis, Eq.(C.9) simplifies into:

$$\begin{Bmatrix} x(\xi,t) \\ y(\xi,t) \end{Bmatrix} = -\frac{4HL_0}{\pi^2 c_T}\sin\left(\frac{\pi}{L_0}\xi\right)\sin\left(\frac{\pi c_T}{L_0}t\right) * \begin{Bmatrix} \dot{\theta}^2\sin\theta - \ddot{\theta}\cos\theta \\ \dot{\theta}^2\cos\theta + \ddot{\theta}\sin\theta \end{Bmatrix} \quad . \tag{C.10}$$

It corresponds to a forced vibration of a string whose natural angular frequency is that of the first mode: $\omega_C = (\pi/L_0)c_T$.

When the string tension variations (associated with the wire length changes) are taken into account, the wave equation for the transverse motion become

$$\frac{\partial^2}{\partial t^2}\begin{Bmatrix} x \\ y \end{Bmatrix} - \left[c_T^2 + \frac{c_L^2 - c_T^2}{L_0}\left(-2z_0\cos(\Omega t) + \frac{1}{2}\int_0^{L_0}\left(\frac{\partial r}{\partial \xi}\right)^2 d\xi \right) \right] \frac{\partial^2}{\partial \xi^2}\begin{Bmatrix} x \\ y \end{Bmatrix} = H\begin{Bmatrix} \dot{\theta}^2\sin\theta - \ddot{\theta}\cos\theta \\ \dot{\theta}^2\cos\theta + \ddot{\theta}\sin\theta \end{Bmatrix} \quad , \tag{C.11}$$

where $c_L = \sqrt{E \cdot A/\mu_0}$ is the propagation speed of the longitudinal waves. Again the fork tips motion has been described as $\Delta z_{tips} = 2z_0\cos(\Omega t)$. Note that $\left(c_T^2/c_L^2\right) = \varepsilon$, and so Eqs.(C.11) can be simplified by taking $\left(c_L^2 - c_T^2 \simeq c_L^2\right)$.

Assuming again that the wire vibration will correspond mainly to the first mode and introducing variable separation, the (x,y) vibration patterns can be expressed as

$$\begin{Bmatrix} x \\ y \end{Bmatrix} = \sin\left(\frac{\pi}{L_0}\xi\right)\begin{Bmatrix} T_x(t) \\ T_y(t) \end{Bmatrix} \quad . \tag{C.12}$$

Thus:

$$\frac{1}{2}\int_0^{L_0}\left(\frac{\partial r}{\partial \xi}\right)^2 d\xi = \frac{1}{2}\int_0^{L_0}\left(\frac{\partial\sqrt{x^2+y^2}}{\partial \xi}\right)^2 d\xi = \frac{\pi^2}{4L_0}\sqrt{T_x^2(t) + T_y^2(t)} \quad . \tag{C.13}$$

Taking into account $\left(c_T^2/c_L^2\right) = \varepsilon$ and $\omega_C = (\pi/L_0)c_T$, Eqs.(C.13) become:

$$\frac{d^2}{dt^2}\begin{Bmatrix} T_x \\ T_y \end{Bmatrix} + \omega_C^2\left(1 + \frac{1}{L_0}\frac{1}{\varepsilon}\left(\frac{\pi^2}{4L_0}\left(T_x^2 + T_y^2\right) - 2z_0\cos(\Omega t)\right)\right)\begin{Bmatrix} T_x \\ T_y \end{Bmatrix} = H\begin{Bmatrix} \dot{\theta}^2\sin\theta - \ddot{\theta}\cos\theta \\ \dot{\theta}^2\cos\theta + \ddot{\theta}\sin\theta \end{Bmatrix} . \qquad \text{(C.14)}$$

These equations are qualitatively identical to Eqs. (5.8), the only difference being the coefficient appearing in the cubic terms (associated to the fact that in the DM the shape of the oscillating wire is triangular whereas in the CM it has a sinusoidal profile).

Bibliography

[1] J. Ficher, Functional Specification - Measurement of the transverse beam distribution in the LHC rings, EDMS 328147, CERN, Switzerland 2003.

[2] Sapinski M., 2008, “Model of Carbon Wire Heating in Accelerator Beam”, CERN-AB-2008-030 BI, CERN.

[3] Bosser J., 1996, “Beam Instrumentation”, CERN, p 253 – 255.

[4] Wilke, M.,1994., “Status and Test Report on the LANL-Boeing APLE/HPO Flying-Wire Beam-Profile Monitor,” Los Alamos LA-12732-SR Status Report, UC-906, Issued: July, 1994.

[5] Blokland W., 1997, “A new flying wire system for the Tevatron”, Particle accelerator conference, 1997.

[6] Gilpatrick J. D., 1998, “Techniques for Intense-Proton-Beam Profile Measurements”, Los Alamos National Laboratory.

[7] Shiraishi S., 2009, “Analysis of Tevatron Flying Wire and Diffusion Measurement”, University of Chicago.

[8] Igarashi S., 2002, “Flying wire beam profile monitors at the KEK PS main ring”, Nuclear Instruments and Methods in Physics Research A 482 (2002) 32–41.

[9] Sapinski M., 2008, “Model of Carbon Wire Heating in Accelerator Beam”, CERN-AB-2008-030 BI, CERN.

[10] Steinbach Ch., 1985, “A scanning wire beam profile monitor”, IEEE Transactions on Nuclear Science. Vol. NS-32, NO. 5, October 1985.

[11] Bosser J., 1984, “Transverse emittance measurement with a rapid wire scanner at the CERN SPS”, Nuclear Instruments and Methods in Physics Research A235 (1985) 475-480.

[12] Sapinski M., 2012 “Beam interaction with thin materials: heat deposition, cooling phenomena and damage limits”, BIW’12 Workshop – Newport News – VA/USA.

[13] Vuitton C., 2012, Private communication, CERN.

[14] Gerard D.,2012, Private communication, CERN.

[15] Lozowski W.R., 2008, “Carbon micro-ribbon and strip polarimeter targets for the AGS and RHIC”, Nuclear Instruments and Methods in Physics Research A 590 (2008) 157–163.

[16] Roncarolo F., 2005, “Accuracy of the Transverse Emittance Measurements of the CERN Large Hadron Collider”, Ecole Polytechnique Fédérale de Lausanne.

[17] Koopman J., 2009, “Fast wire scanner calibration”, DIPAC’09 Conference – 25-27 May 2009 /Basel-CH.

[18] Tigner M., 2008, Private communication to Bernd Dehning.

[19] Iida N., 1998, “A method for measuring vibrations in wire scanner beam profile monitors”, Proc of APAC'98, Tsukuba, Japan, March 1998 pp.546-548.

[20] Vibrating Wire Strain Gauge, Data sheet 1102-12 R01, Encardio-Rite Electronics PVT. LTD.

[21] Spot-Weldable Strain Gauge, Copyright 6/2009 by Durham Geo-Enterprises. Geotechnical and Structural Instrumentation.

[22] Kuhinek D., 2007, “Enhanced Vibrating Wire Strain Sensor”, Instrumentation and Measurement Technology Conference - IMTC 2007 Warsaw, Poland, May 1-3, 2007.

[23] Arutunian S., 1999, “Vibrating Wire Scanner for beam profile monitoring”, Proceedings of the 1999 Particle Accelerator Conference, New York, 1999.

[24] Arutunian S., 1999, “Magnetic field distribution measurement by vibrating wire strain gauge”, Proceedings of the 1999 Particle Accelerator Conference, New York, 1999.

[25] Arutunian S., 2010, “Large aperture electron beam scan with vibrating wire monitor in air”, Proceedings of IPAC’10, Kyoto, Japan.

[26] Arutunian S., 2002, “Problems of installation of vibrating wire scanners into accelerator vacuum chamber”, Proceedings of EPAC 2002, Paris, France.

[27] M.El-Attar, A.Ghobarah, T.S.Aziz, Non-linear cable response to multiple support periodic excitation, Engineering Structures 22 (2000) 1301-1312.

[28] C.T.Georgakis, C.A.Taylor, Nonlinear dynamics of cable stays. Part I: sinusoidal cable support excitation, Journal of Sound and Vibration 281 (2005) 537-564.

[29] H.Dresig, U.Schreiber, Vibration Analysis for Planetary Gears. Modeling and Multibody Simulation , Proceedings of the International Conference on Mechanical Engineering and Mechanics, Nanjing, October 2005.

[30] J.Kuria, J.Kihiu, Modeling Parametric Vibration of Multistage Gear Systems as a Tool for Design Optimization, World Academy of Science, Engineering and Technology 2 (2008) 2-22.

[31] W.Kim, L.Y.Ji Yeong Lee, J.Jintai Chung, Dynamic analysis for a planetary gear with time-varying pressure angles and contact ratios, Journal of Sound and Vibration 331 (2012) 883-901.

[32] C.Holden, R. Galeazzi, C.Rodríguez, T.Perez, T.Fossen, M.Blank, M.Almeida, Nonlinear Container Ship Model for the Study of Parametric Roll Resonance, Modeling, identification and control 28(4) (2007) 87-103.

[33] J-L.Le Carrou, F.Gautier, Sympathetic String Modes in the Concert Harp, Acta Acustica united with Acustica 95 (2009) 744-752.

[34] W.Z.Zhang, R.Baskaran, K.L.Turner, Effect of cubic nonlinearitry on auto-parametrically amplified resonant MEMS mass sensor, Sensors and Actuators A 102 (2002) 139-150.

[35] L.Ng, R.Rand, Bifurcations in a Mathieu equation with cubic nonlinearities, Chaos, Solitons and Fractals 14 (2002) 173-181.

[36] H.Alberg, Parametrically excited vibrations – Numerical and analytical investigation of simple mechanical systems, Rakenteiden Mekaniikka 18(2) (1985) 3-14.

[37] N.B.Tufilaro, Nonlinear and chaotic string vibrations, American Journal of Physics 57(5) (1988) 408-414.

[38] C.Gough, The nonlinear free vibration of a damped elastic string, Journal of the Acoustical Society of America 75(6) (1983) 1770-1776.

[39] B.Bank, L.Sujbert, A piano model including longitudinal string vibrations, Proceedings of the 7th International Conference on Digital Audio Effects (DAFx'04), Naples 2004, pp. 89-94.

[40] G.V.Anand, Large-Amplitude Damped Free Vibration of a Stretched String, Journal of the Acoustical Society of America 45(5) (1969) 1089-1096.

[41] S.A.Nayfeh, A.H.Nayfeh, D.T.Mook, Nonlinear Response of a Taut String to Longitudinal and Transverse End Excitation, Journal of Vibration and Control 1 (1995) 307-334.

[42] D.R.Rowland, Parametric resonance and nonlinear string vibrations, American Journal of Physics 72(6) (2004) 758-766.

[43] T.Tolonen, V.Välimäki, M.Karjalainen, Modeling of Tension Modulation Nonlinearity in Plucked Strings, IEEE Transactions on Speech and Audio Processing 8(3) (2000) 300-310.

[44] J.Pakarinen, V.Välimäki, M.Karljainen, Physics-Based Methods for Modeling Nonlinear Vibrating Strings, Acta Acustica united with Acustica 91 (2005) 312-325.

[45] A.Itö, Successive Subharmonic Bifurcations and Chaos in a Nonlinear Mathieu Equation, Progress of Theoretical Physics 61(3) (1979) 815-824.

[46] H.Kidachi, H.Onogi, Note on the Stability of the Nonlinear Mathieu Equation, Progress of Theoretical Physics 98(4) (1997) 755-773.

[47] J.Herranz, A.Barjau, B.Dehning, Vibration measurements of a wire scanner – experimental setup and models, Journal of Mechanical Systems and Signal Processing (2015)

[48] J.Herranz, A.Barjau, B.Dehning, Ewald Effinger, Jonathan Emery, Wire scanners, Ana Guerrero, Carlos Pereira, Wire scanners and vibrations – models and measurements, International Beam Instrumentation Conference 2015 (IBIC 2015), Melbourne.

[49] A.Barjau, J.Herranz, B.Dehning, Dynamical models of a wire scanner, Journal of Vibration and Acoustics, Accepted.

[50] W.Andreazza, N.Chritin, B.Dehning, J.Emery, D.Gudkov, J.Herranz Alvarez, P.Magagnin, E.Piselli, R.Veness, S.Samuelsson, Experience from the construction of a new fast wire scanner prototype for the CERN-SPS and its optimisation for installation in the CERN-PS Booster, International Beam Instrumentation Conference 2015 (IBIC 2015), Melbourne.

[51] S. Samuelsson, Mechanical optimisation of a high-precision fast wire scanner at CERN, Master Thesis, Chalmers University of Technology, Gothenburg, Sweden 2013.

[52] Lambrechts P., 2003, “Trajectory planning and feedforward design for electromechanical motion systems, Technische Universiteit Eindhoven”.

[53] Jonathan Emery, Ana Barjau, Bernd Dehning, Juan Herranz Alvarez, Pierre-Jean Lapray, Matteo Macchini, 2015, CERN Beam Wire-Scanner instrument Electronics and Control Architecture: Design and Validation Methodology from Simulation to Field tests, Preprint submitted to 2016 European Control Conference.